
Electronic Thesis and Dissertation Repository

3-26-2021 2:30 PM

Non-Linear Effects of Solution Parameters and Gamma Radiation on Nickel Oxidation Dynamics

Razieh Karimihaghighi, *The University of Western Ontario*

Supervisor: Wren, Jungsook Clara, *The University of Western Ontario*

A thesis submitted in partial fulfillment of the requirements for the Doctor of Philosophy degree in Chemistry

© Razieh Karimihaghighi 2021

Follow this and additional works at: <https://ir.lib.uwo.ca/etd>

 Part of the [Materials Science and Engineering Commons](#), and the [Physical Chemistry Commons](#)

Recommended Citation

Karimihaghighi, Razieh, "Non-Linear Effects of Solution Parameters and Gamma Radiation on Nickel Oxidation Dynamics" (2021). *Electronic Thesis and Dissertation Repository*. 7789.
<https://ir.lib.uwo.ca/etd/7789>

This Dissertation/Thesis is brought to you for free and open access by Scholarship@Western. It has been accepted for inclusion in Electronic Thesis and Dissertation Repository by an authorized administrator of Scholarship@Western. For more information, please contact wlsadmin@uwo.ca.

ABSTRACT

Nickel is the main component in nickel-based superalloys which are known for their superior corrosion resistance and mechanical properties. These alloys are used in nuclear power plants, mainly for thin-walled heat exchanger tubing where these materials are exposed to a continuous flux of ionizing radiation. The long-term corrosion behaviour of these alloys at high temperatures and in the presence of γ -radiation is not well understood. Moreover, the mechanism by which nickel improves the corrosion resistance of these alloys is also not known. Therefore, a mechanistic understanding of the nickel oxidation process is required to develop a predictive corrosion model for nickel-containing alloys.

This thesis presents a systematic study of the corrosion dynamics of pure nickel in different solution environments. Aqueous corrosion is an electrochemical process involving many elementary steps, which include the interfacial transfer of electrons and metal atoms, solution reactions of metal cations (hydrolysis), mass transport processes, and precipitation of metal oxide. The kinetics of the elementary reactions are strongly coupled, which leads to systemic feedback between different elementary steps. To predict the long-term corrosion behaviour of nickel-containing alloys, it is important to identify the key elementary processes that control the overall corrosion rate. In this thesis, the effect of γ -radiation and solution environment (temperature, pH, ionic strength) on the short-term and long-term corrosion behaviour of pure nickel is investigated. A combination of electrochemical techniques and coupon-exposure tests combined with post-test analyses is used to study the nickel oxidation process.

The findings of this work indicate that the overall nickel oxidation dynamics evolve through different phases as corrosion progresses. The elementary steps that control the overall metal oxidation rate in each phase were identified. Phase I involves net electron/metal atom transfer at the metal-solution interface ($\text{Ni}^0_{(m)} \rightleftharpoons \text{Ni}^{2+}_{(solv)} + 2 e^-$), diffusion of Ni^{2+} from the interfacial region into the bulk solution, and hydrolysis of Ni^{2+} to produce $\text{Ni}(\text{OH})_2$, which can condense as colloids. In Phase II, in addition to the elementary steps that comprise Phase I, additional elementary steps involving the Ni^{2+} hydrolysis product $\text{Ni}(\text{OH})_2$, and interfacial electron transfer ($\text{Ni}^{2+}/\text{Ni}(\text{OH})_2 + \text{OH}^- \rightleftharpoons \text{Ni}(\text{OH})_3 + e^-$) occur that accelerate the precipitation of mixed $\text{Ni}^{\text{II}}/\text{Ni}^{\text{III}}$ hydroxide, growing a hydrogel network. Phase III occurs after sufficient mixed $\text{Ni}^{\text{II}}/\text{Ni}^{\text{III}}$ hydroxide colloids have precipitated to allow nucleation and growth as solid crystalline particles on the surface.

This study also reveals the non-linear nature of nickel corrosion dynamics over long time periods. It is the combination of solution parameters that dictates how fast the system can transition through different dynamic phases, and which final dynamic phase the overall metal oxidation process can reach. The kinetics of the elementary steps are strongly coupled and describing the overall metal oxidation dynamics based on linear dynamics is not valid. The mechanism proposed in this thesis deviates from the corrosion mechanisms that underpin most existing corrosion rate models. The new mechanism presented here is capable of accounting for many phenomena observed (in relation to the effects of solution parameters on nickel corrosion) that are not explainable using existing mechanistic models. The proposed mechanism can also explain the corrosion behaviour of nickel in the presence of γ -radiation. From the time-dependent electrochemical studies,

different metal oxidation rate parameters can be extracted which are required to develop a predictive corrosion model for nickel-containing alloys.

KEYWORDS

Nickel; Nickel based alloys; Oxide Film Formation; Metal Dissolution; Interfacial Reactions; Electrochemical Reactions; Water Radiolysis; Gamma-Radiation.

SUMMARY FOR LAY AUDIENCE

Nickel is an important element in nickel-based superalloys that are commonly used for system components in nuclear power plants, mainly for thin-walled heat exchanger tubing. These materials are exposed to a continuous flux of ionizing radiation, which can affect their long-term corrosion behaviour. The underlying processes that determine the properties of the oxides formed and their long-term corrosion behaviour are not well understood, particularly at high temperatures and in the presence of γ -radiation.

This thesis presents a systematic study of the corrosion dynamics of pure nickel and presents a mechanistic understanding of the corrosion process. The effect of γ -radiation and solution environment (temperature, pH, ionic strength) on the short-term and long-term corrosion behaviour of pure nickel was investigated using a combination of electrochemical techniques and coupon-exposure tests.

The results presented in this thesis show that the overall nickel oxidation process evolves through different dynamic phases as corrosion progresses. Phase I involves net electron/metal atom transfer at the metal-solution interface to form Ni^{2+} , diffusion of Ni^{2+} from the interfacial region into the bulk solution, and hydrolysis of Ni^{2+} to produce $\text{Ni}(\text{OH})_2$, which can condense as colloids. In Phase II, additional elementary steps involving the Ni^{2+} hydrolysis product $\text{Ni}(\text{OH})_2$, and interfacial electron transfer to form $\text{Ni}(\text{OH})_3$ occur, which accelerate the precipitation of mixed $\text{Ni}^{\text{II}}/\text{Ni}^{\text{III}}$ hydroxide which grows as a hydrogel network. Phase III occurs after sufficient mixed $\text{Ni}^{\text{II}}/\text{Ni}^{\text{III}}$ hydroxide colloids have precipitated to allow nucleation and growth of solid crystalline particles on the surface.

The mechanism proposed in this thesis deviates from the corrosion mechanisms that underpin most existing corrosion rate models. The new mechanism presented here is capable of accounting for many phenomena observed (in relation to the effects of solution parameters on nickel corrosion) that are not explainable using existing mechanistic models. The proposed mechanism can also explain the corrosion behaviour of nickel in the presence of γ -radiation. From the time-dependent electrochemical studies, different metal oxidation rate parameters can be extracted which are required to develop a predictive corrosion model for nickel-containing alloys.

DEDICATION

To my family:

Iman

& the memory of our angel Nikki

CO-AUTHORSHIP STATEMENT

This dissertation is coauthored with my supervisor, Dr. J. Clara Wren. Giles Whitaker helped with editing. Dr. Jiju Joseph also helped with all editing and all the post-test solution analysis presented in the thesis.

This dissertation includes manuscripts in preparation (Chapters 4 and 5).

Chapter 4: Dr. M. Momeni helped with the design of the experiments.

Chapter 5: K. O'Donnell helped with the experimental set-ups.

Chapter 6: Nanofabrication Western facilities were used for SEM imaging and Surface Science Western facilities were used for Auger and XPS spectroscopy.

Chapter 7: T. Do helped with the experimental set-ups. Nanofabrication Western facilities were used for SEM imaging and Surface Science Western facilities were used for Auger and XPS spectroscopy.

ACKNOWLEDGEMENTS

I would like to thank my supervisor, Dr. Clara Wren for her guidance and support throughout my years of graduate study. Dr. Wren's continues guidance and encouragement have been invaluable during the past few years. Thank you for believing in my work and for always urging me to do better when you knew I could.

I would also like to thank Dr. Jiju Joseph for her support, guidance, advice and patience. This accomplishment would not be possible without your help.

I would also like to thank Giles Whitaker who helped me with the writing and editing my work. I would also like to thank Dr. Nicholas Payne who helped me with the discussing results and editing my work.

I would also like to thank Dr. Dave Wren who guided me with the writing process and provided valuable professional advices.

Many thanks go to my wonderful friends and colleagues, both past and present, in the Wren lab.

A special thanks to my parents for their constant love and support. They have always encouraged me in everything I have pursued.

And finally, my deepest thanks are reserved for my husband, Iman, who believes in me with more conviction than I believe in myself. Thank you for being with me through this journey.

TABLE OF CONTENT

ABSTRACT.....	ii
KEYWORDS	iv
SUMMARY FOR LAY AUDIENCE.....	v
DEDICATION	vii
CO-AUTHORSHIP STATEMENT.....	viii
ACKNOWLEDGEMENTS	ix
TABLE OF CONTENT	x
LIST OF TABLES	xvii
LIST OF FIGURES.....	xviii
LIST OF ACRONYMS.....	xxvii
CHAPTER 1: INTRODUCTION.....	1
1.1. THESIS MOTIVATION.....	1
1.2. RESEARCH OBJECTIVE AND APPROACHES	5
1.3. THESIS OUTLINE	6
1.4. REFERENCES.....	8
CHAPTER 2: TECHNICAL BACKGROUND AND LITERATURE REVIEW	10
2.1. MATERIALS BACKGROUND.....	10
2.1.1. Nickel Metal and Nickel Based Alloys.....	10
2.2. CORROSION ENVIRONMENT	12

2.2.1.	Primary Heat Transport System.....	12
2.2.2.	Secondary Heat Transport System.....	14
2.3.	PRINCIPLES OF CORROSION	15
2.3.1.	Corrosion of a Bare Metal Surface	16
2.3.2.	Effect of Mass Transport on the Corrosion Process	21
2.3.3.	Corrosion in the Presence of an Oxide Layer	30
2.4.	CORROSION OF NICKEL	33
2.4.1.	Nickel (II) Hydroxide (Ni(OH) ₂)	34
2.4.2.	Nickel (II) Oxide (NiO)	36
2.4.3.	Ni ₃ O ₄	38
2.4.4.	Ni ₂ O ₃	38
2.4.5.	NiOOH.....	38
2.5.	REVIEW OF CORROSION OF NICKEL AND NICKEL-BASED ALLOYS	40
2.5.1.	Hydrolysis and Solubility Behaviour of Nickel Ions.....	40
2.5.2.	Pourbaix Diagram of Nickel System	42
2.5.3.	Review of the Corrosion of Nickel and Nickel Oxide Formation	46
2.5.4.	Review of Corrosion of Nickel-Based Alloys	50
2.5.5.	Review of Effect of Ionic Strength and Conductivity on Corrosion	51
2.6.	RADIATION CHEMISTRY AND WATER RADIOLYSIS.....	52
2.6.1.	Types of Ionizing Radiation.....	53

2.6.2.	Primary Radiolysis Process.....	56
2.6.3.	Aqueous Reactions of Radiolysis Products	60
2.6.4	Radiolysis of Reactor Coolant Water	61
2.6.5.	Radiation-Induced Nanoparticle Formation	63
2.7.	REFERENCES.....	64
CHAPTER 3: EXPERIMENTAL PROCEDURES AND TECHNIQUES.....		72
3.1.	ELECTROCHEMICAL TECHNIQUES.....	72
3.1.1.	Three-electrode electrochemical cell.....	72
3.1.2.	Cyclic Voltammetry and Potentiodynamic Polarization	74
3.1.3.	Potentiostatic Polarization.....	76
3.2.	SURFACE ANALYSIS TECHNIQUES.....	77
3.2.1.	Optical Microscopy	77
3.2.2.	Scanning Electron Microscopy.....	77
3.2.3.	Energy Dispersive X-ray Spectroscopy.....	81
3.2.4.	Auger Electron Spectroscopy	81
3.2.5.	X-ray Photoelectron Spectroscopy	83
3.3.	SOLUTION ANALYSIS	86
3.3.1.	Inductively Coupled Plasma-Optical Emission Spectroscopy	86
3.4.	EXPERIMENTAL PROCEDURES	88
3.4.1.	Material and Solution Preparation.....	88

3.4.2. Electrochemical Experiment.....	89
3.4.3. Radiation Exposure Tests	89
3.4.4. Coupon Exposure Experiments ($T \geq 80$ °C).....	90
3.5. REFERENCES.....	91
CHAPTER 4: NON-LINEAR EFFECTS OF SOLUTION PARAMETERS ON NICKEL OXIDATION	92
4.1. INTRODUCTION.....	92
4.2. EXPERIMENTAL	96
4.3. RESULTS AND DISCUSSION	97
4.3.1 E_{corr} vs E^{eq}_{rxn} of Metal Redox Half-Reactions	97
4.3.2. Cyclic Voltammetry	111
4.3.3. Current-Potential Relationships Under Potentiostatic Polarization.....	118
4.3.4. Evolution of the Dynamic Phases of Metal Oxidation	128
4.4. CONCLUSIONS.....	133
4.5. REFERENCES.....	137
CHAPTER 5: COMBINED EFFECT OF pH AND IONIC STRENGTH ON NICKEL OXIDATION	141
5.1. INTRODUCTION.....	141
5.2. EXPERIMENTAL	148
5.3. RESULTS AND DISCUSSION	148

5.3.1. Time-Dependent Behaviour of E_{corr}	150
5.3.2. The $i_{meas - PD}$ vs E_{elec} Relationship as a Function of t_{corr}	163
5.3.3. The $\log i_{meas}$ vs E_{elec} Relationship During PD vs CV.....	168
5.3.4. Time-Dependent Behaviour of $i_{meas - PS}$ During Potentiostatic Polarization	182
5.3.5. Time-Dependent Behaviour of Metal Oxidation Products.....	190
5.4. CONCLUSIONS.....	192
5.5. REFERENCES.....	195
 CHAPTER 6: COMBINED EFFECTS OF pH, IONIC STRENGTH AND γ-RADIATION ON NICKEL OXIDATION IN SOLUTIONS OF SMALL STAGNANT VOLUMES AT 150 °C	 198
6.1. INTRODUCTION.....	198
6.2. EXPERIMENTAL	205
6.2.1 Materials and Solutions	205
6.2.2. Coupon Exposure Tests.....	206
6.2.3 Irradiation.....	207
6.2.4. Post-Test Analyses	208
6.3. RESULTS AND DISCUSSION	209
6.3.1. Effect of Ionic Strength in the Absence of Radiation (No RAD).....	209
6.3.2. Effect of Ionic Strength in The Presence of Radiation (RAD).....	225

6.4. CONCLUSIONS.....	258
6.5. REFERENCES.....	262
CHAPTER 7: INVESTIGATING THE TIME-DEPENDENT EFFECT OF pH AND RADIATION ON THE CORROSION OF NICKEL IN NON-BUFFERED SOLUTION AT 150 °C	265
7.1. INTRODUCTION.....	265
7.2. EXPERIMENTAL	268
7.2.1. Materials and Solutions	268
7.2.2. Coupon Exposure Tests.....	269
7.2.3. Post-Test analysis.....	270
7.3. Results and Discussion.....	271
7.3.1. Corrosion Dynamics of Nickel in the absence of Radiation (No RAD)	272
7.3.2. Dynamics of Ni Corrosion in the Presence of Gamma Radiation (RAD).....	279
7.3.3. Characterization of Oxide Formed on the Surface	288
7.3.4. Corrosion Mechanism for Nickel Corrosion in Presence of γ -radiation	292
7.3.5. Analysis of Unusual Surface Features at pH 6.0.....	298
7.3.6. Effect of Initial Solution pH on Unusual Surface Features	307
7.3.7. Liesegang Pattern Formation Via Ostwald Ripening	309
7.4. CONCLUSIONS.....	313
7.5. REFERENCES.....	315

CHAPTER 8: THESIS SUMMARY AND FUTURE WORK.....	317
8.1. SUMMARY	317
8.2. OVERALL CONCLUSION	325
8.3. FUTURE WORK.....	324
APPENDIX A.....	326
CURRICULUM VITAE.....	331

LIST OF TABLES

Table 2.1: Elemental composition of some of the most commonly used nickel-based alloys in steam generators (Wt.%).....	11
Table 2.2: The chemistry of PHTS in CANDU and PWR	14
Table 2.3: Chemistry of Secondary System	15
Table 4.1: Elementary reactions involved in the overall metal oxidation process	104
Table 5.1: Elementary Reactions Involved in the Overall Metal Oxidation Process	145
Table 6.1: Elementary Reactions Involved in the Overall Metal Oxidation Process	203
Table 6.2: Solution preparation method, ionic strengths (I_s) and conductivity (κ).....	206

LIST OF FIGURES

Figure 1.2: Schematics of corrosion product transport.....	4
Figure 2.1: Schematic illustration of the Butler-Volmer relationships for metal oxidation and solution reduction reactions.	20
Figure 2.2 : Electron transfer and mass transfer of species during reduction reaction of $O + e^- \rightleftharpoons R$	23
Figure 2.3: Concentration profiles (solid lines) and diffusion layer approximation (dashed lines); $x = 0$ corresponds to the electrode surface and δ is the diffusion layer thickness of: a) oxidizing species (O) and b) reducing species (R).	24
Figure 2.4: Growth of the diffusion-layer thickness with time: a) oxidizing species (O) , b) reducing species (R)	26
Figure 2.5: Contribution of the diffusion and migration components in mass transport process at a distance (x) from the electrode surface when negative potential is applied to the electrode.	28
Figure 2.6: Schematic illustration of the corrosion reactions in the presence of an oxide layer and their fluxes as considered in the Mass and Charge Balance (MCB) model.....	32
Figure 2.7: The crystal structure of α -Ni(OH) $_2$ · x H $_2$ O: (a) unit cell projection and (b) ball-and-stick unit cell for $x = 0.67$ (actual value varies, $0.5 \leq x \leq 0.7$).....	35
Figure 2.8: The crystal structure of β -Ni(OH) $_2$: (a)unit cell projection and (b) ball-and-stick unit cell.....	36
Figure 2.9: Nickel oxide crystal structure. Nickel sites are shown as grey spheres and oxygen sites are shown in white.	37

Figure 2.10: Left: Crystal structure of γ -NiOOH. Right: structure of the layered oxide with rhombohedral lattices.....	39
Figure 2.11: The solubility of Ni ^{II} in water at 25 °C.	41
Figure 2.12: Potential/pH diagram for Ni-H ₂ O at 25 °C	43
Figure 2.13: Pourbaix diagram for nickel at 25, 100, 200 and 300 °C	45
Figure 2.14: The radiation track of a fast electron (spur size not to scale).....	57
Figure 2.15: Water radiolysis as a function of time following absorption of radiation energy as a pulse. The right-hand panel shows the expansion of spurs with time	59
Figure 3.1: Schematic of three-component electrochemical cell	73
Figure 3.2: Potential sweep applied versus time in a CV experiment.	75
Figure 3.3: Potential sweep applied versus time in a PD experiment.....	76
Figure 3.4: A schematic diagram of the scanning electron microscopy technique.	79
Figure 3.5: Ionization of a core hole (K) by the primary electron beam, results in the decay of an electron from a higher energy level (L1).....	83
Figure 3.6: Schematic of the principle of XPS and the produced photoelectron.....	85
Figure 3.7: Schematic of Inductively Coupled Plasma-Optical Emission Spectroscopy (ICP-OES) instrument.....	87
Figure 4.1: E_{corr} observed at three different pHs under continuous Ar-purging.	101
Figure 4.2: The log $i_{meas - CV}$ vs E_{elec} relationships observed during cyclic voltammetry with different upper vertex potentials at three pHs at 80 °C.	112
Figure 4.3: Tafel slopes observed during the 3 rd CV cycle with different upper vertex potentials at three pHs at 80 °C.....	115

Figure 4.4: Comparison of current-potential relationships during the 3 rd CV cycle at potential ranges near E_{corr} observed at early stages (upper panel) and at later stages (lower panel).	118
Figure 4.5: Time-dependent behaviours of $i_{meas - P S}$ observed at various E_{elec} under potentiostatic polarization at pH 6.0 and pH 10.6 in Ar-sparged and high I_s solutions at 80 °C.....	122
Figure 4.6: Optical images showing the evolution of the surface during R1 to R4 for pH 6.0.....	127
Figure 4.7: Schematic representation of the elementary steps occurring during Phase I, II and III.....	131
Figure 5.1: Schematic representation of the elementary steps occurring during Phase I, II, and III.....	147
Figure 5.2: Time-dependent behaviours of E_{corr} and the $\log i_{meas - P D}$ vs E_{elec} relationship observed during potentiodynamic polarization.....	152
Figure 5.3: The solubility of Ni^{2+} in water at 25 and 80 °C	162
Figure 5.4: $\log i_{meas}$ vs $\Delta E_{i=0}$ relationships observed during PD scans performed after different corrosion durations in two different I_s solutions at pH 6.0 and pH 10.6.	165
Figure 5.5: Cyclic voltammograms obtained for Ni electrodes in either high or low I_s solutions at pH 6.0 and pH 10.6.....	168
Figure 5.6: Comparison of the 3 rd cycle CVs obtained, (a) in high vs low I_s solution at pH 6.0 and pH 10.6, and (b) at pH 6.0 vs pH 10.6 in the high and low I_s solutions.	172
Figure 5.7: Comparison of the $\log i_{meas - C V}$ vs E_{elec} relationship with the $\log i_{meas - PD}$ vs E_{elec} relationship observed as a function of t_{corr}	177

Figure 5.8: Time-dependent behaviours of $i_{meas - PS}$ observed at various E_{elec} under potentiostatic polarization at pH 6.0 and pH 10.6 in low versus high I_s solutions..	183
Figure 5.9: Illustration of the periods of metal oxidation kinetic stages observed during potentiostatic polarization at an E_{elec} in potential range R3.	184
Figure 5.10: Effect of I_s on time-dependent behaviour of $i_{meas - PS}$ at an E_{elec} in each anodic potential range at pH 6.0 versus at pH 10.6..	186
Figure 5.11: The amount of nickel ions dissolved in the solution vs t at pH 6.0 and 10.6 for low and high ionic strength.	191
Figure 6.1: The Rate Determining Steps (RDS) arising during the corrosion process. For metal oxidation.....	202
Figure 6.2: Experimental setup for coupon exposure tests in the presence and absence of gamma radiation.....	207
Figure 6.3: The solubility of Ni^{2+} in water at 25 and 150 °C	209
Figure 6.4: Nickel samples corroded at pH 6.0 at three ionic strengths in the absence of γ -radiation for test durations of 5-144 h.....	212
Figure 6.5: The colours of standard Ni hydroxide/oxide samples (Alfa Aesar) observed by optical microscopy.	213
Figure 6.6: Nickel samples corroded at pH 6.0 at three ionic strengths and in the absence of γ -radiation (same samples as presented in Figure 6.5).....	215
Figure 6.7: Surface profiles of Liesegang rings formed on nickel surfaces corroded for 144 h in the absence of radiation in mid and high I_s pH 6.0 solutions.	219

Figure 6.8: Concentration of dissolved nickel ions for nickel samples corroded at pH 8.4 and 10.6 at three ionic strengths compared to that of pH 6.0 shown in Figure 6.4B, in the absence of γ -radiation for test durations of 144 h.....	220
Figure 6.9: Nickel samples corroded at pH 8.4 at three ionic strengths and in the absence of γ -radiation for test durations of 144 h.....	222
Figure 6.10: Nickel samples corroded at pH 10.6 at three ionic strengths and in the absence of γ -radiation for test durations of 144 h.....	223
Figure 6.11: Nickel samples corroded at pH 6.0 at three ionic strengths and in the presence of γ -radiation (dose rate $1.8 \text{ kGy}\cdot\text{h}^{-1}$) for test durations of 5-144 h.....	226
Figure 6.12: Concentration of dissolved nickel ions for nickel samples corroded at pH 6.0 at three ionic strengths in the presence and absence of γ -radiation.	227
Figure 6.13: Nickel samples corroded at pH 6.0 at three ionic strengths and in the presence of γ -radiation (same samples as presented in Figure 6.10).....	230
Figure 6.14: Distribution and size of circular patterns on corroded nickel surfaces after 144 h in the presence of γ -radiation at mid and high I_s	231
Figure 6.15: TEM image showing the presence of nanoparticle clusters in low I_s solution after 120 h of corrosion in the presence of γ -radiation.	232
Figure 6.16: Depth profiles for Ni and O determined by AES, of nickel coupons corroded for 120 h in the presence and absence of γ -radiation at pH 6.0 with high and low ionic strengths.	234
Figure 6.17: The schematics of the H_2O_2 half reaction on metal oxidation occurring during Stage 1 of the corrosion process.....	237

Figure 6.18: The schematics of the effect of γ -radiation on Stage 2 of the corrosion process.....	240
Figure 6.19: The schematics of the effect of γ -radiation on Stage 3 of the corrosion process.....	242
Figure 6.20: SEM image showing the surface morphology of the 144 h, pH 6.0 low ionic strength sample.	243
Figure 6.21: SEM and FIB cut image of the center of a Liesegang ring observed on a nickel surface corroded for 144 h in high ionic strength pH 6.0 solution in the presence of γ -radiation.	246
Figure 6.22: EDX analysis of the center of the Liesegang region illustrates the presence of inclusion sites in this area.....	248
Figure 6.23: EDX analysis of a cross-section of the central area of a Liesegang ring on nickel corroded for 144 h in the presence of γ -radiation in a high I_S pH 6.0 solution...	249
Figure 6.24: Schematic of formation of the Liesegang rings and the hole in the center of the ring.	251
Figure 6.25: Concentration of dissolved nickel ions for nickel samples corroded at pH 8.4 and 10.6 at three ionic strengths compared to that of pH 6.0 shown in Figure 6.11B....	252
Figure 6.26: Nickel coupons corroded in de-aerated buffered solutions with three different ionic strengths at pH 8.4 in the presence of γ -radiation (at dose rate of 1.8 $\text{kGy}\cdot\text{h}^{-1}$) for test durations of 144 h.....	255
Figure 6.27: Nickel coupons corroded in de-aerated buffered solutions with three different ionic strengths at pH 10.6 in the presence of γ -radiation (at dose rate of 1.8 $\text{kGy}\cdot\text{h}^{-1}$) for test durations of 5-144 h	256

Figure 6.28: Ni and O Depth Profiles determined by AES, of nickel coupons corroded for 120 h in the presence of γ -radiation	257
Figure 7.1 Experimental setup for coupon exposure tests in the absence and presence of gamma radiation.....	270
Figure 7.2: The solubility of Ni ions in water at 25 and 150 °C	271
Figure 7.3: Nickel coupons corroded in de-aerated non-buffered solution at initial pH 6.0 in the absence of radiation for test duration of 5-144 h	273
Figure 7.4: Ni hydroxide/oxide (Alfa Aesar) characteristic colours observed by optical microscopy.....	274
Figure 7.5: Evolution of circular surface features on nickel corroded in a solution with initial pH 6.0 in the absence of γ -radiation. All optical images have the same scales (25 μm scalebar).....	276
Figure 7.6: Nickel samples corroded in de-aerated non-buffered solution at initial pH 6.0, 8.4 and 10.6 in the absence of γ -radiation during test durations of 5-144 h.....	278
Figure 7.7: SEM images of nickel corroded at initial pHs 6.0, 8.4 and 10.6 in the absence of γ -radiation from the same experiments.....	279
Figure 7.8: Nickel coupons corroded in de-aerated non-buffered solutions at initial pH 6.0 in the presence of γ -radiation at a dose rate of $1.8 \text{ kGy}\cdot\text{h}^{-1}$	281
Figure 7.9 TEM image of solution in contact with nickel coupons corroded for 72 h at pH 6.0. Nanoparticle clusters have formed due to saturation of Ni ions in solution.....	284
Figure 7.10: Nickel coupons corroded in de-aerated non-buffered solution at initial pH 6.0, 8.4 and 10.6 in the presence of γ -radiation during test durations of 5-144 h).	287

Figure 7.11: SEM images of nickel corroded at initial pHs 6.0, 8.4 and 10.6 in the presence of γ -radiation from the same experiments presented in Figure 7.10.....	288
Figure 7.12: The Ni 2p bands from the high resolution XPS of a nickel surface corroded for A) 120 h without radiation (No RAD) at initial pH 6.0	290
Figure 7.13: Surface colours on nickel coupons corroded at initial pH 6.0 in the presence of γ -radiation.....	291
Figure 7.14: The schematics of the H_2O_2 half reaction on metal oxidation occurring during Stage 1 of the corrosion process.....	294
Figure 7.15: The schematics of the effect of γ -radiation on Stage 2 of the corrosion process.....	296
Figure 7.16: The schematics of the effect of γ -radiation on Stage 3 of the corrosion process.....	297
Figure 7.17: Optical images of particular morphological features observed after 24 h of nickel corrosion at 150 °C in de-aerated pH 6.0 solution in the presence of γ -radiation.	299
Figure 7.18: Wave patterns on the surface after 72 h of nickel corrosion at pH 6.0 due to non-uniform metal dissolution and oxide formation, and the FIB cut of the wave pattern.	300
Figure 7.19: Liesegang ring growth on nickel samples corroded in deaerated non-buffered solution at initial pH 6.0 in the presence of γ -radiation.	303
Figure 7.20: Localized metal dissolution in the center and surrounding regions of Liesegang rings after 72 h of nickel corrosion in the presence of γ -radiation.	305

Figure 7.21: A Liesegang ring on a nickel surface after 72 h of corrosion in the presence of radiation.	306
Figure 7.22: The circular surface features during the corrosion of nickel in solution with initial pH 8.4, in the presence of γ -radiation.	307
Figure 7.23: Nickel surface corroded at pH 10.6 in the presence of γ -radiation for 120 h. Particular features were observed on the sample surface	308
Figure 7.24: Schematic representation of particle growth in solution by Ostwald ripening	310
Figure 7.25: A schematic representation of redox-assisted Ostwald ripening	312
Figure 7.26: Liesegang banding via redox-assisted Ostwald ripening	313

LIST OF ACRONYMS, TERMS AND SYMBOLS

Symbols	Terms	Units
A	Surface Area of the Electrode	cm^2
$(a_A)_{int}$	Interfacial Activity of Ion A	-
BE	Binding Energy	eV
C	Concentration	M
C_{sat}	Saturation Concentration	M
D_j	Diffusion Coefficient of Species j	cm^2/s
E^o	Standard Cell Potential	V_{RHE}
E_{app}	Applied Electrode Potential	V_{RHE}
E_{corr}	Corrosion Potential	V_{RHE}
$E_{corr}(\tau_0)$	Corrosion Potential Value When The System Reaches The First Steady State	V_{RHE}
$E_{corr}(\tau_f)$	Corrosion Potential Value When The System Reaches The Final Steady State	V_{RHE}
E_{elec}	Electrode Potential	V_{RHE}
E_{rxn}^{eq}	Equilibrium Potential of Redox Reaction	V_{RHE}
E_{ox}^{eq}	Equilibrium Potential of Oxidation Reaction	V_{RHE}
E_{red}^{eq}	Equilibrium Potential of Reduction Reaction	V_{RHE}
$E_{i=0}$	Potential of Zero Current	V_{RHE}
$E_{i=0,CV}$	Potential of Zero Current During Cyclic Voltammetry Scan	V_{RHE}

$E_{i=0,f}$	Potential of Zero Current During Cyclic Voltammetry in Forward Scan	V _{RHE}
$E_{i=0,r}$	Potential of Zero Current During Cyclic Voltammetry in Revers Scan	V _{RHE}
$E_{i=0,PD}$	Potential of Zero Current During Potentiodynamic Scan	V _{RHE}
E_k	Kinetic Energy	J
E_{x-ray}	Energy of Single X-ray Photon	J
F	Faraday Constant	Coulomb/mol
i_{corr}	Corrosion Current Density	A/cm ²
i_{meas}	Measured Current Density	A/cm ²
$i_{meas-CV}$	Measured Current Density During Cyclic Voltammetry scan	A/cm ²
$i_{meas-PS}$	Measured Current Density During Potentiostatic Polarization	A/cm ²
i_{ox}	Oxidation Current Density	A/cm ²
i_{red}	Reduction Current Density	A/cm ²
i_{ox}^{eq}	Oxidation Current Density at Equilibrium	A/cm ²
i_{red}^{eq}	Reduction Current Density at Equilibrium	A/cm ²
I_s	Ionic Strength	M
k_{trans}	1 st Order Rate Coefficient for Transporting Ions	1/s
n	Stoichiometric Number of Electrons Involved in an Electrode Reaction	-
Ni_m^0	Metal Atom Bound To The Solid Metal Phase	-
Ni_{solv}^{2+}	Fully Solvated Ni ²⁺ Ion	-

$[Ni^{2+}]_{int}$	Concentration of Ni^{2+} At Interface	M
$[Ni^{2+}]_{bulk}$	Concentration of Ni^{2+} in Bulk	M
R	Gas Constant	J/K.mol
S1	Kinetic Stage 1	-
S2	Kinetic Stage 2	-
S3	Kinetic Stage 3	-
<i>trans</i>	Ion Transport	-
α	Electrochemical Transfer Coefficient	-
β_{rxn}	Tafel Slope of Redox Reactions	mV/dec
δ	Diffusion Layer Thickness	nm
ΔG_f^o	Standard Gibbs Free Energy of Formation Change	J/mol
$\delta\phi$	Electrostatic Potential Difference Between Two Points or Phases	V
η	Over Potential	V
κ	Ionic Conductivity	S/m
λ_{eq}	Equivalent Conductivity	cm ² /Ω·equiv
Λ	Molar Conductivity	S·m ² /mol
μ_j	Ion Mobility of Species j	cm ² /V·S
η_j	Charge on Species j	-
ν_A	Rate of Process A	-
$\nu_{\#1}(t)$	Overall Metal Oxidation Rate at Time t	M/cm.s
$\nu_{M1}(t)$	Metal Oxidation Rate at Time t ($Ni \leftrightarrow Ni^{2+}$)	M/cm.s
$\nu_{M2}(t)$	Metal Oxidation Rate at Time t ($Ni^{2+} \leftrightarrow Ni^{3+}$)	M/cm.s

$v_{trans}(t)$	Ion Transfer Rate at Time t	M.cm/s
v_{hyd}	Rate of Hydrolysis Process	M.cm/s
v_{gel}	Rate of Hydrogel Formation	M.cm/s
σ	Stoichiometric Coefficient	-
φ	Work Function	J

Acronyms

Terms

<i>CANDU</i>	Canada Deuterium Uranium
<i>CE</i>	Counter Electrode
<i>CV</i>	Cyclic Voltammetry
<i>EDX</i>	Energy Dispersive X-Ray Spectroscopy
<i>ICP – OES</i>	Inductively Coupled Plasma-Optical Emission Spectroscopy
<i>PD</i>	Potentiodynamic Polarization
<i>PHWR</i>	Pressurized Heavy Water Reactor
<i>PS</i>	Potentiostatic Polarization
<i>PWR</i>	Pressurized Water Reactor
<i>RDS</i>	Rate Determining Step
<i>RE</i>	Reference Electrode
<i>RHE</i>	Reversible Hydrogen Electrode
<i>WE</i>	Working Electrode
<i>XPS</i>	X-ray Photoelectron Spectroscopy

CHAPTER 1

INTRODUCTION

1.1. THESIS MOTIVATION

Nuclear energy is one of the low carbon emitting energy sources that can produce large amounts of energy per unit mass of fuel. Nuclear power plants generate 10% of the world's electricity, 15% of Canada's electricity, and more than 60% of Ontario's electricity supply. There are a number of types of nuclear power plant in operation in different parts of the world. The most common designs are the boiling water reactor (BWR), pressurized light water reactor (PLWR or PWR) and pressurized heavy water reactor (PHWR) which in here PWR and PHWR are discussed..

The PWR uses 3-4% enriched uranium dioxide (UO_2) (i.e., 3-4% ^{235}U with the bulk mostly ^{238}U) as fuel, and light water for both coolant and moderator. The most common nuclear reactors in Canada are PHWRs which are Canadian-designed CANDU® (Canada Deuterium Uranium) reactors that use natural uranium dioxide (containing only 0.7% ^{235}U) as the fuel, and heavy water as both coolant and moderator.

In both PWR and PHWR reactors the primary heat transport system (PHTS) conveys the heat generated by the fission reaction in the reactor core to the steam

generator to produce steam (**Figure 1.1**). In the secondary circuit, the steam is used to drive the steam turbine, which is connected to the generator that transforms the mechanical energy into electrical energy by electromagnetic induction.

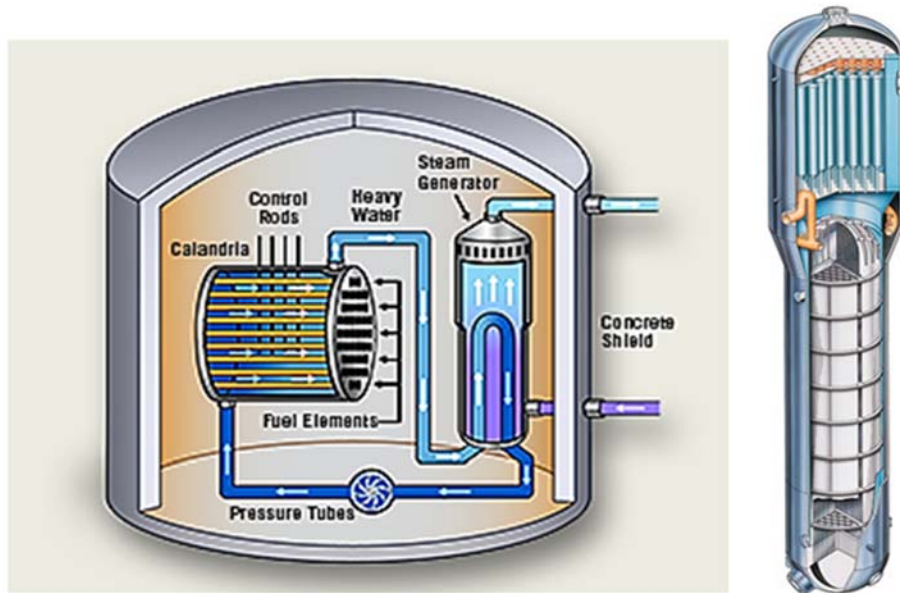


Figure 1.1: Schematics of a CANDU® (Canada Deuterium Uranium) reactor and steam generator.

The configuration and materials used in the heat transport system vary by reactor type. Heat exchanger tubes are usually constructed using nickel-based alloys (Inconel 600 and 690, and Incoloy 800) [1,2]. These alloys are selected for their good mechanical and stress corrosion cracking resistance. These properties are vital since, during steam generator operation, they are exposed to radiation (due to transport of neutron activated corrosion products and fission products in the PHTS) and high-temperatures (between ~ 250 and 310 °C) [2–4]. The high corrosion resistance of these alloys is attributed to the preferential formation of passive oxide films on the alloy surfaces [5–7]. Despite their

high corrosion resistance, corrosion can still occur, due to the exposure to high temperatures (between ~ 250 and 310 °C) and an oxidizing environment [8–10]. The underlying processes that determine the properties of the oxides formed and the evolution of their properties as corrosion progress are not well understood [1], particularly at high temperatures and in the presence of radiation.

One of the major concerns for nuclear power plants is the performance of reactor materials under radiation. In the presence of a continuous flux of ionizing radiation condition (reactor core), the coolant water can decompose to chemically reactive species (R 1.1) which include both highly oxidizing (e.g., •OH, H₂O₂) and highly reducing species (e.g., •H, •e_{aq}⁻), and their concentration reaches a steady state [11–15].



These radiolysis products will determine the aqueous redox conditions of the water and influence the corrosion kinetics of materials in radiation-exposed systems. Corrosion of these alloys can lead to the release of corrosion products, Ni cations in particular. The release of Ni cations and their deposition in the primary coolant circuit of the nuclear reactor is considered to be one of the most important challenges in the nuclear industry with regard to material degradation and longevity of the heat transport system. These products can also be transported to and deposit in the reactor core where they can be neutron activated and become radioactive. If these radioactive species become re-suspended, they can be transported outside the reactor core and can redeposit on piping and components located outside the biological shield of the reactor core, creating radioactive hot spots (**Figure 1.2**). These activated corrosion products pose a

radiological hazard to plant workers and make any maintenance activities during decommissioning or planned reactor shutdown very expensive [16].

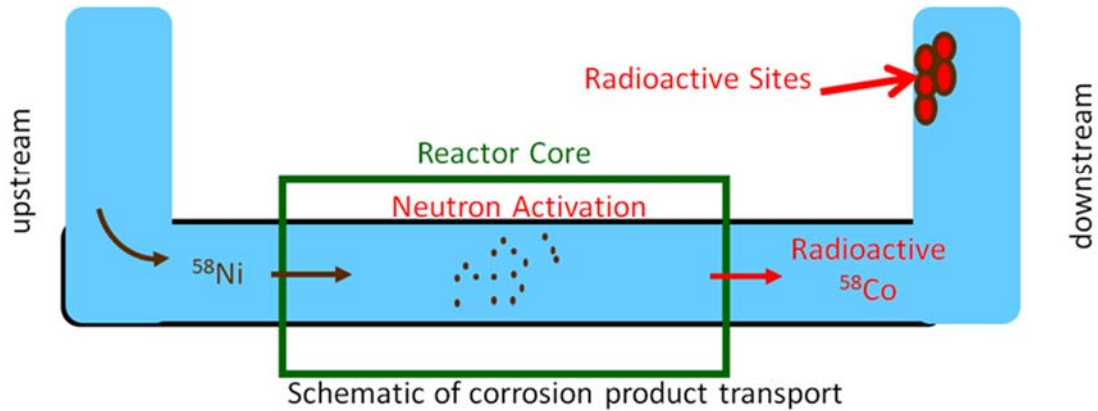


Figure 1.2: Schematics of corrosion product transport.

Corrosion is an electrochemical process involving a series of elementary processes which include electrochemical reactions, solution reactions, transport processes and oxide particle nucleation and growth. The effect of solution parameters on corrosion is mainly through the effect of these parameters on elementary processes. Therefore, it is important to identify the key elementary processes that control the overall corrosion rate [17,18].

Since Ni is the balancing metal for the nickel-based alloys, in order to predict the corrosion behaviour of these alloys, it is important to have a good understanding of the long-term corrosion behaviour of Ni metal under similar conditions. The corrosion behaviour of Ni, particularly under γ -radiation, is not well understood and the effect of solution parameters on nickel corrosion has not been reported.

1.2. RESEARCH OBJECTIVE AND APPROACHES

The main objective of this thesis is to advance the fundamental understanding of the effect of radiation and solution parameters on the corrosion behaviour of pure nickel. In this work, systematic studies are being performed to understand the effect of temperature, pH, ionic strength and γ -radiation on short- and long-term nickel corrosion behaviour. These studies were performed using a combination of electrochemical techniques and coupon-exposure tests, with and without γ -radiation. The electrochemical techniques used in this thesis include Corrosion Potential (E_{CORR}), Cyclic Voltammetry (CV), Potentiodynamic Polarization (PD) and Potentiostatic Polarization (PS) measurements. The coupon-exposure tests were performed using nickel coupons immersed in solution in sealed quartz vials under different exposure conditions. After each experiment a comprehensive post-test analysis of the metal surface was performed using optical microscopy, scanning electron microscopy (SEM), X-ray photoelectron spectroscopy (XPS) and Auger electron spectroscopy (AES). Dissolved metal analysis was also carried out via inductively coupled plasma- optical emission spectroscopy (ICP-OES). This work will improve the understanding of the corrosion behaviour of nickel-containing alloys in which nickel is the principal element.

1.3. THESIS OUTLINE

CHAPTER 1: INTRODUCTION

This chapter contains the thesis motivation, objectives, approaches, and thesis outline.

CHAPTER 2: TECHNICAL BACKGROUND AND LITERATURE REVIEW

In this chapter the materials background, literature reviews, and theoretical background are presented.

CHAPTER 3: EXPERIMENTAL PROCEDURES AND TECHNIQUES

This chapter describes the techniques used to obtain the data reported in Chapters 4 to 7.

CHAPTER 4: NON-LINEAR EFFECTS OF SOLUTION PARAMETERS ON NICKEL OXIDATION

The effects of pH in combination with other solution parameters on Ni oxidation were investigated by electrochemical techniques. The evolution of the elementary reactions and mass transfer/transport steps that control the overall metal oxidation rate was investigated using corrosion potential measurements and current vs potential relationships under potentiodynamic and potentiostatic conditions. The solution parameters investigated were pH, ionic strength, temperature, and γ -radiation.

CHAPTER 5: COMBINED EFFECT OF pH AND IONIC STRENGTH ON NICKEL OXIDATION

The the combined effect of pH and ionic strength (I_s) on the evolution of Ni oxidation was investigated under Ar saturated conditions at pH 6.0 or pH 10.6, at 80 °C, using electrochemical techniques. The electrochemical analyses performed were E_{CORR} measurement as a function of corrosion time, potentiodynamic (PD) polarization, multiple cycles of CV with different vertex potentials, and potentiostatic (PS) polarization measurements.

CHAPTER 6: COMBINED EFFECT OF pH, IONIC STRENGTH AND γ -RADIATION ON NICKEL OXIDATION IN SOLUTIONS OF SMALL STAGNANT VOLUMES AT 150 °C

The effect of pH, ionic strength and γ -radiation on the long-term corrosion of nickel was investigated in high ionic strength solutions at 150 °C. Coupon exposure tests at pH (6.0, 8.4 and 10.6) were performed in the absence and presence of γ -radiation in small-volume stagnant solutions. The effect of ionic strength was studied by maintaining a constant pH throughout the test duration. The long-term corrosion dynamics were studied by examining the changes in oxide composition and morphology and dissolved Ni^{2+} concentration as a function of corrosion time.

CHAPTER 7: INVESTIGATING THE TIME-DEPENDENT EFFECT OF PH AND γ -RADIATION ON THE CORROSION OF NICKEL IN NON-BUFFERED SOLUTION AT 150 °C

This chapter investigates the time-dependent corrosion behaviour of nickel in low ionic strength solutions (non-buffered solutions) in the presence and absence of γ -radiation. The corrosion dynamics were investigated by performing coupon exposure tests complemented by post-test surface and dissolved metal analysis.

CHAPTER 8: THESIS SUMMARY AND FUTURE WORK

This chapter provides a brief conclusion to the thesis, and recommended future work.

1.4. REFERENCES

- [1] A.Y. Musa, J.C. Wren, Combined effect of gamma-radiation and pH on corrosion of Ni-Cr-Fe alloy inconel 600, *Corros. Sci.* 109 (2016) 1–12.
<https://doi.org/10.1016/j.corsci.2016.03.015>.
- [2] D. Fénon, *Nuclear Corrosion Science and Engineering*, Cambridge, 2012.
<https://doi.org/10.1533/9780857095343.6.939>.
- [3] P. Aaltonen, H. Hannien, *Water Chemistry and Behaviour of Materials in PWRs And BWRs*, Int. At. Energy Agency. IAEA-TECDO (1997).
- [4] W.G. Cook, D. Lister, *Chemistry in CANDU Process Systems: In The Essectial CANDU*, UNENE, 2014.
- [5] L. Marchetti, S. Perrin, F. Jambon, M. Pijolat, Corrosion of nickel-base alloys in primary medium of pressurized water reactors: New insights on the oxide growth mechanisms and kinetic modelling, *Corros. Sci.* 102 (2016) 24–35.
<https://doi.org/10.1016/j.corsci.2015.09.001>.
- [6] X. Tang, S. Wang, L. Qian, Y. Li, Z. Lin, D. Xu, Y. zhang, Corrosion behavior of

nickel base alloys, stainless steel and titanium alloy in supercritical water containing chloride, phosphate and oxygen, *Chem. Eng. Res. Des.* 100 (2015) 530–541. <https://doi.org/10.1016/j.cherd.2015.05.003>.

- [7] J. Everaerts, E. Salvati, H. Li, W. Li, A.M. Korsunsky, Mechanical properties of thermally grown submicron oxide layers on a nickel-based superalloy, *Corros. Sci.* 165 (2020) 108388. <https://doi.org/10.1016/j.corsci.2019.108388>.
- [8] Y.S. Lim, D.J. Kim, S.W. Kim, S.S. Hwang, H.P. Kim, Characterization of internal and intergranular oxidation in Alloy 690 exposed to simulated PWR primary water and its implications with regard to stress corrosion cracking, *Mater. Charact.* 157 (2019) 109922. <https://doi.org/10.1016/j.matchar.2019.109922>.
- [9] E. Chajduk, A. Bojanowska-Czajka, Corrosion mitigation in coolant systems in nuclear power plants, *Prog. Nucl. Energy.* 88 (2016) 1–9. <https://doi.org/10.1016/j.pnucene.2015.11.011>.
- [10] P.M. Scott, P. Combrade, General corrosion and stress corrosion cracking of Alloy 600 in light water reactor primary coolants, *J. Nucl. Mater.* 524 (2019) 340–375. <https://doi.org/10.1016/j.jnucmat.2019.04.023>.
- [11] J.W.T. Spinks, R.J. Woods, *An Introduction To Radiation Chemistry*, Wiley, 1990.
- [12] I. Draganic, *The Radiation Chemistry of Water*, Elsevier, 2012.
- [13] M.A.J. Rodgers, *Radiation Chemistry: Principles And Applications*, Wiley, 1987.
- [14] A.O. Allen, *The Radiation Chemistry of Water and Aqueous Solutions*, Van Nostrand, 1961.
- [15] J.C. Wren, Steady-state radiolysis: Effects of dissolved additives, *ACS Symp. Ser.* 1046 (2010) 271–295. <https://doi.org/10.1021/bk-2010-1046.ch022>.
- [16] M. Momeni, Gamma-Radiation Induced Corrosion of Alloy 800, *Electron. Thesis Diss. Repos.* 5011, University of Western Ontario (2017).
- [17] D. Guo, Corrosion Dynamics of Carbon Steel in Used Fuel Container Environments, *Electron. Thesis Diss. Repos.* 5897, University of Western Ontario (2018).
- [18] D. Guo, M. Li, J.M. Joseph, J.C. Wren, A New Method for Corrosion Current Measurement: the Dual-Electrochemical Cell (DEC), *J. Electrochem. Soc.* 167 (2020) 111505–111604. <https://doi.org/10.1149/1945-7111/aba6c8>.

CHAPTER 2

TECHNICAL BACKGROUND AND LITERATURE REVIEW

2.1. MATERIALS BACKGROUND

2.1.1. Nickel Metal and Nickel Based Alloys

Nickel is an important material with widespread use in a variety of applications in science and engineering. Some important applications of this material are in electrochemical sensors [1], secondary battery electrodes [2,3], electrochemical treatment of wastewater [4], electro-catalysts for various applications including oxygen evolution [5,6], and the oxidation of organic compounds [7,8].

Another important application of nickel is its use as the main component in many nickel-based super alloys with superior corrosion resistance and mechanical properties [9,10]. Nickel-based alloys are a well-known example of a multicomponent alloy with a composition carefully balanced to give the desired properties. These alloys are made to function under severe mechanical and corrosive operational conditions [11], and to improve their reliability, their compositions are tailored to the operational conditions [12].

One common application of nickel-based alloys (Alloy 600, 800 and 690) is for system components in nuclear power plants, in particular pressurized water reactors (PWR) and Canadian Deuterium Uranium (CANDU®) reactors, mainly as thin-walled heat exchanger tubing and piping[13]. These alloys are selected for their good mechanical properties and stress corrosion cracking resistance. These properties are vital, since during steam generator operation they are exposed to radiation and high temperature conditions [14,15]. The elemental compositions of these alloys are presented in **Table 2.1**.

Table 2.1: Elemental composition of some of the most commonly used nickel-based alloys in steam generators (Wt.%) [16]

	Ni	Cr	Fe	Mn	Si	Cu	Ti	Al
Alloy 800	30.0-35.0	19.0-23.0	> 39.5	<1.5	1	–	0.15-0.60	0.15-0.60
Alloy 690	>58.0	28.0-31.0	7.0-11.0	0.5	< 0.5	< 0.5	< 0.5	–
Alloy 600	72.0	14.0-17.0	6.0-10.0	<1	0.5	0.5	–	–

The high corrosion resistance of these alloys is attributed to preferential formation of passive oxide films on the alloy surfaces [17–19]. Despite the high corrosion resistance of these alloys, corrosion can still occur. During corrosion metal cations release which is an important issue in the nuclear industry and should be minimized in order to ensure the safety of personnel, reduce maintenance and shorten shutdown periods [16].

Unfortunately, the underlying processes that determine the properties of the oxides formed and the evolution of their properties as corrosion progresses are not well understood [13], particularly at high temperatures and in the presence of radiation. To predict the corrosion behaviour of nickel-based alloys, it is essential to have a good understanding of the behaviour of pure Ni metal under the same conditions.

2.2. CORROSION ENVIRONMENT

This section explains the chemistry of the operational environment (steam generator) of nickel-based alloys in CANDU and PWR reactors. Steam generators are heat exchangers which are used to convert water into steam from heat produced in a nuclear reactor core. The overall heat transport system for the nuclear power plant consists of two separate subsystems - the primary and secondary heat transport systems.

2.2.1. Primary Heat Transport System

The Primary Heat Transport System (PHTS) transports primary coolant water, which conveys the heat generated from the fission reaction in the reactor core to the steam generator. The design of the PHTS varies depending on the type of nuclear reactor, but an important consideration in every PHTS design is controlling the water chemistry to minimize the corrosion of alloys, minimizing deposition of corrosion products on the fuel and controlling the concentration of activated corrosion products and fission products.

These objectives are achieved through constant control of the primary coolant water pH, oxygen content and ion concentrations. This section focuses on the published data for CANDU and PWR reactors.

Table 2.2 presents the guidelines for the coolant chemical properties in the PHTS in CANDU and PWR reactors. As can be seen in the table, the water chemistries for the PHTS in PWRs and CANDUs are different. In CANDU reactors, the pH is strictly maintained in the range 10.2-10.4. In CANDU reactors, carbon steel is one material with largest contact with the coolant water in PHTS (used as feeder pipes joining the fuel channels through the headers to the channel heads in the steam generators). Thus, choosing mild alkaline solution pH is to minimize carbon steel corrosion in the operating environment [20].

The concentration of boric acid is maintained at 1200 ppm ($1.2 \text{ g}\cdot\text{kg}^{-1}$), Li (as LiOH for pH adjustment) at 0.35-0.55 mg/kg, and the pressure at $\sim 12.2 \text{ MPa}$ at $310 \text{ }^\circ\text{C}$. However in a PWR, the primary water chemistry has a dissolved oxygen (DO) level of $<5 \text{ ppb}$ and the conductivity is lower, but the solution pH is maintained in the wider range of 6.0 -10.2 [20,21].

Table 2.2: The chemistry of PHTS in CANDU and PWR [20,21]

Chemical Properties	CANDU	PWR
Conductivity	0.86-1.4 mS/m	0.02 mS/m
pH _{25°C}	10.2-10.4	6.0-10.2
Li ⁺	0.35-0.55 mg/kg	Consistent with Li ⁺ station program
Chloride	< 0.05 mg/kg	< 0.15 mg/kg
Sulphate	< 0.05 mg/kg	< 0.15 mg/kg
Boric acid	1.2 g/kg	0-9 g/kg
Oxygen	< 0.01 mg/kg	< 0.005 mg/kg

2.2.2. Secondary Heat Transport System

The Secondary Heat Transport System (Secondary System) produces the steam required to drive the turbines and generate electricity. Generally, the secondary systems in PWR and CANDU nuclear power plants have different steam generator configurations and the materials used for the various components, and their chemistry environments, are dependent upon on the particular type of component in question.

Normally, the materials used in various components are classified into two types: all ferrous, and copper-containing. In systems with iron-based materials the operational chemistry pH is kept alkaline to control corrosion of iron-based equipment. An alkaline pH helps to promote the formation of passive oxide films on the iron surface, and this is mostly achieved by adding ammonia or other amines to maintain the pH at 10.2 – 10.4.

In a copper-based system, the maximum pH of the system should be about 9.2 – 9.4. Since copper corrosion is known to be accelerated in the presence of ammonia, particularly in the presence of oxygen, ammonia is not used or is used minimally. Moreover, hydrazine is added to reduce the risk of cracking of the tube materials. [20] The chemistry of the secondary heat transport system (mainly in CANDU reactors) is shown in **Table 2.3**.

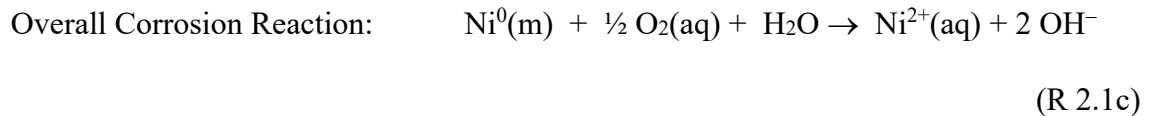
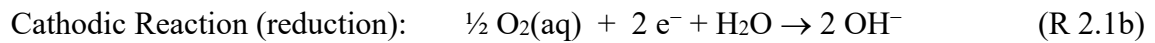
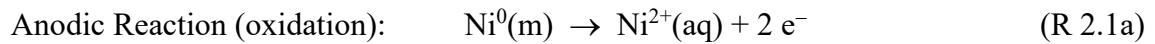
Table 2.3: Chemistry of Secondary System [20]

Parameter	Typical Specification Range
pH	9.5<pH<10 (for all ferrous system)
Dissolved O ₂	< 10 µg/kg
Hydrazine	20-30 µg/kg
Na ⁺	< 0.05 µg/kg
Cl ⁻ , SO ₄ ²⁻	< 0.05 µg/kg

2.3. PRINCIPLES OF CORROSION

2.3.1. Corrosion of a Bare Metal Surface

Corrosion is an electrochemical process typically involving metal oxidation coupled with solution reduction half-reactions. Each half-reaction includes (1) the net electron transfer between the redox pair (O and R, M^0 and M^{n+}) in the interfacial region, and (2) the overall transport of redox pairs to and from the interfacial region and the bulk solution. Net electron transfer during nickel ($Ni^0(m)$) corrosion in an aerated solution may occur via:



The rate of corrosion is equal to the rate of the metal oxidation half-reaction, and this rate must also be the same as the rate of the solution reduction half-reaction since charge and mass must be conserved during any chemical reaction. The rate of electron transfer is strongly influenced by mass transport of redox pairs (O and OH^- , Ni^0 and Ni^{2+}) to/from the interfacial region and the bulk solution. Section 2.3.1 focuses on interfacial electron transfer during oxidizing and reducing half reactions.

Corrosion occurs because the metal-solution system is trying to reach chemical equilibrium. The thermodynamic driving force for each half-reaction is [22,23]:

$$-\Delta_{ox}G = -nF(E_{corr} - E_{ox}^{eq}) = -nF\eta_{ox} \quad (\text{Eq. 2.1a})$$

$$-\Delta_{red}G = -nF(E_{red}^{eq} - E_{corr}) = -nF\eta_{red} \quad (\text{Eq. 2.1b})$$

Where $\Delta_{ox}G$ and $\Delta_{red}G$ are the Gibbs free energy change in metal oxidation half-reaction and solution reduction half-reaction, E_{ox}^{eq} and E_{red}^{eq} are the equilibrium potentials for the metal oxidation half-reaction and the solution reduction half-reaction, and E_{corr} is the electrochemical potential of the corroding system at the time of reaction, n is the number of electrons transferred, F is Faraday's constant (96,485 C/mol). By convention the reference potential is the standard reduction potential for hydrogen. The net Gibbs free energies of reactions in electrochemical potential units are also known as overpotentials [23].

The equilibrium potential for each half reaction is expressed by the Nernst equations [23]:

$$E_{ox}^{eq} = E_{(Ni^{2+}/Ni)}^o + \frac{RT}{nF} \ln \left(\frac{a_{eq}^{Ni^{2+}}}{a_{eq}^{Ni^0}} \right) \quad (\text{Eq. 2.2a})$$

$$E_{red}^{eq} = E_{(O_2/OH^-)}^o + \frac{RT}{nF} \ln \left(\frac{a_{eq}^{O_2}}{a_{eq}^{OH^-}} \right) \quad (\text{Eq. 2.2b})$$

Where R is the gas constant (8.314 J/mol), T is the temperature (in Kelvin), $E_{(Ni^{2+}/Ni)}^o$ and $E_{(O_2/OH^-)}^o$ are the standard reduction potentials for the corresponding half-reactions, and $a_{eq}^{Ni^{2+}}$, $a_{eq}^{Ni^0}$, $a_{eq}^{O_2}$ and $a_{eq}^{OH^-}$ represent the chemical activities of the corresponding

species when the corroding system reaches equilibrium. The activity of a pure solid metal species is 1.0 by definition [23].

If the rate of each half reaction at E_{corr} is controlled by the interfacial transfer rate of electrons, the charge transfer rate can be expressed by the Butler-Volmer equations [23]:

$$i_{ox} = i_{ox}^{Eq} \cdot \left\{ \exp \left(\alpha_{ox} \cdot \left(\frac{nF}{RT} \right) \cdot \eta_{ox} \right) - \exp \left((1 - \alpha_{ox}) \cdot \left(\frac{nF}{RT} \right) \cdot \eta_{ox} \right) \right\} \quad (\text{Eq. 2.3a})$$

$$i_{red} = i_{red}^{Eq} \cdot \left\{ \exp \left(\alpha_{red} \cdot \left(\frac{nF}{RT} \right) \cdot \eta_{red} \right) - \exp \left((1 - \alpha_{red}) \cdot \left(\frac{nF}{RT} \right) \cdot \eta_{red} \right) \right\} \quad (\text{Eq. 2.3b})$$

Where i_{ox}^{Eq} and i_{red}^{Eq} are the exchange currents for the metal oxidation and the solution reduction half-reactions at equilibrium, and α_{ox} and α_{red} are known as transfer coefficients. They represent the relative dependence of the forward and reverse reaction rates on overpotential. This coefficient indicates the fraction of the electrostatic potential energy that affects oxidation and reduction reactions which are typically 0.5. The Butler-Volmer relationships are schematically presented in **Figure 2.1**.

Due to mass and charge balance during corrosion, the charge transfer rate due to metal oxidation must be the same as that due to solution reduction:

$$i_{ox} = |i_{red}| = i_{corr} \quad (\text{Eq. 2.4a})$$

If the E_{corr} is sufficiently far away from the equilibrium potentials of the two half-reactions, the anodic and cathodic currents can be approximated by:

$$i_{ox} \approx i_{ox}^{E_{ox}^{eq}} \cdot \left\{ \exp \left(\alpha_{ox} \cdot \left(\frac{nF}{RT} \right) \cdot (E_{corr} - E_{ox}^{eq}) \right) \right\} \quad (\text{Eq. 2.4b})$$

$$i_{red} \approx i_{red}^{E_{red}^{eq}} \cdot \left\{ - \exp \left((1 - \alpha_{red}) \cdot \left(\frac{nF}{RT} \right) \cdot (E_{red}^{eq} - E_{corr}) \right) \right\} \quad (\text{Eq. 2.4c})$$

If the anodic current is entirely due to metal oxidation, it is referred to as the corrosion current and thus it signifies the rate of corrosion. The net current of the corroding system is, however, zero. So, to obtain the corrosion current the system is often polarized by applying an external voltage, E_{elec} . Under polarization, the net current can be determined by the Wagner-Traud equation derived from the Butler-Volmer equations (Eq. 2.5) [23]:

$$i_p^{elec} \approx i_{corr} \cdot \left\{ \exp \left(\alpha_{ox} \cdot \left(\frac{nF}{RT} \right) \cdot (E_{elec} - E_{corr}) \right) - \exp \left(\alpha_{red} \cdot \left(\frac{nF}{RT} \right) \cdot (E_{elec} - E_{corr}) \right) \right\} \quad (\text{Eq. 2.5})$$

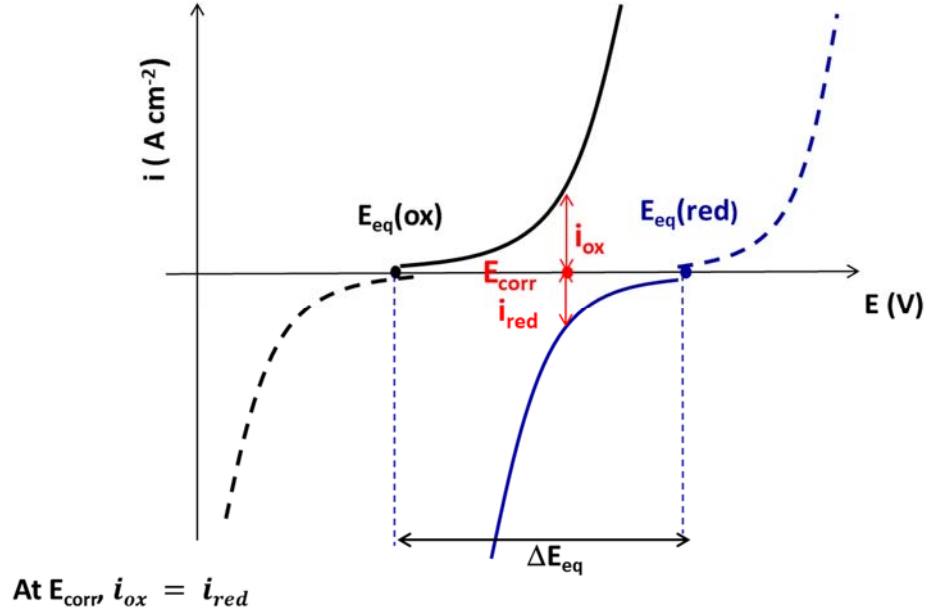


Figure 2.1: Schematic illustration of the Butler-Volmer relationships for metal oxidation and solution reduction reactions.

When E_{elec} is sufficiently higher or lower than E_{corr} , the anodic or cathodic current as a function of polarization potential can be approximated by

$$i_{ox}^{elec} \approx i_{corr} \cdot \left\{ \exp \left(\alpha_{ox} \cdot \left(\frac{nF}{RT} \right) \cdot (E_{elec} - E_{corr}) \right) \right\} \quad (\text{Eq. 2.6a})$$

$$i_{red}^{elec} \approx i_{corr} \cdot \left\{ - \exp \left(\alpha_{red} \cdot \left(\frac{nF}{RT} \right) \cdot (E_{elec} - E_{corr}) \right) \right\} \quad (\text{Eq. 2.6b})$$

If the metal surface and the concentrations of metal cations and solution redox species near the surface (in the metal-solution interfacial region) do not change significantly with time, the corrosion rate and hence the E_{corr} will remain constant with time.

2.3.2. Effect of Mass Transport on the Corrosion Process

This section describes the mass transfer process as an important factor in corrosion and electrochemistry processes. Despite the fact that corrosion and electrochemical reactions are controlled by electron transfer kinetics, the balance between the cathodic and the anodic reactions strongly depends on the mass transport of redox-active species [24–26].

Generally, mass transfer is the movement of species from one location in solution to another, or from the metal surface to the solution and/or from the solution to the metal surface. This is due to the driving force caused by differences in electrical or chemical potential at the two locations or from solution convection. Mass transfer in solution occurs via three modes:

1. *Diffusion*: Movement of a species due to a concentration gradient (i.e. chemical potential).
2. *Migration*: Movement of charged species due to an electric field gradient (a gradient of electrical potential).
3. *Convection*: Solution flow due to natural convection (convection caused by density gradients) and/or forced convection, due to stirring the solution or using a rotating disk electrode [23].

The mass transfer of a species j in solution is governed by the Nernst-Planck equation. Considering just one-dimensional diffusion along the x-axis, the three terms for the contributions of diffusion, migration, and convection to the flux are from left to right respectively:

$$J_j(x) = -D_j \frac{\partial C_j(x)}{\partial x} - \frac{\eta_j F}{RT} D_j C_j \cdot \frac{\partial \phi(x)}{\partial x} + C_j v(x) \quad (\text{Eq. 2.7})$$

where $J_j(x)$ is the flux of species j (mol/cm²) at distance x from the surface (**Figure 2.2**), D_j is the diffusion coefficient (cm²/s), $\frac{\partial C_j(x)}{\partial x}$ is the concentration gradient at distance x , $\frac{\partial \phi(x)}{\partial x}$ is the potential gradient, C_j and η_j are the concentration (mol/cm³) and charge (dimensionless) of species j , respectively, and $v(x)$ is the rate (cm/s) of the solution flux along the x axis. The convection component is small in the absence of stirring or vibrations in the electrochemical cell, and it can be eliminated in calculations [23].

To explain this process, let us consider a one-electron transfer solution reduction reaction. In the oxidation reaction similar mass transport phenomena are involved but in the reverse direction. During a reduction reaction ($O + e^- \rightarrow R$), the concentration of the species O at the electrode surface, $C_O(x = 0)$, decreases and becomes lower than its concentration in the bulk solution far from the electrode surface, C_O^* . However the species R is produced at the electrode surface, so that the concentration of R increases at the surface ($C_R(x = 0)$) and this concentration becomes higher at the surface than in the bulk solution ($C_R(x = 0) > C_R^*$).

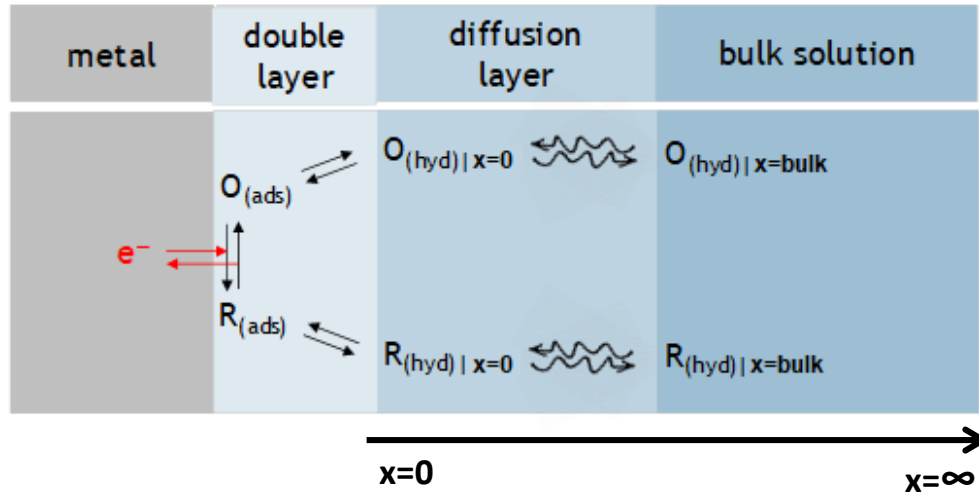


Figure 2.2 : Electron transfer and mass transfer of species during reduction reaction of $O + e^- \rightleftharpoons R$. $O_{(ads)}$ and $R_{(ads)}$ represents the species O and R adsorbed on the metal surface, $O_{(hyd)|x=0}$ and $R_{(hyd)|x=0}$ the species O and R presents at $x=0$, and $O_{(hyd)|x=bulk}$ and $R_{(hyd)|x=bulk}$ O and R species in the bulk solution.

So, the species R being transported from the surface to the bulk solution (and species O from bulk to surface) can affect the steady-state potential. The concentrations of O and R at the electrode determine the equilibrium potential of the half reaction, as governed by the Nernst equation for the half-reaction:

$$E = E^0 + \frac{RT}{nF} \ln \frac{C_O(x=0)}{C_R(x=0)} \quad (\text{Eq. 2.8})$$

At $x = 0$, solution stirring is ineffective, since the (x) term is considered zero (at $x = 0$) and a stagnant layer of thickness (δ_O, δ_R) known as the diffusion layer exists at the electrode surface and the concentrations of O and R beyond $x = \delta_O, \delta_R$ are C_O^* and C_R^* (Figure 2.3).

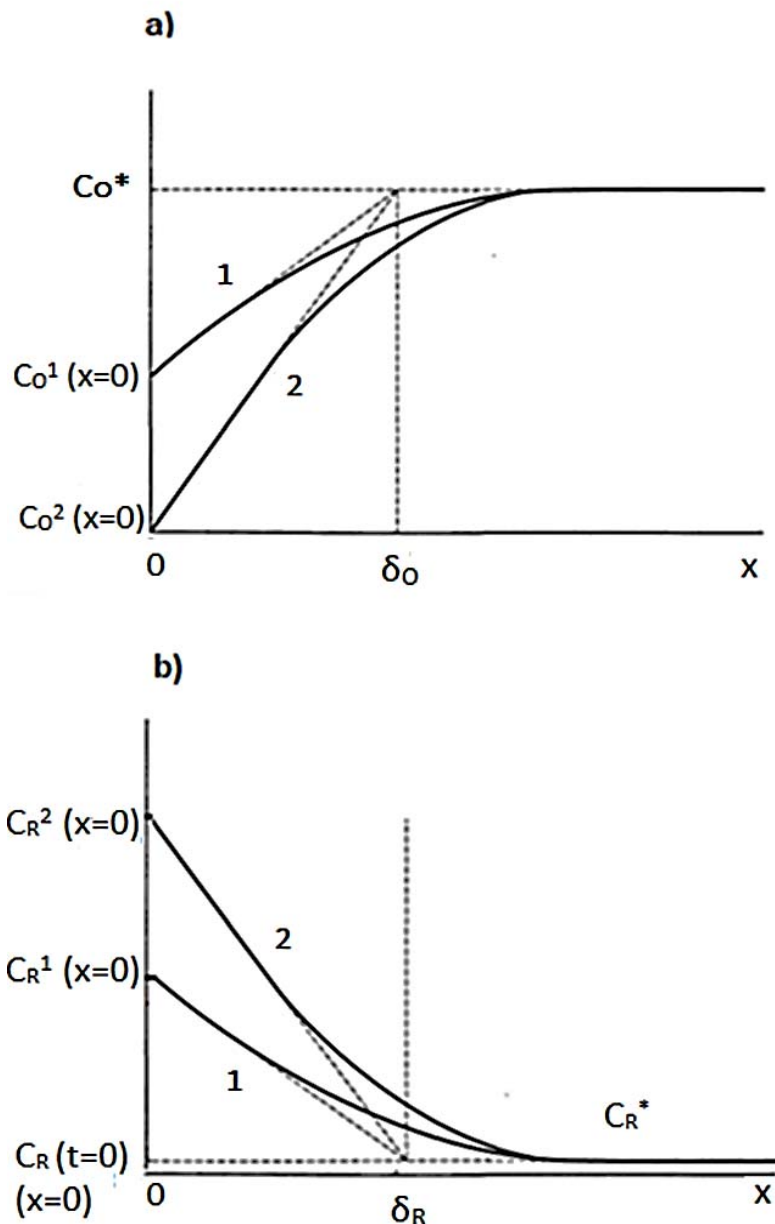


Figure 2.3: Concentration profiles (solid lines) and diffusion layer approximation (dashed lines); $x = 0$ corresponds to the electrode surface and δ is the diffusion layer thickness of: a) oxidizing species (O) and b) reducing species (R). Concentration profiles are shown at two different electrode potentials: (1) C_{O^*} and C_R^* are bulk concentrations of O and R respectively. (2) $C_{O,R}(x=0)$ ($t=0$) and $C_{O,R}^1(x=0)$ and $C_{O,R}^2(x=0)$ are concentration of species O and R at the interface at time 0, 1 and 2 respectively [25,26].

If we assume that the rate of mass transfer (v_{trans}) of species O is governed by the diffusion term, it is proportional to the concentration gradient (e.g. O) at the electrode surface [23]:

$$v_{trans} \propto \left(\frac{dC_O}{dx}\right)_{x=0} = D_O \left(\frac{dC_O}{dx}\right)_{x=0} = D_O [C_O^* - C_O(x=0)]/\delta_O \quad (\text{Eq. 2.9})$$

and the current density in the diffusion-controlled process can be determined based on the surface concentration:

$$\frac{i}{nFA} = v_{trans} = D_O [C_O^* - C_O(x=0)]/\delta_O \quad (\text{Eq. 2.10})$$

The diffusion thickness as a function of time is defined by this equation:

$$\delta(t) = 2\sqrt{D_O \cdot t} \quad (\text{Eq. 2.11})$$

And consequently, current is defined as:

$$\frac{i}{nFA} = v_{trans} = \frac{D_O^{1/2}}{2t^{1/2}} [C_O^* - C_O(x=0)] \quad (\text{Eq. 2.12})$$

Based on this equation, it is predicted that the diffusion layer grows linearly with $t^{1/2}$ and consequently current decays linearly with $t^{-1/2}$. In the presence of convection, the current density decays until it eventually approaches the steady-state value characterized by $\delta(t) = \delta_O$. However in the absence of convection, the current continues to decay [23,28] (**Figure 2.4**).

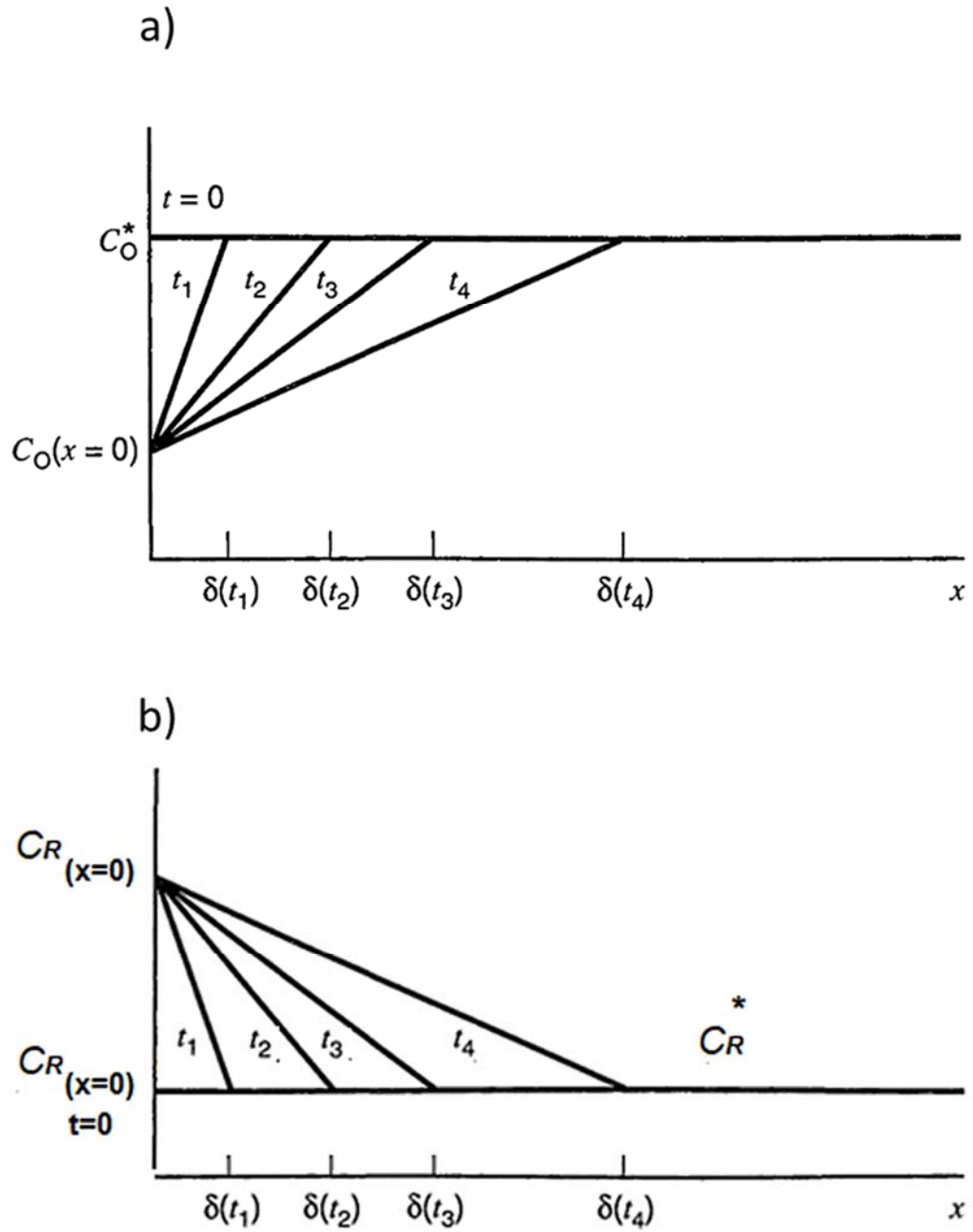


Figure 2.4: Growth of the diffusion-layer thickness with time: a) oxidizing species (O) , b) reducing species (R) [25,26].

For the solution reduction reaction ($O + e^- \rightarrow R$), R is produced at the electrode surface, so that C_R at the surface ($x = 0$) $> C_R^*$. Therefore, the same equations and concepts govern the diffusional mass transport of species R and control the current density (**Figure 2.2**).

2.3.2.1. Migration and Diffusion

To simplify the formulation of mass transport, the contribution of the migrational component to the flux is often considered to be negligible and the flux of electroactive species to or from the electrode is mainly assessed using the diffusion concentration gradients of the electroactive species (diffusional transport). However there is always a varying contribution of migration to the total current (flux of a species) which at a given time vary at different locations in solution (**Figure 2.5**).

Near the electrode, where the concentration gradients of the electroactive species arise, ions are transported by both diffusion and migration processes. The flux of ions at the electrode surface controls the rate of reaction and, consequently, the oxidation and/or reduction current. That current can be separated into diffusion and migration currents [23].

$$-J_j = \frac{i_j}{n_j F A} = \frac{i_{d,j}}{n_j F A} + \frac{i_{m,j}}{n_j F A} \quad (\text{Eq 2.13a})$$

$$\frac{i_{d,j}}{n_j F A} = D_j \frac{dC_j}{dx} \quad (\text{Eq 2.13b})$$

$$\frac{i_{m,j}}{n_j F A} = \frac{n_j F D_j}{RT} C_j \frac{d\phi}{dx} \quad (\text{Eq 2.13c})$$

Where J_j is the flux of mass transport of species j , $i_{d,j}$ is the diffusion current and $i_{m,j}$ are the migration currents of species j .

In the bulk solution (away from the electrode), concentration gradients are generally small, and the total current is carried mainly by migration. In low ionic strength solution the rate of the migration component plays an important role in the mass transport process. Migration occurs concurrently with the electron transfer reactions and the equivalent current density is determined using Eq. 2.13c.

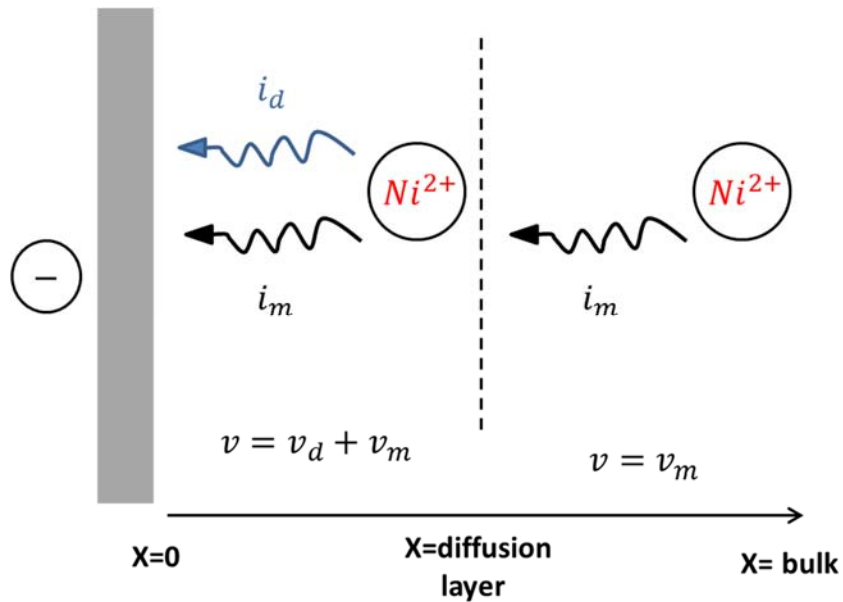


Figure 2.5: Contribution of the diffusion and migration components in mass transport process at a distance (x) from the electrode surface when negative potential is applied to the electrode. i_m corresponds to the contribution of migration to the current density and i_d is the contribution of diffusion to the current density.

The migrational component and diffusion constant are mainly governed by the ion mobility, μ , which is the limiting ion velocity in an electric field. Mobility has units of $\text{cm}^2 \cdot \text{V}^{-1} \cdot \text{s}^{-1}$. When a field of certain strength is applied to an ion, it will move under the force thus produced, resulting in continuous motion at a certain velocity.

$$\mu_j = \frac{|m_j|FD_j}{RT} \quad (\text{Eq 2.14})$$

The ion mobility is also determined by the equivalent conductivity (λ_{eq}) [29,30];

$$\mu = \frac{\lambda_{eq}}{F} \quad (\text{Eq 2.15})$$

The equivalent conductivity of a solution is defined as the conductance of an electrolyte solution containing one gram equivalent of the electrolyte ($\text{cm}^2 \text{mol}^{-1} \Omega^{-1}$) and is determined by [30]:

$$\lambda_{eq} = \frac{\Lambda_{\text{mol}}}{\sum_j |m_j| v_j} \quad (\text{Eq 2.16})$$

where Λ_{mol} is the molar conductivity, which is the sum of the contributions of its individual ions:

$$\Lambda_{\text{mol}} = (\sigma_+ \lambda_+ + \sigma_- \lambda_-) \quad (\text{Eq 2.17})$$

Here σ is a stoichiometric coefficient referring to the number of ions in a mole of electrolyte, λ are the ion conductivities, and the subscripts + and – refer to cation and anion, respectively.

Also solution ionic conductivity is strongly correlated with ion mobility and ion transport. The ionic conductivity is movement of the charge due to the motion in electrolyte solution and it is given by [30,31]:

$$\kappa = C_s \Lambda_{\text{mol}} = \sum_j C_j |z_j| v_j \lambda_{eq} = F \sum_j C_j |z_j| \sigma_j \mu_j \quad (\text{Eq. 2.18})$$

The conductivity, κ , is an intrinsic property of the solution and is expressed in $\text{S}\cdot\text{cm}^{-1}$ ($\Omega^{-1}\cdot\text{cm}^{-1}$). Since the current flow through the solution is achieved by the movement of different species, κ is the sum of contributions from all ionic species, j .

Solution conductivity detects the presence of ions in solution and is used to assess ionic strength (I_s) which the term $\sum_j C_j Z_j$ in κ (**Eq. 2.18**) is proportional to that [31–33] and the equivalent conductance of individual ions in a mixed ion solution can be reported as a function of the ionic strength [34]. The ionic strength of solution can be calculated based on the equation below:

$$I = \frac{1}{2} \sum_{j=1}^{j=n} C_j z_j^2 \quad (\text{Eq. 2.19})$$

2.3.3. Corrosion in the Presence of an Oxide Layer

The above discussion can be adapted to include the effect of the presence of an oxide layer. In the presence of an oxide layer the rate of both migration and diffusion can be affected due to changes in the potential gradient (potential drop) at the surface and limited ion transport through the oxide layer.

The oxide layer is a corrosion reaction potential barrier, which one effect of that is reducing the effective overpotential that drives metal oxidation [22]:

$$\eta_{ox} \approx E_{corr} - E_{ox}^{eq} - \Delta V_{oxide} \quad (\text{Eq. 2.20})$$

Accordingly, the corrosion rate decreases in the presence of an oxide layer due to potential drop, with the current given by [22]:

$$i_{ox}^{corr} \approx i_{ox}^{E_{ox}^{eq}} \cdot \left\{ \exp \left(\alpha_{ox} \cdot \left(\frac{nF}{RT} \right) \cdot (E_{corr} - E_{ox}^{eq} - \Delta V_{oxide}) \right) \right\} \quad (\text{Eq. 2.21})$$

The magnitude of the potential barrier depends on the physical and electrochemical nature of the oxide. For example, the addition of chromium to an alloy of nickel increases the corrosion resistance of the alloy metal, because a very passive chromium oxide forms on the metal surface under many environmental conditions.

Moreover, in the presence of an oxide layer, the overall corrosion process involves more than two phases and more than one interface. In order to complete the corrosion reaction, a net flux of positive charge (metal cations, holes) must proceed from the m|ox interface to the ox|sol interface. At this point the cation can dissolve into the solution phase or be incorporated into the oxide phase. At the same time a net flux of negative charge (electrons, oxygen anions) must proceed from the ox|sol interface to the m|ox interface [13,22,35]. Hence the presence of oxide layer can limit the rate of mass transport of ions and consequently limit the rate of corrosion. These processes are schematically presented in **Figure 2.6**.

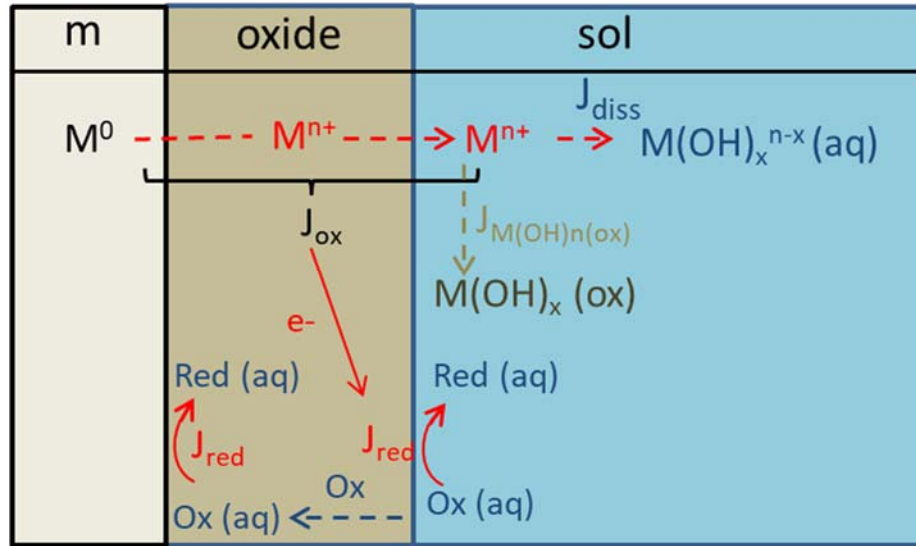
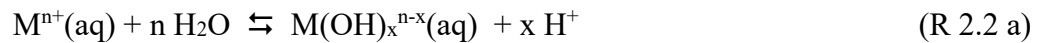


Figure 2.6: Schematic illustration of the corrosion reactions in the presence of an oxide layer and their fluxes as considered in the Mass and Charge Balance (MCB) model [13,34,35].

Because corrosion involves the net transfer of metal cations and not just electrons, the oxide potential barrier also increases as the oxide thickness increases. (This is not the case for electron or hole transfer between an inert semiconductor and a solution phase.) Transition metal cations in solution are easily hydrolysed to form metal hydroxides under mildly acidic to basic solution conditions and the hydroxide may precipitate:



The precipitated hydroxide can grow as a layer on the corroding metal and/or be dehydrated to form an oxide as corrosion progresses. The rate of oxide/hydroxide growth

will depend on the metal cation hydrolysis equilibria (R 2.2 a) and hence on the oxidation state of the metal cation and the solution pH.

Changing the solution redox environment will change E_{corr} , as noted earlier. One means of altering the redox conditions is a flux of ionizing radiation which generates both oxidizing and reducing species in solution. If the impact of the radiation is to increase the oxidizing potential of the solution this may initially increase the rate of metal oxidation. However, an increase in the metal oxidation rate can also induce faster growth of an oxide layer. A higher oxidizing potential, depending on the solution pH and temperature, could also promote conversion of one type of oxide layer to another passive oxide layer.

2.4. CORROSION OF NICKEL

Before exploring the corrosion of nickel in more depth, a review of the possible oxides that can be formed during corrosion of nickel would be beneficial. Nickel has the electron configuration $[\text{Ar}] 3d^8 4s^2$ [36] and there are four possible oxidation states of nickel during oxidation, Ni^{I} , Ni^{II} , Ni^{III} and Ni^{IV} , depending on potential [37–41].

Although in nickel based alloys the protective oxide layer is attributed to formation of Cr, Mo, Cu oxide on the surface, in this thesis it is illustrated that the nickel oxides have a significant contribution in impeding nickel corrosion and hence nickel based-alloys [42]. Despite extensive studies on nickel oxides, there are many outstanding questions regarding both the structure and the activity of nickel oxides [43].

2.4.1. Nickel (II) Hydroxide (Ni(OH)₂)

Nickel(II) hydroxide has two well-characterized polymorphs, α and β . The α structure consists of Ni(OH)₂ layers with intercalated anions or water. The real composition of the α -hydroxide may be represented as Ni(OH)₂.xH₂O, where 0.5 < x < 0.7. There is evidence that some α -Ni(OH)₂ materials have Ni–O coordination numbers greater than six [44–47] (**Figure 2.7**). The β structure comprises a hexagonal close-packed structure of Ni^{II} and OH⁻ ions (**Figure 2.8**) [45,46].

During Ni(OH)₂ precipitation from aqueous solutions, well-crystallized β -Ni(OH)₂ is not the primary product. Ni(OH)₂ precipitation mainly results in poorly crystallized α -type hydroxides which can then convert to β -Ni(OH)₂ by ageing of such compounds, but always contain adsorbed foreign ions and water. Crystallized nickel hydroxide does not show large well-shaped crystals [45]; these crystals are mainly filament-like [48] oxides with a green colour.

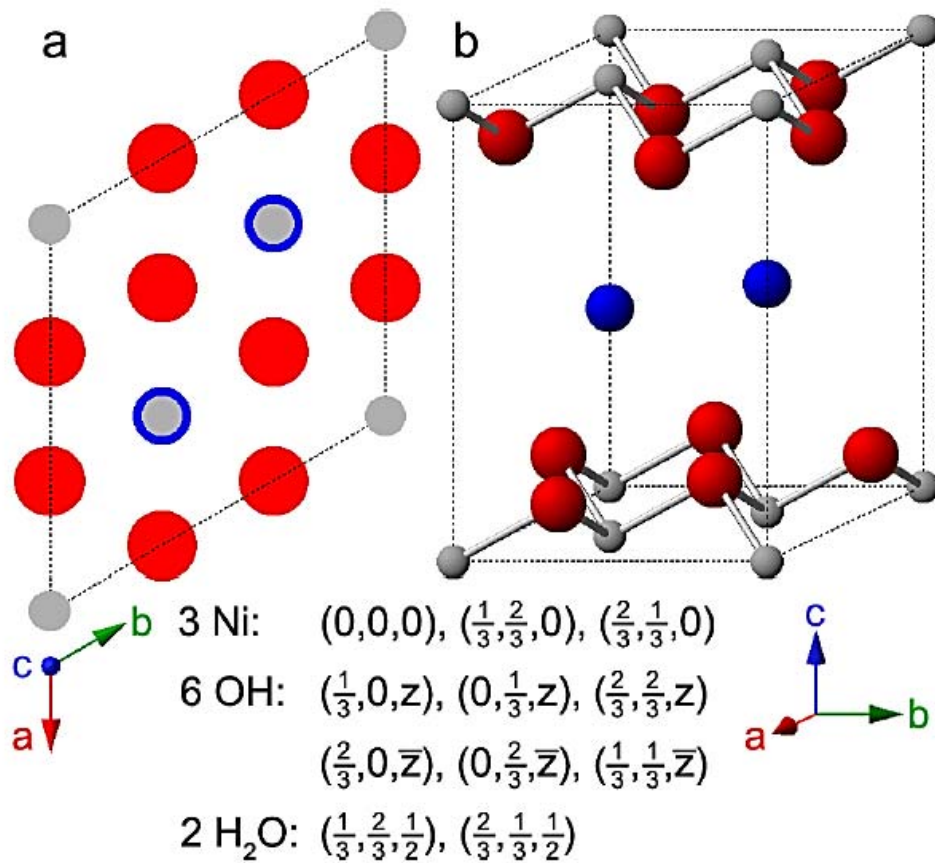


Figure 2.7: The crystal structure of α -Ni(OH)₂·xH₂O : (a) unit cell projection and (b) ball-and-stick unit cell for $x = 0.67$ (actual value varies, $0.5 \leq x \leq 0.7$). Grey spheres = Ni²⁺, Red spheres = OH⁻, Blue spheres = H₂O [49].

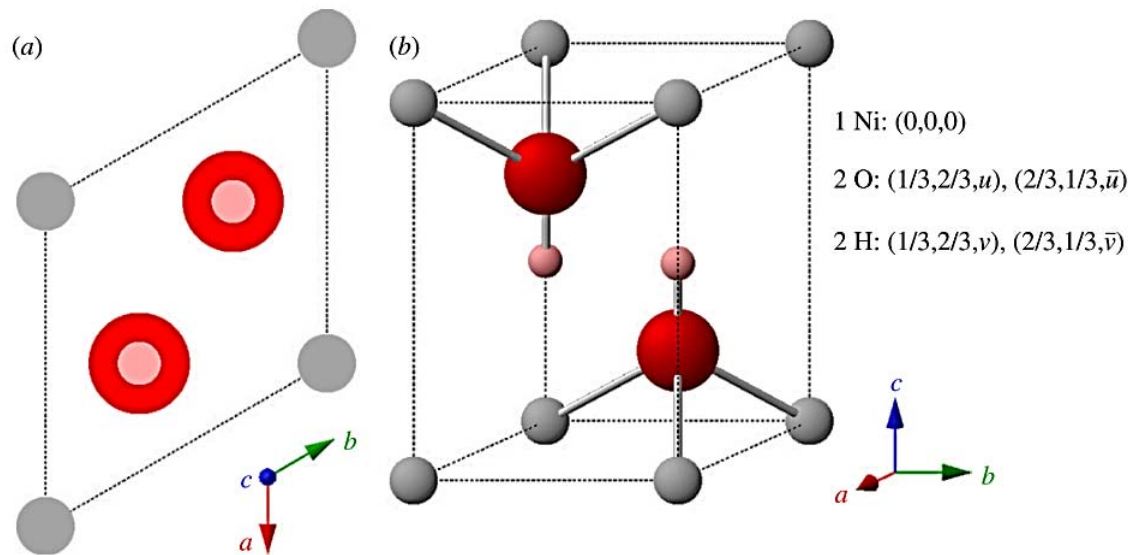


Figure 2.8: The crystal structure of β -Ni(OH)₂ : (a) unit cell projection and (b) ball-and-stick unit cell ($u = 0.24$ and $v = 0.47$; or $u = 0.2221$ and $v = 0.4275$). Gray spheres, Ni²⁺; Red spheres, O²⁻; Pink spheres H⁺ [50].

2.4.2. Nickel (II) Oxide (NiO)

Nickel(II) oxide (bunsenite) can be produced by nickel oxidation, chemical deposition and the sol gel method [44,51]. NiO has octahedral structure (**Figure 2.9**) which is similar to the NaCl crystal structure and known as the rock salt structure. Stoichiometric NiO is (1:1) and is considered an insulator at room temperature, with a conductivity $\kappa < 10^{-13}$ 1/ Ω cm [52]. However, nickel oxide is rarely stoichiometric (i.e., Ni_{1.00} O_{1.00}) which means that a different stoichiometry ($Ni_{1-\delta}O$) is observed, in which the ratio between nickel and oxygen is not exactly 1:1 [51,52]. This is due to the presence of a small number of Ni³⁺ ions in the crystal lattice as well as Ni²⁺ ions [53], excess oxygen and/or Ni vacancies, which gives nickel oxide p-type semiconductor properties [51]. It is reported that the conductivity of the oxide is proportional to the concentration

of the Ni^{3+} ions in the lattice [53], and the optical band-gap of NiO is in the range 3.4 eV [54] to 4.3 eV [55].

The colours of nickel oxides are highly sensitive to their stoichiometries and the presence of higher oxidation state nickel ions in the structure, even in trace amounts, can result in a colour change [56]. Stoichiometric NiO is green and non-stoichiometric NiO is black.

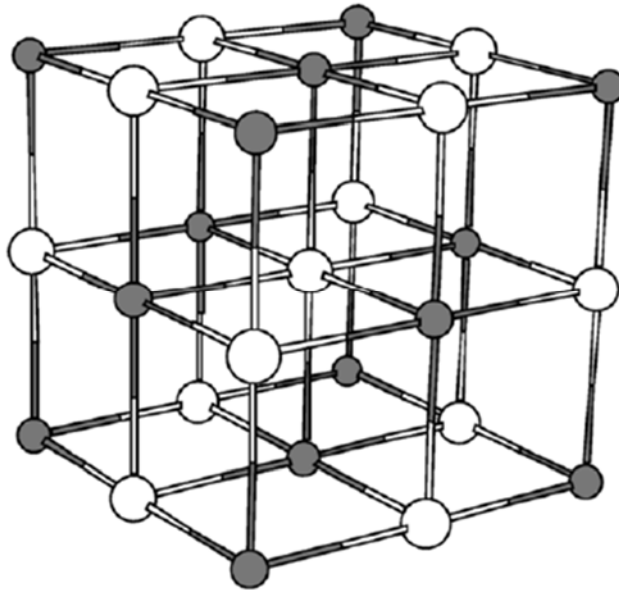


Figure 2.9: Nickel oxide crystal structure. Nickel sites are shown as grey spheres and oxygen sites are shown in white [57].

2.4.3. Ni₃O₄

Ni₃O₄ has an orthorhombic crystal structure and precipitates in neutral and alkaline solutions due to its low solubility at high pH; however, it is highly soluble in acidic solutions. After Ni₃O₄ has formed, it is very difficult to reduce [41]. The band gap of this oxide is 3.7 eV[58].

In this oxide nickel has mixed Ni^{II}/Ni^{III} oxidation state and it usually occurs in the hydrated form, Ni₃O₄.2H₂O; however at high temperatures (above 140 °C), it begins to dehydrate and lose weight [59].

2.4.4. Ni₂O₃

Ni (III) oxide (Ni₂O₃) has a dark grey to black colour. This oxide has a hexagonal crystal structure [60,61] with $a_0 = 4.61$ Å and $c_0 = 5.61$ Å [61]. The band gap reported for this oxide is 3.38 [62] to 5.71 eV [63].

2.4.5. NiOOH

A well-known Ni(III) oxide is nickel oxyhydroxide (NiOOH), and the redox pair NiOOH / Ni(OH)₂ is commonly used in nickel-based secondary batteries due to phases which are active for the oxygen evolution reaction [49]. There are two possible nickel oxyhydroxy compounds, β- and γ-NiOOH, with different unit cell parameters and symmetries, which generate two-layered nickel oxyhydroxides [49,65,66].

Under strong oxidation conditions, the redox reaction β-Ni(OH)₂ → β-NiOOH occurs. It has been reported that the X-ray diffraction pattern for β-NiOOH indicates a hexagonal structure derived from that of β-Ni(OH)₂, with similar cell parameters.

Therefore, the structure of β -NiOOH is assumed to be well represented by that of β -Ni(OH)₂ [66]. However, γ -NiOOH has a layered rhombohedral crystal structure, with corresponding hexagonal parameters of $a=4.883 \text{ \AA}$, $b=2.920 \text{ \AA}$, $c=9.24 \text{ \AA}$ [45,65,66]

Nickel transformation to hydroxides or oxyhydroxides is rapid at highly positive potentials and in strongly alkaline solutions.

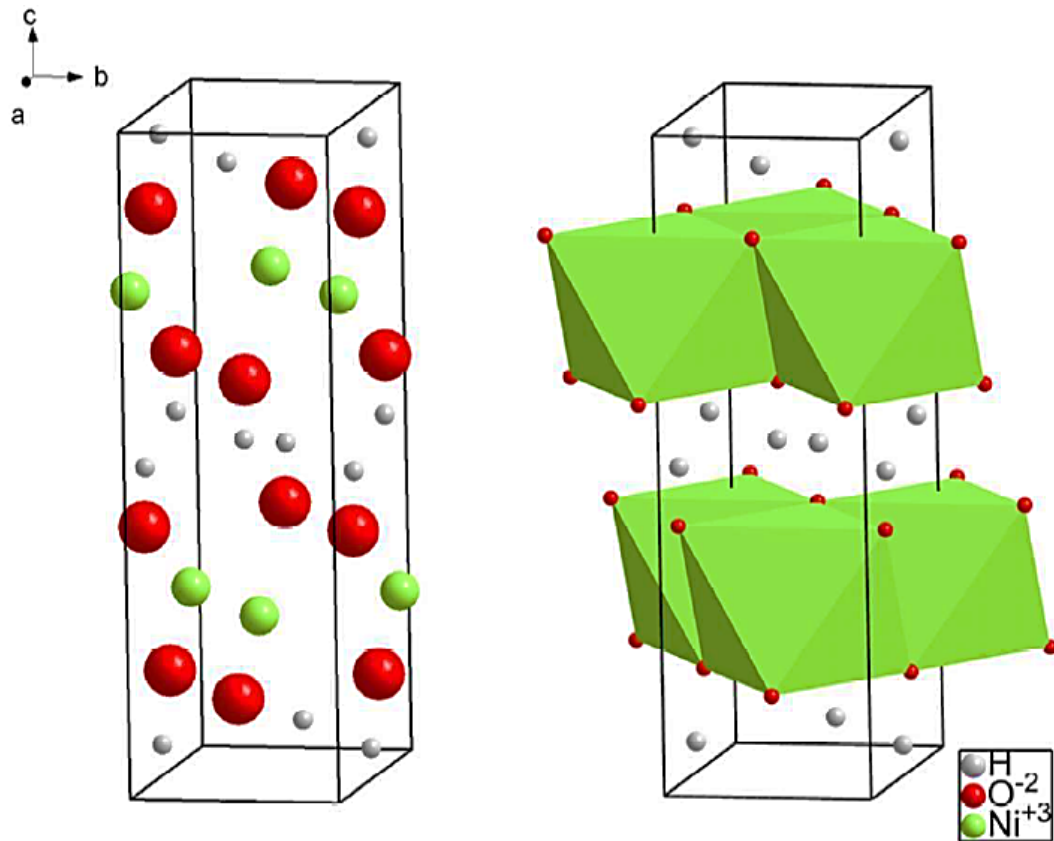


Figure 2.10: Left: Crystal structure of γ -NiOOH. Right: structure of the layered oxide with rhombohedral lattices. $a=4.883 \text{ \AA}$, $b=2.920 \text{ \AA}$, $c=9.24 \text{ \AA}$ [66]

2.5. REVIEW OF CORROSION OF NICKEL AND NICKEL-BASED ALLOYS

2.5.1. Hydrolysis and Solubility Behavior of Nickel Ions

To predict the corrosion behaviour of nickel-based alloys, it is essential to have a good understanding of pure Ni metal corrosion behaviour in aqueous media. This fundamental understanding includes the solubility of nickel ions in water.

The hydrolysis equilibria of the oxidized nickel species produce nickel hydroxyl monomers in solution: $\text{NiOH}^+(\text{aq})$, $\text{Ni}(\text{OH})_2(\text{aq})$, $\text{Ni}(\text{OH})_3^-(\text{aq})$, and $\text{Ni}(\text{OH})_4^{2-}(\text{aq})$. The total solubility of nickel ions in solution is equal to the sum of the concentrations of all monomers which contribute to the dissolution of the solid. The rate of hydration/hydrolysis of metal cations increases with pH but the solubility of metal cations decreases with solution pH [44,67]. The pH dependence of nickel solubility is illustrated in **Figure 2.11** [44].

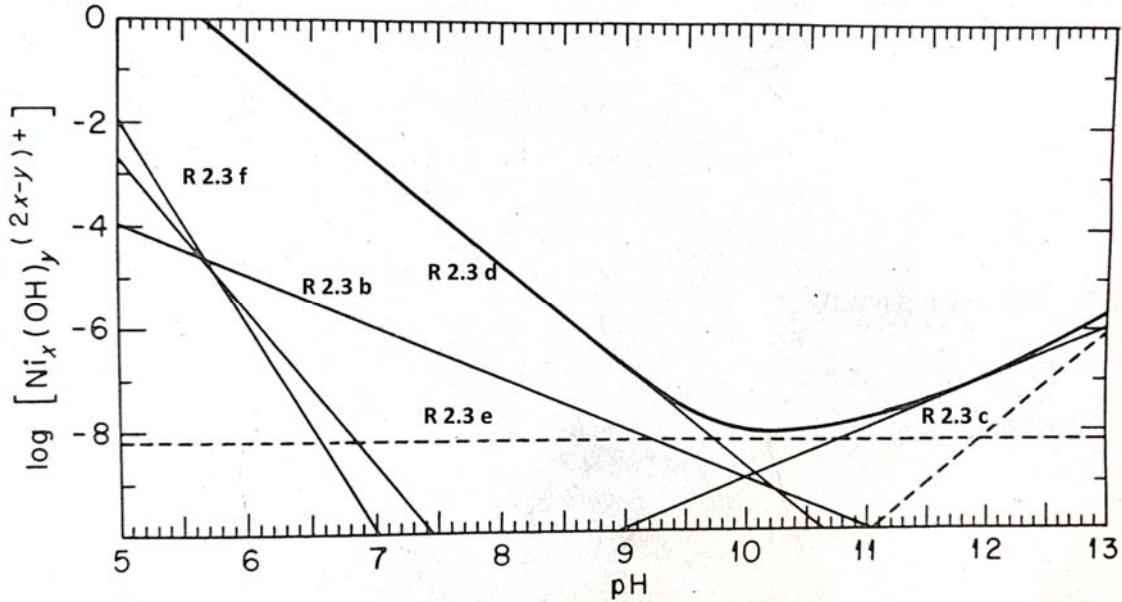


Figure 2.11: The solubility of Ni^{II} in water at 25 °C. Each line refers to a reaction which is presented in reaction the text [67].

The solubility of each species can be determined by the thermodynamic relationship [68]:

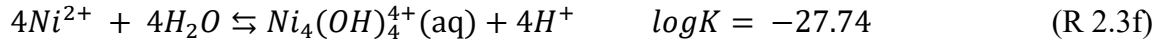


$$\log K_{sp} = \frac{-\Delta G_{reaction}^0}{2.303RT} = \log \left(\frac{a_{Ni^{2+}} a_{OH^{-}^2}}{a_{Ni(OH)_2}} \right)$$

$$\log a_{Ni^{2+}} = \log K_{sp} + (2pK_w) - 2pH \quad (Eq\ 2.21)$$

In which K_{sp} is the solubility equilibrium constant, ΔG^0 is the free energy of the reaction ($\text{kJ}\cdot\text{mol}^{-1}$), R is the gas constant ($8.314\ \text{J}\cdot\text{mol}^{-1}\cdot\text{K}^{-1}$), and T is the temperature. Some other hydration equations are provided below, the equilibrium constants of which can be determined based on thermodynamic relationships [67]:





To determine the equilibrium constants at different temperatures, it is essential to find the free energy of each reaction at the desired temperature. In this way, the solubility diagram can be determined at the desired temperature.

2.5.2. Pourbaix Diagram of Nickel System

The Pourbaix diagram, also known as the potential/pH diagram, is one of the most common ways to map out thermodynamically stable phases of particular species at a range of pH and potentials. This diagram predicts areas of immunity (no corrosion), passivity (formation of protective oxide on the surface) and corrosion (dissolved metal ions in solution) [44,48].

Since this diagram only considers the stable thermodynamic phase, it only provides information about the driving force for system reactions but not any kinetic information. Pourbaix diagrams are commonly given at room temperature, atmospheric pressure, and molar concentrations of 10^{-6} M, and changing any of these parameters will yield a different diagram [44,69]. There are various published E-pH diagrams for the Ni-

H₂O system available at different temperatures. One E-pH diagram for the Ni-H₂O system at 25 °C is illustrated in **Figure 2.12**.

In **Figure 2.12**, it can be seen that as potential increases (depending on the solution pH) passivation of Ni can occur at four different potentials and involve the redox reactions: $\text{Ni} \rightleftharpoons \text{NiO}$, $\text{NiO} \rightleftharpoons \text{Ni}_3\text{O}_4$, $\text{Ni}_3\text{O}_4 \rightleftharpoons \text{Ni}_2\text{O}_3$, $\text{Ni}_2\text{O}_3 \rightleftharpoons \text{NiO}_2$ [40,70].

However, below the potential of formation of $\text{NiO} \rightleftharpoons \text{Ni}_3\text{O}_4$, protective nickel oxides can be formed directly from nickel metal. As this suggests, the potential/pH diagram can be modified with the Ni redox reactions $\text{Ni} \rightarrow \text{Ni}_3\text{O}_4$, $\text{Ni} \rightarrow \text{Ni}_2\text{O}_3$ and $\text{Ni} \rightarrow \text{NiO}_2$ which are presented with dashed lines in **Figure 2.12**. Moreover the oxides can be metastable in the “corrosion” region of the diagram, so that the relevant lines may be extended into the region of low pH [40].

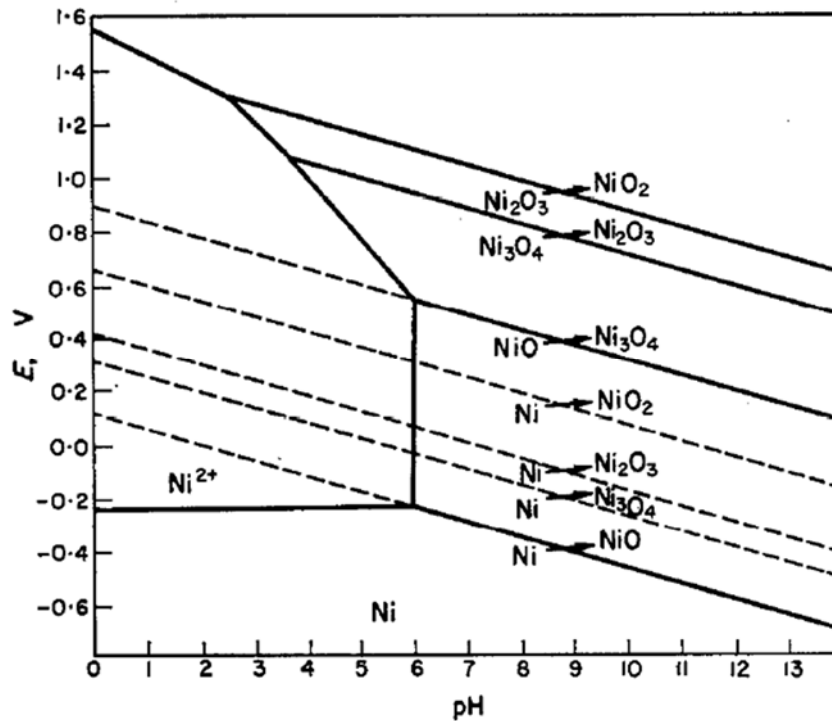


Figure 2.12: Potential/pH diagram for Ni-H₂O at 25 °C [40].

In another study, **Figure 2.13**, Ni_3O_4 , Ni_2O_3 and NiO_2 were not considered to be involved in passive film formation. In this diagram the passivity of nickel is considered to result from the formation of $\beta\text{-Ni(OH)}_2$, NiO and $\gamma\text{-NiOOH}$. In this study the thermodynamically stable immune nickel metal at low potential is considered to be the $\text{Ni}_{0.5}\text{H}$ hydride. In this study, increasing temperature from 25 to 300 °C increases the contribution of NiO to passivity, since at high temperatures bunsenite is more stable than the hydroxide [44].

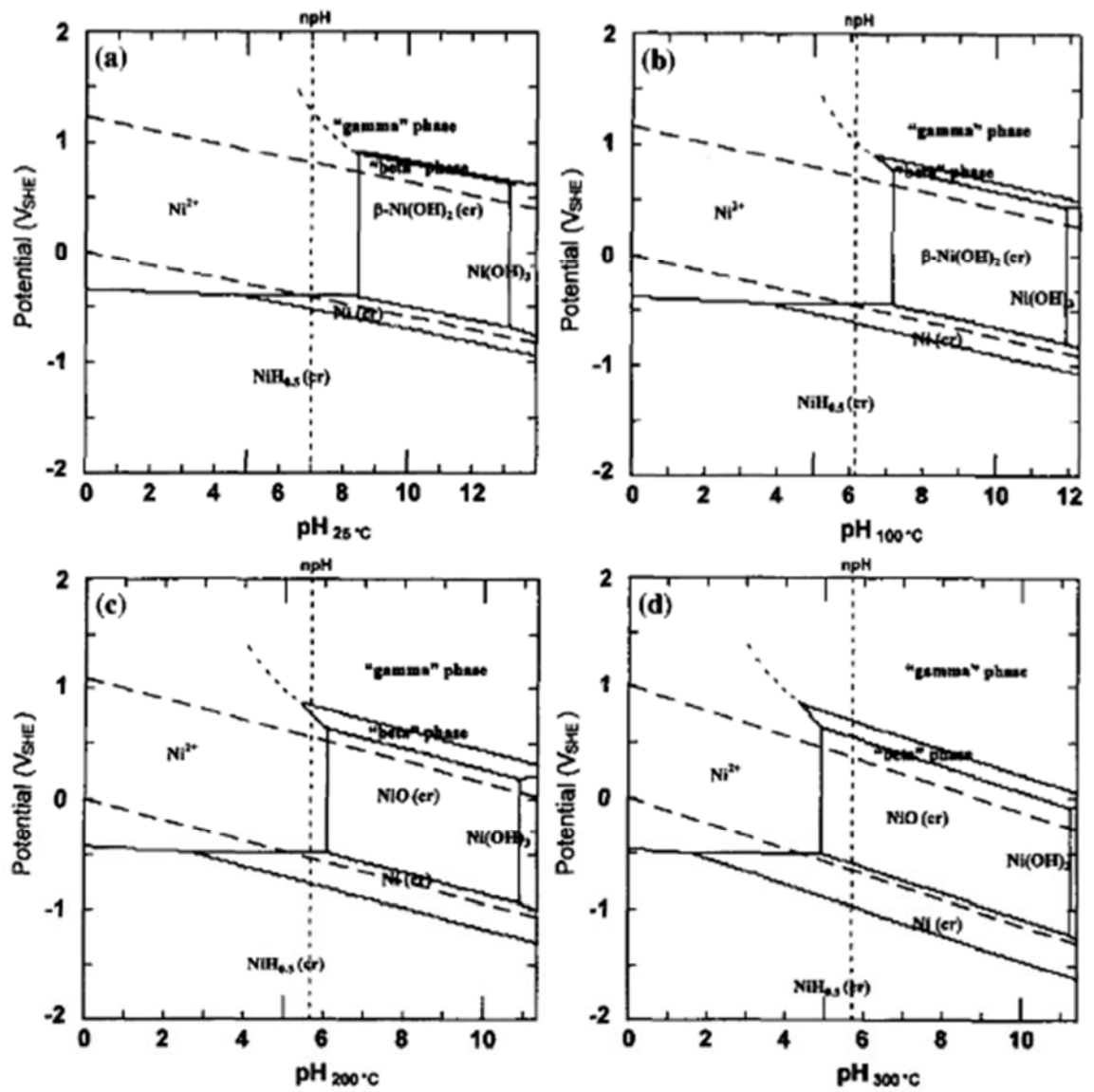


Figure 2.13: Pourbaix diagram for nickel at 25, 100, 200 and 300 °C [44,71].

2.5.3. Review of the Corrosion of Nickel and Nickel Oxide Formation

Nickel oxidation and oxide formation have been investigated extensively. The focus of these studies varied from nickel applications such as batteries, catalysts, and industrial applications in which the corrosion behaviour of pure nickel and/or Ni-containing alloys are studied.

Thian et al. [72] investigated the effect of nickel content on the corrosion behaviour of high-strength low alloy steel in simulated concrete pore solution. They found that addition of 3 wt% of nickel to the carbon steel reduced the corrosion current from 730 nA/cm² to 17 nA/cm² under the contaminated concrete conditions. This was attributed to the formation of a protective oxide film. Nickel was enriched in the oxide layer, consequently decreasing the defect density and the thickness of the oxide film.

Grégoire et al. [73,74] studied the influence of various test conditions on the corrosion of pure nickel at 700 °C, which enabled them to come to some conclusions on the oxidation kinetics. The testing parameters involved the composition of the atmosphere and the presence or absence of Na₂SO₄ and Na₂SO₃. Based on their results they proposed a mechanism for nickel hot corrosion based on the boundary conditions. They proposed that sulphidation mechanisms ($\text{NiO (s)} + \text{SO}_3 \text{ (g)} \rightarrow \text{NiSO}_4 \text{ (g)}$) are the main process governing corrosion in the studied conditions which is limited by the p_{SO_3} and its diffusion through the porous NiO scales. Sulphidation produced high porosity corrosion oxides on pure nickel due to inward transport of sulphur molecules and of oxygen from the oxide/gas interface towards the metal/oxide interface.

Yang et al. [75] investigated the mechanical and corrosion properties of nickel-aluminium bronze (NAB) with four Ni content levels in 3.5 wt.% NaCl solution. Increasing the Ni content increased the yield strength and hardness of the alloys. The results from coupon immersion corrosion tests and impedance spectroscopy illustrated that an increase in Ni (4.5–10 wt.%) improved the corrosion resistance of the NAB alloys in 3.5 wt.% NaCl solution.

Dubey et al. [51] studied the effect of stoichiometry on the structural, thermal and electronic properties of nickel oxide at 400 to 1100 °C. In this study, non-stoichiometric nickel oxide samples ($Ni_{1-\delta}O$) were prepared by the thermal decomposition method and characterized by XRD, XPS and FTIR. The results showed that nickel oxide prepared by heating the precursor below 700 °C has an excess of oxygen which can change the oxidation state of nickel. An excess of Ni^{3+} ions was therefore observed at these temperatures.

Gromoboy et al. [40] carried out potentiostatic and galvanostatic studies on Ni in acid solutions. They measured the passivation potentials due to direct oxidation of nickel to different oxides: NiO, Ni_3O_4 , Ni_2O_3 and NiO_2 , and determined a modified potential/pH diagram for Ni- H_2O . They state that performing different heat treatment processes on nickel results in changing in nickel structure; and hence change in passivation potential and behaviour. This corresponds to formation of different oxide layers on nickel.

Jouen et al. [76] investigated the atmospheric corrosion of nickel in industrial, urban and rural environments. In these environments and the presence of anions such as Cl^- , SO_4^{2-} , NO_3^- and CO_3^{2-} , nickel undergoes a pitting corrosion process accompanied by

the formation of soluble corrosion products. Pits are associated with the formation of nickel oxides, mainly sulphates and chlorides with small amounts of nitrate, and surrounded by carbonate species. They also reported that the corrosion rate is higher in industrial areas than in rural areas.

Hall et al. [54] studied the oxidation and reduction of Ni electrodes in alkaline solutions by cyclic voltammetry (CV), galvanostatic and potentiostatic polarization, X-ray diffraction (XRD) and X-ray photoelectron spectroscopy (XPS). They reported that the polished nickel surface is covered by a layer of α -Ni(OH)₂ overlaid by non-stoichiometric nickel oxide. Above the RHE potential, NiO_x, α -Ni(OH)₂, β -Ni(OH)₂ and β -NiOOH form reversibly. Below the reversible hydrogen electrode (RHE) potential, these oxides mostly reduce back to Ni on subsequent cathodic polarization. By repeating oxidation and reduction, strain is induced on the sample surface which may lead to surface mechanical failure.

Hutton et al. [77] studied the electrodeposition of nickel hydroxide nanoparticles (NPs) on polycrystalline boron-doped diamond (pBDD). To achieve this, OH⁻ was electrogenerated by applying a potential of -1.1 V (Ag/AgCl) to the electrode in solution with highly supersaturated nickel hydroxide for short periods of time (approximately seconds). The results show that the deposition of nickel hydroxide nanoparticles occurs by direct precipitation of NPs on the surface. This was confirmed by XPS, FE-SEM, and AFM. The size of the NPs could be tuned by controlling the reaction conditions, particularly the [OH⁻] electrogeneration time.

Huntz et al. [78] studied the effect of impurities on the mechanical characteristics of the NiO film and the oxidation mechanism of nickel at 800 °C in air. The morphology of the oxide and the porosity depend on the impurity of nickel. In pure nickel, NiO was found in a simple oxide layer with equiaxial grains. The growth rate of this oxide layer is controlled by the diffusion efficiency of Ni^{2+} . When impurities are present (Mn, Mg, Ti, Si), two oxide layers form which act as an effective barrier, so that the growth rate of NiO is slower on nickel with impurities.

Dey et al. [60] studied the synthesis of Ni (III) oxide nanoparticles at room temperature. Pure Ni_2O_3 nanoparticles were synthesized by oxidation of $\text{Ni}(\text{NO}_3)_2 \cdot 6\text{H}_2\text{O}$ nickel precursors in a basic solution containing NaOH and NaOCl. Precipitation of black Ni_2O_3 occurred almost immediately after adding the hypochlorite solution. The precipitate was collected and dried in a hot air oven to obtain crystals of pure Ni(III) oxide nanoparticles. The structure, morphology, surface charge and chemical compositions of the pure dried powder were characterized by XRD, TEM, zeta potential and EDX which demonstrated that the particles were Ni_2O_3 . In order to investigate the temperature effect on particle size, they carried out the synthesis reaction at different temperatures. They showed that increasing the temperature from 0 to 25, 50 and 70 °C increases the size of NPs from 25.8 to 34.2, 42.6, and 49.7 nm respectively.

2.5.4. Review of Corrosion of Nickel-Based Alloys

Since the main objective of this thesis is to advance the fundamental understanding of the corrosion behaviour of nickel-based alloys, this section focuses on existing studies involving these alloys.

Musa et al. [13] studied the effect of γ -radiation on the corrosion of Inconel 600 (75.5% Ni, 16.5% Cr, 8.2% Fe) at pH_{25 °C} 6.0, 8.4 and 10.6 at 150 °C. They studied the corrosion by analyzing both the dissolved metal loss and examining the corroded surfaces. They reported that in the presence of γ -radiation water decomposes to a range of oxidizing species. This increases the initial rate of metal oxidation, but in the study, at longer times the effect varied with pH. At pH_{25 °C} 10.6 where the solubilities of Fe^{II} and Ni^{II} are near minimum, radiation predominantly increases the rate of solid oxide/hydroxide formation. However, at a lower pH, radiation predominantly increases metal ion dissolution.

Zhong et al. [79] studied the oxide films formed on Alloy 690 (61% Ni, 29.15% Cr, 9.19% Fe) exposed to 600 °C supercritical water. They used X-ray diffraction, X-ray photoelectron spectroscopy, scanning electron microscopy equipped with energy dispersive X-ray spectroscopy, and Raman spectroscopy. The results showed that the oxide film formed on the surface had a double-layer structure, with an outer layer rich in Ni and Fe and an inner layer rich in Cr, after short- and long-term exposure.

Momeni et al. [71] studied the effect of pH, temperature and γ -radiation on the corrosion of Alloy 800 (35% Ni, 19% Cr, 39.5% Fe). They showed that corrosion of Alloy 800 involves a series of elementary processes along with metal oxidation reactions

which lead to dissolution and/or precipitates of metal ions on the surface. The pH and γ -radiation affect the rates of the individual elementary processes and hence influence the overall corrosion rate and corrosion pathway. The combined effect of pH and γ -radiation is to increase the overall dissolution of $\text{Ni}^{2+}(\text{aq})$ at pH 6.0; however, at pH 10.6 they promote the formation of a passive oxide layer.

2.5.5. Review of Effect of Ionic Strength and Conductivity on Corrosion

This section focuses on studies on the effect of ionic strength and conductivity on the corrosion of different alloys and metals, and on the solubility and mass transport of ions under various conditions.

Wang et al. [80] studied the effect of solution conductivity on the corrosion behaviour of 304 stainless steel (SS) in a high temperature (300 °C) aqueous medium. They used potentiodynamic polarization, electrochemical impedance spectroscopy (EIS), scanning electron microscopy (SEM), X-ray diffraction (XRD), and X-ray photoelectron spectroscopy (XPS). The results indicated that an increase in conductivity can increase both the anodic and cathodic reactions at the same time. They suggested that an increase in conductivity directly influences the diffusion process and the oxide structure.

Liu et al. [81] studied the effect of ionic strength and temperature on iron sulfide precipitation kinetics, solubility, and phase transformations. They reported that by chemically adding ferrous ion solution [Fe(II) solution] and sulfide solution [S(-II) solution], FeS is precipitated, which is accelerated by an increase of temperature and

ionic strength. The freshly precipitated FeS was found to be mackinawite (tetragonal $(\text{Fe})_{1+x}\text{S}$ (where $x = 0$ to 0.11)) which converted to troilite (hexagonal $\text{Fe}_{(1-x)}\text{S}$ ($x = 0$ to 0.2)) when the ionic strength was reduced. Once troilite had formed, there was no evidence of further transformation to any other stable FeS phase.

Behazin et al. [48] studied the effect of temperature, ionic strength and radiation on the corrosion of Stellite-6 (62% Co, 32% Cr, 6% W). The results showed that changes in the ionic strength can affect the degree of oxidation of Stellite-6, especially at high temperatures and in the presence of a radiation field. At higher ionic strengths, a thicker oxide film formed on the surface and the rate of dissolution of Cr was higher.

2.6. RADIATION CHEMISTRY AND WATER RADIOLYSIS

In this thesis, the effect of ionizing radiation on the corrosion of nickel in an aqueous environment is investigated. To provide some background on the effect of ionizing radiation on the aqueous environment, a brief overview of radiation chemistry and water radiolysis is presented here.

Radiation chemistry is the study of the chemical effects produced in a system exposed to high energy ionizing radiation. The forms of ionizing radiation discussed here are electromagnetic radiation (x - and γ -rays) and charged particles (α - and β -particles) that can cause ionization (along with some excitation) of molecules in a medium, which requires energies in the range 10 keV to 10 MeV [82,83]. Ionizing radiation results from the decay of radioactive materials, or can be generated artificially by the acceleration of charged particles.

Radiation chemistry is different from photochemistry, which employs low energy infrared (IR) and ultraviolet (UV) sources. These lower energy sources in the 10^{-2} to 10^0 eV energy range are considered non-ionizing. In photochemistry the interaction predominantly induces vibrational or electronic excitations in the target molecules. In these types of interactions, a photon interacts with a single molecule in a one-to-one manner and the frequency of the radiation can be tuned to interact with a selected molecular group. Due to the high specificity and one-to-one interaction involved, photochemistry is usually described as a “solute-oriented process”, in which the bulk solution remains unaffected by the presence of the radiation. In contrast, in radiation chemistry the high energy ionizing radiation (keV-MeV range) excites or ionizes a large number of molecules indiscriminately along the radiation track, a straight line that radiation particle moves in.

In radiation chemistry, the energy absorption mechanisms are not dependent on molecular structure and are almost entirely dependent on atomic composition. Since all molecules are equally likely to interact with the radiation, the bulk solution is the most affected. Hence, radiation chemistry of solutions is described as a “solvent-oriented process” [83,84].

2.6.1. Types of Ionizing Radiation

As described earlier, ionizing radiation includes high-energy electromagnetic radiation (e.g., X-rays and γ -rays), high-energy charged particles (e.g. (α) and (β) particles) and fast electrons from accelerators [83,84]. Ionizing radiation transfers its energy to an interacting medium mainly by colliding non-discriminately with the

electrons bound to atoms and molecules in the medium. Due to its high kinetic energy, each radiation particle undergoes a series of collisions before it loses most of its kinetic energy and thermalizes. An important parameter in evaluating the chemical effects produced in the interacting medium upon interaction with radiation, is the rate of radiation energy transfer per unit length, also described as the rate of linear energy transfer, LET. The LET depends on the mass of the radiation particle and is higher for α -particles than for β -particles or γ -photons. The changes observed in matter following exposure to radiation vary depending on the type of radiation.

Heavy particles, such as α -particles, lose their energy mainly through inelastic collisions with electrons located along the radiation path. Alpha-particles are the nuclei of helium atoms, emitted by radioactive nuclei. They have discrete energies that are characteristic of the particular radioisotope decay process [79]. Due to their large size compared with the electrons they perturb, only small amounts of energy are lost with each collision, and the large α -particles are thus not easily deflected from their paths. The large collision cross-section of α -particles with electrons prevents these particles from penetrating deeply into a medium and therefore they have a very short penetration depth (10-100 μ m) in water. This results in a very dense collection of excited and ionized particles along a short stretch of the radiation track [79].

For low mass particles (e.g. β -particles), energy loss occurs mainly through inelastic collisions and β -particles consequently have a large penetration depth. The β -particles from a particular radioactive element are not emitted with uniform energy but with energies ranging from zero to a maximum value (E_{β}) that is characteristic of the element. Since β -particles share the same mass as the electrons with which they interact,

the particles can lose up to half of their energy with each collision and can be deflected through a large angle. β -particles can interact with additional electrons to lose their remaining energy. Also, the electrons with which the β -particles interacted can propagate the electron ejection process, but with reduced efficiency through each cascade. The penetration range for β -particles is 1 to 2 cm in water, and these particles create a low-density collection of ions or excited molecules along their radiation track [79].

Gamma rays are electromagnetic radiation with energies in the range of 40 keV to 4 MeV and have the largest penetration depth of the forms of ionizing radiation (tens of cm in water) [79]. A given gamma source emits γ -rays of specific energies. For example, γ -rays from the decay of Co-60 have an energy of either 1.173 MeV or 1.332 MeV, whereas those from Cs-137 have an energy of 0.66 MeV. Gamma-rays transfer most of their energy by Compton scattering if their energy exceeds 0.01 MeV [79]. Compton scattering is a phenomenon in which the γ -ray interaction with matter causes electron ejection from the molecule and the resulting γ -ray photon emerges with reduced energy. Each ejected electron from a high-energy collision acts similarly to a β -particle and produces a characteristic ionization cascade. The most probable Compton scattering events are either near 100% energy transfer or near 0% energy transfer. Due to the low probability of inelastic Compton scattering, the penetration depth of γ -radiation is large relative to all other radiation forms.

2.6.2. Primary Radiolysis Process

Ionizing radiation transfers its energy predominantly through collisions with electrons in the medium. The initial energy transfer rate depends on the density of electrons in the interacting matter. Due to their high initial energies, each radiation particle undergoes a series of collisions while it loses its energy and eventually becomes “thermalized”. The multiple interactions are not selective and depend only on the relative abundance of electrons in the interacting matter. The amount of low LET energy absorbed by a solution can be simply expressed in units of energy absorbed per mass ($\text{J}\cdot\text{kg}^{-1}$), also known as Gray (Gy), where $1 \text{ Gy} = 1 \text{ J}\cdot\text{kg}^{-1}$.

When passing through liquid water, the radiation particle will undergo collisions with water molecules. The average energy transferred per collision typically ranges from 60 to 100 eV [79]. This amount of energy is a very small fraction of the initial energy of the radiation particle (of the order of 1 MeV), so the collisions do not slow the particle or change the radiation path appreciably (except at the very end of the radiation track). The radiation particle moves in a straight line that is referred to as a radiation track. The initial consequence of each energy transfer collision is ionization or electronic excitation of a water molecule. This creates ion pairs (H_2O^+ and e^-_{hot}) or electronically excited water molecules (H_2O^*) along the radiation track. The electron of this ion pair is referred to as a ‘hot’ electron because it has sufficiently high kinetic energy to excite or ionize one or more neighbouring water molecules (the 60 - 100 eV transferred in a collision is well in excess of the ionization energy of a water molecule (12.6 eV) [79]. Secondary (or subsequent tertiary) ionization caused by this ‘hot’ electron will occur very near (within a few nm or a few atom lengths) to the first ionization that created the ‘hot’ electron,

resulting in a cluster of 2-3 ion pairs (or excited water molecules) near the radiation track. This cluster is referred to as a “spur”, as represented schematically in **Figure 2.14** for low LET radiation [80].

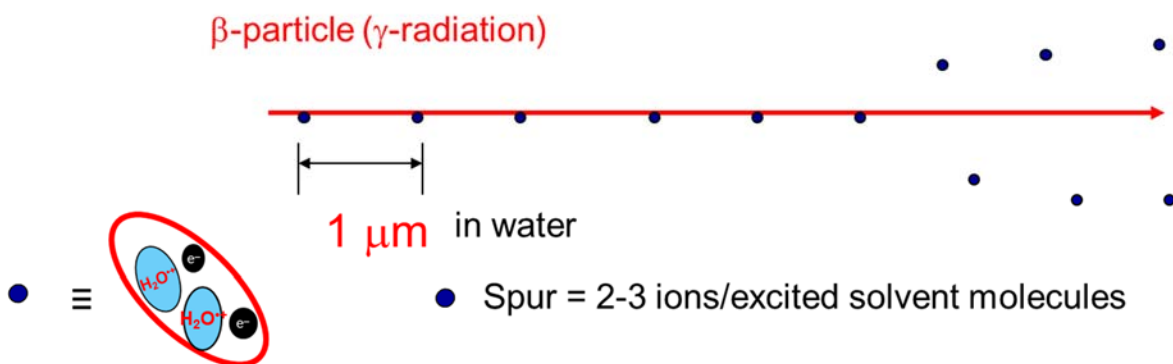


Figure 2.14. The radiation track of a fast electron (spur size not to scale).

Following ionization, the electrons formed in a spur can have sufficiently high kinetic energy to move away from their H_2O^+ counter-cations. This process is referred to as expansion of the spur. As the spur expands, the ‘dry’ electrons that arose from water molecule ionization will be solvated and become hydrated electrons ($\bullet\text{e}_{\text{aq}}^-$). The water cations and any excited water molecules in the spur will interact with other solvent water molecules. Various intra- and inter-molecular energy transfer processes will occur that can lead to bond formation and bond breaking as illustrated in **Figure 2.15**. The ion pairs within the spur continually experience Coulombic attraction with each other. The recombination of ion pairs due to the Coulombic interaction between the charged counter ions is referred to as geminate recombination. Radical pairs can also experience geminate recombination, but this is not driven by electrostatic attraction. This can lead to recombination of ions or radicals, thereby reducing the net chemical decomposition

caused by absorption of radiation energy. When the water decomposition products have moved outside the range of influence by Coulombic attraction of their counter partners (ions or radicals), the radiation products are said to be *out-of-spur* and they can be considered as free ions and free radicals.

The Coulombic influence of counter ions diminishes as the spur expands and the counter ions and radicals are no longer distinguishable from other ions and radicals formed in other neighbouring spurs or already present in the bulk phase. Once the system reaches this stage, the subsequent physical and chemical processes of these ‘free’ species can be treated as ordinary bulk phase chemistry. The time frame during which spur expansion occurs is approximately 100 ns in liquid water at 25 °C: see **Figure 2.15**. The species present at this stage are normally referred to as ‘primary’ radiolysis products and their concentrations per absorbed unit of energy are the primary radiolysis yields (in this sense primary does not refer to the first species created upon interaction of a radiation particle with a water molecule but rather to the starting point of the chemical evolution of an irradiated system). For a specific type of radiation and a given absorbing medium, the primary radiolysis yield depends on the amount of energy absorbed by the medium. . The radiation chemical yield of the species is expressed by the term “G-value” which is defined as the number of species produced per 100 eV absorbed energy, or $\mu\text{mol}\cdot\text{J}^{-1}$ in SI units.

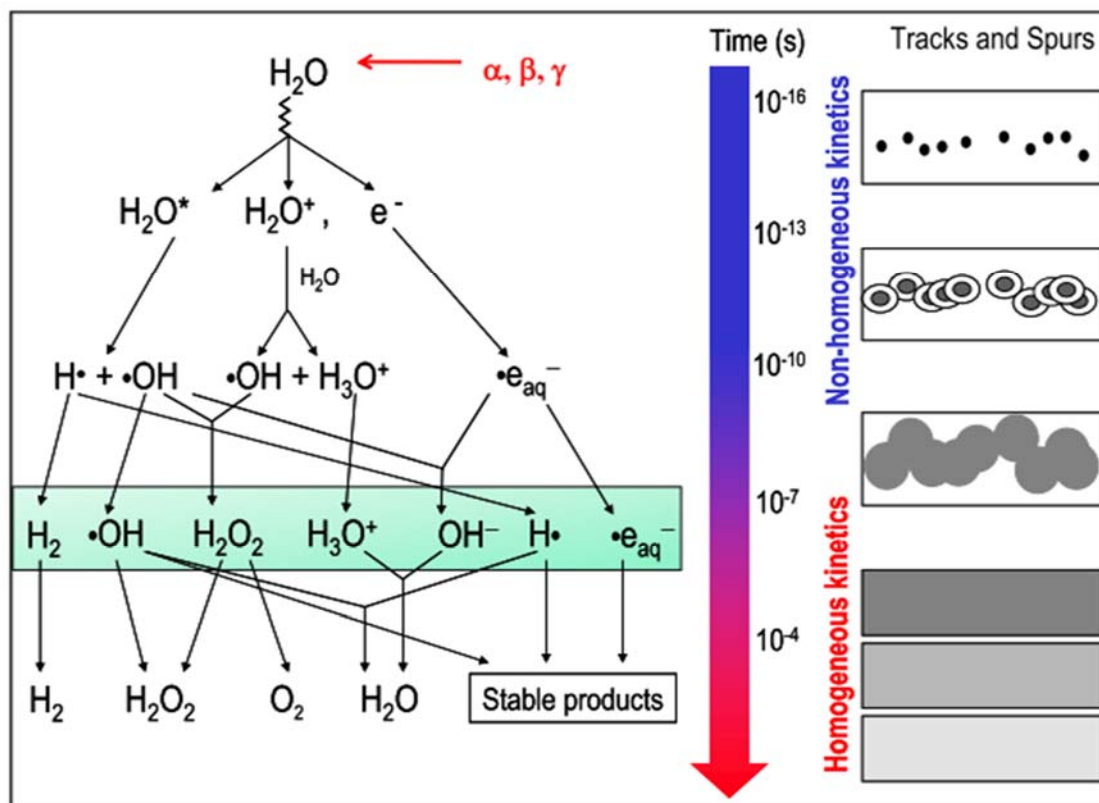


Figure 2.15: Water radiolysis as a function of time following absorption of radiation energy as a pulse. The right-hand panel shows the expansion of spurs with time [85].

The process of spur formation along a radiation track is important in determining the chemical yields of radiolysis products. The spur density along the track depends on the collision rate of the radiation particle with the bound electrons in the water molecules. If the spur density is sufficiently high, as in the case for high LET α -radiation, the ions and radicals in a spur can interact with those of an adjacent spur before they diffuse into the bulk water phase. This can lead to a higher ratio of molecular to radical primary radiolysis products. For low LET radiation like γ -rays the spurs are spread out along the radiation track as shown in **Figure 2.14**. Due to the relatively large distance between

adjacent spurs the reactive species more easily diffuse away from the radiation track and escape recombination to form molecular products. This results in a higher ratio of radical to molecular radiolysis products.

2.6.3. Aqueous Reactions of Radiolysis Products

Once formed, the primary water radiolysis products will undergo homogeneous bulk phase chemical reactions. These include reactions with other water radiolysis products, water molecules and water dissociation ions (H^+ and OH^-), and with any solute species that may be present (such as O_2 from air in contact with the water, or dissolved metal ions). This stage is referred to as the chemical stage (>100 ns). The products of reactions of the primary radiolysis products with each other are referred to as secondary radiolysis products. These reactions can be described very effectively using simple, classical rate equations. However, the chemical kinetics are complex because, even for a simple system containing only water (H and O), there are a surprisingly large number of species (molecules, ions and radicals) present. They require a quite large set of closely coupled reactions to model the chemical system. About 50 elementary reactions are required to describe the radiolysis kinetics of a pure water system.

Under a continuous radiation flux, water molecules continuously interact with radiation particles to form primary radiolysis products and their concentrations increase rapidly. However these species also begin to react very rapidly with each other and other species in the system and the chemical kinetics reach a pseudo-steady state on a time scale that is of the order of minutes (quite long in comparison to the time scale in which

primary radiolysis products are formed (μs after deposition of a particle's energy)). It is the pseudo-steady-state concentrations of reactive species and not the primary radiolytic yields of reactive species that are crucial in evaluating the corrosion of reactor materials [80]. In reaching steady-state the back reactions of acid-base equilibria become important and some cyclic (autocatalytic) reaction sequences can be established [80]. The steady-state concentrations of water radiolysis products are also strongly influenced by pH and dissolved species [86,87]. The steady-state concentrations of reactive species arising from radiolysis cannot be easily predicted by a simple assessment of individual reactions and their reaction rates.

2.6.4. Radiolysis of Reactor Coolant Water

In a nuclear reactor, both radioactive fission products and neutron-activated products are present. The fission products are mainly embedded or trapped within the fuel matrix, which is encased in fuel rods. The net chemical effects induced by ionizing radiation in solids are typically less than in liquids due to the decreased probability of primary radiolytic products escaping the geminate recombination reactions. Therefore, it is the radiolytic decomposition of coolant water that is of most concern in a reactor. The effect of alpha radiation is limited to less than 0.1 mm from its source, and hence limited to within the fuel and fuel sheath; it cannot reach the reactor coolant that circulates outside the fuel sheath. Neutron radiation also contributes to the total radiation flux in the reactor core, but the effects of neutrons on matter are initiated through collision with atomic nuclei as opposed to electrons and are beyond the scope of this work. Therefore,

the types of radiation that can most induce chemical effects influencing nuclear reactor materials degradation will be β - or γ -radiation due to their large penetration depths. The effect of γ -radiation in the bulk phase of the reactor coolant is greater than that of β -radiation, due to its greater penetration depth.

The impact of coolant radiolysis on materials performance is responsible for a number of nuclear reactor operational and safety issues. As indicated in **Figure 2.15**, ionizing radiation generates redox active species in the coolant water ranging from oxidizing (e.g., $\bullet\text{OH}$, H_2O_2 and O_2) to reducing (e.g., $\bullet\text{H}$, $\bullet\text{e}_{\text{aq}}^-$ and $\bullet\text{O}_2^-$). These redox-active species can influence the corrosion rates of surrounding metal surfaces. The strongly oxidizing radiolysis products such as H_2O_2 influence the rate of oxidation of structural materials [35,88–90].

In this study, a ^{60}Co γ -irradiation cell was used to experimentally simulate the radiation environment of a nuclear reactor system. The ^{60}Co source decays to ^{60}Ni in the following way:



The ^{60}Co radiation source has a half-life of 5.3 years and emits γ -photons with two characteristic energies: 1.332 MeV and 1.173 MeV [83]. A β -particle is also emitted with an energy of 0.318 MeV, but this particle is easily blocked from entering the samples by the metal shielding around the sample container.

2.6.5. Radiation-Induced Nanoparticle Formation

Corrosion of structural materials exposed to the coolant water can lead to the release of dissolved metal ions (such as cobalt, iron and chromium) into the coolant. The oxidizing and reducing species produced by radiolysis of coolant water can interact very effectively with metallic corrosion products, changing their oxidation states. Since the solubility of hydrated metal species varies considerably depending on their oxidation state, this can lead to the formation of insoluble solids (colloids or nanoparticles) in the coolant. This can have major implications for the nuclear power plant as it reduces heat transfer efficiency, due to the deposition of corrosion products in the coolant pipes. Activity transport is another concern since some of these corrosion products can become radioactive by passing through the reactor core [48,71,91], and deposition of these solids outside the biological shield of the reactor can pose a risk to radiation workers.

The formation of metal oxide nanoparticles from dissolved metal ions in the presence of γ -radiation has been studied by our group [92–97]. We have reported the formation of γ -FeOOH, Co_3O_4 , and Cr_2O_3 nanoparticles using γ -radiation, from metal cations initially dissolved in aqueous solutions [92–97]. Depending on the equilibrium potential of the redox reaction involved, either the oxidizing or reducing water radiolysis products are used. The reducing power of $\bullet\text{e}_{\text{aq}}^-$ is used in the formation of chromium oxide nanoparticles, whereas for the iron and cobalt systems the oxidizing powers of $\bullet\text{OH}$ and H_2O_2 are utilized [92–97]. In these systems the advantage of a large difference in the solubilities of the initially dissolved metal ions and their oxidized or reduced counterparts are utilized for nanoparticle formation.

2.7. REFERENCES

- [1] Y. Wang, C. Yin, Q. Zhuang, An electrochemical sensor modified with nickel nanoparticle/nitrogen-doped carbon nanosheet nanocomposite for bisphenol A detection, *J. Alloys Compd.* 827 (2020) 154335. <https://doi.org/10.1016/j.jallcom.2020.154335>.
- [2] C. Daniel, J.O. Besenhard, *Handbook of Battery Materials*, Wiley, 2012.
- [3] J.H. Lim, D.H. Lee, H.J. Oh, J.H. Jin, W.M. & JUNG, Lithium-nickel based positive electrode active material, method of preparing the same, and lithium secondary battery including the same, 10,608,251, 2020.
- [4] D. Wang, W. Yan, G.G. Botte, Exfoliated nickel hydroxide nanosheets for urea electrolysis, *Electrochem. Commun.* 13 (2011) 1135–1138. <https://doi.org/10.1016/j.elecom.2011.07.016>.
- [5] X. Li, F.C. Walsh, D. Pletcher, Nickel based electrocatalysts for oxygen evolution in high current density, alkaline water electrolyzers, *Phys. Chem. Chem. Phys.* 13 (2011) 1162–1167. <https://doi.org/10.1039/c0cp00993h>.
- [6] A.M. Al-Enizi, M. Ubaidullah, J. Ahmed, H. Alrobei, S.M. Alshehri, Copper nickel@reduced graphene oxide nanocomposite as bifunctional electro-catalyst for excellent oxygen evolution and oxygen reduction reactions, *Mater. Lett.* 260 (2020) 126969. <https://doi.org/10.1016/j.matlet.2019.126969>.
- [7] Y. Miao, L. Ouyang, S. Zhou, L. Xu, Z. Yang, M. Xiao, R. Ouyang, Electrocatalysis and electroanalysis of nickel, its oxides, hydroxides and oxyhydroxides toward small molecules, *Biosens. Bioelectron.* 53 (2014) 428–439. <https://doi.org/10.1016/j.bios.2013.10.008>.
- [8] E. Urbańczyk, A. Maciej, A. Stolarczyk, M. Basiaga, W. Simka, The electrocatalytic oxidation of urea on nickel-graphene and nickel-graphene oxide composite electrodes, *Electrochim. Acta.* 305 (2019) 256–263. <https://doi.org/10.1016/j.electacta.2019.03.045>.
- [9] W. Xia, X. Zhao, L. Yue, Z. Zhang, A review of composition evolution in Ni-based single crystal superalloys, *J. Mater. Sci. Technol.* 44 (2020) 76–95. <https://doi.org/10.1016/j.jmst.2020.01.026>.
- [10] M. Dodaran, A.H. Etefagh, S.M. Guo, M.M. Khonsari, W.J. Meng, N. Shamsaei, S. Shao, Effect of alloying elements on the γ' antiphase boundary energy in Ni-base superalloys, *Intermetallics.* 117 (2020) 106670. <https://doi.org/10.1016/j.intermet.2019.106670>.
- [11] Subhash Mahajan, *Encyclopedia of Materials: Science and Technology*, Pergamon, 2001.
- [12] A. Shirzadi, S. Jackson, *Structural Alloys for Power Plants Operational Challenges*

and High-Temperature Materials, Woodhead Publishing, 2014.

- [13] A.Y. Musa, J.C. Wren, Combined effect of gamma-radiation and pH on corrosion of Ni-Cr-Fe alloy inconel 600, *Corros. Sci.* 109 (2016) 1–12. <https://doi.org/10.1016/j.corsci.2016.03.015>.
- [14] D. Fénon, *Nuclear Corrosion Science and Engineering*, Cambridge, 2012. <https://doi.org/10.1533/9780857095343.6.939>.
- [15] P. Aaltonen, H. Hannien, *Water Chemistry and Behaviour of Materials in PWRs AND BWRs*, Int. At. Energy Agency. IAEA-TECDO (1997).
- [16] P.M. Scott, P. Combrade, General corrosion and stress corrosion cracking of Alloy 600 in light water reactor primary coolants, *J. Nucl. Mater.* 524 (2019) 340–375. <https://doi.org/10.1016/j.jnucmat.2019.04.023>.
- [17] L. Marchetti, S. Perrin, F. Jambon, M. Pijolat, Corrosion of nickel-base alloys in primary medium of pressurized water reactors: New insights on the oxide growth mechanisms and kinetic modelling, *Corros. Sci.* 102 (2016) 24–35. <https://doi.org/10.1016/j.corsci.2015.09.001>.
- [18] X. Tang, S. Wang, L. Qian, Y. Li, Z. Lin, D. Xu, Y. zhang, Corrosion behavior of nickel base alloys, stainless steel and titanium alloy in supercritical water containing chloride, phosphate and oxygen, *Chem. Eng. Res. Des.* 100 (2015) 530–541. <https://doi.org/10.1016/j.cherd.2015.05.003>.
- [19] J. Everaerts, E. Salvati, H. Li, W. Li, A.M. Korsunsky, Mechanical properties of thermally grown submicron oxide layers on a nickel-based superalloy, *Corros. Sci.* 165 (2020) 108388. <https://doi.org/10.1016/j.corsci.2019.108388>.
- [20] W.G. Cook, D. Lister, *Chemistry in CANDU Process Systems: in the essential CANDU*, UNENE, 2014.
- [21] P. Frattini, *PWR Primary Water Chemistry Guidelines*, EPRI, 2003.
- [22] M. Momeni, J.C. Wren, A mechanistic model for oxide growth and dissolution during corrosion of Cr-containing alloys, *Faraday Discuss.* 180 (2015) 113–135. <https://doi.org/10.1039/c4fd00244j>.
- [23] A. J. Bard Larry R., Faulkner, *Electrochemical Methods Fundamentals and Applications*, Wiley, 2001.
- [24] R. Oltra, Mass transport control of localised corrosion processes: in situ local probing and modelling, *Corros. Eng. Sci. Technol.* 53 (2018) 2–8. <https://doi.org/10.1080/1478422X.2017.1374051>.
- [25] A.H. Fakeeha, F.A. Abdelaleem, The Interaction between Corrosion Processes and Mass Transfer at Rough Surfaces, *J. King Saud Univ. Eng. Sci.* 8 (1996) 51–69. [https://doi.org/10.1016/S1018-3639\(18\)31065-1](https://doi.org/10.1016/S1018-3639(18)31065-1).

- [26] Z. Nagy, D.A. Thomas, Effect of Mass Transport on the Determination of Corrosion Rates From Polarization Measurements., *Electrochem. Soc. Ext. Abstr.* 85–2 (1985) 230–231.
- [27] E.L. Cussler, Mass Transfer and Diffusion, in: *Encycl. of Phys. Sci. and Tech.*, Elsevier, 2003
- [28] G.B. Gibbs, Diffusion layer growth in a binary system, *J. Nucl. Mater.* 20 (1966) 303–306. [https://doi.org/10.1016/0022-3115\(66\)90042-0](https://doi.org/10.1016/0022-3115(66)90042-0).
- [29] V. PacákováK. Štulík, *Encyclopedia of Analytical Science*, Elsevier, 2005.
- [30] H. Strathmann, Electromembrane Processes: Basic Aspects and Applications, in: *Compr. Membr. Sci. Eng.*, Elsevier Ltd., 2017: pp. 355–392. <https://doi.org/10.1016/b978-0-12-409547-2.12257-7>.
- [31] J. Owen, Ionic Conductivity, in: *Compr. Polym. Sci. Suppl.*, Pergamon Press, 1989.
- [32] B.B. McCleskey, K.K. Nordstrom, J.N. Ryan, Comparison of electrical conductivity calculation methods for natural waters, *Limnol. Oceanogr. Methods.* 10 (2012) 952–967. <https://doi.org/10.4319/lom.2012.10.952>.
- [33] A. Persat, R.D. Chambers, J.G. Santiago, Basic principles of electrolyte chemistry for microfluidic electrokinetics. Part I: Acid-base equilibria and pH buffers, *R. Soc. Chem.* 9 (2009) 2437–2453. <https://doi.org/10.1039/b906465f>.
- [34] R.L. Miller, W.L. Bradford, N.E. Peters, Specific conductance: theoretical considerations and application to analytical quality control, *US Geol. Surv. Water-Supply Pap.* 2311 (1988). <https://doi.org/10.3133/wsp2311>.
- [35] M. Behazin, J.J. Noël, J.C. Wren, Combined effects of pH and γ -irradiation on the corrosion of Co-Cr alloy stellite-6, *Electrochim. Acta.* 134 (2014) 399–410. <https://doi.org/10.1016/j.electacta.2014.04.079>.
- [36] G.L. Miessler, D.A. Tarr, *Inorganic Chemistry*, Prentice Hall, 1999.
- [37] C.Y. Lin, P.P. Power, Complexes of Ni(i): A “rare” oxidation state of growing importance, *Chem. Soc. Rev.* 46 (2017) 5347–5399. <https://doi.org/10.1039/c7cs00216e>.
- [38] M.F. Amr El-Sayed, R.K. Sheline, The Infrared Spectrum and Structure of Hexacyanodnickelate(I) Ion, 1 [Ni₂(CN)₆]⁴⁻, *J. Am. Chem. Soc.* 78 (1956) 702–706. <https://doi.org/10.1021/ja01585a002>.
- [39] P.L. Brown, C. Ekberg, *Hydrolysis of Metal Ions*, Wiley, 2016. <https://doi.org/10.1016/b978-0-08-011441-5.50022-2>.
- [40] T.S. De Gromoboy, L.L. Shreir, The formation of nickel oxides during the passivation of nickel in relation to the potential/pH diagram, *Electrochim. Acta.* 11

- (1966) 895–904. [https://doi.org/10.1016/0013-4686\(66\)87066-4](https://doi.org/10.1016/0013-4686(66)87066-4).
- [41] M. Okuyama, S. Haruyama, Passive film formed on nickel in a neutral solution, *Corros. Sci.* 14 (1974) 1–14. [https://doi.org/10.1016/S0010-938X\(74\)80003-X](https://doi.org/10.1016/S0010-938X(74)80003-X).
- [42] X. Zhanga, D. Zagidulina, D. W. Shoesmith, Characterization of film properties on the Ni single bond Cr single bond Mo Alloy C-2000, *Electrochim. Acta.* 89 (2013) 814–822.
- [43] A.J. Tkalych, K. Yu, E.A. Carter, Structural and Electronic Features of β -Ni(OH)₂ and β -NiOOH from First Principles, *J. Phys. Chem. C.* 119 (2015) 24315–24322. <https://doi.org/10.1021/acs.jpcc.5b08481>.
- [44] B. Beverskog, I. Puigdomenech, Revised Pourbaix diagrams for nickel at 25–300°C, *Corros. Sci.* 39 (1997) 969–980. [https://doi.org/10.1016/S0010-938X\(97\)00002-4](https://doi.org/10.1016/S0010-938X(97)00002-4).
- [45] P. Oliva, J. Leonardi, J.F. Laurent, C. Delmas, J.J. Braconnier, M. Figlarz, F. Fievet, A. de Guibert, Review of the structure and the electrochemistry of nickel hydroxides and oxy-hydroxides, *J. Power Sources.* 8 (1982) 229–255. [https://doi.org/10.1016/0378-7753\(82\)80057-8](https://doi.org/10.1016/0378-7753(82)80057-8).
- [46] C. Xing, F. Musharavati, H. Li, E. Zalezhad, O.K.S. Hui, S. Bae, B.Y. Cho, Synthesis, characterization, and properties of nickel-cobalt layered double hydroxide nanostructures, *RSC Adv.* 7 (2017) 38945–38950. <https://doi.org/10.1039/c7ra06670h>.
- [47] K.I. Pandya, W.E. O’Grady, D.A. Corrigan, J. McBreen, R.W. Hoffman, Extended X-ray absorption fine structure investigations of nickel hydroxides, *J. Phys. Chem.* 94 (1990) 21–26. <https://doi.org/10.1021/j100364a005>.
- [48] M. Behazin, Radiation induced corrosion of Stellite-6, *Electron. Thesis Diss. Repos.* 2432, University of Western Ontario (2014).
- [49] D.S. Hall, An Electrochemical and Spectroscopic Investigation of Nickel Electrodes in Alkaline Media for Applications in Electro-Catalysis An Electrochemical and Spectroscopic Investigation of Nickel, *Thesis Diss University of Ottawa.* (2014). <http://dx.doi.org/10.20381/ruor-6575>
- [50] D.S. Hall, D.J. Lockwood, C. Bock, B.R. MacDougall, Nickel hydroxides and related materials: A review of their structures, synthesis and properties, *Proc. R. Soc. A Math. Phys. Eng. Sci.* 471 (2015).
- [51] P. Dubey, N. Kaurav, R.S. Devan, G.S. Okram, Y.K. Kuo, The effect of stoichiometry on the structural, thermal and electronic properties of thermally decomposed nickel oxide, *RSC Adv.* 8 (2018) 5882–5890. <https://doi.org/10.1039/c8ra00157j>.
- [52] M. Nachman, L.N. Cojocar, L. V. Rîbco, Electrical Properties of Non-

- Stoichiometric Nickel Oxide, *Phys. Status Solidi*. 8 (1965) 773–783.
<https://doi.org/10.1002/pssb.19650080316>.
- [53] A.L. Dicks, Fuel Cells - Molten Carbonate Fuel Cells | Cathodes, *Encycl. Electrochem. Power Sources*. (2009) 462–466. <https://doi.org/10.1016/B978-044452745-5.00265-3>.
- [54] D.S. Hall, C. Bock, B.R. MacDougall, The Electrochemistry of Metallic Nickel: Oxides, Hydroxides, Hydrides and Alkaline Hydrogen Evolution, *J. Electrochem. Soc.* 160 (2013) F235–F243. <https://doi.org/10.1149/2.026303jes>.
- [55] S. Pizzini, R. Morlotti, Thermodynamic and Transport Properties of Stoichiometric and Nonstoichiometric Nickel Oxide, *J. Electrochem. Soc.* 114 (1967) 1179. <https://doi.org/10.1149/1.2426441>.
- [56] B. Subramanian, M. Mohamed Ibrahim, V. Senthilkumar, K.R. Murali, V. Vidhya, C. Sanjeeviraja, M. Jayachandran, Optoelectronic and electrochemical properties of nickel oxide (NiO) films deposited by DC reactive magnetron sputtering, *Phys. B Condens. Matter*. 403 (2008) 4104–4110. <https://doi.org/10.1016/j.physb.2008.08.014>.
- [57] S. Dudarev, G. Botton, S. Savrasov, C. Humphreys, A. Sutton, Electron-energy-loss spectra and the structural stability of nickel oxide: An LSDA+ U study, *Phys. Rev. B*. 57 (1998) 1505.
- [58] A.M. Ferrari, M. Ferrero, C. Pisani, An ab initio periodic study of NiO supported at the Pd(100) surface. Part 2: The nonstoichiometric Ni₃O₄ phase, *J. Phys. Chem. B*. 110 (2006) 7918–7927. <https://doi.org/10.1021/jp0573994>.
- [59] W.L. Dudley, Nickelo-nickelic hydrate, ni₃o₄.2h₂O, *J. Am. Chem. Soc.* 18 (1896) 901–903. <https://doi.org/10.1021/ja02096a003>.
- [60] S. Dey, S. Bhattacharjee, M.G. Chaudhuri, R.S. Bose, S. Halder, C.K. Ghosh, Synthesis of pure nickel(iii) oxide nanoparticles at room temperature for Cr(vi) ion removal, *RSC Adv.* 5 (2015) 54717–54726. <https://doi.org/10.1039/c5ra05810d>.
- [61] P.S. Aggarwal, A. Goswami, An oxide of tervalent nickel, *J. Phys. Chem.* 65 (1961) 2105. <https://doi.org/10.1021/j100828a503>.
- [62] H. Suzuki, N. Ogura, T. Kaneko, T. Kato, Highly Stable Persistent Photoconductivity with Suspended Graphene Nanoribbons, *Sci. Rep.* 8 (2018) 1–9. <https://doi.org/10.1038/s41598-018-30278-z>.
- [63] H. R. Pouretedal, F. Momenzadeh, Synthesis, characterization and study of photocatalytic activity of nanocomposites of oxides and sulfides of Ni(II) and Ni(III), *Bulg. Chem. Commun.* (2015) 108–110.
- [64] Š. Trafela, J. Zavašnik, S. Šturm, K.Ž. Rožman, Formation of a Ni(OH)₂/NiOOH active redox couple on nickel nanowires for formaldehyde detection in alkaline media, *Electrochim. Acta*. 309 (2019) 346–353.

<https://doi.org/10.1016/j.electacta.2019.04.060>.

- [65] R.S. McEwen, Crystallographic studies on nickel hydroxide and the higher nickel oxides, *J. Phys. Chem.* 75 (1971) 1782–1789. <https://doi.org/10.1021/j100681a004>.
- [66] M. Casas-Cabanas, J. Canales-Vazquez, J. Rodriguez-Carvaja, M. Rosa Palacín, Characterizing nickel battery materials: Crystal structure of β -NiOOH, *Mater. Res. Soc. Symp. Proc.* 1126 (2009) 131–136. <https://doi.org/10.1557/proc-1126-s14-05>.
- [67] C.F. Baes, R.E. Mesmer., *Hydrolysis of Cations*, Wiley, 1976.
- [68] F. Scholz, H. Kahlert, The calculation of the solubility of metal hydroxides, oxide-hydroxides, and oxides, and their visualisation in logarithmic diagrams, *ChemTexts.* 1 (2015) 1–9. <https://doi.org/10.1007/s40828-015-0006-0>.
- [69] J.D. Verink, Simplified Procedure for Constructing Pourbaix Diagrams, in: *Uhlig's Corros. Handb. Third Ed.*, 2011: pp. 93–101. <https://doi.org/10.1002/9780470872864.ch7>.
- [70] T.P. Murphy, M.G. Hutchins, Oxidation states in nickel oxide electrochromism, *Sol. Energy Mater. Sol. Cells.* 39 (1995) 377–389. [https://doi.org/10.1016/0927-0248\(96\)80003-1](https://doi.org/10.1016/0927-0248(96)80003-1).
- [71] M. Momeni, Gamma-Radiation Induced Corrosion of Alloy 800, *Electron. Thesis Diss. Repos.* 5011, University of Western Ontario (2017).
- [72] Y. Tian, C. Dong, G. Wang, X. Cheng, X. Li, The effect of nickel on corrosion behaviour of high-strength low alloy steel rebar in simulated concrete pore solution, *Constr. Build. Mater.* 246 (2020) 118462. <https://doi.org/10.1016/j.conbuildmat.2020.118462>.
- [73] B. Grégoire, X. Montero, M.C. Galetz, G. Bonnet, F. Pedraza, Mechanisms of hot corrosion of pure nickel at 700°C: Influence of testing conditions, *Corros. Sci.* 141 (2018) 211–220. <https://doi.org/10.1016/j.corsci.2018.06.009>.
- [74] B. Grégoire, X. Montero, M.C. Galetz, G. Bonnet, F. Pedraza, Correlations between the kinetics and the mechanisms of hot corrosion of pure nickel at 700 °C, *Corros. Sci.* 155 (2019) 134–145. <https://doi.org/10.1016/j.corsci.2019.04.022>.
- [75] F. Yang, H. Kang, E. Guo, R. Li, Z. Chen, Y. Zeng, T. Wang, The role of nickel in mechanical performance and corrosion behaviour of nickel-aluminium bronze in 3.5 wt.% NaCl solution, *Corros. Sci.* 139 (2018) 333–345. <https://doi.org/10.1016/j.corsci.2018.05.012>.
- [76] S. Jouen, M. Jean, B. Hannoyer, Atmospheric corrosion of nickel in various outdoor environments, *Corros. Sci.* 46 (2004) 499–514. [https://doi.org/10.1016/S0010-938X\(03\)00143-4](https://doi.org/10.1016/S0010-938X(03)00143-4).
- [77] L.A. Hutton, M. Vidotti, A.N. Patel, M.E. Newton, P.R. Unwin, J. V. MacPherson,

- Electrodeposition of nickel hydroxide nanoparticles on boron-doped diamond electrodes for oxidative electrocatalysis, *J. Phys. Chem. C.* 115 (2011) 1649–1658. <https://doi.org/10.1021/jp109526b>.
- [78] A.M. Huntz, M. Andrieux, R. Molins, Relation between the oxidation mechanism of nickel, the microstructure and mechanical resistance of NiO films and the nickel purity. I. Oxidation mechanism and microstructure of NiO films, *Mater. Sci. Eng. A.* 415 (2006) 21–32. <https://doi.org/10.1016/j.msea.2005.08.225>.
- [79] X. Zhong, X. Wu, E.H. Han, Characteristics of Oxidation and Oxygen Penetration of Alloy 690 in 600 °C Aerated Supercritical Water, *J. Mater. Sci. Technol.* 34 (2018) 561–569. <https://doi.org/10.1016/j.jmst.2016.11.001>.
- [80] J. Wang, J. Wang, E.H. Han, Influence of Conductivity on Corrosion Behavior of 304 Stainless Steel in High Temperature Aqueous Environment, *J. Mater. Sci. Technol.* 32 (2016) 333–340. <https://doi.org/10.1016/j.jmst.2015.12.008>.
- [81] Y. Liu, Z. Zhang, N. Bhandari, Z. Dai, F. Yan, G. Ruan, A.Y. Lu, G. Deng, F. Zhang, H. Al-Saiari, A.T. Kan, M.B. Tomson, New Approach to Study Iron Sulfide Precipitation Kinetics, Solubility, and Phase Transformation, *Ind. Eng. Chem. Res.* 56 (2017) 9016–9027. <https://doi.org/10.1021/acs.iecr.7b01615>.
- [82] D.R. Lide, *Handbook of Chemistry and Physics*, Taylor & Francis, 2004.
- [83] J.W.T. Spinks, R.. Woods, *An Introduction To Radiation Chemistry*, Wiley, 1990.
- [84] J. Wren, Steady-state radiolysis: effects of dissolved additives, in: *Nuclear Energy and the Environment*, ACS Publ. (2010) 271–295. <https://doi.org/10.1021/bk-2010-1046.ch022>
- [85] G.V. Buxton, An Overview of the Radiation Chemistry of Liquids, in: M. SpothemMaurizot, M. Mostafavi, T. Douki, J. Belloni (Eds.), *Radiat. Chem. From Basics to Appl. Mater. Life Sci.*, EPD science, France, 2008.
- [86] J.M. Joseph, B.S. Choi, P. Yakabuskie, J.C. Wren, A combined experimental and model analysis on the effect of pH and O₂ (aq) on γ -radiolytically produced H₂ and H₂O₂, *Radiat. Phys. Chem.* 77 (2008) 1009–1020.
- [87] P.A. Yakabuskie, J.M. Joseph, C.R. Stuart, J.C. Wren, Long-term γ -radiolysis kinetics of NO₃⁻ and NO₂⁻ solutions, *J. Phys. Chem. A.* 115 (2011) 4270–4278. <https://doi.org/10.1021/jp200262c>.
- [88] K. Daub, X. Zhang, J.J. Noël, J.C. Wren, Effects of γ -radiation versus H₂O₂ on carbon steel corrosion, *Electrochim. Acta.* 55 (2010) 2767–2776. <https://doi.org/10.1016/j.electacta.2009.12.028>.
- [89] Q.W. Knapp, J.C. Wren, Film formation on type-316L stainless steel as a function of potential: Probing the role of gamma-radiation, *Electrochim. Acta.* 80 (2012) 90–99. <https://doi.org/10.1016/j.electacta.2012.06.090>.

- [90] K. Daub, X. Zhang, J.J. Noël, J.C. Wren, Gamma-radiation-induced corrosion of carbon steel in neutral and mildly basic water at 150°C, *Corros. Sci.* 53 (2011) 11–16. <https://doi.org/10.1016/j.corsci.2010.09.048>.
- [91] Modelling of Transport of Radioactive Substances in the Primary Circuit of Water Cooled Reactors., Int. At. Energy Agency. IAEA-TECDO (2012).
- [92] P.A. Yakabuskie, J.M. Joseph, P. Keech, G.A. Botton, D. Guzonas, J.C. Wren, Iron oxyhydroxide colloid formation by gamma-radiolysis, *Phys. Chem. Chem. Phys.* 13 (2011) 7198–7206. <https://doi.org/10.1039/c1cp20084d>.
- [93] T.I. Sutherland, C.J. Sparks, J.M. Joseph, Z. Wang, G. Whitaker, T.K. Sham, J.C. Wren, Effect of ferrous ion concentration on the kinetics of radiation-induced iron-oxide nanoparticle formation and growth, *Phys. Chem. Chem. Phys.* 19 (2017) 695–708. <https://doi.org/10.1039/c6cp05456k>.
- [94] L.M. Alrehaily, J.M. Joseph, J.C. Wren, Radiation-induced formation of chromium oxide nanoparticles: Role of radical scavengers on the redox kinetics and particle size, *J. Phys. Chem. C* 119 (2015) 16321–16330. <https://doi.org/10.1021/acs.jpcc.5b02540>.
- [95] L.M. Alrehaily, J.M. Joseph, J.C. Wren, Radiation-induced formation of Co₃O₄ nanoparticles from Co²⁺(aq): Probing the kinetics using radical scavengers, *Phys. Chem. Chem. Phys.* 17 (2015) 24138–24150. <https://doi.org/10.1039/c5cp02828k>.
- [96] L.M. Alrehaily, J.M. Joseph, M.C. Biesinger, D.A. Guzonas, J.C. Wren, Gamma-radiolysis-assisted cobalt oxide nanoparticle formation, *Phys. Chem. Chem. Phys.* 15 (2013) 1014–1024. <https://doi.org/10.1039/c2cp43094k>.
- [97] L.M. Alrehaily, J.M. Joseph, A.Y. Musa, D.A. Guzonas, J.C. Wren, Gamma-radiation induced formation of chromium oxide nanoparticles from dissolved dichromate, *Phys. Chem. Chem. Phys.* 15 (2013) 98–107. <https://doi.org/10.1039/c2cp43150e>.

CHAPTER 3

EXPERIMENTAL PROCEDURES AND TECHNIQUES

This chapter describes the general experimental procedures, electrochemical methods, and surface and solution analysis techniques used in this study. Any additional information and experimental details that are specific to each chapter are provided in the experimental sections of those chapters.

3.1. ELECTROCHEMICAL TECHNIQUES

In this study, a series of electrochemical experiments were performed as a function of time on nickel samples, with different solution parameters. These electrochemical experiments were augmented with surface and solution analyses in order to develop a solid understanding of nickel corrosion.

3.1.1. Three-electrode Electrochemical Cell

A three-compartment electrochemical cell, made of Pyrex glass, was used to perform all the electrochemical experiments. The three-electrode cell consists of a

working electrode (the electrode of interest (WE)), a counter electrode (with high activity (CE)), and a reference electrode (a stable electrode of known potential (RE)).

During electrochemical tests, the electrodes are exposed to the electrolyte solution in the cell and are connected to a potentiostat to measure or control the potential and/or flowing current. A schematic of the three-electrode electrochemical cell is shown in **Figure 3.1**.

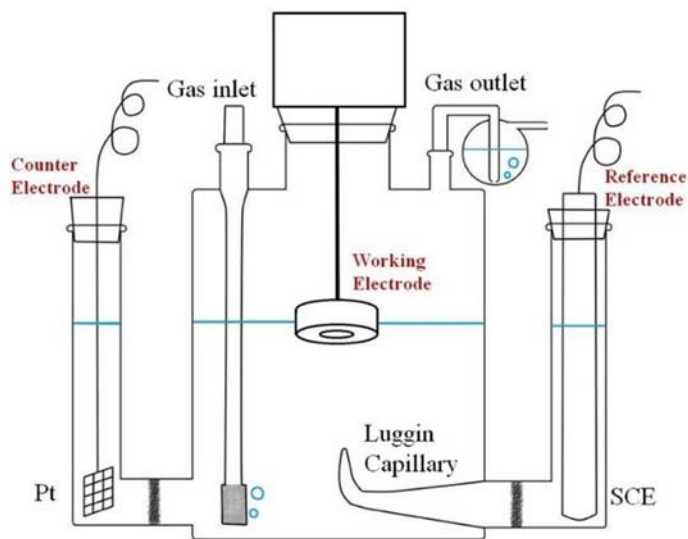


Figure 3.1: Schematic of three-component electrochemical cell [1].

In this study nickel samples were used as the working electrode (WE), platinum mesh (Alfa Aesar, 99.9% purity) was used as the counter electrode (CE), and the reference electrode (RE) was a saturated calomel electrode (SCE, Fisher Scientific), while for tests in a γ -radiation field an Hg|HgO reference electrode (Radiometer Analytical) was used (-0.129 V vs SCE) because of its superior radiation stability.

The current measured during an electrochemical test is the current flow between the WE and CE and the potential measured is the electric potential difference between WE and RE. To maintain the stability of the RE, the WE and RE are connected through a high impedance voltmeter inside the potentiostat to ensure negligible current flow through the external measurement circuit between WE and RE [2].

3.1.2. Cyclic Voltammetry and Potentiodynamic Polarization

Cyclic Voltammetry (CV) is a common technique used in electrochemical studies and has proven very useful in understanding fairly complicated electrode reactions [3]. In a CV experiment, the potential of the WE is ramped linearly with time from the initial potential (E_{initial}) to the final potential (E_{final}) at a certain scan rate. After the final potential is reached, the WE potential is swept back to E_{initial} [4,5]. The E_{initial} and E_{final} are chosen to be above the potential of water reduction and below the potential of water oxidation, respectively (within the water stability region, which depends on solution pH) [5]. A potential ramp in CV scan is illustrated in **Figure 3.2**.

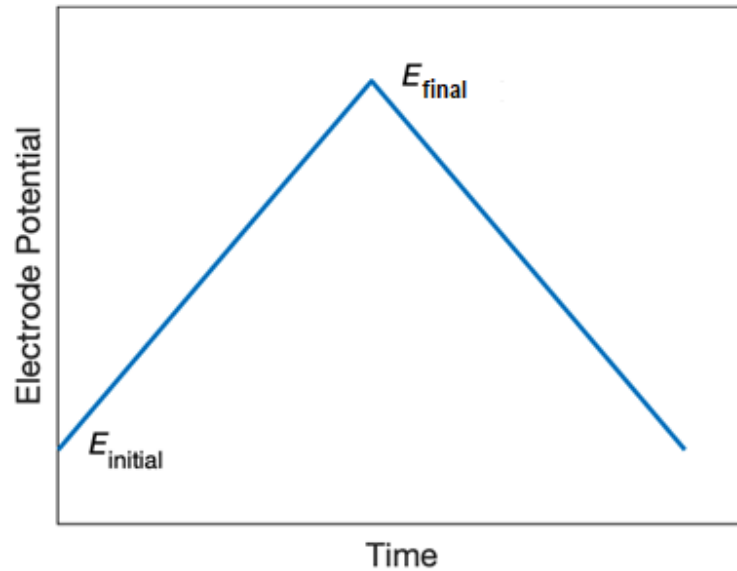


Figure 3.2: Potential sweep applied versus time in a CV experiment.

The potential sweep can be repeated for as many cycles as needed. During each cycle the corresponding current response is measured and plotted versus the applied potential (the working electrode's potential) to give the cyclic voltammetry trace. The measured current at any potential shows the net charge transfer taking place at the WE. This gives useful information about the sequence of electrochemical redox reactions occurring on the WE [3–5].

Unlike CV, in a potentiodynamic polarization (PD) (**Figure 3.3**), the initial electrode potential is usually the corrosion potential (or E_{app}) and the applied potential is swept back to a negative limit. PD is a common approach for studying the kinetics of cathodic and anodic reactions.

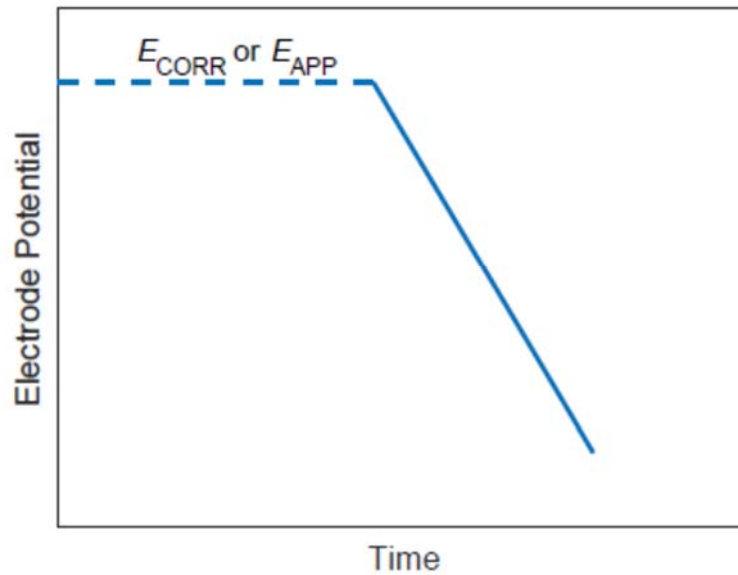


Figure 3.3: Potential sweep applied versus time in a PD experiment.

3.1.3. Potentiostatic Polarization

In a potentiostatic polarization experiment a constant external potential (with respect to the reference electrode) is applied to the WE, and held for certain period, and the current produced in response is measured. The produced current (net current) is the sum of the currents from all the oxidation and reduction processes. Cathodic polarizations refer to an applied potential $E_{app} < E_{corr}$ and negative cathodic current, while anodic polarizations are where $E_{app} > E_{corr}$ and positive anodic current. Potentiostatic polarization provides useful information about the time-dependent behaviour of the current. This can often provide insights into the changes occurring on the working electrode as the system approaches a steady state and on processes such as oxide film growth.

3.2. SURFACE ANALYSIS TECHNIQUES

A combination of different surface analysis techniques was used to characterize the morphology and composition of the oxides formed on the surface after electrochemical or coupon exposure tests. The principles behind these techniques are described below:

3.2.1. Optical Microscopy

Optical microscopy is a technique that provides useful information about the surface morphology and topography. In this study the images were produced using a Leica DVM 6A digital microscope. In a digital optical microscope, the instrument detector is essentially a digital camera and images are displayed on a computer screen. This image is produced by focusing the lens on a particular point of the sample.

This microscope can produce multi-focus (composite images to give greater depth of field), high resolution and 3D images of the surface morphology. In spite of having lower resolution than SEM, the ability to observe the colours of the oxides on the electrode surface can give useful information about the surface composition and the overall corrosion behaviour over large surface areas of the sample.

3.2.2. Scanning Electron Microscopy

SEM is the most useful microscopic technique used to study surface morphology [6]. The resolution of an image taken by SEM is much higher than that obtained by an optical microscope. The essential elements of SEM are represented in **Figure 3.4**. A high-resolution electron beam is directed onto the sample surface and the reflected electron intensity is measured and displayed on a cathode-ray screen to produce an

image. The electrons are generated in an electron gun and directed using electric and magnetic fields to achieve the required incident beam at the sample surface. The principal elements of the electron column are the electron column, the anode, the condenser lens, the objective lens, and the scanning or deflection coils [7].

Depending on the amount of current and the resulting performance, different types of electron guns exist but the most commonly used types are tungsten or LaB₆ thermionic [7]. An electron gun typically operates over an accelerating voltage range of 0.1-30 keV [6]. Anodes, which consist of two plates with positive charge, deflect the electrons generated away from the source. One or two condenser lenses in the electron column focus the electron beam to a very small spot size, typically 0.4 to 5 nm in diameter, and collimate them into a relatively parallel stream. The beam of electrons is accelerated using a scanning coil that move the beam along the sample. The objective lens focuses the electron beams on the surface of the sample in the smallest surface diameter [6,7].

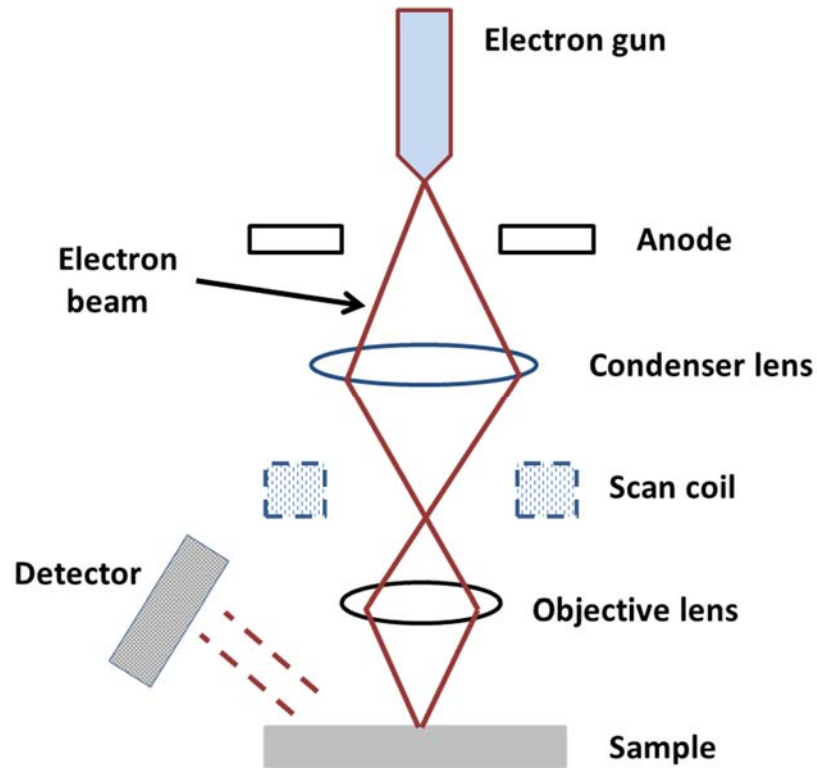


Figure 3.4: A schematic diagram of the scanning electron microscopy (SEM) technique.

Using an electron beam for imaging is only possible in a vacuum in order to give unimpeded passage for the electrons from the source to the sample surface and from the sample surface to the detector. This prevents any collisions between electron and gas (air) molecules thus guaranteeing the direction of electron motion, which is a requirement for focusing [7]. So, for an SEM instrument, samples are analyzed in a vacuum chamber.

Electrons can interact with the surface in a number of ways, but for production of the SEM image, two of these effects are important. Firstly, secondary electrons, which are produced via inelastic interactions between the electron beam and the specimen material result in the ejection of weakly bonded (less than 50 eV) electrons. These electrons only arise from the top few nanometers of the sample surface and are collected above the

sample by a detector and used to generate high resolution topographical images of the surface. The intensities of these electrons are independent of the atomic number of the specimen components [6,7].

Secondly, electrons from elastic scattering of the electron beam by the specimen are called backscattered electrons. Backscattered electrons mostly consist of high-energy primary electrons and due to collisions with specimen atoms at particular angles, their path is deflected, or they are backscattered with lower energy.

The escape depth of backscattered electrons is greater than that of secondary electrons and as a result in the generated image the resolution of the surface is lower than that obtained from secondary electrons. So, these electrons are used for SEM imaging contrast because the intensity of the backscattered electrons is strongly sensitive to atomic mass [8] and affected by the chemical composition, the crystal structure and the internal magnetic properties of the specimen. Hence, compositional information can be obtained based on contrast and intensity differences, yielding atomic number distribution, electron channeling patterns, or magnetic field properties.

The combined use of both secondary and backscattered electron imaging modes provides valuable information not typically available through either imaging method alone. In this study SEM analysis was performed using a LEO (Zeiss) 1540XB FIB/SEM microscope at the Western Nanofabrication Facility.

3.2.3. Energy Dispersive X-ray Spectroscopy

Energy dispersive X-ray spectroscopy (EDX) is a common method used to determine elemental composition in a very small sample of material (at the micro- or nano-scale). In a properly equipped SEM, when the electron beam interacts with the surface the atoms on the surface are excited and emit X-rays with energies characteristic of the atomic structure of the elements. These X-rays are detected by the energy dispersive detector (EDX) and by determining their energies, the elements present in the sample can be determined [9].

The LEO (Zeiss) 1540XB FIB/SEM microscope used for SEM is also equipped with an EDX detector which was used for EDX analysis in this study.

3.2.4. Auger Electron Spectroscopy

Auger electron spectroscopy (AES) is one of the most commonly used surface analytical techniques for quantifying the chemical composition of the first few monolayers of the sample surface. The sensitivity of this method is of the order of 0.1 atomic % with a spatial resolution of the order of 10 nm [6].

The primary source in the AES method is electrons. An electron beam is generated using thermionic sources such as a tungsten hairpin filament or lanthanum hexaboride (LaB₆). Then the electrons pass through a series of focusing magnetic coils and are finally used to bombard the sample surface [7].

The Auger process is essentially a three-electron process (**Figure 3.5**). It is initiated by the ejection of inner shell electrons via the interaction of the high-energy electron beam with atoms. This leaves the atom in an excited state. The excited atom can

lose energy through ejection in two different ways. Firstly, the core hole created in the inner shell is rapidly filled by an electron from a higher energy outer shell. Secondly, this goes together with either the ejection of an X-ray photon of the appropriate energy, or by the ejection of another electron.

The ejected X-ray is characteristic of the originating atom, and the basis of the analytical technique known as X-ray fluorescence (XRF). The secondary ejected electron is the Auger electron and its energy is characteristic of the particular element it was ejected from [6]. The schematic diagram (Fig 3.5) shows the Auger electron process and the Auger electron energy (E_{Auger}) is written as in:

$$E_{Auger} = BE_K - BE_{L1} - BE_{L2,3} - \varphi$$

Where the BE_K , BE_{L1} and $BE_{L2,3}$ are the binding energies of the three participating electrons and φ is the work function and the extra energy needed to remove an electron from a doubly ionized atom [6].

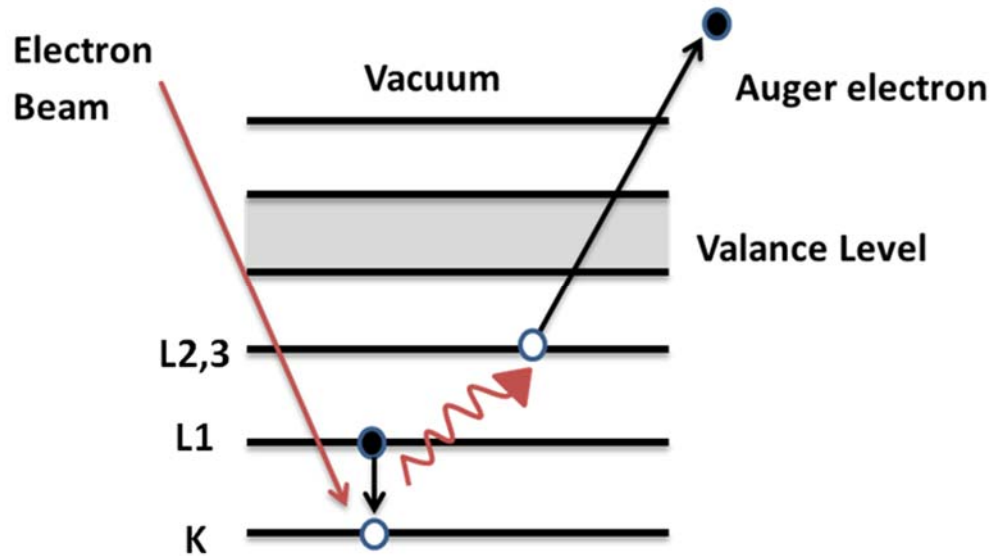


Figure 3.5: Ionization of a core hole (K) by the primary electron beam, results in the decay of an electron from a higher energy level (L1). The released energy ejects an electron from a third energy level (L2,3), which is known as the Auger electron (Auger).

To analyze samples cross-sectionally, AES instrument incorporates ion beam sputtering to remove material from the sample surface. Each cycle of a depth profile analysis consists of sputtering a small area of the sample surface, stopping, measuring the Auger spectrum, and using the equations for elemental qualification such as dropping concentration and thin film structure [7].

3.2.5. X-ray Photoelectron Spectroscopy

X-ray photoelectron spectroscopy (XPS) is a surface analysis technique that is commonly used to characterize the chemical state of the elements in the first 1–30 monolayers of a surface. This unique characterization method provides information on the chemical bonding state of elements in the specimen with relative ease.

In the XPS method (**Figure 3.6**) the sample surface is irradiated in a vacuum with X-rays with a constant energy, $E_{x\text{-ray}}$. This causes photoelectrons (which are core electrons), to be emitted from the sample surface. The kinetic energy spectrum (E_k) of these photoelectrons is related to their ionization energies (or binding energies, BE) and the incident energy $h\nu$. The relationship between $E_{x\text{-ray}}$ and the kinetic energy of the photoelectron, E_k , is expressed by: [10]

$$E_{x\text{-ray}} = E_k + BE + \varphi$$

where BE is the binding energy of the electron relative to the Fermi level and φ the work function of the specimen, in the case of a solid. The value of BE and the chemical shift (difference depending on elemental state) are utilized for the identification of an element and an estimation of its chemical bonding state in the specimen [10].

Typically, an XPS spectrum is a plot of the measured photoelectron intensity as a function of the kinetic energy of the electrons detected.

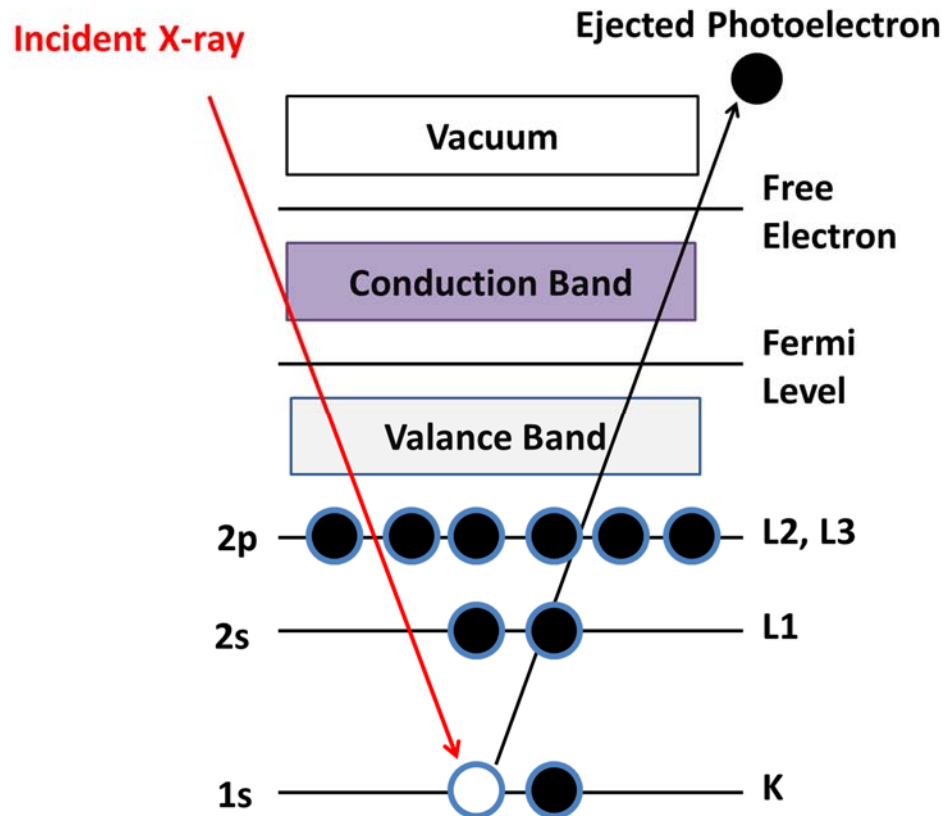


Figure 3.6: Schematic of the principle of XPS and the produced photoelectron.

Each element generates a set of XPS lines or peaks at characteristic binding energy values. Each peak corresponds to electrons which ejected from different orbitals of an atom and the binding energies relate to the energies of those orbitals. The location and intensity of the peak allow us to determine the composition of the surface to be determined with spatial differentiation. The sizes of the peaks correspond to the amounts of a particular element in the sample volume that was irradiated [11].

In this instrument the x-rays mostly have energies of $< 1.5 \text{ keV}$, which means that that E_K can be no larger than 1.5 keV . This leads to shallow escape depths for the photoelectrons. So, this technique can only measure the chemical properties of the top few nm of a surface, but can be combined with ion etching which can remove surface

layers allowing new layers to be analyzed. In this way XPS can also be used to determine elemental composition as a function of depth [10].

In this study XPS was utilized to determine the chemical composition of oxide layers. These analyses were performed using a KRATOS Axis Nova spectrometer using monochromatic Al K_{α} radiation and operating at 210 W, with a base pressure of 10^{-8} Pa, and XPS analysis performed to measure the chemical composition of the first few monolayers of a surface. This technique has a sensitivity of the order of 0.1 atomic % and a spatial resolution of the order of 10 nm [10].

3.3. SOLUTION ANALYSIS

In this study, in order to develop a solid understanding of nickel corrosion, all experiments included solution analysis to determine the concentration of metal ions dissolved in solution. This analysis was performed using an ICP-OES instrument.

3.3.1. Inductively Coupled Plasma-Optical Emission Spectroscopy

ICP-OES is an analytical technique used for the detection of atoms or ions in solution. This technique is a type of emission spectroscopy that uses plasma to excite atoms or ions in solution (**Figure 3.7**). Plasma consists of a high temperature ionized gas, in this case argon which contains a significant number of argon ions. The plasma is generated by subjecting the argon gas through a plasma torch with electrons. Inductively coupled plasma is produced using a coil with a rapidly oscillating magnetic field. The argon gas itself becomes the plasma (it's not subjected to an existing plasma torch). The

electrons collide with argon atoms releasing more electrons and forming argon ions and transfer into plasma.

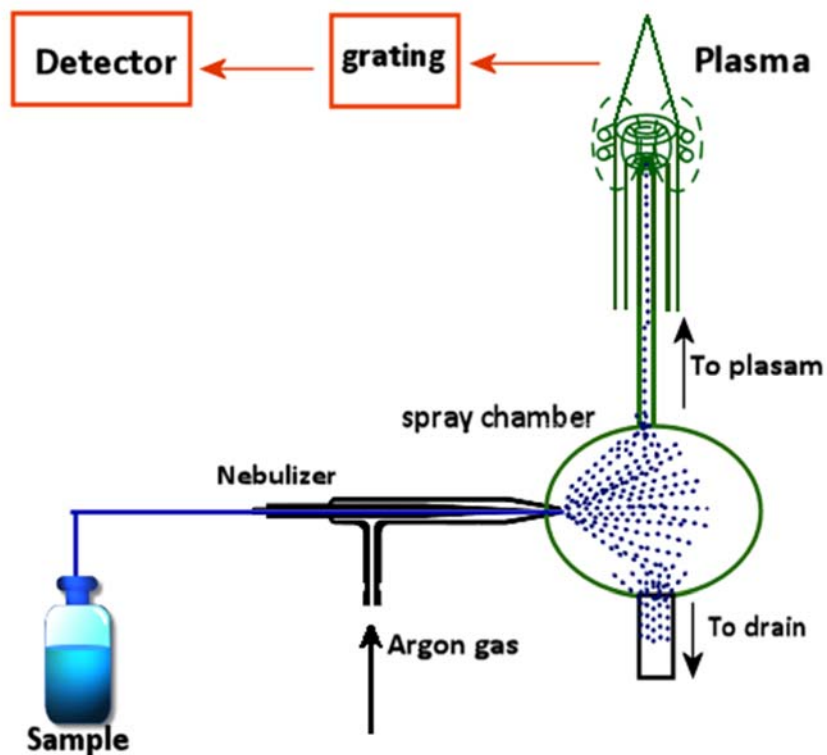


Figure 3.7: Schematic of Inductively Coupled Plasma-Optical Emission Spectroscopy (ICP-OES) instrument.

When a solution of interest enters the plasma torch after being nebulized, the atoms or ions in solution are ionized and excited. On relaxation to the ground state, electromagnetic radiation is emitted, usually with several characteristic wavelengths for each element. This light is separated into individual wavelengths using a diffraction grating or multi-wavelength detector which allows for quantitative determination of their concentrations (using standards and calibration curves).

3.4. EXPERIMENTAL PROCEDURES

3.4.1. Material and Solution Preparation

The working electrode used in all experiments was nickel purchased from Good Fellow Inc. with impurities of (in ppm) Cu <2500, Fe <4000, Mg <2000, Mn <3500, Si <1500, Ti <1000, C <1500, S <100. A 6.35 mm diameter Nickel rod was cut into 3 mm thick cylindrical pieces, referred to as “coupons”. Each coupon had a total surface area of 1.182 cm². For electrochemical tests only one circular face with an area of 0.3017 cm² was exposed to the solution cm².

Prior to each experiment the flat electrode surfaces were mechanically abraded sequentially with 400, 600, 800, 1200 grit silicon carbide papers, and then mirror-polished with a Texmet microcloth (Buehler) using a 1 μm MetaDi Supreme diamond paste suspension (Buehler). Finally, samples were rinsed with a 1:1 acetone/ethanol mixture in ultrasonic bath for 5 min to remove surface residues, and then rinsed with Type I water and dried using a stream of Ar.

All experiments were conducted in argon-purged solutions at pH 10.6, 8.4 or 6.0 with 0.01, 0.001 and 0 M concentrations of sodium borate (Na₂B₄O₇·10H₂O). The solution pH was adjusted to 10.6 by adding the required amount of 2 M sodium hydroxide (NaOH) solution, and to pH 6.0 and 8.4 by adding boric acid (H₃BO₃, analytical grade, Caledon Laboratories Ltd.). All solutions were prepared using water purified using a Nano pure Diamond UV ultra-pure water system from Barnstead International to give a resistivity of 18.2 MΩcm.

3.4.2. Electrochemical Experiment

The electrochemical tests at room temperature and 80 °C were carried out using a standard three-electrode electrochemical cell [12,13]. The counter electrode was a platinum mesh, the working electrode used was the nickel sample, and the reference electrode was a saturated calomel electrode (SCE) for room temperature experiments, and a Ag/AgCl electrode for 80°C experiments.

For all experiments, the solutions were purged with argon gas for an hour before and throughout the duration of the tests to remove oxygen from the solution.

Prior to the start of an electrochemical test, the working electrode was cathodically cleaned for 5 minutes.

The electrochemical tests were performed using BioLogic VMP-300 Multipotentiostats. Three techniques were used in this study: CV, potentiostatic polarization and potentiodynamic polarization.

3.4.3. Radiation Exposure Tests

All irradiation experiments were conducted in an MDS Nordion Gammacell 220 Excel Cobalt-60 irradiator. An electrochemical cell or autoclave containing the coupon vials was placed inside the gamma cell sample chamber, which was then lowered into the irradiation zone, a cylindrical cavity surrounded by 11 tubular pencils containing ⁶⁰Co. The radiation dose rate in the irradiation chamber during the experiments was 2.5 kGy·h⁻¹, where 1 Gy = 1 J absorbed per kg of water.

3.4.4. Coupon Exposure Experiments ($T \geq 80$ °C)

All coupon exposure tests were performed under argon cover gas. The samples were prepared in an Ar-purged glove box. The test solution was purged with argon (ultra-high purity grade, Praxair) for 45 min prior to transfer to the glove box. The freshly polished coupons were placed on a pedestal at the bottom of a quartz vial. After the coupons had been placed on the pedestal, the vials were filled with 7 mL of argon-purged test solution to fully immerse the coupons in the solution.

The sample vials were then placed in a 300 mL AISI 316 stainless steel autoclave purchased from Parr Instrument Company. At the time of closure, the autoclave was filled with 20 mL (only 7% of the autoclave volume) Type 1 water (Barnstead International NANOpure Diamond UV, 18.2 M Ω ·cm) to maintain the same pressure inside and outside the vial during the experiment. After the autoclave was sealed, a leak test was performed, and the headspace of the vessel was purged with argon to remove any residual oxygen. The autoclave was then heated to the desired temperature (80 °C or 150 °C) before being lowered into the irradiation zone. The high-temperature experiments were also carried out without exposure to gamma radiation. The durations of the corrosion exposure experiments were 5, 24, 48, 72, 120 and 144 h.

3.5. REFERENCES

- [1] D. Guo, Corrosion Dynamics of Carbon Steel in Used Fuel Container Environments, Electron. Thesis Diss. Repos. 5897, University of Western Ontario (2018).
- [2] K.J. Vetter, *Electrochemical Kinetics: Theoretical and Experimental Aspects*, Academic Press, 1967.
- [3] A.J. Bard, L.R. Faulkner, *Electrochemical Methods Fundamentals and Applications*, Wiley, 2001.
- [4] N. Elgrishi, K.J. Rountree, B.D. McCarthy, E.S. Rountree, T.T. Eisenhart, J.L. Dempsey, A Practical Beginner's Guide to Cyclic Voltammetry, *J. Chem. Educ.* 95 (2018) 197–206.
- [5] J. Wang, *Analytical Electrochemistry*, Wiley, 2000.
- [6] D.J. O'connor, B.A. Sexton, R.S.C. Smart, *Surface Analysis Method in Materials Science*, Springer, 2003.
- [7] S. Zhang, L. Li, KumarA, *Materials Characterization Techniques*, CRC press, 2008.
- [8] R.F. Egerton, *Physical Principles of Electron Microscopy: An Introduction to TEM, SEM, and AEM*, Springer, 2005.
- [9] S. Ebnesajjad, C. Ebnesajjad, *Surface Treatment Of Materials For Adhesive Bonding*, William Andrew, 2013.
- [10] H. Konno, X-ray Photoelectron Spectroscopy, *Mater. Sci. Eng. Carbon.* (2016) 153–171.
- [11] M.C. Biesinger, B.P. Payne, A.P. Grosvenor, L.W.M. Lau, A.R. Gerson, R.S.C. Smart, Resolving surface chemical states in XPS analysis of first row transition metals, oxides and hydroxides: Cr, Mn, Fe, Co and Ni, *Appl. Surf. Sci.* 257 (2011) 2717–2730.
- [12] M. Guo, The Electrochemical and corrosion study of copper for nuclear waste containers under deep geological disposal conditions, Electron. Thesis Diss. Repos. 7371, University of Western Ontario (2020).
- [13] ASM Handbook, *Fundamentals, Corrosion: Testing, and Protection*, 13A, ASM International, 2003. <https://doi.org/10.31399/asm.hb.v13a.9781627081825>

CHAPTER 4

NON-LINEAR EFFECTS OF SOLUTION PARAMETERS ON NICKEL OXIDATION

4.1. INTRODUCTION

Nickel and nickel-based alloys with high nickel content are widely used in many industrial applications. Due to their high corrosion resistance, these alloys are used for thin-walled heat exchanger tubing in the steam generators in nuclear power plants [1,2]. In these applications, the nickel alloys are exposed to γ -radiation at high temperatures. To predict the corrosion behaviour of nickel-based alloys, it is essential to understand the oxidation kinetics of Ni metal as a function of solution reaction and transport parameters.

Aqueous corrosion is an electrochemical process involving many elementary steps, which include interfacial transfer of electrons and metal atoms at the metal-solution boundary, solution reactions (hydrolysis), mass transport processes (diffusion and migration of oxidant(s) and metal cations), and oxide particle nucleation and growth [3–7]. Different solution parameters affect the kinetics of the elementary steps differently, which leads to different metal oxidation paths and overall oxidation rates. The kinetics of

the elementary reactions are not independent of each other but strongly coupled, which leads to a cyclic feedback loop (systemic feedback) between different elementary steps [8–13]. Due to systemic feedback the overall metal oxidation rate does not follow linear dynamics [9,11,12,14]. Therefore, to predict the long-term corrosion behaviour of metals and alloys, it is important to identify the key elementary processes that control the overall corrosion rate.

In this study, the combined effects of pH (6.0, 8.4 and 10.6) and other solution parameters on Ni oxidation were investigated using electrochemical techniques. The other solution parameters were either the presence or absence of γ -radiation at room temperature, and high and low ionic strengths (I_s) at 80 °C in the absence of γ -radiation.

Different solution parameters affect interfacial electron transfer, interfacial mass (metal atom) transfer and solution-phase processes differently. In the absence of other oxidants, $[H^+]$ affects the electron transfer rate of proton reduction, which is coupled with metal oxidation. For metal oxidation, metal cation solvation also contributes to the determination of the overall oxidation rate. The solvation rate increases with pH. On the other hand, the maximum solvation yield, which is the solubility of the metal cation, decreases with pH. Hence, pH could affect the rate and yield of electron/metal atom transfer, as well as those of hydrolysis and metal hydroxide precipitation.

Increasing temperature from room temperature to 80 °C has a minor effect on interfacial charge transfer but can increase the rate of a thermal process because rearranging chemical bonds is typically a more energetic process than outer-sphere electron transfer. Ionic strength (I_s) and solution conductivity affect ion mobility through

the effect on concentration gradients [15–18] and thus an increase in I_s increases the rate of Ni^{2+} transport from the interface to the bulk solution.

Gamma radiation decomposes water to produce redox active species such as H_2O_2 , without affecting the solvent properties of the water or mass transport behaviour in the solution [19,20]. Hence, radiolysis affects the overall metal oxidation rate primarily via production of H_2O_2 , thereby increasing the driving force (i.e., overpotential) for metal oxidation.

Thus, different combinations of the solution parameters will affect the strengths of feedback loops between elementary reactions, and particularly between the interfacial transfer of electrons/metal-atoms and the solution-phase chemical processes.

The evolution of elementary reactions and the mass transfer/transport steps that control the overall metal oxidation rate were investigated by measurements of corrosion potential as a function of time ($E_{corr}(t)$) and the current vs potential relationships under potentiodynamic and potentiostatic conditions.

Corrosion potential is one of the most common parameters measured when evaluating corrosion [21]. In this study, $E_{corr}(t)$ is evaluated with respect to the equilibrium potentials (E_{rxn}^{eq}) of various elementary metal redox half-reactions that can occur over long-term corrosion. Each elementary half-reaction has a characteristic current-potential relationship [11,22]. E_{corr} represents the electrode potential (E_{elec}) at which the net metal oxidation current (i_{ox}) is equal to the net oxidant reduction current ($|i_{red}|$) under naturally corroding conditions [10,11,21,22]. Hence, although E_{corr} alone does not provide kinetic information, comparison of $E_{corr}(t)$ with various E_{rxn}^{eq} can provide mechanistic information on the evolution of the metal redox half-reaction(s) that

may occur as corrosion progresses. Most corrosion rate analysis techniques and models recognize the importance of measuring E_{corr} and establishing the i_{meas} vs E_{elec} relationship, from which the i_{ox} at E_{corr} can be extracted [10,23–25]. However, the dependences of the time-dependent behaviour of E_{corr} on solution parameters have rarely been investigated.

It is the i_{corr} , the i_{ox} at E_{corr} , that represents the corrosion rate. However, i_{corr} cannot be measured directly, but requires the measurement of current (i_{meas}) as a function of externally applied E_{elec} away from E_{corr} and extrapolation of the i_{meas} vs E_{elec} relationship to obtain the i_{ox} or $|i_{red}|$ at $E_{elec} = E_{corr}$ [10,22,26]. As presented later, the change in E_{corr} with time was not gradual in a given solution environment. The change in E_{corr} with time arises from (1) a change in the current-potential relationship (Tafel constant, β_{rxn}) due to a change in the elementary half-reactions involved, and/or (2) change in current due to the **potential-independent** chemical processes of metal oxidation products and/or depletion of solution oxidants at the interface. Hence, in this study, the i_{meas} vs E_{elec} relationship was investigated by cyclic voltammetry (CV) and potentiostatic polarization. The polarization experiments were conducted for metal oxidation at different pH at 80 °C only, and in the absence of radiation.

In this study we compared both the $E_{corr}(t)$ and i_{meas} vs E_{elec} relationship data observed under different solution conditions to establish a metal oxidation mechanism, which can account for the evolution of metal redox half-reactions as oxidation progresses and the effects of solution parameters on this evolution.

4.2. EXPERIMENTAL

The experimental procedures used in this thesis are described fully in Chapter 3; however, a brief description is provided in this section. A pure Ni rod 0.620 cm in diameter was cut into circular, flat, 3 mm thick coupons. Only one circular face of the samples with a surface area of 0.302 cm² was exposed to the solution. Prior to each experiment the flat electrode surfaces were polished (using a series of silicon carbide papers and mirror-polished on a Texmet microcloth (Buehler) with the 1 μm MetaDi Supreme diamond paste suspension as described in Chapter 3), cleaned with deionized water (Type 1 water) and dried under argon gas.

All experiments were conducted in argon-purged conditions, at pH 6.0, 8.4 and 10.6 using 0.01 M sodium borate (Na₂B₄O₇·10H₂O) solution which the pH is adjusted with boric acid at pH 6.0 and 8.4 and NaOH at pH 10.6. All solutions were prepared with Type 1 water with a resistivity of 18.2 MΩ·cm.

E_{corr} , CV and PS experiments were performed at 80 °C and for three different pHs. A three-compartment electrochemical cell, made of Pyrex glass, was used for all the experiments. Ni samples were used as the working electrode (WE), platinum mesh (Alfa Aesar, 99.9% purity) served as the counter electrode (CE), and the reference electrode (RE) used was a saturated calomel electrode (SCE, Fisher Scientific). The Hg|HgO (–0.129 V vs SCE) RE was used for radiation experiments, because of its superior radiation stability. For all experiments the electrolyte solution was Ar-purged for 1 hour prior to the experiment and purging continued throughout the test duration.

All irradiation experiments were conducted in an MDS Nordion Gamma cell 220 Excel Cobalt-60 irradiator. The gamma cell irradiator provided an absorbed radiation

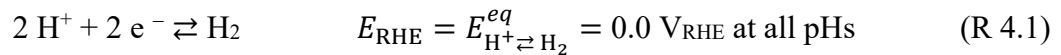
dose of $2.6 \text{ kGy}\cdot\text{h}^{-1}$. An electrochemical cell containing electrodes was placed inside the gamma cell sample chamber, and then lowered into the irradiation zone, which consists of a cylindrical cavity surrounded by 11 tubular pencils containing ^{60}Co .

4.3. RESULTS AND DISCUSSION

4.3.1 $E_{corr}(t)$ vs E_{rxn}^{eq} of Metal Redox Half-Reactions

Figure 4.1 compares the $E_{corr}(t)$ observed during corrosion of Ni electrodes in three different pHs: (a) at room temperature (RT) without γ -radiation present, (b) at RT with γ -radiation present, and (c) at $80 \text{ }^\circ\text{C}$ in high and low I_s solutions. For an electrochemical half-reaction (rxn) the potential parameter that controls its net rate is the overpotential, $\eta_{rxn} = E_{elec} - E_{rxn}^{eq}$ [10,22,26]. Hence, the E_{rxn}^{eq} of some of elementary Ni redox half-reactions are also shown in the figure.

To compare the results obtained at different pHs at a specific temperature, $E_{corr}(t)$ is presented on the V_{RHE} scale in **Figure 4.1**. The V_{RHE} scale uses the reversible hydrogen electrode (RHE) potential as a reference potential. The E_{RHE} on the standard hydrogen electrode (SHE) potential scale decreases by $60 \text{ mV}_{\text{SHE}}$ per unit pH increase, but on the V_{RHE} scale $E_{\text{RHE}} = 0.0 \text{ V}_{\text{RHE}}$ at all pHs:



Note that the RHE potential of $0.0 \text{ V}_{\text{RHE}}$ is for the chemical activity of H_2 at its standard state. That is, dissolved H_2 is in partitioning equilibrium with gaseous H_2 ($\text{H}_{2(\text{g})}$)

at partial pressure of 1 atm (the standard state of H₂). The fraction of H_{2(g)} in normal air is $\sim 0.6 \times 10^{-6}$, which yields the $E_{\text{H}^+ \rightleftharpoons \text{H}_2}^{eq}$ value of 0.37 V_{RHE} at all pHs. The fraction of H₂ in the Ar gas used in this study was not available, but it should be less than the fraction in normal air. Hence, the $E_{\text{H}^+ \rightleftharpoons \text{H}_2}^{eq}$ value under the studied conditions should be higher than 0.37 V_{RHE}.

The E_{rxn}^{eq} of redox half-reactions involving solid nickel redox species (presented in **Figure 4.2 and in Appendix**) also decrease by 60 mV_{SHE} per unit pH increase. Because of the same 60 mV_{SHE} increase per ΔpH , the E_{rxn}^{eq} values on the V_{RHE} scale are independent of pH. Hence, the difference in E_{corr} on the V_{RHE} scale directly corresponds to the difference in η_{rxn} for each half-reaction, irrespective of pH.

In **Figure 4.1**, only the E_{rxn}^{eq} of redox half-reactions involving metal hydroxide species are presented. As discussed in more detail later, crystalline oxide particles such as NiO, Ni₃O₄ and Ni₂O₃ are thermodynamically more stable than Ni(OH)₂ and Ni(OH)₃. However, direct chemical oxidation of metal (Ni⁰) to these oxides during aqueous corrosion is not kinetically favoured, compared to the electrochemical pathway via oxidation of Ni⁰ to dissolved Ni²⁺ and/or Ni³⁺ followed by precipitation as Ni(OH)₂ and/or Ni(OH)₃ colloids and growth of oxides of distinct crystal phases [27,28].

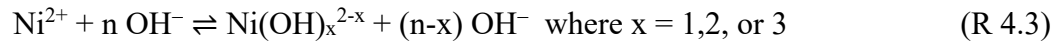
Note that for the E_{rxn}^{eq} presented in **Figure 4.1**, a chemical (redox) activity of 1.0 was used for the solid species, Ni⁰, Ni(OH)₂, Ni(OH)₃ and Ni₃O₄, independent of their mass (which is above the critical mass allowing them to be considered as solid). Transition metal hydroxides are hygroscopic and hence, initially condense as colloids in

water and/or aggregate to form a hydrogel network [12,29,30]. The chemical activities of metal hydroxides in colloidal form or in a hydrogel network will not be 1.0.

Also not shown in the figure are the E_{rxn}^{eq} of half-reactions involving dissolved metal cations, e.g.,



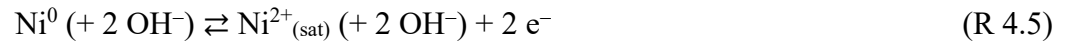
The equilibrium potential of the reaction ($E_{\text{Ni}^0 \rightleftharpoons \text{Ni}^{2+}}^{eq}$) depends on the chemical activity (~concentration) of Ni^{2+} in the interfacial region ($(a_{\text{Ni}^{2+}})_{int}$). As discussed in more detail later, $(a_{\text{Ni}^{2+}})_{int}$ is determined not only by the net electron/metal atom transfer step but also the transport of Ni^{2+} from the interfacial region to the bulk solution, and/or other removal processes of Ni^{2+} from the interfacial region. There exists no true chemical equilibrium state for the interfacial mass transfer process; otherwise equilibrium potential of the reaction ($E_{\text{Ni}^0 \rightleftharpoons \text{Ni}^{2+}}^{eq}$) would be determined by $(a_{\text{Ni}^{2+}})_{int}$. However, a quasi-equilibrium (steady state) exists when the solution is saturated with the metal cation. Metal cations dissolved in water are constantly in hydrolysis equilibrium:



When the total concentration of dissolved metal cations ($\text{Ni}^{2+} + \text{Ni}(\text{OH})^+ + \text{Ni}(\text{OH})_2 \cdot n\text{H}_2\text{O} + \text{Ni}(\text{OH})_3^-$) exceeds its saturation limit, the dissolved species precipitate with OH^- as an $\text{Ni}(\text{OH})_2$ salt [31–33]:



Due to the hydrolysis and phase-partitioning equilibria, the redox half-reaction of Ni^0 to $\text{Ni}^{2+}_{(sat)}$ is also at equilibrium when the oxidation half-reaction of Ni^0 to amorphous $\text{Ni}(\text{OH})_2$ is at equilibrium:



Hence, the E_{rxn}^{eq} of the two half-reactions on the V_{RHE} scale are the same at all pHs:

$$E_{\text{Ni}^0 \rightleftharpoons \text{Ni}^{2+}_{(\text{sat})}}^{eq} = E_{\text{Ni}^0 \rightleftharpoons \text{Ni}(\text{OH})_2}^{eq} \quad (\text{R 4.7})$$

Note that $[\text{Ni}^{2+}_{(\text{sat})}]$ depends on pH.

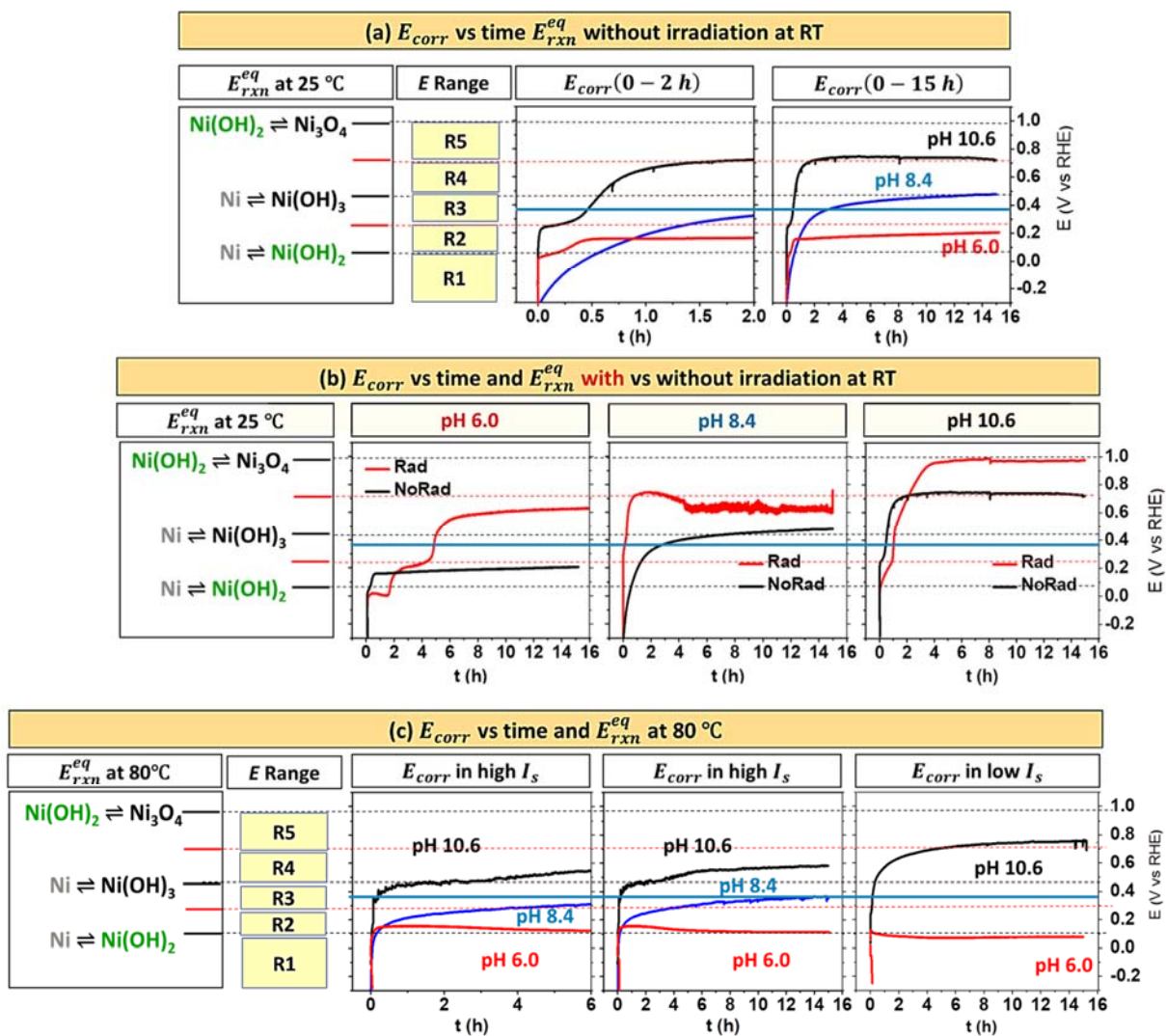


Figure 4.1: $E_{corr}(t)$ observed at three different pHs under continuous Ar-purging, (a) at room temperature without γ -radiation present, (b) at room temperature with or without γ -radiation present, and (c) at 80 °C in high or low ionic strength solution. The first column in each figure is the E_{rxn}^{eq} diagram of metal redox half-reactions with the E_{rxn}^{eq} values represented by bars next to the redox pairs [36–39]. The red bars in the E_{rxn}^{eq} diagram represent the mid-potential between two E_{rxn}^{eq} values and the blue line represent the proton reduction equilibrium potential at $P_{H_2} = 0.6 \times 10^{-6}$.

Figure 4.1 shows that depending on solution conditions, E_{corr} changes with time and this change is not gradual over a certain period of time. Instead as E_{corr} progresses over time it evolves through distinct periods of linear increase at different rates. An abrupt change in dE_{corr}/dt indicates a change in the metal redox half-reaction(s) controlling the current-potential relationship. The progression of metal redox half-reaction(s) is discussed in detail throughout the chapter. To aid the discussion, the elementary reactions and transport steps involved in the overall metal oxidation process are listed in **Table 4.1**.

Initial E_{corr} :

In all cases, upon removal of the externally applied potential for cathodic cleaning E_{corr} rose rapidly (within 150 s) to a value that depended on pH, temperature and radiation environment. After the initiation of metal oxidation, the chemical activity of the initial product Ni^{2+} in the interfacial region ($(a_{Ni^{2+}})_{int}$) changes very rapidly. Along with the metal cation production, remaining O_2 in solution and H^+ are also consumed (or OH^- is produced) by oxidant reduction reactions. The rate of increase of $(a_{Ni^{2+}})_{int}$ and $(a_{OH^-})_{int}$ depends on the production and removal rates of Ni^{2+} and OH^- in the interfacial region. The Ni^{2+} production process is net electron/metal atom transfer (M1 in **Table 4.1**). In the very early stages of corrosion the predominant Ni^{2+} removal process is the transport of Ni^{2+} from the interfacial region to the bulk solution (trans in **Table 4.1**). However, it is expected that solution pH remains mainly constant in buffered solution and the production of $[OH^-]$ at the interface does not significantly contribute to the E_{corr}

evolution. Hence, the reduction current density remains nearly constant (see PS polarization section in Chapter 5) and is not the focus here.

After the initiation of metal oxidation in the solution free of dissolved Ni^{2+} , $(a_{\text{Ni}^{2+}})_{int}$ increases rapidly. However, the increase in $(a_{\text{Ni}^{2+}})_{int}$ slows down the net rate of (M1) because an increase in $(a_{\text{Ni}^{2+}})_{int}$ increases the rate of the reverse reaction of (M1) (M1r in **Table 4.1**). The increase in $(a_{\text{Ni}^{2+}})_{int}$ also increases the rate of (trans). The rate of (trans) quickly approaches that of (M1), and $(a_{\text{Ni}^{2+}})_{int}$ becomes nearly constant with time. Accordingly, i_{ox} and E_{corr} also reach near steady-state values (or change slowly with time).

Although metal oxidation occurs during the initial rapid transition, we will refer to the E_{corr} value when the system reaches the first steady, or slowly-changing, state as the “initial E_{corr} ” ($E_{corr}(\tau_0)$), hereafter. Our results show that $E_{corr}(\tau_0)$ (on the V_{RHE} scale) depends strongly on pH. The other solution parameters, temperature, I_s , and radiolytically produced oxidant, have relatively small effects on $E_{corr}(\tau_0)$.

The strong pH dependence of $E_{corr}(\tau_0)$ on the V_{RHE} scale was unexpected. The effect of $[\text{H}^+]$ on the proton reduction current has been taken into account by plotting E_{corr} and E_{rxn}^{eq} on the V_{RHE} scale. In addition, $E_{corr}(\tau_0)$ did not have any systematic dependence on $E_{\text{H}^+ \rightleftharpoons \text{H}_2}^{eq}$. Instead, $E_{corr}(\tau_0)$ was close to either one of the E_{rxn}^{eq} of metal redox half-reactions or the mid-potentials between two E_{rxn}^{eq} values (represented by red lines in **Figure 4.1**).

Table 4.1: Elementary reactions involved in the overall metal oxidation process

Rxn ID	Reaction Type	Chemical Equation	Rate ID
M1	Electron/metal-atom transfer	$\text{Ni}^0 _{\text{int}} \rightleftharpoons \text{Ni}^{2+} _{\text{int}} + 2 e^-$	ν_{M1} $i_{\text{M1}} = nF \cdot \nu_{\text{M1}}$
	<p>This is a reversible process, consisting of two reaction steps ($\nu_{\text{M1}} = \nu_{\text{M1f}} - \nu_{\text{M1r}}$):</p> <p>(M1f): $\text{Ni}^0 \rightarrow \text{Ni}^{2+} + 2 e^-$ $\nu_{\text{M1f}} = k_{\text{M1f}} \cdot (a_{\text{Ni}^0})_{\text{int}} \approx k_{\text{M1f}}$</p> <p>(M1r): $\text{Ni}^{2+} + 2 e^- \rightarrow \text{Ni}^0$ $\nu_{\text{M1r}} = k_{\text{M1r}} \cdot (a_{\text{Ni}^{2+}})_{\text{int}}$</p> <p>where $(a_{\text{Ni}^{2+}})_{\text{int}}$ represents the chemical activity of Ni^{2+} in the interfacial region.</p>		
trans	Ion diffusion	$\text{Ni}^{2+} _{\text{int}} \rightarrow \text{Ni}^{2+} _{\text{bulk}}$	ν_{trans}
M2	Electron transfer	$\text{Ni}^{2+}/\text{Ni}(\text{OH})_2 + \text{OH}^- \rightleftharpoons \text{Ni}(\text{OH})_3 + e^-$	ν_{M2} $i_{\text{M2}} = nF \cdot \nu_{\text{M2}}$
	<p>This is a reversible process, consisting of two reaction steps ($\nu_{\text{M2}} = \nu_{\text{M2f}} - \nu_{\text{M2r}}$):</p> <p>(M2f): $\text{Ni}^{2+}/\text{Ni}(\text{OH})_2 + \text{OH}^- \rightarrow \text{Ni}(\text{OH})_3 + e^-$ $\nu_{\text{M2f}} \approx k_{\text{M2f}} \cdot (a_{\text{Ni}^{\text{II}}})_{\text{int}}$</p> <p>(M2r): $\text{Ni}(\text{OH})_3 + e^- \rightarrow \text{Ni}^{2+}/\text{Ni}(\text{OH})_2 + \text{OH}^-$ $\nu_{\text{M2r}} = k_{\text{M2r}} \cdot (a_{\text{Ni}^{\text{III}}})_{\text{int}}$</p> <p>where $(a_{\text{Ni}^{\text{II}}})_{\text{int}}$ and $(a_{\text{Ni}^{\text{III}}})_{\text{int}}$ represent the overall redox activities of Ni^{II} and Ni^{III} species (dissolved and colloidal) in the interfacial region.</p>		
hyd	Hydrolysis	$\text{Ni}^{2+} + n \text{OH}^- \rightleftharpoons \text{Ni}(\text{OH})_x^{2-x} + (n-x) \text{OH}^-$	ν_{hyd}
gel	Hydrogel formation	$\text{Ni}(\text{OH})_2 + \text{Ni}(\text{OH})_3 \rightarrow x\text{Ni}(\text{OH})_2 \cdot y\text{Ni}(\text{OH})_3(\text{gel})$	ν_{gel}
oxide	Crystalline oxide growth	$\text{Ni}(\text{OH})_2 \cdot 2\text{Ni}(\text{OH})_3(\text{gel}) \rightarrow \text{Ni}_3\text{O}_4(\text{cryst}) + 4 \text{H}_2\text{O}$	ν_{oxide}

During the rapid transition that occurs within 150 s, precipitation of colloids and crystalline particles is negligible, and pH has a negligible effect on the rate of (trans). The significant effect of pH on $E_{corr}(\tau_0)$ indicates that the net rate of (M1), which requires transfer of not only electrons but also Ni atoms, is primarily controlled by solvation and hydrolysis of Ni^{2+} . The rates of solvation and hydrolysis of metal cations increase with $[\text{OH}^-]$, while the saturation limit decreases with $[\text{OH}^-]$. When the solution in the interfacial region becomes saturated, the metal atoms cannot be transferred any faster than the rate of Ni^{2+} removal from the interfacial region. Initially the main removal process is (trans). The lower $E_{corr}(\tau_0)$ and subsequent slower increase in E_{corr} with time at pH 8.4 than at the other two pHs at RT can then be attributed to the higher solvation and hydrolysis rates at pH 8.4 than at pH 6.0, but higher saturation capacity for Ni^{2+} at pH 8.4 than at pH 10.6.

Evolution of E_{corr} :

The normal expectation for an electrochemical reaction is that once $(a_{\text{Ni}^{2+}})_{int}$ reaches a (pseudo-) steady-state value, i_{ox} and E_{corr} should remain constant with time, and the i_{ox} vs E_{corr} relationship should follow Butler-Volmer kinetics [10,37]. However this expectation is only valid for electron transfer reactions on bare metal surfaces without mass transport control effect from oxide layer and/or potential drop [7,37].

What we observed was that following the initial rapid transition E_{corr} indeed reached a near steady-state $E_{corr}(\tau_0)$, but only temporarily. E_{corr} continued to change with time, and the change was not gradual (at a parabolic rate). Instead, E_{corr} evolved through distinct periods of linear increase (constant dE_{corr}/dt) at different rates. An

abrupt change in dE_{corr}/dt is usually associated with a change in the metal-oxidation half-reaction(s) controlling the current-potential relationship. In accordance with the distinct periods of linear states observed, and the E_{rxn}^{eq} of the nickel redox reactions, the E_{corr} evolution is classified into 5 ranges of potential R1 to R5.

- **R1:** $E < E_{Ni^0 \rightleftharpoons Ni(OH)_2}^{eq}$
- **R2:** $E_{Ni^0 \rightleftharpoons Ni(OH)_2}^{eq} \leq E < E_{Ni^0 \rightleftharpoons Ni(OH)_2 / Ni^0 \rightleftharpoons Ni(OH)_3}^{mid}$
- **R3:** $E_{Ni^0 \rightleftharpoons Ni(OH)_2 / Ni^0 \rightleftharpoons Ni(OH)_3}^{mid} < E \leq E_{Ni^0 \rightleftharpoons Ni(OH)_3}^{eq}$
- **R4:** $E_{Ni^0 \rightleftharpoons Ni(OH)_3}^{eq} \leq E < E_{Ni^0 \rightleftharpoons Ni(OH)_3 / Ni(OH)_2 \rightleftharpoons Ni_3O_4}^{mid}$
- **R5:** $E_{Ni^0 \rightleftharpoons Ni(OH)_3 / Ni(OH)_2 \rightleftharpoons Ni_3O_4}^{mid} < E \leq E_{Ni(OH)_2 \rightleftharpoons Ni_3O_4}^{eq}$

A slow change in E_{corr} with time indicates that the electrochemical metal oxidation kinetics are in a (pseudo-) steady state. Depending on the solution conditions, $E_{corr}(t)$ evolved from an initial steady state value to different steady state value(s). The number of steady states that the metal oxidation system passes through before reaching the final steady state, the durations of the steady states, and the steady-state values depended on the solution parameters. Examining the steady-state E_{corr} values and the rates of transition from one steady state to the next, and how solution parameters affect these values can provide mechanistic information on how metal oxidation progresses.

The key observations on the effects of solution parameters on the evolution of $E_{corr}(t)$ can be summarized as follows:

- Although $E_{corr}(t)$ evolved very differently depending on solution parameters, the steady state E_{corr} coincided with one of the E_{rxn}^{eq} of the half-reactions involving metal hydroxides, or the mid-potential between two of the E_{rxn}^{eq} values. The mid-potential between two of the E_{rxn}^{eq} values is considered due to repeatedly observing this coincidence in other electrochemical results, see CV results).
- The final steady-state E_{corr} value was higher and the rate of progression through different steady states was faster in the presence than in the absence of γ -radiation at all tested pHs.
- In the absence of radiation (i.e., same Ar-purged redox environment), pH affected the initial and the final steady state E_{corr} .

Temperature and I_s had a negligible effect on the initial E_{corr} but a more significant effect on the final E_{corr} .

- The transition to the final steady state occurred earlier at higher pHs and at higher temperatures.

These observations indicate that pH affects the kinetics of metal oxidation at an early stage. This effect is results from contributions of (1) proton reduction which decreases with pH, and (2) the rates of solvation and hydrolysis of Ni^{2+} which increase with pH. However, this doesn't mean that both effects contribute to determination of the overall metal oxidation rate equally.

What we observed was that E_{corr} progresses through one of the E_{rxn}^{eq} values of metal oxidation half-reactions in a semi stepwise manner. At pH 6.0, E_{corr} increased steadily to a value close to $E_{Ni^0 \rightleftharpoons Ni(OH)_2}^{eq}$ within 2-3 min and did not deviate significantly from the value for the rest of the test duration. At pH 10.6, E_{corr} increased stepwise with short breaks first at $E_{Ni^0 \rightleftharpoons Ni(OH)_2}^{eq}$ and then to $E_{Ni^0 \rightleftharpoons Ni(OH)_2/Ni(OH)_3}^{mid}$ before reaching $E_{Ni^0 \rightleftharpoons Ni(OH)_3}^{eq}$ even within 2-3 min, followed by more gradual increase to $E_{Ni^0 \rightleftharpoons Ni(OH)_2 \rightleftharpoons Ni_3O_4}^{mid}$. After reaching $E_{Ni^0 \rightleftharpoons Ni(OH)_2 \rightleftharpoons Ni_3O_4}^{mid}$, E_{corr} increased at a much slower rate for the rest of the test duration. Stepwise increases in E_{corr} could be more clearly seen at room temperature and/or under more oxidizing radiation conditions. These observations indicate that the rate determining step (RDS) for the full redox reaction occurring on the metal electrode is the metal oxidation half-reaction and not the reduction of oxidants (H^+ and/or O_2) that are coupled with the metal oxidation, and that the overall metal oxidation evolves with time as the intermediate products accumulate and begin to react at appreciable rates.

Under the kinetic conditions when $(a_{Ni^{2+}})_{int}$ cannot exceed its saturation limit (i.e., pH 6.0 at RT without radiation present), the metal oxidation rate is primarily determined by the kinetics of (M1), (trans) and (hyd). However, the interfacial region becomes saturated faster at a higher pH, and the oxidation and precipitation of Ni^{2+} as mixed Ni^{II}/Ni^{III} hydroxide colloid particles ((M2), (gel) and (oxide) in **Table 4.1**) occur earlier. Because precipitation of hydroxides and oxides further influences (M1) and (trans), once (M2), (gel) and (oxide) begin to occur at a substantial rate, the metal oxidation kinetics change very rapidly. Hence, pH affects the metal oxidation kinetics at

an early stage, leading to very different metal oxidation paths at different pHs, and eventually a different final (pseudo-) steady-state E_{corr} on the V_{RHE} scale.

Temperature has a negligible effect on (M1) (having a very low activation energy) or (trans). However, increasing temperature accelerates the rates of thermal solution processes (hyd), (gel) and (oxide), and either increase or decrease their reaction yields depending on whether they are exothermic or endothermic. Ionic strength (I_s) affects ion mobility [15,38] and hence, increasing I_s increases the rate of (trans).

The transition from one steady state to another occurs earlier and more steady states are observed in the presence of radiation. As described earlier, γ -irradiation makes the solution environment more oxidizing without affecting the solvation properties of water. Under a more oxidizing environment, the normal expectation is that E_{corr} would increase because of increasing $|i_{red}|$ and hence, i_{ox} . However, if oxidant reduction is a rate determining step, the E_{corr} at steady state should be different for different oxidizing environments.

Figure 4.1 shows that E_{corr} evolved through distinct periods of linear increase at different rates, and this value can be higher than the E_{rxn}^{eq} value of oxidant reduction half-reaction. Hence, when the E_{corr} observed for corrosion in solutions under continuous Ar-purging is higher than $E_{H^+ \rightleftharpoons H_2}^{eq}$ ($\sim 0.37 V_{RHE}$), it is often assumed that residual O_2 is responsible for corrosion. However, as discussed earlier, the E_{corr} value coincides with E_{rxn}^{eq} values of nickel oxidation half-reactions or mid-potential between two E_{rxn}^{eq} . Hence, the RDS for the full redox reaction occurring on the metal electrode is the metal oxidation half-reaction and not the reduction of oxidants (H^+ and/or O_2) that are coupled with the metal oxidation. Therefore, that residual O_2 is not necessarily required for nickel

oxidation under Ar-purging conditions or for the E_{corr} value to be higher than $E_{H^+ \rightleftharpoons H_2}^{eq}$. This does not mean that purging with Ar may not remove all the O₂ initially dissolved or the residual O₂ is not involved in nickel oxidation. Indeed, the final steady-state $E_{corr(\tau_f)}$ higher than $E_{H^+ \rightleftharpoons H_2}^{eq}$ is due to decrease in the overall metal oxidation half-reaction as more insoluble hydroxide/oxide grows on the metal surface (E_{corr} value at pH 10.6 in the absence of radiation), and presence of highly oxidizing agents in the presence of radiation.

An abrupt change in dE_{corr}/dt is associated with a change in the metal-oxidation half-reaction(s) that control(s) the current-potential relationship. For electrode reactions, the change in E_{elec} with time arises from (1) a change in the current-potential relationship (Tafel constant, β_{rxn}) due to a change in the electrochemical half-reaction, and/or (2) a change in current due to the **potential-independent** chemical processes of metal oxidation products:

$$\frac{dE_{elec}}{dt} = \left. \frac{dE_{elec}}{d(\log i_{rxn})} \right|_t \cdot \left. \frac{d(\log i_{rxn})}{dt} \right|_{E_{elec}} = \beta_{rxn}(t) \cdot \left. \frac{d(\log i_{rxn})}{dt} \right|_{E_{elec}}$$

Hence, we have performed cyclic voltammetry (CV), which provides information on $\frac{dE_{elec}}{d(\log i_{rxn})}$, and potentiostatic (PS) polarization tests which provide information on $\frac{d(\log i_{rxn})}{dt}$. The CV and PS polarization tests performed at three different pHs in high I_s solutions at 80 °C are presented.

4.3.2. Cyclic Voltammetry

Cyclic voltammetry was performed on nickel electrodes in high I_s solutions at three pHs (6.0, 8.4 and 10.6). For all three pHs, 5 cycles of CV were performed over different potential scan ranges, from the cathodic cleaning potential ($-0.30 V_{RHE}$) to different upper vertex potentials, and back to $-0.30 V_{RHE}$. The potential scan rate was 5 mV/s in all cases, and each cycle took $\sim 9, 7,$ and 5 min to scan one cycle in upper vertex potentials 1.0, 0.70, and 0.4 V_{RHE} respectively. The $\log|i_{meas-CV}|$ values as a function of E_{elec} obtained during the first 3 CV cycles with different upper vertex potentials at different pHs are compared in **Figure 4.2**. Note that in the figure E_{elec} is presented on the V_{RHE} scale.

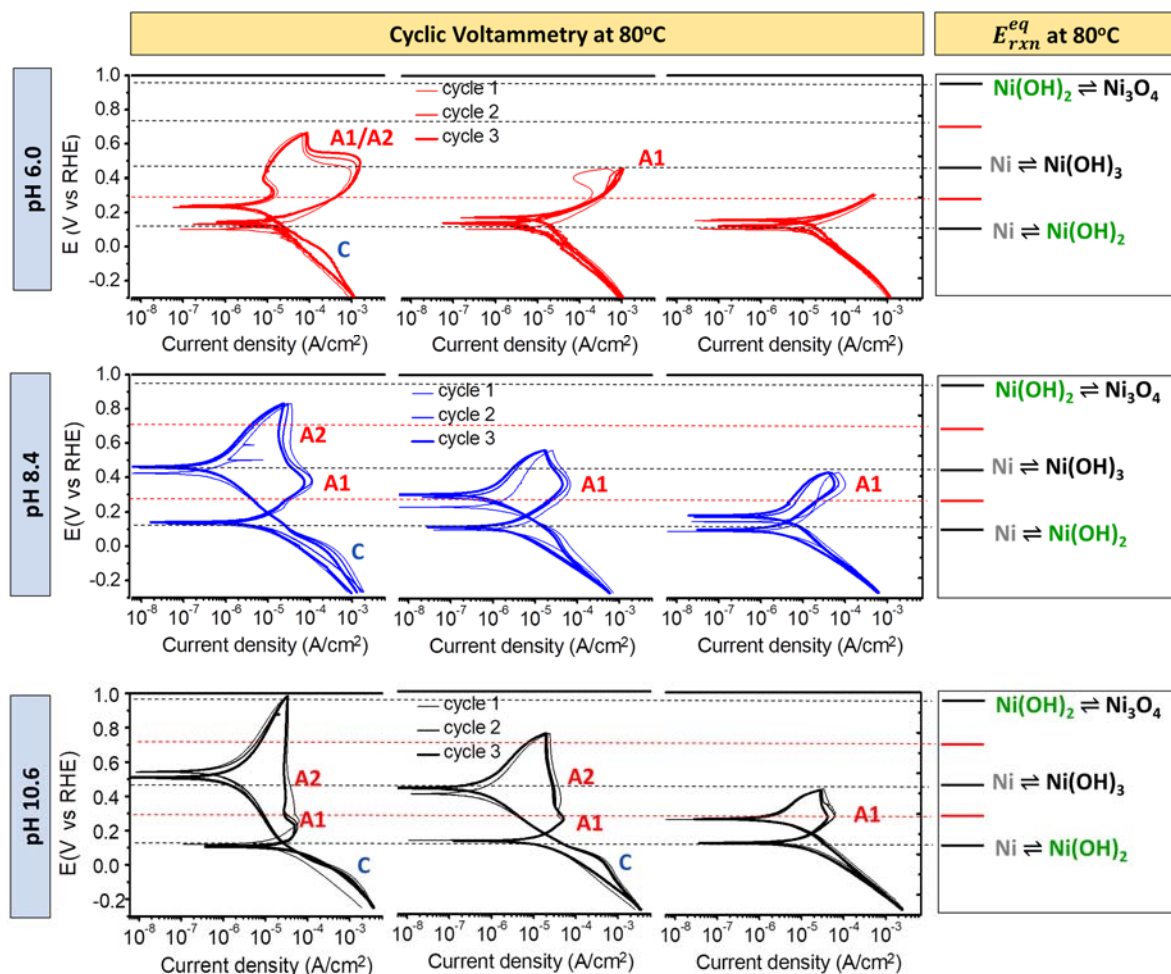


Figure 4.2: The $\log|i_{meas-CV}|$ vs E_{elec} relationships observed during cyclic voltammetry with different upper vertex potentials at three pHs at 80 °C. Each plot contains 3 consecutive cycles (thinnest to thickest from 1st to 3rd cycle). The righthand panel is the equilibrium potential diagram of metal redox half-reactions with the E_{rxn}^{eq} values represented by bars and the corresponding redox pairs next to the bars. The red bars represent the mid-potential between two E_{rxn}^{eq} values.

The $\log|i_{meas-CV}|$ vs E_{elec} relationships observed on different cycles were similar for all three pHs. The main change occurred between the 1st and 2nd CV cycle performed with the highest upper vertex potential, and no further changes were observed after the 3rd cycle. In comparison, the $\log|i_{meas-CV}|$ vs E_{elec} relationships observed

during the forward and reverse scans during a given cycle were very different. The difference was more significant in the CVs obtained with higher upper vertex potentials and at higher pHs. Nevertheless, common features can be observed.

- In all cases, the potential of zero current on the reverse scan ($E_{i=0,r}$) did not coincide with that on the forward scan ($E_{i=0,f}$). $E_{i=0,f}$ was near $E_{\text{Ni}^0 \rightleftharpoons \text{Ni}(\text{OH})_2}^{eq}$, *independent* of pH, vertex potential or cycle number. $E_{i=0,r}$ was also nearly independent of pH and cycle number, but depended strongly on vertex potential. Nevertheless, $E_{i=0,r}$ was always close to one of the E_{rxn}^{eq} or mid-potential values, except for pH 6.0 and pH 8.4 with vertex potentials lower than $E_{\text{Ni}^0 \rightleftharpoons \text{Ni}(\text{OH})_3}^{eq}$.
- On the forward scan, two anodic current peaks, labeled as A1 and A2, were observed. Vertex potential had a negligible effect on the peak potentials of A1 and A2. (At pH 6.0, peaks A1 and A2 were not separated and hence the broad peak was denoted as A1/A2 in **Figure 4.2**) However, these anodic peaks appeared at lower potentials at higher pHs. The peak currents of A1 and A2 increased with successive cycles at pH 6.0, but decreased for the higher pHs.
- The anodic peaks were not observed on the reverse scan, except for A1 at pH 6.0.
- Only one broad cathodic peak (labeled as C) was observed at potentials below $E_{\text{Ni}^0 \rightleftharpoons \text{Ni}(\text{OH})_2}^{eq}$ on the reverse scan, whenever A2 was observed on the forward scan.

To examine the effect of pH versus vertex potential on the $\log |i_{meas-CV}|$ vs E_{elec} relationship in detail, the 3rd cycle CVs were compared in **Figure 4.3**:

- The $\log |i_{meas-CV}|$ vs E_{elec} relationship in the cathodic potential range on the forward scan was different from that of the reverse scan. The difference increased with pH and vertex potential.
- On the reverse scan, the $\log |i_{meas-CV}|$ vs E_{elec} relationship in the cathodic potential range (below $E_{i=0,r}$) contained two significant components, linear dependence of $\log |i_{meas-CV}|$ on E_{elec} (Tafel relation) and peak C. The $\log |i_{meas-CV}|$ components that increased linearly with E_{elec} are indicated with broken lines in **Figure 4.3**.
- When the vertex potential was below $E_{Ni^0 \rightleftharpoons Ni(OH)_2}^{eq}$, peak C was absent and the cathodic Tafel slope was -215 ± 5 mV/dec at all three pH. This is due to presence of partially oxidation process in this range of potential.
- At higher vertex potentials, peak C was present, and the cathodic Tafel slope (magnitude) of the base line current decreased with vertex potential, from -215 ± 5 mV/dec to -160 ± 5 mV/dec. The peak current of C (above the base-line current) was nearly independent of the cathodic Tafel slope or pH.

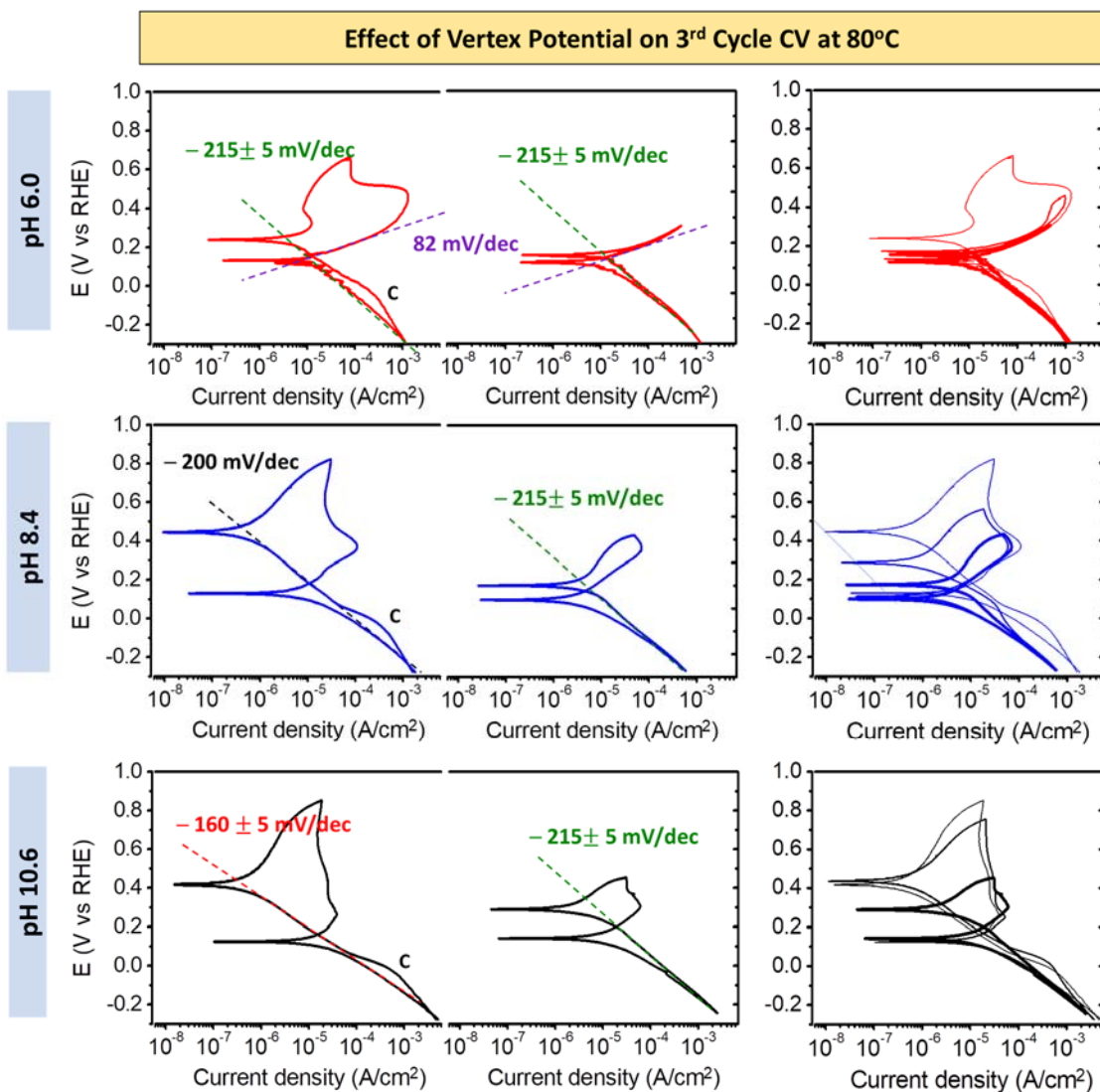


Figure 4.3: Tafel slopes observed during the 3rd CV cycle with different upper vertex potentials at three pHs at 80 °C. The righthand-side panel compares the 3rd cycle CVs with different vertex potentials at each pH.

These observations indicate that peaks A1 and A2 are associated with the precipitation of mixed Ni^{II}/Ni^{III} hydroxide (step (gel) in **Table 4.1**). For the precipitation to occur in the interfacial region, the rate of (M1) that produces Ni²⁺ must be high enough to saturate the interfacial region and induce the partial oxidation of Ni²⁺/Ni(OH)₂ to

Ni(OH)₃ (step (M2)) that can trigger colloid or hydrogel formation of mixed Ni^{II}/Ni^{III} hydroxide (step (gel) in **Table 4.1**). The condensation/precipitation of the mixed hydroxides decreases the overall transport of Ni²⁺/Ni(OH)₂ from the interfacial region to the bulk solution (step (trans)). Accordingly, the rate of (M1) decreases and overall metal oxidation decreases. The overall consequence is that $i_{meas-CV}$ decreases, not increase, with E_{elec} after the A1 current peak.

The rate of (M1) increases with E_{elec} . However, for (gel) and (M2) to proceed it requires a higher overpotential at a lower pH because of the higher solubility of the metal hydroxides. Hence, peak A1 appears at a higher E_{elec} , and the current of the A1 peak is higher, at a lower pH.

When the rate of (M1) becomes equal to the rate of (trans), the overall metal oxidation kinetics reach steady-state and become potential-independent. (The contribution of (M2) to $i_{meas-CV}$ at these potentials is negligible compared to that of (M1).)

Peak A2 follows peak A1 due to increased oxidation of Ni²⁺/Ni(OH)₂ to Ni(OH)₃ (step (M2)) in the hydrogel network at potentials higher than $E_{Ni^0 \rightleftharpoons Ni(OH)_3}^{eq}$. Following peak A1, the rate of (M1) has reduced, limited by the rate of (trans). At potentials above $E_{Ni^0 \rightleftharpoons Ni(OH)_3}^{eq}$, the rate of (M2) increases exponentially with E_{elec} . Ni(OH)₃ is nearly insoluble and does not transport out of the interfacial region. This further impedes the overall transport of Ni²⁺/Ni(OH)₂ from the interface to the bulk solution. Hence, an increase in (M2) temporarily increases the anodic current, but $i_{meas-CV}$ quickly decreases back to the mass transport-limited current at higher potentials.

Peak C was observed only after the potential scan was reversed after peak A2 was observed and it appeared at potentials below $E_{\text{Ni}^0 \rightleftharpoons \text{Ni}(\text{OH})_2}^{eq}$, independent of $E_{i=0,r}$ or the vertex potential. Hence, peak C can be attributed to the current arising from the reduction of $\text{Ni}^{2+}/\text{Ni}(\text{OH})_2$ to Ni^0 in the hydrogel network. The Ni^0 produced from the reduction on the reverse scan may not transfer back to the metal phase but form metallic nanoparticles in the hydrogel network [39,40].

The peak current value of C had no correlation with the Tafel slope of the baseline current. Proton reduction (R 4.1) is a near irreversible process because of the very rapid recombination of radical species ($\bullet\text{H}$) to H_2 . Hence, the proton reduction current is expected to exhibit only cathodic Tafel behaviour. The baseline current exhibiting linear dependence on E_{elec} varied from -217 mV/dec to -150 mV/dec, with increasing vertex potential. These observations indicate that the Tafel slope (in magnitude) larger than -140 mV/dec is not due to slower proton transport from the bulk solution to the surface due to corrosion product precipitation. Rather, this cathodic Tafel slope greater than that of proton reduction is due to the larger contribution of reduction of the metal oxidation product $\text{Ni}(\text{OH})_3$. This is further supported by the observation that peak C was present only when peak A2 was observed.

The effect of pH on the $\log |i_{meas}|$ vs E_{elec} relationship near the $E_{corr}(t)$ observed under the same solution conditions (Ar-purging, pH, high I_s and 80 °C) can be seen more clearly in **Figure 4.4**. Comparing the CVs this way reveals many interesting and unexpected effects of pH on the current-potential relationship.

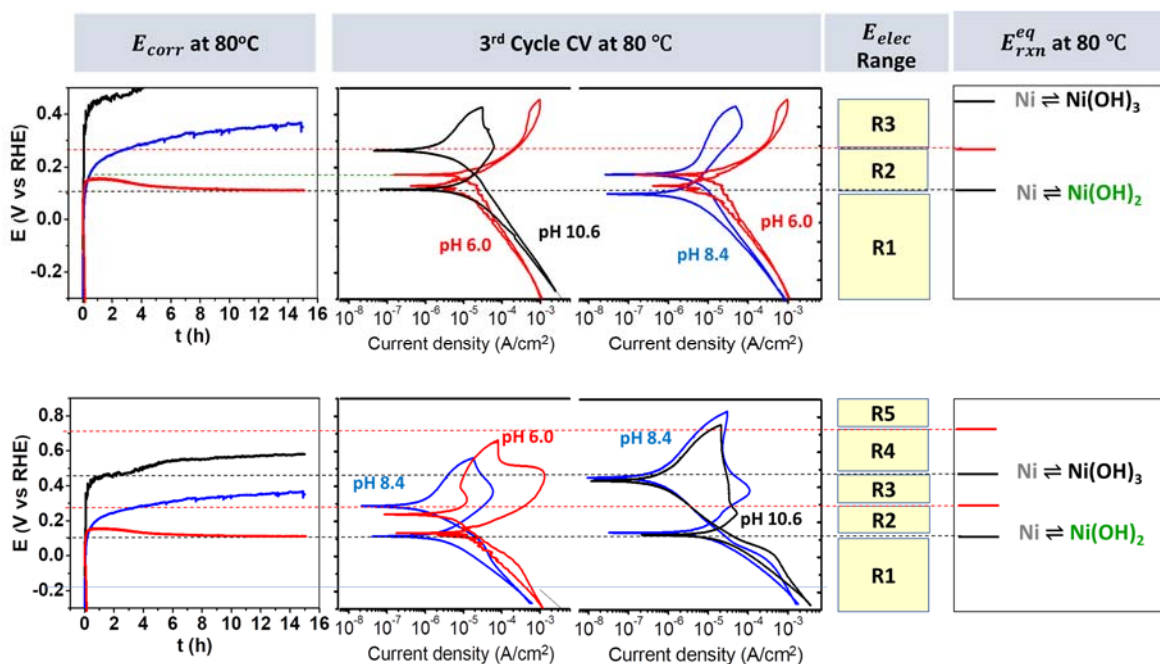


Figure 4.4: Comparison of current-potential relationships during the 3rd CV cycle at potential ranges near E_{corr} observed at early stages (upper panel) and at later stages (lower panel). Also shown on the right-hand side is the E_{rdx}^{eq} diagram of metal redox half-reactions.

The effects of pH on the $\log |i_{meas-CV}|$ vs E_{elec} relationship observed during CV are:

- At each pH, the $|i_{meas-CV}|$ values in the potential range R1 ($E \leq 0.08$ V_{RHE}) on the forward and reverse CV scans were same only at $E_{elec} < -0.2$ V_{RHE}. Interestingly, the $|i_{meas-CV}|$ values at these low potentials were highest at pH 10.6, and lowest at pH 8.4.
- At $E_{elec} > -0.2$ V_{RHE}, the $|i_{meas-CV}|$ values in the cathodic potential range were lower on the forward scan than on the reverse scan and this difference was larger at higher pHs. Nevertheless, when the potential was scanned forward near

$E_{\text{Ni}^0 \rightleftharpoons \text{Ni}(\text{OH})_2}^{eq}$ the $|i_{meas-CV}|$ at pH 10.6 converged to that of pH 6.0, while that of pH 8.4 diverged more from that of pH 6.0.

- Despite the large difference in $|i_{meas-CV}|$ in R1, $E_{i=0,f}$ was near $E_{\text{Ni}^0 \rightleftharpoons \text{Ni}(\text{OH})_2}^{eq}$, independent of pH. This was also the initial E_{corr} observed at pH 6.0 and pH 8.4.
- At E_{elec} above $E_{i=0,f}$, $\log |i_{meas-CV}|$ increased faster with E_{elec} and over a wider potential range at a lower pH. The pH-dependence of the anodic current was different from that of the cathodic current. The difference was most significant at pH 6.0; the anodic Tafel slope was ~ 82 mV/dec while the cathodic Tafel slope in **R1** was ~ 217 mV/dec (**Figure 4.3**).
- On the reverse scan with vertex potential equal to $E_{\text{Ni}^0 \rightleftharpoons \text{Ni}(\text{OH})_3}^{eq}$, the $E_{i=0,r}$ values at pH 6.0 and pH 8.4 did not coincide with any of the E_{rxn}^{eq} of metal redox half-reactions, but the $E_{i=0,r}$ values at both pHs were the same at 60 mV above $E_{\text{Ni}^0 \rightleftharpoons \text{Ni}(\text{OH})_2}^{eq}$. This was also the 1st steady-state E_{corr} value observed at pH 6.0. The E_{corr} continued to increase at pH 8.4. These observations indicate that overall metal oxidation in the potential range R2 ($0.08 < E \leq 0.28$ V_{RHE}) at these pHs is partially controlled by (trans) in addition to (M1).
- At pH 10.6, $|i_{meas-CV}|$ increased more slowly with E_{elec} , and reached a maximum current at a lower potential compared to those observed at the lower pHs. The $E_{i=0,r}$ coincided with $E_{\text{Ni}^0 \rightleftharpoons \text{Ni}(\text{OH})_2/\text{Ni}(\text{OH})_3}^{eq}$ when the vertex potential was at $E_{\text{Ni}^0 \rightleftharpoons \text{Ni}(\text{OH})_3}^{eq}$. These observations indicate that at pH 10.6, overall metal oxidation in the potential ranges R2 and R3 ($0.26 < E \leq 0.45$ V_{RHE}) is strongly influenced by the kinetics of precipitation of mixed hydroxides.

- This potential was also the $E_{i=0,r}$ observed at pH 6.0 and pH 8.4 when the vertex potential was in R4 ($0.45 < E \leq 0.70 \text{ V}_{\text{RHE}}$) ($> E_{\text{Ni}^0 \rightleftharpoons \text{Ni}(\text{OH})_3}^{eq}$). It was also the E_{corr} value at which the rate of change of E_{corr} began to diminish at pH 8.4, (i.e., the onset potential of the pseudo-steady state).
- The $E_{i=0,r}$ was at $E_{\text{Ni}^0 \rightleftharpoons \text{Ni}(\text{OH})_3}^{eq}$ at pH 10.6 when the vertex potential was in R4. This was also the $E_{i=0,r}$ at pH 8.4 but with the vertex potential in R5. This was also the 1st steady-state E_{corr} value observed at pH 10.6.

These observations suggest that not only proton reduction, but also metal oxidation current contribute to the $|i_{meas-CV}|$ in the potential range R1 ($E_{elec} < E_{\text{Ni}^0 \rightleftharpoons \text{Ni}(\text{OH})_2}^{eq}$). As discussed earlier, the net rate of (M1) (see **Table 4.1**) depends on not only E_{elec} but also the solvation rate of Ni^{2+} , which increases with pH, until the interfacial region becomes saturated. The lower $|i_{meas-CV}|$ at pH 8.4 than at pH 6.0 is due to the increased rate of solvation while the higher $|i_{meas-CV}|$ at pH 10.6 than at pH 6.0 is due to near-immediate saturation at pH 10.6.

These observations also imply that relying on cathodic Tafel behaviour to obtain i_{ox} at E_{elec} (i.e., i_{corr} , the corrosion rate), as in conventional polarization techniques, may not be valid.

The CV results indicate that even under the same solution redox conditions, the $\log |i_{meas-CV}|$ vs E_{elec} relationship depends on pH. Note that the different oxidant (H^+) concentrations at different pHs were taken into account by plotting E_{elec} on the V_{RHE} scale. These observations indicate that an E_{corr} above 0.0 V_{RHE} does not necessarily

mean that another oxidant such as O_2 is present in the solution, or that metal oxidation cannot occur when E_{corr} is below the E_{rxn}^{eq} of the metal oxidation half-reaction.

The metal oxidation mechanism as a function of E_{elec} is discussed in detail later. The observations indicate that the overall metal oxidation current depends not only on E_{elec} but also on the chemical reactions and transport processes of intermediate oxidation products. Interfacial atom transfer, chemical reactions and transport are generally slower than interfacial electron transfer reactions. Hence, the metal redox half-reactions in the interfacial region do not reach (quasi-) chemical equilibrium but remains in a dynamic state. As a result, the $|i_{meas-CV}|$ vs E_{elec} relationship depends strongly on various solution parameters such as pH. (The effect of I_s is discussed in Chapter 5.)

As observed for E_{corr} , there were distinct potential ranges exhibiting characteristic $\log |i_{meas-CV}|$ vs E_{elec} relationships. These potential ranges coincide with those determined from the time-dependent behaviour of E_{corr} . The time-dependent behaviour of $|i_{meas-CV}|$ under potentiostatic polarization in the different potential ranges is examined next.

4.3.3. Current-Potential Relationships Under Potentiostatic Polarization

The time-dependent behaviours of $\log |i_{meas-PS}|$ observed at various E_{elec} under potentiostatic polarization at pH 6.0 and pH 10.6 in Ar-purged, high I_s solutions at 80 °C are presented in **Figure 4.5**.

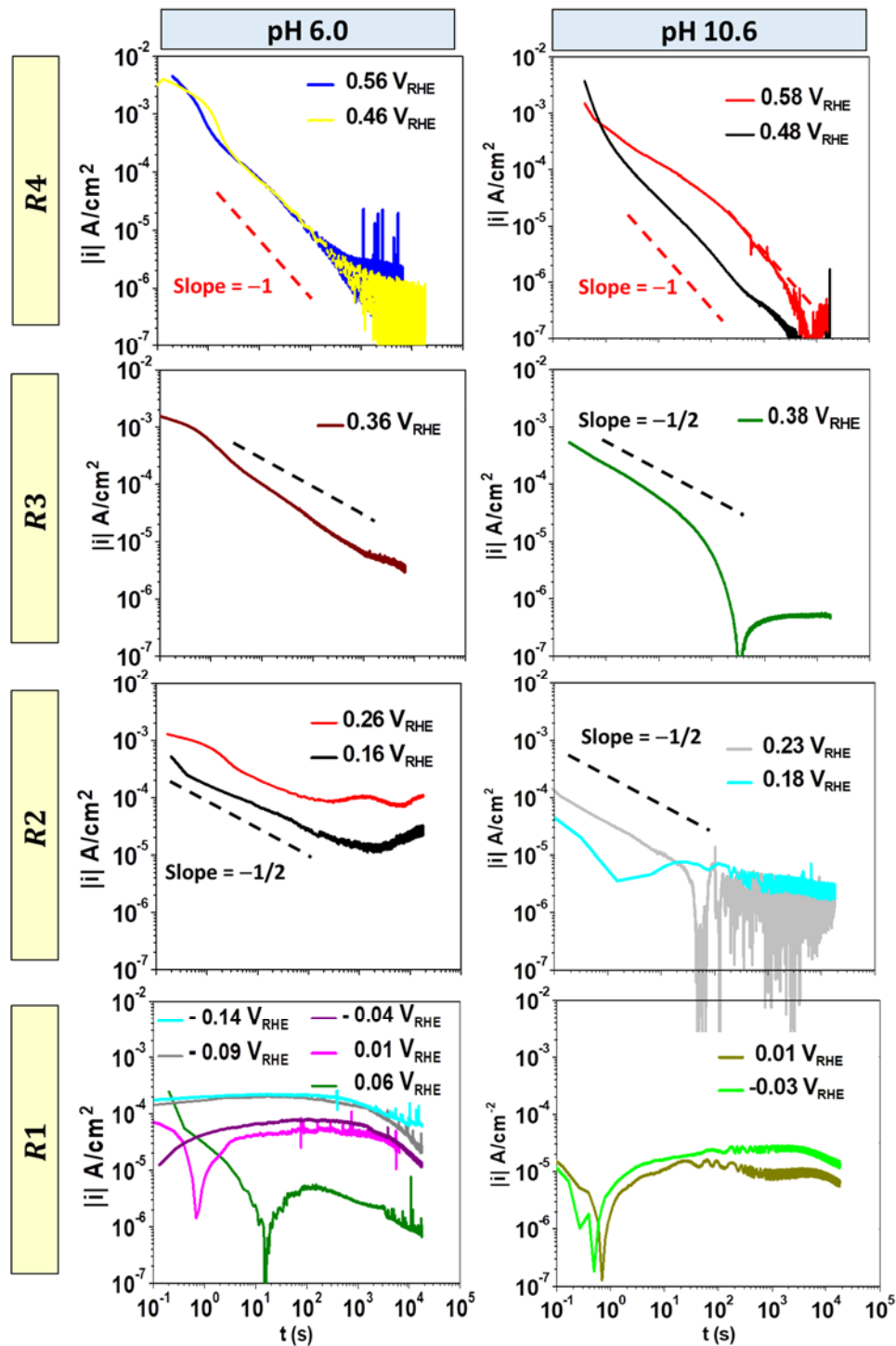


Figure 4.5: Time-dependent behaviours of $|i_{meas-PS}|$ observed at various E_{elec} under potentiostatic polarization at pH 6.0 and pH 10.6 in Ar-sparged and high I_s solutions at 80 °C. The data are grouped together according to potential ranges. Dashed lines with slopes of -0.5 (black) and -1.0 (red) are presented for reference.

Figure 4.5 shows that even under potentiostatic polarization and constant purging conditions, $|i_{meas-PS}|$ changed with time over an extended period before reaching a steady state value. The time to reach a pseudo-steady or slowly changing state was greater for higher E_{elec} values. The time dependence of $|i_{meas-PS}|$ also varied with E_{elec} . Nevertheless, $|i_{meas-PS}|$ showed similar time-dependent behaviour at E_{elec} within the same potential range defined based on the E_{elec} and CV results (see **Figures 4.1** and **4.4**). The time-dependences of $|i_{meas-PS}|$ at the two different pHs were also similar at E_{elec} (on the V_{RHE} scale) in the same potential range. These characteristics are summarized below.

- At E_{elec} in the potential range R1, $|i_{meas-PS}|$ was negative and nearly constant with time at very negative potentials. At these potentials, $|i_{meas-PS}|$ is primarily due to proton reduction. However, at $E_{elec} > -0.2 V_{RHE}$, the potential at which the forward and reverse CV began diverging (**Figures 4.2** to **4.4**), $|i_{meas-PS}|$ was initially positive, but decreased with time and switched to negative, and reached a negative steady-state value. The initial anodic current value was larger at a higher E_{elec} , while the final steady-state cathodic current value was smaller. The observation of an initial anodic current at E_{elec} further supports the claim that net metal oxidation is not negligible initially but decreases with time as the chemical activity of the metal cation in the interfacial increases.
- At E_{elec} in R2, $|i_{meas-PS}|$ remained positive throughout the test duration. The slope of $\log|i_{meas-PS}|$ vs $\log t$ was close to -0.5 , meaning that $|i_{meas-PS}|$ (at $t > 1$ s) decreased approximately proportionally to \sqrt{t} , before it reached a near steady-state value by 150 s. The initial $|i_{meas-PS}|$ (at $t > 1$ s) more slowly changing

current at times < 1 s is discussed in Chapter 5. A similar time to when E_{corr} began changing at a slow rate following the initial rapid rise from the cleaning potential (**Figure 4.1**). The initial and the steady-state current values increased with E_{elec} , and at the same E_{elec} they were larger at pH 6.0 than at pH 10.6.

- At E_{elec} in R3, $|i_{meas-PS}|$ decreased with time nearly proportionally to \sqrt{t} or slightly faster, similar behaviour to that observed in R2. However, in R3 the initial current did not increase much with E_{elec} . The decrease in $|i_{meas-PS}|$ also continued for a longer duration, and at pH 10.6 it switched to a negative current.
- At E_{elec} in R4, $|i_{meas-PS}|$ ($t > 1$ s) decreased nearly linearly with time (the slope of the $\log|i_{meas-PS}|$ vs $\log t$ is -1.0) to a very small current.

Earlier we showed that upon removal of the externally applied potential for cathodic cleaning the open circuit potential rose very rapidly (over 150 s) to an initial E_{corr} value that depended on pH, temperature and radiation environment (**Figure 4.1**). At 80 °C in the absence of radiation the initial E_{corr} value was near $E_{Ni^0 \rightleftharpoons Ni(OH)_2}^{eq}$ at pH 6.0 and 8.4, a potential in R3.

Earlier we also argued that the initial rapid increase in E_{corr} is due to a rapid change in $(a_{Ni^{2+}})_{int}$ and less likely change in $(a_{OH^-})_{int}$ due to using buffered solution. The rate of increase of $(a_{Ni^{2+}})_{int}$ depends on the production and removal rates of Ni^{2+} in the interfacial region. When metal oxidation initiates, the main Ni^{2+} production is (M1) in **Table 4.1** and the main Ni^{2+} removal process is (trans) in **Table 4.1**. The kinetics of (M1) and (trans) are, however, strongly coupled for metal oxidation, and the rate of increase of

$(a_{\text{Ni}^{2+}})_{int}$ diminishes rapidly. The main transport mechanism is ion diffusion of Ni^{2+} and hence, the pseudo 1st order rate coefficient for (trans), k_{trans} , decreases with \sqrt{t} .

Because of the strong feedback between (M1) and (trans), the net metal oxidation current, i_{ox} , should decrease with \sqrt{t} at early stages of metal oxidation at a given E_{elec} under externally polarized conditions. On the other hand, under naturally corroding conditions mass and charge conservation dictates that the E_{elec} during the initial rapid transition increases proportionally to \sqrt{t} (results not shown). The \sqrt{t} dependence of $|i_{meas-PS}|$ is indeed what we observed at E_{elec} in R2 and R3. The initial (pseudo steady-state) E_{corr} was at $E_{\text{Ni}^0 \rightleftharpoons \text{Ni}(\text{OH})_2}^{eq}$, the boundary potential between R1 and R2, at pH 6.0 and pH 8.4 and at $E_{\text{Ni}^0 \rightleftharpoons \text{Ni}(\text{OH})_2/\text{Ni}(\text{OH})_3}^{eq}$, the boundary potential between R2 and R3, at pH 10.6.

At $E_{elec} > E_{\text{Ni}^0 \rightleftharpoons \text{Ni}(\text{OH})_3}^{eq}$ (in R4), $|i_{meas-PS}|$ ($t > 1$ s) decreased nearly linearly with time. At these potentials, metal oxidation to $\text{Ni}^{2+}/\text{Ni}(\text{OH})_2$ occurs fast and early, accelerating further oxidation to $\text{Ni}(\text{OH})_3$ (M2) and precipitation of mixed $\text{Ni}^{\text{II}}/\text{Ni}^{\text{III}}$ hydroxide (gel). The Ni^{2+} continues to transport out into the bulk solution (trans) but at a much slower rate, while the net rate of (M2) decreases at the rate of $\text{Ni}(\text{OH})_3$ production in the interfacial region, which is constant with time at a constant E_{elec} . Accordingly, the overall metal oxidation rate or current decreases linearly with time. The dependence of i_{ox} on E_{elec} at different times is discussed in more detail in Chapter 5.

As shown earlier in **Figure 4.1**, E_{corr} continued to change with time. At 80 °C in Ar-purged, high I_s solution without radiation present E_{corr} remained in R2 at pH 6.0 (approaching the lower boundary of R2 at longer times). At pH 8.4, E_{corr} continued to

move through R2 into R3, where E_{corr} increased at a slower rate while remaining in R3. At pH 10.6, E_{corr} moved through R3 and remained at the boundary potential between R3 and R4 for a few hours, followed by a slow increase within R4. It is important to mention that there is an intermediate steady state – at the mid potential where E_{corr} remained at.

The optical images showing the evolution of the surface during R1 to R4 for pH 6.0 are shown in **Figure 4.6**. For the potential range -0.24 to -0.14 the surface looks relatively clean, whereas for the potential range -0.04 to 0.56 the formation of a greenish brownish gel layer is observed on the surface. The greenish-brown colour is attributed to the formation of $\text{Ni}(\text{OH})_2$ and $\text{Ni}(\text{OH})_3$ as described in more detail in Chapters 6 and 7.

As shown earlier in **Figure 4.1**, E_{corr} continued to change with time. At $80\text{ }^\circ\text{C}$ in Ar-purged, high I_s solution without radiation present, E_{corr} remained in R2 at pH 6.0 (approaching the lower boundary of R2 at longer times). At pH 8.4, E_{corr} continued to move through R2 into R3, where E_{corr} increased at a slower rate while remaining in R3. At pH 10.6, E_{corr} moved through R3 and remained at the boundary potential between R3 and R4 for a few hours, followed by a slow increase within R4.

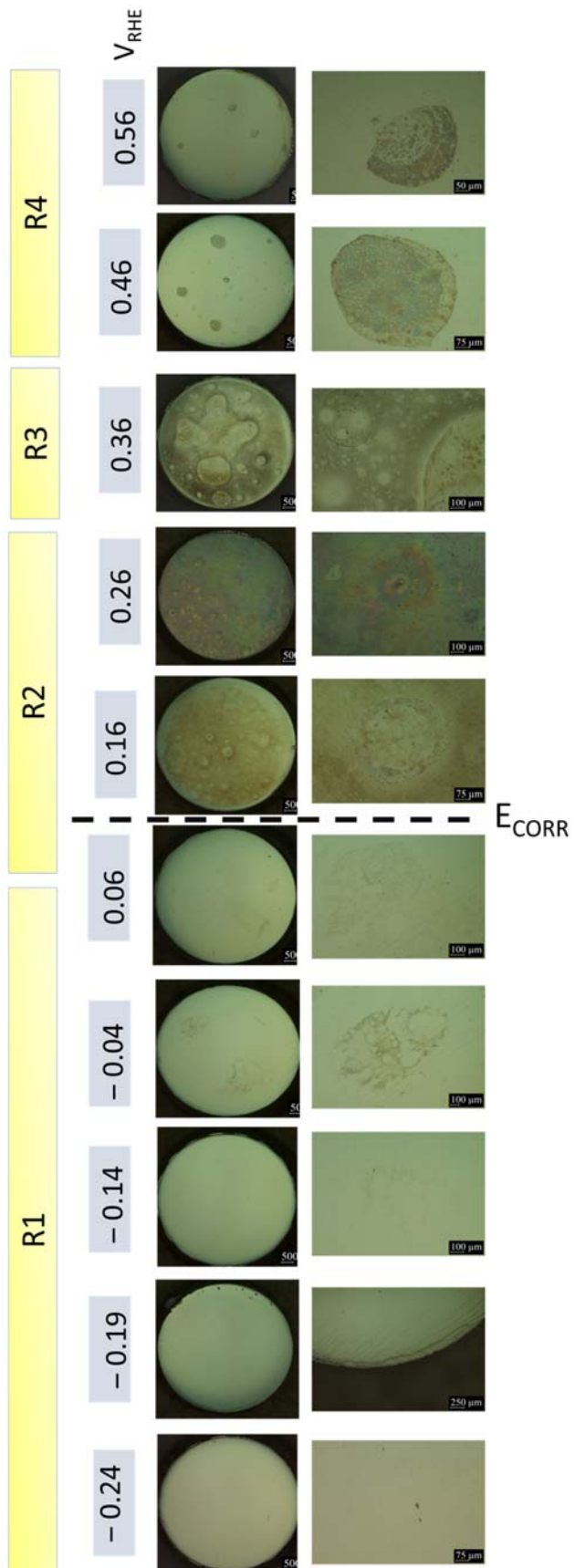


Figure 4.6: Optical images showing the evolution of the surface during R1 to R4 for pH 6.0

For long-term corrosion kinetics, the $\log|i_{meas-CV}|$ vs E_{elec} relationship obtained from the CV, and/or the long-term steady-state current under potentiostatic polarization, cannot be used directly to obtain the corrosion rate as a function of E_{corr} , even in controlled and constant solution environments. However, the time-dependence of E_{corr} , the potential-dependence of $\log|i_{meas-PD}|$ under potentiodynamic polarization, and the time-dependence of $|i_{meas-PS}|$ under potentiostatic polarization all have common characteristic behaviours at potentials within each potential range. These results collectively provide mechanistic information on the evolution of the corrosion dynamics over long-term corrosion that can adequately explain the observed effects of solution parameters on the corrosion pathway and the evolution of the corrosion rate with time.

4.3.4. Evolution of the Dynamic Phases of Metal Oxidation

Based on the observations we can propose that the overall metal oxidation dynamics evolve through different dynamic phases, as metal oxidation progresses and the initial and intermediate oxidation products accumulate in the interfacial region.

Dynamic phase refers to the ranges of electrochemical/chemical conditions under which the overall metal oxidation rate may change but the elementary (rate-determining) steps that comprise the overall process, and the (pseudo-) 1st-order rate coefficients of the individual steps, do not change within the state. (An analogy: a dynamic state is equivalent to an electrical circuit, consisting of a series of specific RC (or impedance) components; each elementary step is equivalent to each RC component; the chemical conditions (chemical potential or free energy of reaction) are equivalent to the external

voltage applied; R to the 1st-order rate coefficient; i to the overall rate; (C is to the rate of change in the overall rate (i) when the conditions (V_{ext}) change).

Dynamic Phase I:

This phase represents the reaction conditions and time during which (“dynamic phase”) electrochemical metal oxidation is taking place, and is limited to production of Ni²⁺. The overall metal oxidation process consists of the elementary steps (M1f) and (M1r), (trans) and (hyd) in as defined in **Table 4.1**, and schematically presented in **Figure 4.7**. Discussion on the coupled kinetics is beyond the scope of this work and will be reported elsewhere. However, it should be noted that the kinetics of the individual steps are not independent of each other. At any given time, mass and charge conservation dictate that:

$$v_{\#1}(t) \approx v_{M1}(t) \approx v_{trans}(t) + v_{hyd}(t) \quad (\text{Eq 4.1 a})$$

$$v_{M1}(t) = v_{M1f}(t) - v_{M1r}(t) \quad (\text{Eq 4.1 b})$$

$$i_{ox}(t) \approx i_{M1f}(t) - i_{M1r}(t) = |i_{red}(t)| \quad (\text{Eq. 4.1 c})$$

where $v_{\#1}(t)$ and $i_{ox}(t)$ represent the overall metal oxidation rate at time t (in units of M·cm/s or mol/cm²·s) and the net metal oxidation current (in units of A/cm²) at time t . The current is related to the rate by Faraday’s laws of electrolysis ($i_{ox}(t) = nF v_{SS\#1}(t)$).

Dynamic Phase II:

Under the conditions where $(a_{Ni^{2+}})_{int}$ can reach its saturation limit and remain there, the electrochemical and chemical reactions of Ni²⁺ begin to occur at substantial rates. The overall metal oxidation process consists of steps (M2f) and (M2r) and (gel) in

addition to (M1f) and (M1r), (trans) and (hyd) as defined in **Table 4.1**, and schematically presented in **Figure 4.7**. In this phase, mass and charge conservation dictates that:

$$\nu_{\#1}(t) \approx \nu_{M1}(t) \approx \nu_{trans}(t) + \nu_{gel}(t) + \nu_{M2}(t) \quad (\text{Eq 4.2 a})$$

$$\nu_{M1}(t) = \nu_{M1f}(t) - \nu_{M1r}(t), \nu_{M2}(t) = \nu_{M2f}(t) - \nu_{M2r}(t) \quad (\text{Eq 4.2 b})$$

$$i_{ox}(t) \approx i_{M1}(t) + i_{M2}(t) = |i_{red}(t)| \quad (\text{Eq. 4.2 c})$$

In this dynamic phase, the kinetics of the elementary steps are strongly coupled; the increase in $\nu_{M2}(t)$ increases $\nu_{gel}(t)$ but decreases $\nu_{trans}(t)$ because of the lower solubility of Ni^{III}. The net effect of $\nu_{M2}(t)$ can either increase or decrease $\nu_{M1}(t)$ and $i_{ox}(t)$, depending on the competition kinetics between the different steps. Because of the systemic feedback in this phase, small changes in kinetic parameters affecting any of the elementary steps can accelerate or decelerate the overall metal oxidation to reach a steady state at which the rates of individual steps no longer change.

Dynamic Phase III:

After sufficient mixed Ni^{II}/Ni^{III} hydroxide colloids have precipitated they can nucleate and grow as solid crystalline particles on the surface. In this dynamic phase, overall metal oxidation is generally suppressed by growth of oxide on the metal surface (step (oxide) in **Table 4.1**). However, the type, morphology and size of oxide that grows on the metal surface depend strongly on the relative rates of Ni^{II} and Ni^{III} production in the interfacial region. Spatial variation in the corrosion behaviour is also accelerated because crystal growth requires nucleation.

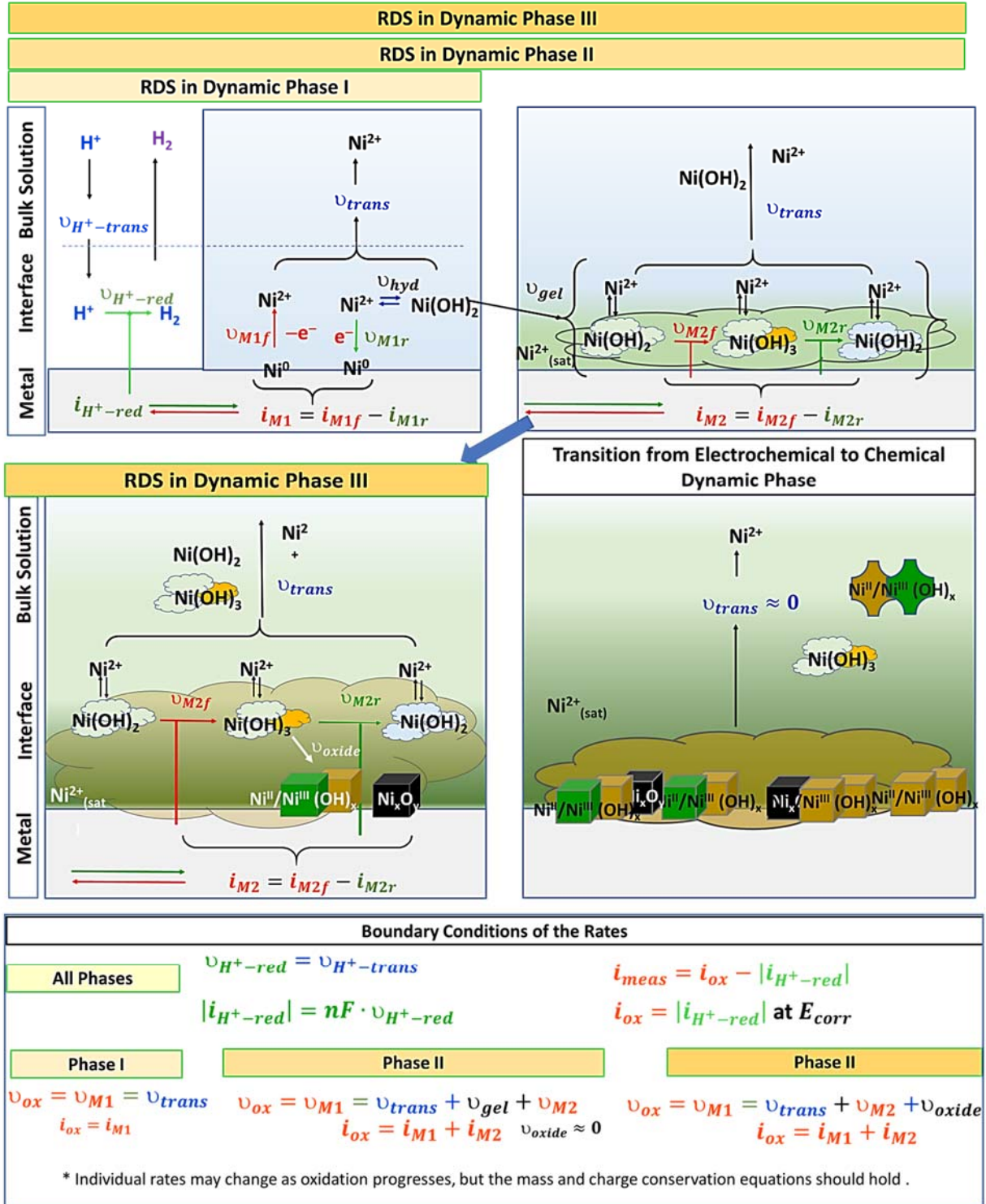


Figure 4.7: Schematic representation of the elementary steps occurring during Phase I, II and III. The elementary steps involve electron-metal atom transfer (M1f and M1r), ion diffusion (trans), hydrolysis (hyd), electron transfer (M2f) and (M2r), hydrogel formation (gel) and oxide crystal growth (oxide growth).

The different effects of a solution parameter (such as pH) on the corrosion behaviour in corrosion environments with other varying parameters (such as temperature, oxidant concentration, ionic strength) can then be rationalized by how the different solution parameters influence the kinetics of the elementary steps, and thus how far metal oxidation can progress and how fast it can move through the different dynamic phases.

For example, at pH 6.0 in a less oxidizing environment (without radiation present), E_{corr} quickly rose through R1 into R2 and remained in R2 for the rest of test duration; $|i_{meas-PS}|$ decreased with \sqrt{t} independent of E_{elec} in R2 under potentiostatic polarization; the log $|i_{meas-CV}|$ vs E_{elec} relationships on the forward and reverse CV scans were similar (small hysteresis due to change in $(a_{Ni^{2+}})_{int}$) when the upper vertex potential was in R2; and the anodic Tafel slope in R2 on the forward scan was 82 mV/dec, independent of vertex potential and cycling. These observations indicate that at this pH, metal oxidation does not progress beyond Dynamic Phase I.

At pH 8.4, E_{corr} moved through R1 and R2 into R3 in 2 h, and at pH 10.6 E_{corr} reached R3 in a very short time (< 150 s). These observations further support the claim that pH does not affect the potential dependence of the rates of (M1f) and (M1r), but the overall rate of Ni^{2+} removal from the interfacial region via (trans) and (hyd). Increasing pH lowers the Ni^{2+} saturation limit, and the metal oxidation system reaches Dynamic Phase II at earlier times.

In Ar-purged, high I_s solution without radiation present, metal oxidation at pH 8.4 progresses only to Phase II and the final steady-state E_{corr} approaches $E_{Ni^0 \rightleftharpoons Ni(OH)_3}^{eq}$. At pH 10.6, metal oxidation progresses beyond the formation of mixed Ni^{II}/Ni^{III} hydroxide and into Dynamic Phase III.

More oxidizing environments such as that obtained under irradiation accelerate the progression of metal oxidation through the different dynamic phases mainly because they increase $|i_{\text{red}}(t)|$ and hence the rates of (M1) and (M2). The increase in (M1) and (M2) induces faster saturation and earlier formation of hydrogel and oxide growth, which can quickly suppress (M1) and (M2). Hence, γ -radiation or aeration may increase the corrosion rate in the early stages of corrosion but may reduce the overall corrosion damage over longer durations.

On the other hand, gas-purging, electrode rotation or ionic strength affect the rate of Ni^{2+} transport from the interfacial region to the bulk solution. Depending on their effects on the relative rates of (trans) versus (gel) and (oxide), their effects can be very different at different pHs. For example, as discussed in more detail in Chapter 5, I_s has a significant effect on overall metal oxidation at pH 6.0 but a negligible effect at pH 10.6. At pH 10.6, the rate of (trans) is already suppressed in the early stages of corrosion and hence, I_s has no further effect on the overall metal oxidation rate.

4.4. CONCLUSIONS

In this chapter the oxidation kinetics of Ni metal as a function of solution reaction and transport parameters were investigated using electrochemical techniques. The evolution of the elementary reactions and mass transfer/transport steps that control the overall metal oxidation rate was investigated using corrosion potential measurements and current vs potential relationships under potentiodynamic and potentiostatic conditions. The solution parameters investigated were pH, ionic strength, temperature, and γ -radiation. Different solution parameters affect the kinetics of the elementary steps

differently, which alters metal oxidation pathways and overall oxidation rates. The pH of the solution can affect the rate and yield of electron/metal atom transfer, as well as hydrolysis and metal hydroxide precipitation. Temperature has a minor effect on interfacial charge transfer but can increase the rate of thermal processes. Ionic strength affects ion mobility through its effect on concentration gradients, and therefore an increase in ionic strength increases the rate of metal cation transport from the interface to the bulk solution.

The corrosion potential (E_{corr}) measurements performed under specific solution conditions have shown that E_{corr} does not stay at the initial (pseudo-) steady state but evolves to a different steady state(s) as metal oxidation progresses and metal oxidation products accumulate and undergo reactions. The number of steady states that the metal oxidation system passes through before reaching the final steady state, the durations of the steady states, and the steady-state values depend on solution parameters. Although $E_{corr}(t)$ evolves very differently depending on the solution parameters, the E_{corr} values at the steady (or slow-changing) states coincide with one of the E_{rxn}^{eq} of the half-reactions involving metal hydroxides, or the midpoint between two of the E_{rxn}^{eq} values. In a given solution redox environment, pH affects both the initial and final steady state E_{corr} , whereas temperature has a negligible effect on the initial E_{corr} but a more significant effect on the final E_{corr} . The transitions from the initial to the intermediate, and to the final steady state occurred earlier at higher pHs and at a higher temperature. In the presence of radiation, the transition from one steady state to another occurs earlier and more steady states are observed.

The $|i_{meas-CV}|$ vs E_{elec} relationship observed during CV scans with different vertex potentials, and the time-dependent behaviour of $|i_{meas-PS}|$ at various E_{elec} under potentiostatic polarization, have shown that because electrochemical metal oxidation involves interfacial transfer of not only electrons but also metal atoms, the overall metal oxidation progresses evolve through different dynamic phases consisting of different elementary rate-determining steps (RDS) as the oxidation products accumulate in the interfacial region and undergo their own electrochemical and chemical reactions. These measurements have shown the contribution of nickel hydroxides to the dynamics of metal oxidation, demonstrating a transition in the rate dependence on diffusion at lower E_{elec} to Ni^{II}/Ni^{III} hydroxide formation at higher E_{elec} , which limited the diffusion of Ni^{II}.

The results show that the overall nickel oxidation dynamics evolve through different dynamic phases (or dynamic states) as corrosion progresses. Dynamic state refers to the ranges of electrochemical/chemical conditions under which the overall metal oxidation rate may change but the elementary (rate-determining) steps that comprise the overall process, and the (pseudo-) 1st-order rate coefficients of the individual steps, do not change within the state. In Dynamic Phase I the elementary steps that control the overall metal oxidation rate are the net electron/metal atom transfer at the metal-solution boundary ($Ni^0_{(m)} \rightleftharpoons Ni^{2+}_{(solv)} + 2 e^-$), and diffusion of Ni²⁺ from the interfacial region into the bulk solution, and hydrolysis of Ni²⁺ to produce Ni(OH)₂ that can condense as colloids. Dynamic Phase II represents the dynamic state of metal oxidation, at which not only the elementary steps that comprise Dynamic Phase I, but also additional elementary steps involving Ni²⁺ hydrolysis product, Ni(OH)₂. The additional steps include interfacial electron transfer ($Ni^{2+}/Ni(OH)_2 + OH^- \rightleftharpoons Ni(OH)_3 + e^-$) that accelerates the precipitation

of mixed $\text{Ni}^{\text{II}}/\text{Ni}^{\text{III}}$ hydroxide growing a hydrogel network. In this phase, the kinetics of the elementary steps are strongly coupled, and describing the overall metal oxidation dynamics as a function of the independent kinetics of individual steps based on linear dynamics is not appropriate

Dynamic Phase III occurs after sufficient mixed $\text{Ni}^{\text{II}}/\text{Ni}^{\text{III}}$ hydroxide colloids have precipitated to allow nucleation and growth as solid crystalline particles on the surface. In this dynamic phase, metal oxidation is generally suppressed by the growth of oxide on the metal surface. The type, morphology and size of oxide that grows depends strongly on the relative rates of Ni^{II} and Ni^{III} production in the interfacial region.

This study has shown that the influence of one solution parameter (e.g., pH) on metal oxidation is dependent on other parameters (e.g., temperature and redox environment induced by radiolysis). The synergistic effect of different solution parameters on metal oxidation arises because each elementary reaction or mass transport step has its own unique kinetic behaviour and different solution parameters influence the kinetics of individual steps differently. Because the later reactions of initial and intermediate products can affect the kinetics of preceding steps, systemic feedback between different elementary steps can be established at later times leading to an acceleration or deceleration of the overall metal oxidation. Hence, it is the combination of solution parameters that dictates how fast the system can transition through different dynamic phases, and which final dynamic phase the overall metal oxidation process can reach.

4.5. REFERENCES

- [1] E. Chajduk, A. Bojanowska-Czajka, Corrosion mitigation in coolant systems in nuclear power plants, *Prog. Nucl. Energy.* 88 (2016) 1–9.
<https://doi.org/10.1016/j.pnucene.2015.11.011>.
- [2] A.Y. Musa, J.C. Wren, Combined effect of gamma-radiation and pH on corrosion of Ni-Cr-Fe alloy inconel 600, *Corros. Sci.* 109 (2016) 1–12.
<https://doi.org/10.1016/j.corsci.2016.03.015>.
- [3] L. Marchetti, S. Perrin, F. Jambon, M. Pijolat, Corrosion of nickel-base alloys in primary medium of pressurized water reactors: New insights on the oxide growth mechanisms and kinetic modelling, *Corros. Sci.* 102 (2016) 24–35.
<https://doi.org/10.1016/j.corsci.2015.09.001>.
- [4] M. Behazin, J.J. Noël, J.C. Wren, Combined effects of pH and γ -irradiation on the corrosion of Co-Cr alloy stellite-6, *Electrochim. Acta.* 134 (2014) 399–410.
<https://doi.org/10.1016/j.electacta.2014.04.079>.
- [5] M. Momeni, M. Behazin, J.C. Wren, Mass and Charge Balance (MCB) Model Simulations of Current, Oxide Growth and Dissolution during Corrosion of Co-Cr Alloy Stellite-6, *J. Electrochem. Soc.* 163 (2016) C94–C105.
<https://doi.org/10.1149/2.0721603jes>.
- [6] R.P. Morco, A.Y. Musa, M. Momeni, J.C. Wren, Corrosion of carbon steel in the [P14666][Br] ionic liquid: The effects of γ -radiation and cover gas, *Corros. Sci.* 102 (2016) 1–15. <https://doi.org/10.1016/j.corsci.2015.06.027>.
- [7] M. Momeni, J.C. Wren, A mechanistic model for oxide growth and dissolution during corrosion of Cr-containing alloys, *Faraday Discuss.* 180 (2015) 113–135.
<https://doi.org/10.1039/c4fd00244j>.
- [8] J.C. Wren, Steady-state radiolysis: Effects of dissolved additives, *ACS Symp. Ser.* 1046 (2010) 271–295. <https://doi.org/10.1021/bk-2010-1046.ch022>.
- [9] M. Li, Galvanic Corrosion of Carbon Steel-Stainless Steel Welds, *Electron. Thesis Diss. Repos.* 7162, Univ. West. Ontario. (2020).
- [10] D. Guo, M. Li, J.M. Joseph, J.C. Wren, A New Method for Corrosion Current Measurement: the Dual-Electrochemical Cell (DEC), *J. Electrochem. Soc.* 167 (2020) 111505–111604. <https://doi.org/10.1149/1945-7111/aba6c8>.

- [11] D. Guo, Corrosion Dynamics of Carbon Steel in Used Fuel Container Environments, Electron. Thesis Diss. Repos. 5897, University of Western Ontario (2018).
- [12] Y.G. Shin, Nonlinear Dynamics of Carbon Steel Corrosion under Gamma Radiation, Electron. Thesis Diss. Repos. 7339, University of Western Ontario (2020).
- [13] A.M. Jean, Evolution of Cu₂O Morphology During Copper Corrosion in the Presence of Gamma-Radiation, Electron. Thesis Diss. Repos. 4593, University of Western Ontario (2017).
- [14] I.R. Epstein, and J.A. Pojman., An Introduction To Nonlinear Chemical Dynamics: Oscillations, Waves, Patterns, And Chaos, Oxford University Press, 1998.
- [15] H. Strathmann, Electromembrane Processes: Basic Aspects and Applications, in: Compr. Membr. Sci. Eng., Elsevier, 2017 <https://doi.org/10.1016/b978-0-12-409547-2.12257-7>.
- [16] J. Owen, Ionic Conductivity, in: Compr. Polym. Sci. Suppl., Pergamon Press, 1989.
- [17] J.E. Saiers, G.M. Hornberger, The influence of ionic strength on the facilitated transport of cesium by kaolinite colloids, Water Resour. Res. 35 (1999) 1713–1727. <https://doi.org/10.1029/1999WR900055>.
- [18] J.E. Saiers, J.J. Lenhart, Ionic-strength effects on colloid transport and interfacial reactions in partially saturated porous media, Water Resour. Res. 39 (2003). <https://doi.org/10.1029/2002WR001887>.
- [19] L.M. Alrehaily, J.M. Joseph, M.C. Biesinger, D.A. Guzonas, J.C. Wren, Gamma-radiolysis-assisted cobalt oxide nanoparticle formation, Phys. Chem. Chem. Phys. 15 (2013) 1014–1024. <https://doi.org/10.1039/c2cp43094k>.
- [20] R.P. Morco, Radiolysis Kinetics and Its Role in the Overall Dynamics of Materials Degradation, Electron. Thesis Diss. Repos. 7248, University of Western Ontario (2020).
- [21] M. Behazin, Radiation Induced Corrosion of Stellite-6, Electron. Thesis Diss. Repos. 2432, University of Western Ontario (2014).

- [22] A. J. Bard Larry R., Faulkner, *Electrochemical Methods Fundamentals and Applications*, Wiley, 2001.
- [23] B.B. McCleskey, K.K. Nordstrom, J.N. Ryan, Comparison of electrical conductivity calculation methods for natural waters, *Limnol. Oceanogr. Methods*. 10 (2012) 952–967. <https://doi.org/10.4319/lom.2012.10.952>.
- [24] A.Y. Musa, M. Behazin, J.C. Wren, Potentiostatic Oxide Growth Kinetics on Ni-Cr and Co-Cr Alloys: Potential and pH Dependences, *Electrochim. Acta*. 162 (2015) 185–197. <https://doi.org/10.1016/j.electacta.2015.02.176>.
- [25] J. Wang, J. Wang, E.H. Han, Influence of Conductivity on Corrosion Behavior of 304 Stainless Steel in High Temperature Aqueous Environment, *J. Mater. Sci. Technol.* 32 (2016) 333–340. <https://doi.org/10.1016/j.jmst.2015.12.008>.
- [26] Nestor Perez, *Electrochemistry and Corrosion Science*, KluwerAcademic Publishers, 2004.
- [27] S. El Wakkae, T.M. Salem, Oxide Film Formation on the Surface of Metals in Aqueous Solutions and the Evaluation of their Standard Potentials. II Themercuryelectrode, *J. Phys. Colloid Chem.* 54 (1950) 1371–1383. <https://doi.org/10.1021/j150483a013>.
- [28] R.S. McEwen, Crystallographic studies on nickel hydroxide and the higher nickel oxides, *J. Phys. Chem.* 75 (1971) 1782–1789. <https://doi.org/10.1021/j100681a004>.
- [29] P. Taylor, Ostwald ripening in emulsions, *Adv. Colloid Interface Sci.* 75 (1998) 107–163.
- [30] J.H. Yao, K.R. Elder, H. Guo, M. Grant, Theory and simulation of Ostwald ripening, *Phys. Rev.* 47 (1993) 14110–14125. <https://doi.org/10.1103/PhysRevB.47.14110>.
- [31] S. V. Mattigod, D. Rai, A.R. Felmy, L. Rao, Solubility and solubility product of crystalline Ni(OH)₂, *J. Solution Chem.* 26 (1997) 391–403. <https://doi.org/10.1007/BF02767678>.
- [32] C.F. Baes, R.E. Mesmer, *Hydrolysis of Cations*, Wiley, 1976.
- [33] B. Beverskog, I. Puigdomenech, Revised Pourbaix diagrams for nickel at 25–300°C, *Corros. Sci.* 39 (1997) 969–980. <https://doi.org/10.1016/S0010->

938X(97)00002-4.

- [34] Noel de Nevers, *Physical and Chemical Equilibrium for Chemical Engineers*, Wiley, 2012.
- [35] M. Okuyama, S. Haruyama, Passive film formed on nickel in a neutral solution, *Corros. Sci.* 14 (1974) 1–14. [https://doi.org/10.1016/S0010-938X\(74\)80003-X](https://doi.org/10.1016/S0010-938X(74)80003-X).
- [36] T.S. De Gromoboy, L.L. Shreir, The formation of nickel oxides during the passivation of nickel in relation to the potential/pH diagram, *Electrochim. Acta.* 11 (1966) 895–904. [https://doi.org/10.1016/0013-4686\(66\)87066-4](https://doi.org/10.1016/0013-4686(66)87066-4).
- [37] K. Kakaei, M.D. Esrafil, A. Ehsani, Graphene and Anticorrosive Properties, in: *Graphene Surfaces*, 1st ed., Academic Press, 2019: pp. 303–337. <https://doi.org/10.1016/B978-0-12-814523-4.00008-3>.
- [38] V. Pacáková, K. Štulík, *Encyclopedia of Analytical Science*, Elsevier, 2005.
- [39] L.M. Alrehaily, J.M. Joseph, J.C. Wren, Radiation-induced formation of Co_3O_4 nanoparticles from $\text{Co}^{2+}(\text{aq})$: Probing the kinetics using radical scavengers, *Phys. Chem. Chem. Phys.* 17 (2015) 24138–24150. <https://doi.org/10.1039/c5cp02828k>.
- [40] L.M. Alrehaily, J.M. Joseph, A.Y. Musa, D.A. Guzonas, J.C. Wren, Gamma-radiation induced formation of chromium oxide nanoparticles from dissolved dichromate, *Phys. Chem. Chem. Phys.* 15 (2013) 98–107. <https://doi.org/10.1039/c2cp43150e>.

CHAPTER 5

COMBINED EFFECT OF pH AND IONIC STRENGTH ON NICKEL OXIDATION

5.1. INTRODUCTION

Nickel is an important material with widespread use in a variety of applications in science and engineering [1–5]. One important application of nickel is its use as the main component in many nickel-based super alloys with superior corrosion resistance and mechanical properties [6,7]. Due to the important role that nickel plays in the corrosion resistivity of nickel-based alloys it is important to have a fundamental understanding of the corrosion behaviour of nickel metal to develop a predictive corrosion model.

Corrosion is an electrochemical process typically involving a series of elementary processes which include net electron transfer between the redox pair, solution reactions, metal ion dissolution, transport processes and oxide formation. It is known that the rate of corrosion is significantly affected by solution conditions such as solution chemistry, pH, temperature, ionic strength [8,9]. To develop a model that can predict the overall rate of nickel corrosion as a function of solution conditions, it is essential to identify the

rate and flux equations and the effect of solution environment on individual elementary processes [10].

The previous study presented in Chapter 4 has shown that under specific solution conditions E_{corr} does not stay at the initial (pseudo-) steady state but evolves to a different steady state(s) as metal oxidation progresses and metal oxidation products accumulate and undergo reactions. Although $E_{corr}(t)$ evolves very differently depending on the solution parameters, the E_{corr} values at the steady (or slow-changing) states coincide with one of the E_{rxn}^{eq} of the half-reactions involving metal hydroxides, or the midpoint between two of the E_{rxn}^{eq} values. In a given solution redox environment, pH affects both the initial and final steady state E_{corr} , whereas temperature has a negligible effect on the initial E_{corr} but a more significant effect on the final E_{corr} . The transitions from the initial to the intermediate and to the final steady state occurred earlier at higher pHs and at higher temperatures.

Based on the $|i_{meas-CV}|$ vs E_{elec} relationship observed during cyclic voltammetry (CV) with different vertex potentials, and the time-dependent behaviours of $|i_{meas-PS}|$ at various E_{elec} under potentiostatic polarization, the previous study has concluded that because electrochemical metal oxidation involves interfacial transfer of not only electrons but also metal atoms, the overall metal oxidation progresses through different dynamic phases. The elementary rate-determining steps (RDS) that control the overall metal oxidation rate evolve as the oxidation products accumulate in the interfacial region and undergo their own electrochemical and chemical reactions. These RDS are summarized in **Table 4.1** and are reproduced here in **Table 5.1**. The RDS and the relationships

between the kinetics of individual steps of the dynamic phases are schematically shown in **Figure 4.7** and are reproduced here in **Figure 5.1**.

The previous study has shown that the effect of one solution parameter (e.g., pH) on metal oxidation depends on other parameters (e.g., temperature and redox environment induced by radiolysis). The synergistic effect of different solution parameters on metal oxidation arises because each elementary reaction or mass transport step has its own unique kinetic behaviour and different solution parameters influence the kinetics of individual steps differently. For example, interfacial charge transfer steps (M1) and (M2) in **Table 5.1** depends on overpotential η_{rxn} ($= E_{elec} - E_{rxn}^{eq}$) and the chemical activities (concentrations) of the redox pairs in the interfacial region. On the other hand, Ni^{2+} transport step (trans) does not depend on η_{rxn} or Ni^{2+} concentration, but (trans) depends on ion diffusion rate coefficient and concentration gradient. Temperature has a negligible effect on the net rate of (M1) or (M2) but a significant effect on the rate of a solution chemical process with high activation energy.

Because the later reactions of initial and intermediate products can affect the kinetics of preceding steps, systemic feedback between different elementary steps can be established at later times leading to an acceleration or deceleration of the overall metal oxidation. Hence, it is the combination of solution parameters that dictates how fast it can transition through different dynamic phases, and which final dynamic phase the overall metal oxidation process can reach.

In this chapter, the combined effect of pH and ionic strength (I_s) on the evolution of Ni oxidation in Ar-purged solution at 80 °C is investigated. It has been well recognized

that the ionic strength of a solution can have a strong effect on double-layer thickness and hence, the electrical **potential** gradient at the electrode-solution interface [11–13], and on the ionic conductivity of the solution and hence, the electrode reaction **kinetics** [9,14–16].

The ionic strength (I_s) of a solution, which is a measure of the concentration of ions in that solution, affects the mobility (μ_j) of ion j in the presence of electric potential gradient (V). For an ideal system, $I_s = \frac{1}{2} \cdot \sum c_j \cdot z_j^2$ where c_j and z_j represent the concentration and charge of ion j , respectively. The Debye length which is characteristic of double layer thickness (δ_{dl}) is inversely proportional to the square root of the ionic strength; $\delta_{dl} \propto 1/\sqrt{I_s}$ [11]. For a solution containing non-interacting ions, the molar ion mobility is related to ionic conductivity (κ_j), or the inverse of solution resistance by $\kappa_j = F \cdot \sum (c_j \cdot z_j \cdot \mu_j)$ where e is the charge of electron, and the ionic strength of a solution is directly related to that [17,18].

The electrochemical redox reactions that occur on corroding metal surface are metal oxidation half-reaction(s) and oxidant reduction redox half-reaction(s). One of the redox species (either reactant or product) involved in individual elementary half-reactions is ionic species (Ni^{2+} and H^+ , respectively, in this study). The overall rate of each elementary half-reaction depends on both the kinetics of interfacial electron transfer at the surface and the transport of the redox active species from the surface to the bulk solution or vice versa. Hence, I_s can affect corrosion rate not only via its influence on the double layer thickness, but more so via its effect on the transport of Ni^{2+} and H^+ .

Table 5.1: Elementary Reactions Involved in the Overall Metal Oxidation Process

Rxn ID	Reaction Type	Chemical Equation	Rate ID
M1	Electron/metal-atom transfer	$\text{Ni}^0 _{\text{int}} \rightleftharpoons \text{Ni}^{2+} _{\text{int}} + 2 e^-$	$\frac{\nu_{\text{M1}}}{i_{\text{M1}}} = nF \cdot \nu_{\text{M1}}$
	<p>This is a reversible process, consisting of two reaction steps ($\nu_{\text{M1}} = \nu_{\text{M1f}} - \nu_{\text{M1r}}$):</p> <p>(M1f): $\text{Ni}^0 \rightarrow \text{Ni}^{2+} + 2 e^-$ $\nu_{\text{M1f}} = k_{\text{M1f}} \cdot (a_{\text{Ni}^0})_{\text{int}} \approx k_{\text{M1f}}$</p> <p>(M1r): $\text{Ni}^{2+} + 2 e^- \rightarrow \text{Ni}^0$ $\nu_{\text{M1r}} = k_{\text{M1r}} \cdot (a_{\text{Ni}^{2+}})_{\text{int}}$</p> <p>where $(a_{\text{Ni}^{2+}})_{\text{int}}$ represents the chemical activity of Ni^{2+} in the interfacial region.</p>		
trans	Ion diffusion	$\text{Ni}^{2+} _{\text{int}} \rightarrow \text{Ni}^{2+} _{\text{bulk}}$	ν_{trans}
M2	Electron transfer	$\text{Ni}^{2+}/\text{Ni}(\text{OH})_2 + \text{OH}^- \rightleftharpoons \text{Ni}(\text{OH})_3 + e^-$	$\frac{\nu_{\text{M2}}}{i_{\text{M2}}} = nF \cdot \nu_{\text{M2}}$
	<p>This is a reversible process, consisting of two reaction steps ($\nu_{\text{M2}} = \nu_{\text{M2f}} - \nu_{\text{M2r}}$):</p> <p>(M2f): $\text{Ni}^{2+}/\text{Ni}(\text{OH})_2 + \text{OH}^- \rightarrow \text{Ni}(\text{OH})_3 + e^-$ $\nu_{\text{M2f}} \approx k_{\text{M2f}} \cdot (a_{\text{Ni}^{\text{II}}})_{\text{int}}$</p> <p>(M2r): $\text{Ni}(\text{OH})_3 + e^- \rightarrow \text{Ni}^{2+}/\text{Ni}(\text{OH})_2 + \text{OH}^-$ $\nu_{\text{M2r}} = k_{\text{M2r}} \cdot (a_{\text{Ni}^{\text{III}}})_{\text{int}}$</p> <p>where $(a_{\text{Ni}^{\text{II}}})_{\text{int}}$ and $(a_{\text{Ni}^{\text{III}}})_{\text{int}}$ represent the overall redox activities of Ni^{II} and Ni^{III} species (dissolved and colloidal) in the interfacial region.</p>		
hyd	Hydrolysis	$\text{Ni}^{2+} + n \text{OH}^- \rightleftharpoons \text{Ni}(\text{OH})_x^{2-x} + (n-x) \text{OH}^-$	ν_{hyd}
gel	Hydrogel formation	$\text{Ni}(\text{OH})_2 + \text{Ni}(\text{OH})_3 \rightarrow x\text{Ni}(\text{OH})_2 \cdot y\text{Ni}(\text{OH})_3(\text{gel})$	ν_{gel}
oxide	Crystalline oxide growth	$\text{Ni}(\text{OH})_2 \cdot 2\text{Ni}(\text{OH})_3(\text{gel}) \rightarrow \text{Ni}_3\text{O}_4(\text{cryst}) + 4 \text{H}_2\text{O}$	ν_{oxide}

To determine the effect of I_s on nickel corrosion rate, various electrochemical analysis tests were conducted on high-purity Ni electrodes in solutions of two different ionic strengths at each pH studied, pH 6.0 or pH 10.6. The electrochemical analyses performed include (1) E_{corr} as a function of corrosion time (t_{corr}), potentiodynamic (PD) polarization to obtain the $|i_{meas-PD}|$ vs E_{elec} relationship on electrodes corroded for different t_{corr} , (3) multiple cycles of CV with different vertex potentials to obtain the $|i_{meas-CV}|$ vs E_{elec} relationship, and (4) measurements of the $|i_{meas-PS}|$ as a function of time at various E_{elec} under potentiostatic (PS) polarization conditions.

These measurements were complemented by performing corrosion tests using nickel coupons immersed in solutions in sealed quartz vials and post-test dissolved metal analysis using ICP-OES.

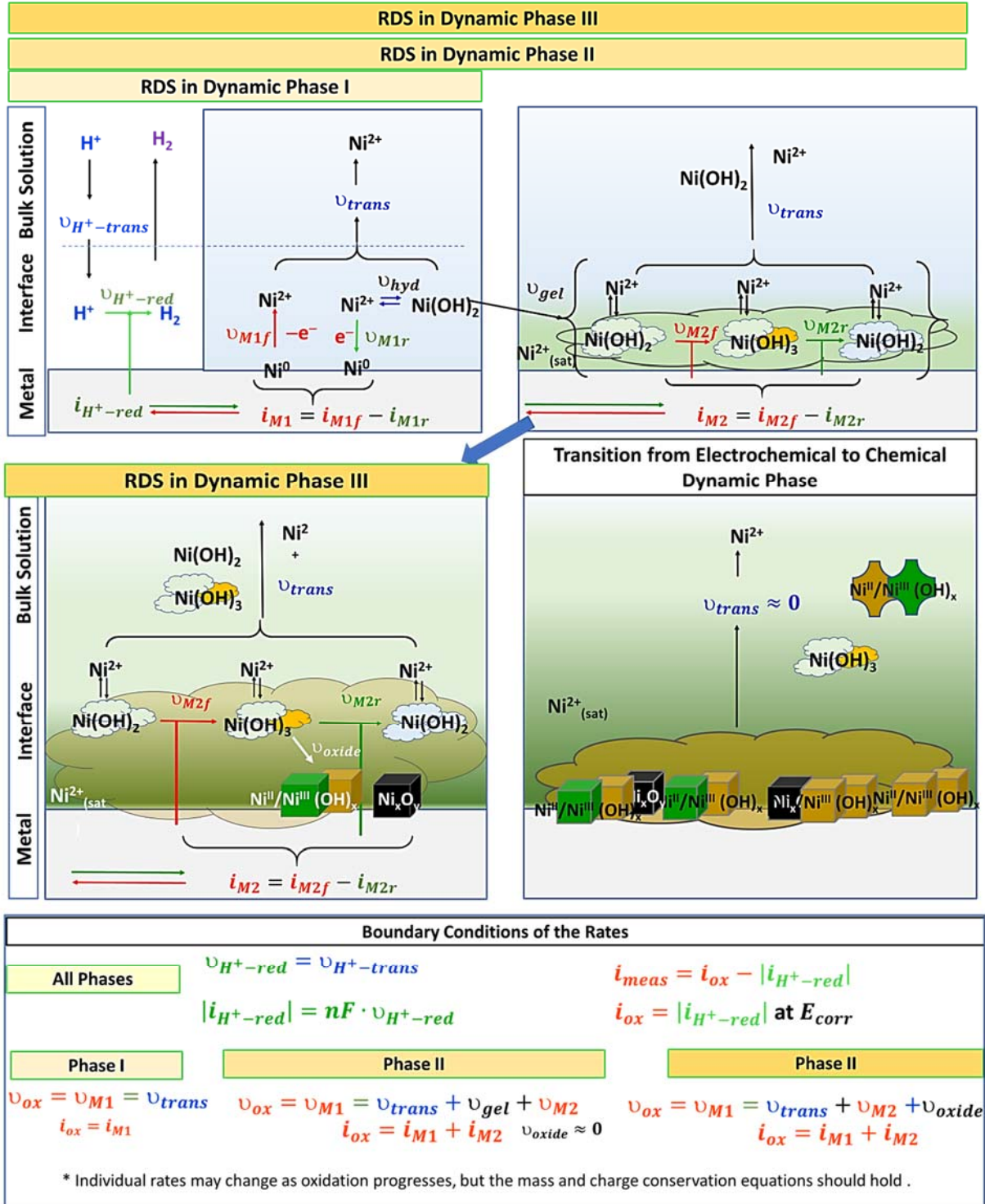


Figure 5.1: Schematic representation of the elementary steps occurring during Phase I, II, and III. The elementary steps involve electron-metal atom transfer (M1f and M1r), ion diffusion (trans), hydrolysis (hyd), electron transfer (M2f) and (M2r), hydrogel formation (gel) and oxide crystal growth (oxide growth).

5.2. EXPERIMENTAL

The experimental procedures used in this thesis are described fully in Chapter 3; however, a brief description is provided in this section. A pure Ni rod 0.620 cm in diameter was cut into circular, flat, 3 mm thick coupons. Only one circular face of the samples with a surface area of 0.302 cm² was exposed to the solution in electrochemical experiments and total surface area of 1.187 cm² were exposed to the solution in coupon exposure tests. Prior to each experiment, the flat electrode surfaces were polished (using a series of silicon carbide papers and mirror-polished on a Texmet microcloth (Buehler) with the 1 μm MetaDi Supreme diamond paste suspension as described in Chapter 3), cleaned with deionized water (Type 1 water) and dried under argon gas.

All experiments were conducted in argon-purged buffer solutions at pH 6.0 and pH 10.6 with two different ionic strengths. At pH 6.0, the ionic strength of the ‘high I_s ’ and ‘low I_s ’ solutions were 20 mM and 6.8 μM and their measured ionic conductivities were 1300 μS·cm⁻¹ and 12 μS·cm⁻¹, respectively. At pH 10.6, the ionic strength of the ‘high I_s ’ and ‘low I_s ’ solutions were 39 mM and 1.0 mM and the corresponding conductivities were 2300 μS·cm⁻¹ and 40 μS·cm⁻¹. All solutions were prepared using Type 1 water (purified using a NANO pure Diamond UV ultra-pure water system from Barnstead International) with a resistivity of 18.2 MΩ·cm. Solutions were prepared using sodium borate (Na₂B₄O₇·10H₂O) for high I_s , boric acid (H₃BO₃) for low I_s , and adjusted pH with boric acid (H₃BO₃) and sodium hydroxide (NaOH), all purchased from Caledon Laboratories Ltd.

In this chapter, a series of electrochemical analyses and coupon exposure tests were performed on nickel. Electrochemical analyses include (1) measurement of E_{corr} as

a function of corrosion time (t_{corr}) for 24 h, (2) potentiodynamic (PD) polarization on electrodes corroded for different t_{corr} , (3) multiple cycles of CV with different vertex potentials to obtain the $|i_{meas-CV}|$ vs E_{elec} relationship, and (4) measurements of the $|i_{meas-PS}|$ as a function of time at various E_{elec} under potentiostatic (PS) polarization conditions.

A dual walled three-compartment electrochemical cell, made of Pyrex glass, was used for all the electrochemical experiments at 80 °C. Ni samples were used as the working electrode (WE), platinum mesh (Alfa Aesar, 99.9% purity) served as the counter electrode (CE), and the reference electrode (RE) used was a silver-silver chloride electrode (Ag/AgCl-Sat. KCl, Fisher Scientific). For all experiments the electrolyte solution was Ar-purged for 1 hour prior to the experiment and purging continued throughout the test duration. The temperature of the test solution was maintained at 80 °C by circulating heated water through the dual walled electrochemical cell. A water bath with thermostat control (Fisher Scientific) was used to control the temperature.

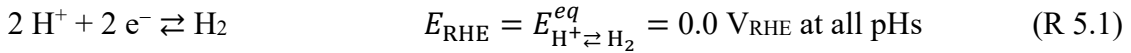
For the coupon exposure tests, the test vials were prepared in an Ar-filled glove box. The freshly polished coupons were placed in individual Pyrex/quartz vials and both sides of the coupon with a total surface area of 1.187 cm² were exposed to the test solution. The Ar-purged test solutions were added to each vial and the vials were sealed using aluminum crimp caps fitted with PTFE silicone septa (Agilent Technologies). The crimp caps provided a vacuum seal to prevent solution evaporation and any ingress/egress of gas during the test duration. The sample vials were then placed in a 300 mL AISI 316 stainless steel autoclave and heated to 80 °C.

5.3. RESULTS AND DISCUSSION

5.3.1. Time-Dependent Behaviour of E_{corr}

The time-dependent behaviours of E_{corr} observed for Ni corrosion in two different I_s solutions at pH 6.0 and pH 10.6 are compared with the equilibrium potentials of nickel redox half-reactions (E_{rxn}^{eq}) in **Figure 5.2**. Also presented in the figure are the E_{elec} vs $\log|i_{meas-PD}|$ plots obtained during potentiodynamic (PD) scans performed after corrosion over different durations (t_{corr}), where $|i_{meas-PD}|$ represents the current measured during PD polarization.

As described in Chapter 4, to compare the results obtained at different pHs, all potentials (E_{corr} , E_{rxn}^{eq} and E_{elec}) are presented on the V_{RHE} scale which uses the reversible hydrogen electrode (RHE) potential (E_{RHE}) as a reference potential.



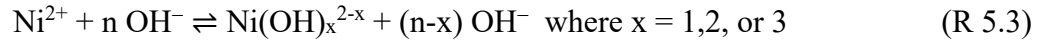
Note that the RHE potential of 0.0 V_{RHE} is for the chemical activity of H_2 at its standard state. That is, dissolved H_2 is in partitioning equilibrium with gaseous H_2 ($\text{H}_{2(g)}$) at partial pressure of 1 atm (the standard state of H_2). The fraction of $\text{H}_{2(g)}$ in normal air is $\sim 0.6 \times 10^{-6}$, which yields the $E_{\text{H}^+ \rightleftharpoons \text{H}_2}^{eq}$ value to be 0.37 V_{RHE} at all pHs. The fraction of H_2 in the Ar gas used in this study was not available, but it should be less than the fraction in normal air. Hence, the $E_{\text{H}^+ \rightleftharpoons \text{H}_2}^{eq}$ value under the studied conditions should be higher than 0.37 V_{RHE} .

The difference in E_{corr} on the V_{RHE} scale directly correlates to the difference in overpotential (η_{rxn}) for half-reaction rxn , irrespective of pH.

In **Figure 5.2** only the E_{rxn}^{eq} of metal redox half-reactions involving Ni(OH)₂ and Ni(OH)₃, using 1.0 for their chemical (redox) activities. The $E_{Ni^0 \rightleftharpoons Ni^{2+}}^{eq}$ of the half-reaction involving solvated Ni²⁺ (R 5.2) is not shown because the chemical activity (~ concentration) of Ni²⁺ in the interfacial region, $(a_{Ni^{2+}})_{int}$, varies with time t and E_{elec} :



Nevertheless, $E_{Ni^0 \rightleftharpoons Ni^{2+}}^{eq}$ can be defined when $(a_{Ni^{2+}})_{int}$ is at its saturation limit as described in Chapter 4. Metal cation is in hydrolysis equilibrium and when it is at its saturation limit it is in phase-partitioning equilibrium with solid metal hydroxide [19–21]:



Due to the chemical equilibria, the redox half-reaction of Ni⁰ to Ni²⁺_(sat) is also at equilibrium when the oxidation half-reaction of Ni⁰ to Ni(OH)₂ is at equilibrium. Hence,

$$E_{Ni^0 \rightleftharpoons Ni^{2+}_{(sat)}}^{eq} = E_{Ni^0 \rightleftharpoons Ni(OH)_2}^{eq} \quad (R\ 5.5)$$

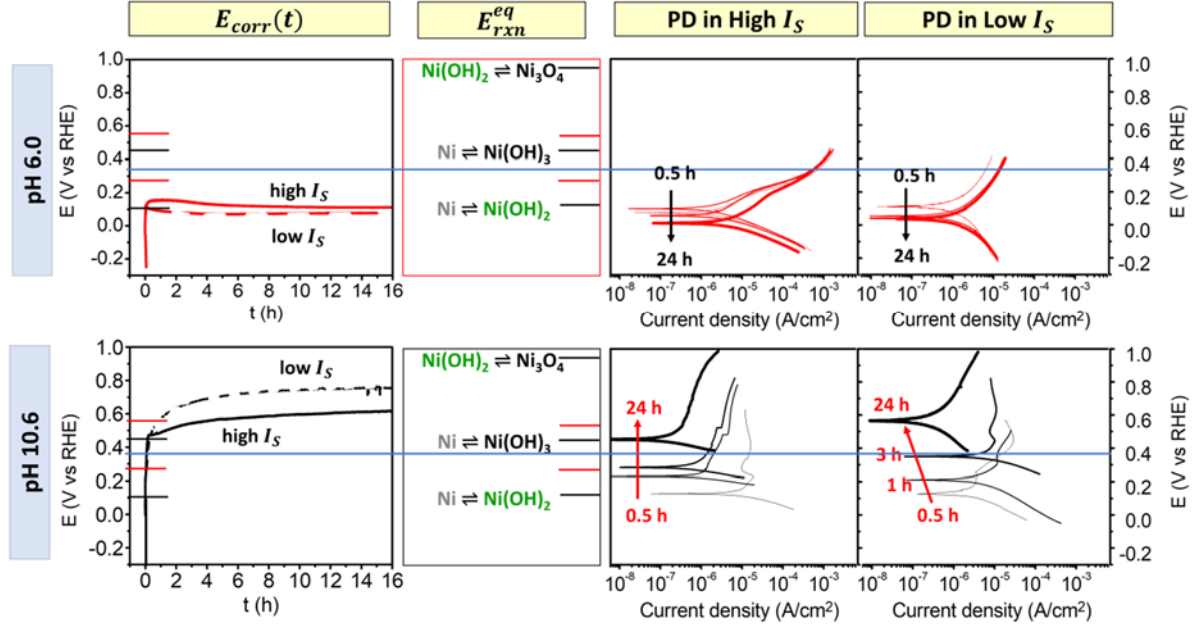


Figure 5.2: Time-dependent behaviours of E_{corr} and the $\log|i_{meas-PD}|$ vs E_{elec} relationship observed during potentiodynamic polarization. The measurements were conducted in Ar-purged solutions of different ionic strengths (I_S) at pH 6.0 and 10.6 at 80 °C. The PD scans were performed after 0.5, 1, 3 and 24-h corrosion. Also shown in the 2nd column are the equilibrium potentials of metal redox half-reactions (black bars) and mid-potentials, $E_{Ni^0 \rightleftharpoons Ni(OH)_2/Ni(OH)_3}^{mid}$ and $E_{Ni^0 \rightleftharpoons Ni(OH)_2/Ni_3O_4}^{mid}$ (see text). The blue line represents the $E_{H^+ \rightleftharpoons H_2}^{eq}$ at $P_{H_2} = 0.6 \times 10^{-6}$ atm. All potentials are on the V_{RHE} scale.

Figure 5.2 shows some unusual and unexpected effects of pH and I_S on time-dependent behaviours of E_{corr} and the $\log|i_{meas-PD}|$ vs E_{elec} relationship that are not normally discussed in corrosion literature. First the observed effects of pH and I_S on $E_{corr}(t)$ are discussed:

- Following the rapid increase in the first 2-3 min, E_{corr} increased more slowly with time. Hereafter, the E_{corr} value at the time when the slower increase in E_{corr}

begins will be referred to as the initial (pseudo-steady state) E_{corr} value ($E_{corr}(\tau_0)$).

- Under all different combinations of pH and I_s , $E_{corr}(\tau_0)$ did not show any systematic dependence on $E_{H^+ \rightleftharpoons H_2}^{eq}$. However, $E_{corr}(\tau_0)$ was higher than 0.0 V_{RHE} (i.e., E_{RHE}) but below 0.37 V_{RHE} (i.e., $E_{H^+ \rightleftharpoons H_2}^{eq}$ for $pH_2 \approx 0.6 \times 10^{-6}$ atm)
- Instead, $E_{corr}(\tau_0)$ coincided with one of the E_{rxn}^{eq} of metal redox half-reactions, $E_{Ni^0 \rightleftharpoons Ni(OH)_2}^{eq}$ at pH 6.0 and $E_{Ni^0 \rightleftharpoons Ni(OH)_3}^{eq}$ at pH 10.6. At pH 10.6, the rapid transition to $E_{corr}(\tau_0)$ occurred in a stepwise manner, with short breaks at $E_{Ni^0 \rightleftharpoons Ni(OH)_2}^{eq}$, and at the mid-potential between $E_{Ni^0 \rightleftharpoons Ni(OH)_2}^{eq}$ and $E_{Ni^0 \rightleftharpoons Ni(OH)_3}^{eq}$ (denoted as $E_{Ni^0 \rightleftharpoons Ni(OH)_2/Ni(OH)_3}^{mid}$ hereafter).
- I_s had a negligible effect on $E_{corr}(\tau_0)$ at each pH.
- pH also affected the progression of E_{corr} with t_{corr} . At pH 6.0, E_{corr} increased to a maximum or an intermediate steady state before decreasing to a final steady-state value slightly below or near $E_{Ni^0 \rightleftharpoons Ni(OH)_2}^{eq}$ in the high or low I_s solution, respectively. At pH 10.6, E_{corr} increased steadily but at a progressively slower rate, reaching a final steady state value near or slightly the mid-potential between $E_{Ni^0 \rightleftharpoons Ni(OH)_2}^{eq}$ and $E_{Ni(OH)_2 \rightleftharpoons Ni_3O_4}^{eq}$ (denoted as $E_{Ni^0 \rightleftharpoons Ni(OH)_2/Ni_3O_4}^{mid}$).
- I_s had a minor effect on the long-term behaviour of E_{corr} . Interestingly, the final E_{corr} reached was higher in the higher I_s solution at pH 6.0, while it was lower in the higher I_s solution at pH 10.6.

These results indicate that the $E_{corr(\tau_0)}$ at pH 6.0 $\approx E_{Ni^0 \rightleftharpoons Ni(OH)_2}^{eq}$ which is also equal to the $E_{Ni^0 \rightleftharpoons Ni^{2+}}^{eq}$ value when $[Ni^{2+}]_{int} = C_{sat}$, and $E_{corr(0)} \approx E_{Ni^0 \rightleftharpoons Ni(OH)_3}^{eq}$ at pH 10.6, while $E_{corr(\tau_0)}$ is below the $E_{H^+ \rightleftharpoons H_2}^{eq}$ value when $pH_2 \approx 0.6 \times 10^{-6}$ atm at both pHs. Hence, the oxidation of Ni^0 to $Ni(OH)_2$ or $Ni(OH)_3$ by H^+ (or H_2O) is possible in Ar-purged solution, even based only on electrochemical potential consideration. The combination of the irreversibility of proton reduction half-reaction and the entropy driven metal oxidation half-reaction allows metal oxidation in aqueous solution without other oxidant(s) present to occur, even when the electrode potential, E_{corr} or E_{elec} , is above $E_{H^+ \rightleftharpoons H_2}^{eq}$. Indeed, the final steady-state $E_{corr(\tau_f)}$ value at pH 10.6 was higher than $E_{H^+ \rightleftharpoons H_2}^{eq}$ and this is not due to metal oxidation by residual O_2 , but due to decrease in the overall metal oxidation half-reaction as more insoluble hydroxide/oxide grows on the metal surface.

The above discussion establishes that residual O_2 is not necessarily required for nickel oxidation under Ar-purging conditions or for the E_{corr} value to be higher than $E_{H^+ \rightleftharpoons H_2}^{eq}$, which is a rationale commonly provided for corrosion of a passive metal observed under deaerated conditions [22,23]. This does not mean that purging with Ar may not remove all the O_2 initially dissolved or the residual O_2 is not involved in nickel oxidation. The E_{corr} observed as a function of t_{corr} presented in **Figure 5.2** do not show any systematic dependence on pH. Instead, the $E_{corr(\tau_0)}$ and $E_{corr(\tau_f)}$ values coincided with one of the E_{rxn}^{eq} of metal redox half-reactions while their values varied with pH.

The observation that the E_{corr} on the V_{RHE} scale varied with pH was not expected. Increasing $[H^+]$ increases the net reduction current ($|i_{red}|$). However, this effect has been

considered by plotting E_{corr} on the V_{RHE} scale, which directly correlates to the overpotential for proton reduction ($|\eta_{H^+ \rightleftharpoons H_2}|$) when the bulk $[H^+]$ and pH_2 remain constant. Even if $[H^+]$ or H_2 transport to and from the metal surface influences the proton reduction rate (or current), the E_{corr} on the V_{RHE} scale should have a systematic dependence on pH. Similarly, we may not know the exact value for $|\eta_{O_2 \rightleftharpoons OH^-}|$, the E_{corr} on the V_{RHE} scale should not depend on pH when the bulk $[OH^-]$ and pO_2 remain constant.

What we observed was that E_{corr} progresses through one of the E_{rxn}^{eq} values of metal oxidation half-reactions in a semi stepwise manner. At pH 6.0, E_{corr} increased steadily to a value close to $E_{Ni^0 \rightleftharpoons Ni(OH)_2}^{eq}$ within 2-3 min and did not deviate significantly from the value for the rest of the test duration. At pH 10.6, E_{corr} increased stepwise with short breaks first at $E_{Ni^0 \rightleftharpoons Ni(OH)_2}^{eq}$ and then to $E_{Ni^0 \rightleftharpoons Ni(OH)_2/Ni(OH)_3}^{mid}$ before reaching $E_{Ni^0 \rightleftharpoons Ni(OH)_3}^{eq}$ even within 2-3 min, followed by more gradual increase to $E_{Ni^0 \rightleftharpoons Ni(OH)_2 \rightleftharpoons Ni_3O_4}^{mid}$. After reaching $E_{Ni^0 \rightleftharpoons Ni(OH)_2 \rightleftharpoons Ni_3O_4}^{mid}$, E_{corr} increased at a much slower rate for the rest of the test duration. Stepwise increases in E_{corr} could be more clearly seen at room temperature and/or under more oxidizing radiation conditions (Chapter 4). These observations indicate that the rate determining step (RDS) for the full redox reaction occurring on the metal electrode is the metal oxidation half-reaction and not the reduction of oxidants (H^+ and/or O_2) that are coupled with the metal oxidation, and that the overall metal oxidation evolves with time as the intermediate products accumulate and begin to react at appreciable rates.

In Chapter 4 and the current chapter it is observed that at given temperature and solution redox environment, E_{corr} reached the value of $E_{Ni^0 \rightleftharpoons Ni(OH)_2}^{eq}$ (or $E_{Ni^0 \rightleftharpoons Ni^{2+}}^{eq}$ when $[Ni^{2+}]_{int} = C_{sat}$) faster at a higher pH. These observations indicate that the time for $[Ni^{2+}]_{int}$ to reach C_{sat} is faster at a higher pH because of the smaller C_{sat} at a higher pH. The faster and earlier saturation of the interfacial region at a higher pH leads to faster and earlier precipitation of $Ni(OH)_2$, initially as colloids. When the colloid production is slow, the hydroxide colloids are easily dispersed into the bulk solution. Hence, at pH 6.0 once the interfacial region becomes saturated and the interfacial charge transfer reaction between Ni^0 and Ni^{2+} reaches (quasi-) equilibrium state, E_{corr} reaches a value close to $E_{Ni^0 \rightleftharpoons Ni(OH)_2}^{eq}$ and remains near the value.

When the colloid production is fast, colloids precipitate and aggregate on the metal surface, growing a loosely connected hydroxide network, known as hydrogel [24]. The loosely connected hydroxide nanoparticles form the (quasi-) stationary phase and the aqueous solution containing Ni^{2+} and OH^- forms the mobile phase in the hydrogel network. The chemical activity of Ni^{II} species in the hydrogel network in contact with the metal is ~ 1.0 . With this high activity Ni^{II} species can oxidize to Ni^{III} until the Ni^{II} and Ni^{III} species reach redox equilibrium. The faster and earlier production of $Ni(OH)_2$ also induces the faster and earlier production of less soluble $Ni(OH)_3$. The production of $Ni(OH)_3$ in the hydrogel network further stabilizes the stationary solid hydroxide phase in the hydrogel. Thus, the interfacial charge transfer reaction between Ni^0 and Ni^{2+} reaches (quasi-) equilibrium state earlier, E_{corr} reaches $E_{Ni^0 \rightleftharpoons Ni(OH)_2}^{eq}$ earlier at pH 10.6 than at pH 6.0. However, at pH 10.6 E_{corr} does not remain at $E_{Ni^0 \rightleftharpoons Ni(OH)_2}^{eq}$ for

long; and once the hydrogel starts growing, the nickel redox half-reaction between $\text{Ni}^{2+}/\text{Ni}(\text{OH})_2$ and $\text{Ni}(\text{OH})_3$ in the hydrogel network quickly reaches (quasi-) equilibrium state and E_{corr} again increases very rapidly to a value near $E_{\text{Ni}^0 \rightleftharpoons \text{Ni}(\text{OH})_3}^{eq}$. The following continuous but slow increase in E_{corr} is due to decrease in the overall diffusion of Ni^{2+} from the metal surface to the bulk solution through the hydrogel network as the hydroxide nanoparticles aggregate more densely in the hydrogel network.

The study presented in Chapter 4 has concluded that the initial rapid increase in E_{corr} that occurred within 150 s is due to rapid change in the chemical activity $(a_{\text{Ni}^{2+}})_{int}$ of the initial oxidation product, solvated Ni^{2+} , in the interfacial region. At early stages of corrosion, the overall metal oxidation process consists of primarily the net interfacial charge transfer step (M1), and hydrolysis and transport of Ni^{2+} from the interfacial region to the bulk solution, steps (hyd) and (trans) in **Table 1**, respectively.

At the start of metal oxidation in solution free of dissolved Ni^{2+} , $(a_{\text{Ni}^{2+}})_{int}$ increases rapidly. Step (M1) is a reversible process, made up of the forward reaction of Ni^0 to Ni^{2+} (M1f) and the reverse reaction of Ni^{2+} to Ni^0 (M1r). The net rate of (M1), ν_{M1} , is the difference in the forward and reverse rates (ν_{M1f} and ν_{M1r} , respectively) [25,26] :

$$\nu_{M1} = \nu_{M1f} - \nu_{M1r} \quad (\text{Eq. 5.1a})$$

$$i_{M1} = nF \cdot \nu_{M1} \quad (\text{Eq. 5.1b})$$

where i_{M1} (in units of $\text{A}\cdot\text{cm}^{-2}$) represents the net oxidation current arising from (M1) and is related to ν_{M1} (in units of $\text{mol}\cdot\text{cm}\cdot\text{s}^{-1}$) by Faraday's law [25,26]:

The rate of each chemical reaction depends on the chemical activity of reactant:

$$v_{M1f} = k_{M1f} \cdot (a_{Ni^0})_{int} \approx k_{M1f} \quad (\text{Eq. 5.1c})$$

$$v_{M1r} = k_{M1r} \cdot (a_{Ni^{2+}})_{int} \quad (\text{Eq. 5.1d})$$

where k_{M1f} and k_{M1r} are the (pseudo-) 1st order rate coefficients for the forward and reverse reactions of (M1), respectively. Note that in these equations, the chemical activities of the reactants are those in the interfacial region and not in the bulk solution.

The chemical activity of solid metal is 1.0 and hence, $(a_{Ni^0})_{int}$ does not change as metal oxidation progresses. However, $(a_{Ni^{2+}})_{int}$ increases with increasing net rate of (M1):

$$d(a_{Ni^{2+}})_{int}/dt \Big|_{M1} = v_{M1f} - v_{M1r} = v_{M1} \quad (\text{Eq. 5.2})$$

where $d(a_{Ni^{2+}})_{int}/dt \Big|_{M1}$ represents the change in $(a_{Ni^{2+}})_{int}$ due to (M1).

The change in $(a_{Ni^{2+}})_{int}$ is affected by not only (M1) but also (trans) or other chemical reactions occurring in the interfacial region, see further discussion below. The above rate equations are mass and charge balance equations and show that the increase in $(a_{Ni^{2+}})_{int}$ increases the rate of (M1r), slowing down the net rate of (M1).

The increase in $(a_{Ni^{2+}})_{int}$ also increases the rate of (trans). Hence, the net production of Ni^{2+} in the interfacial region quickly decreases with time, and $(a_{Ni^{2+}})_{int}$ reaches steady (or slow-changing) state:

$$d(a_{Ni^{2+}})_{int}/dt \Big|_{t < \tau_0} = v_{M1} - v_{trans} > 0 \quad (\text{Eq. 5.3})$$

$$d(a_{Ni^{2+}})_{int}/dt \Big|_{t = \tau_0} = v_{M1} - v_{trans} \approx 0 \quad (\text{Eq. 5.4})$$

where $d(a_{\text{Ni}^{2+}})_{\text{int}}/dt|_{t < \tau_0}$ represents the rate of change in $(a_{\text{Ni}^{2+}})_{\text{int}}$ during the initial rapid E_{corr} transition period ($t < \tau_0$), and $d(a_{\text{Ni}^{2+}})_{\text{int}}/dt|_{t = \tau_0}$ represents the rate of change in $(a_{\text{Ni}^{2+}})_{\text{int}}$ at $t = \tau_0$.

At the early stages of corrosion (Dynamic Phase I in **Figure 5.1**), the overall metal oxidation current, i_{ox} , is primarily due to i_{M1} :

$$v_{\text{ox}} \approx v_{M1} \approx v_{\text{trans}} \quad (\text{Eq. 5.5a})$$

$$i_{\text{ox}} \approx nF \cdot v_{M1} = i_{M1} \quad (\text{Eq. 5.5b})$$

$$\text{net } i_{\text{ox}} = \text{net } |i_{\text{H}^+ \text{ red}}| \quad (\text{Eq. 5.5c})$$

When $(a_{\text{Ni}^{2+}})_{\text{int}}$ reaches a steady state, E_{corr} also reach a steady state because $i_{\text{ox}} = |i_{\text{red}}|$ at E_{corr} . Note that $|i_{\text{red}}|$ reaches steady-state earlier because reduction of dissolved oxidant (proton in this study) involves interfacial transfer of electrons only (particularly in early stages). This is better observed in PS polarization at high negative potentials, where the cathodic current density remained plateau over 150 s of the experiment (see discussion on the PS polarization results). The relationships between the kinetics of elementary steps and the overall metal oxidation rate are schematically shown in **Figure 5.1**.

The observed effects of pH and I_s on $E_{\text{corr}}(\tau_0)$ can then be rationalized from their effects on the kinetics of the elementary steps and the saturation capacity for Ni^{2+} of the interfacial region:

- (M1) is an interfacial charge transfer reaction. However, unlike a redox half-reaction of dissolved species on an inert electrode, metal oxidation requires interfacial transfer

of not only electrons but also Ni atoms. Consequently, ν_{M1} depends on not only E_{elec} (or E_{corr}) (on the V_{RHE} scale) that dictates electron transfer rate, but also $[OH^-]$ and I_s that dictates solvation rate of Ni^{2+} . The rate of solvation of metal cation increases with $[OH^-]$.

- The main transport mechanism for Ni^{2+} ions that is produced right at the metal-solution interface is diffusion through its concentration gradient. Hence, ν_{trans} strongly depends on ion mobility and hence, I_s .
- The saturation capacity of aqueous solution for metal cation depends strongly on pH. Hence, pH affects not only the rate of (M1), but also the maximum reaction yield of (M1) (i.e., $(a_{Ni^{2+}})_{int}$). Once the interfacial region become saturated with Ni^{2+} , metal atoms cannot be transferred from the metal to the solution even when the driving force for electron transfer is high (i.e., large overpotential). The rate of (M1) becomes potential-independent. The potential at which the rate of a half-reaction becomes potential-independent due to limit of interfacial mass transfer is known as “mass transfer overpotential” [25,27,28].

Thus, once the interfacial region become saturated with Ni^{2+} , (M1) can only occur at a rate of Ni^{2+} removal from the interfacial region. Upon saturation, the hydrolysis equilibrium (step (hyd) in **Table 5.1**) shifts to the formation of $Ni(OH)_2$ which precipitates as hydroxide salt (step (gel)) and oxidize to $Ni(OH)_3$ (step (M2)). Hence, the overall Ni^{2+} removal process includes not only (trans) but also (hyd), (gel) and (M2). The overall metal oxidation progresses into Dynamic Phase II in **Figure 5.1**.

The solubility of Ni^{2+} is about four orders of magnitude higher at pH 6.0 than at pH 10.6 (**Figure 5.3**). Hence, the Ni^{2+} concentration in the interfacial region remains below its saturation limit in Ar-purged solutions. The overall metal oxidation may not progress beyond the oxidation of Ni^0 to $\text{Ni}^{2+}/\text{Ni}(\text{OH})_2$ for a long time. The overall rate of metal oxidation (ν_{ox}) at the initial steady state can be described using the kinetics of only (M1) and (trans) (Dynamic Phase I in **Figure 5.1**). Hence, $E_{corr}(\tau_0)$ is at a value near or below $E_{\text{Ni}^0 \rightleftharpoons \text{Ni}(\text{OH})_2}^{eq}$ or $E_{\text{Ni}^0 \rightleftharpoons \text{Ni}^{2+}(\text{sat})}^{eq}$ at pH 6.0.

At pH 10.6, the solubility of Ni^{2+} is very low. Hence, the Ni^{2+} concentration in the interfacial region reaches its saturation limit nearly instantly. The overall metal oxidation now consists of not only (M1), (trans) and (hyd), but also (M2) and (gel) (Dynamic Phase II in **Figure 5.1**). In this phase, the relationship between the overall metal oxidation rate and the rates of the elementary steps are:

$$\nu_{ox} \approx \nu_{M1} \approx \nu_{trans} + \nu_{M2} + \nu_{gel} \quad (\text{Eq. 5.6a})$$

$$i_{ox} = 2F \cdot \nu_{M1} + F \cdot \nu_{M2} \quad (\text{Eq. 5.6b})$$

$$\text{net } i_{ox} = \text{net } |i_{H^+ red}|$$

Note that due to systemic feedback between different elementary steps the rates of individual steps change with time, but the equalities given in the above equations still hold. Hence, at pH 10.6, (M2) becomes an important RDS even at early stages of corrosion, and $E_{corr}(\tau_0)$ reaches a value near $E_{\text{Ni}^0 \rightleftharpoons \text{Ni}(\text{OH})_3}^{eq}$.

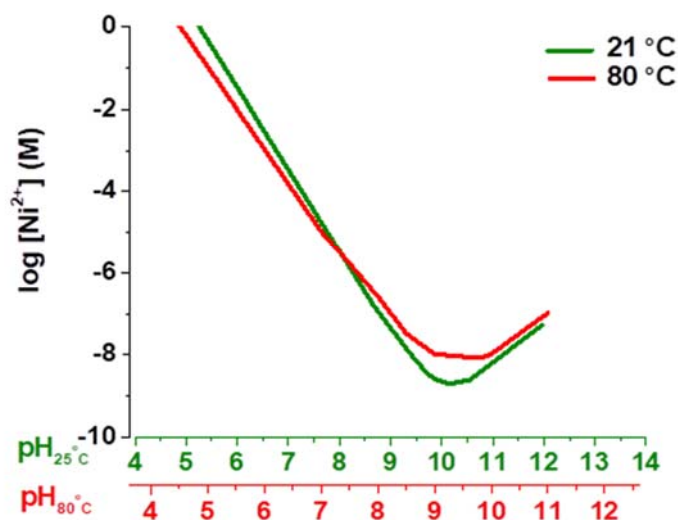


Figure 5.3: The solubility of Ni²⁺ in water at 21 and 80 °C [21,28].

Because of the significant change in RDS with change in pH, $E_{corr}(\tau_0)$ is mainly controlled by pH. Ionic strength influences the overall metal oxidation through its effect on the transport rates of H⁺ and Ni²⁺. Change in I_s does not alter RDS. Hence, I_s has a negligible effect on $E_{corr}(\tau_0)$ and a minor effect on E_{corr} at longer times. However, I_s affects the overall metal oxidation rate because of its effect on (trans), which is coupled strongly with other elementary steps.

The subsequent change in E_{corr} with t_{corr} was much slower, indicating that no further changes in metal oxidation mechanism. Instead, the long-term changes in E_{corr} are mostly due to slow changes in the chemical/electrochemical environments of the interfacial region as metal oxidation products precipitate and grow. The overall metal oxidation rate at longer times must consider the systemic feedback between different elementary steps which can alter the kinetic parameters (pseudo-1st order rate coefficients) of individual steps.

That the overall process occurs in a series of elementary steps and the effects of pH and I_s on metal oxidation kinetics can be better appreciated by examining the $\log|i_{meas-PD}|$ vs E_{elec} relationships during the PD scans performed as a function of t_{corr} .

5.3.2. The $|i_{meas-PD}|$ vs E_{elec} Relationship as a Function of t_{corr}

PD scan is a common electrochemical technique employed to extract corrosion rate [25,30,31]. It is typically performed after E_{corr} reaches (pseudo-) steady state to ensure that the chemical activities of redox species involved in the half-reactions occurring on the electrode surface are in quasi equilibrium (steady state). With the steady-state assumption, the $\log|i_{meas-PD}|$ vs E_{elec} relationship observed in the cathodic potential region is often extrapolated to obtain the net metal oxidation current i_{ox} (= $|i_{red}|$) at $E_{elec} = E_{corr}$ [31,32]. Hence, we performed PD scans with a goal of establishing the i_{ox} as a function of t_{corr} , and determining the long-term progression of corrosion rate from the E_{corr} and the $\log|i_{meas-PD}|$ vs E_{elec} relationship obtained as a function of t_{corr} .

The PD polarization results obtained as a function of t_{corr} are presented together with E_{corr} in **Figure 5.2**. The $\log|i_{meas-PD}|$ vs E_{elec} relationship showed some unusual behaviours. First, the effects of pH and I_s on the potential of zero current, $E_{i=0,PD}$, are discussed.:

- $E_{i=0,PD}$ did not coincide with E_{corr} , and it was always lower than E_{corr} .

- At a given pH and I_s , $E_{i=0,PD}$ varied with t_{corr} . Nevertheless, the $E_{i=0,PD}$ obtained at short t_{corr} (< 0.5 h) was near $E_{Ni^{0} \rightleftharpoons Ni(OH)_2}^{eq}$ at both pHs and in both I_s solutions.
- Although $E_{i=0,PD} \neq E_{corr}$, the dependence of $E_{i=0,PD}$ on t_{corr} closely followed that of E_{corr} . At pH 6.0 at which E_{corr} decreased with t_{corr} , $E_{i=0,PD}$ decreased with t_{corr} . At pH 10.6 both E_{corr} and $E_{i=0,PD}$ increased with t_{corr} .
- The effect of I_s on the progressions of both E_{corr} and $E_{i=0,PD}$ was negligible at shorter t_{corr} and increased slightly at longer t_{corr} .

Interestingly, the relative effect of pH versus I_s on the $\log|i_{meas-PD}|$ vs E_{elec} relationship was opposite to those on E_{corr} and $E_{i=0,PD}$. The effects of pH and I_s on the $\log|i_{meas-PD}|$ vs E_{elec} relationship as a function of t_{corr} can be better appreciated from **Figure 5.4**. In this figure, $\log|i_{meas-PD}|$ was plotted as a function of $\Delta E_{i=0,PD}$ where $\Delta E_{i=0,PD} = E_{elec} - E_{i=0,PD}$:

- At pH 6.0, in a specific I_s solution, the $\log|i_{meas-PD}|$ as a function of $\Delta E_{i=0,PD}$ did not change significantly with t_{corr} (see **Figure 5.2**). However, I_s had a significant effect on the value of $|i_{meas-PD}|$ at a given $\Delta E_{i=0,PD}$ and the dependence of $\log|i_{meas-PD}|$ on $\Delta E_{i=0,PD}$. The $|i_{meas-PD}|$ at all $\Delta E_{i=0,PD}$ were lower, and both cathodic and anodic Tafel slopes ($d(\Delta E_{i=0,PD})/d(\log|i_{meas-PD}|)$) were higher, in the lower I_s solution.
- At pH 10.6, in a specific I_s solution the $\log|i_{meas-PD}|$ as a function of $\Delta E_{i=0,PD}$ changed significantly with t_{corr} (see **Figure 5.2**). I_s also affected the $\log|i_{meas-PD}|$ in the cathodic and anodic potential regions differently.

Although the $\log|i_{meas-PD}|$ as a function of $\Delta E_{i=0,PD}$ progresses with t_{corr} differently depending on pH and I_s , some common dependences were observed:

- At early times of corrosion ($t_{corr} = 0.5$ h in this study) when $E_{i=0,PD} \approx E_{Ni^0 \rightleftharpoons Ni(OH)_2}^{eq}$ at both pHs, the $\log|i_{meas-PD}|$ in the cathodic and anodic potential regions were lower in the lower I_s solution also at both pHs.
- At intermediate stages of corrosion ($t_{corr} = 1$ to 3 h in this study), $E_{i=0,PD}$ decreased to a value below $E_{Ni^0 \rightleftharpoons Ni(OH)_2}^{eq}$ at pH 6.0, while $E_{i=0,PD}$ increased to a value near and above $E_{Ni^0 \rightleftharpoons Ni(OH)_2/Ni(OH)_3}^{mid}$. At this intermediate stage, the effect of I_s on $|i_{meas-PD}|$ at pH 6.0 was opposite to that at pH 10.6. At pH 6.0 the $\log|i_{meas-PD}|$ vs $\Delta E_{i=0,PD}$ relationship did not change significantly with t_{corr} in each I_s solution. The $\log|i_{meas-PD}|$ in both cathodic and anodic potential ranges remained much smaller in the lower I_s solution. At pH 10.6, the $\log|i_{meas-PD}|$ values were larger in the lower I_s solution.
- At the final stage of corrosion ($t_{corr} = 24$ h), $E_{i=0,PD} < E_{Ni^0 \rightleftharpoons Ni(OH)_2}^{eq}$ at pH 6.0 and $E_{i=0,PD} \geq E_{Ni^0 \rightleftharpoons Ni(OH)_3}^{eq}$ at pH 10.6. At pH 6.0, the effect of I_s on the $\log|i_{meas-PD}|$ in the cathodic and anodic potential regions remained large, similar all throughout t_{corr} . At pH 10.6, the effect of I_s on $|i_{meas-PD}|$ diminished with t_{corr} , particularly at E_{elec} near $E_{i=0,PD}$. Interestingly, the $|i_{meas}|$ in the anodic potential range was higher, but the $|i_{meas-PD}|$ in the cathodic potential range was lower, in the lower I_s solution.

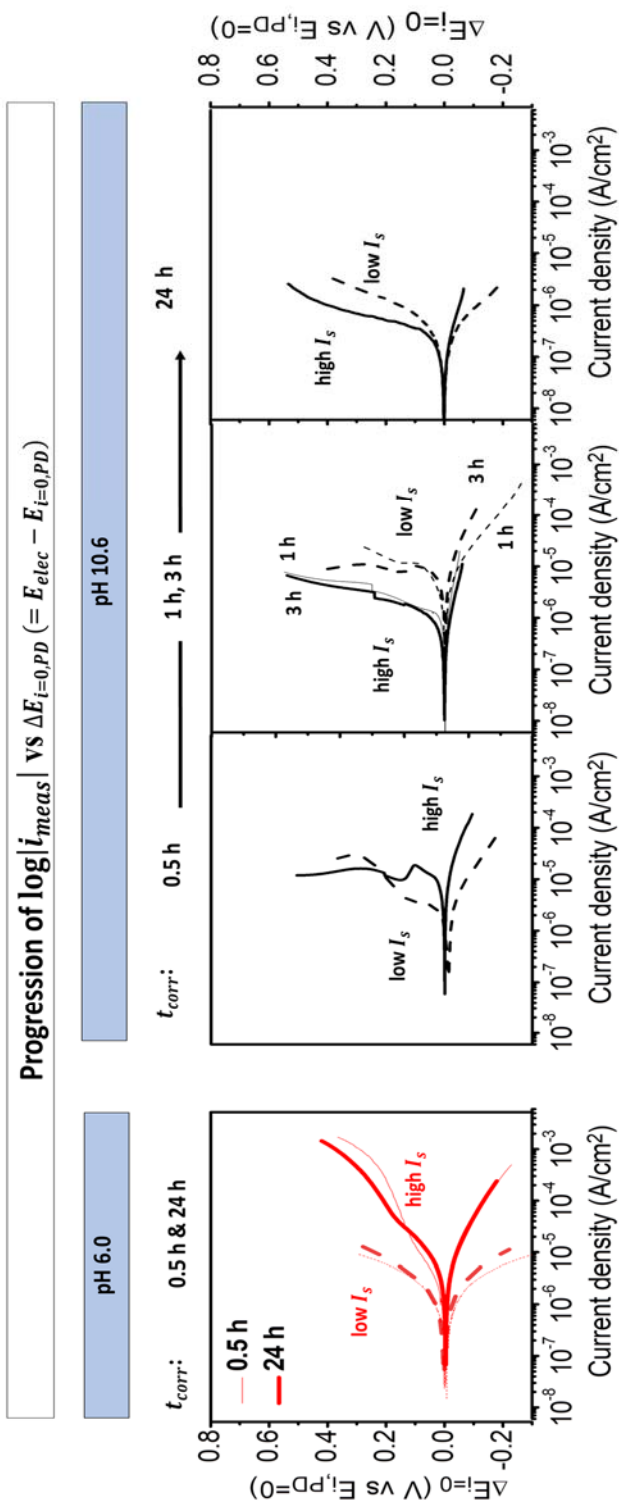


Figure 5.4: $\log|i_{meas}|$ vs $\Delta E_{i=0}$ relationships observed during PD scans performed after different corrosion durations in two different I_s solutions at pH 6.0 and pH 10.6, where $\Delta E_{i=0} = E_{elec} - E_{i=0,PD}$.

The most puzzling observation was that $E_{i=0,PD}$ was always lower than E_{corr} . E_{corr} is the open circuit potential at which the net metal oxidation current, i_{ox} , is the same as the net oxidant (proton in this study) reduction current, $|i_{red}|$. The PD scan was performed from the starting potential of 300 mV below E_{corr} , immediately after the E_{corr} measurement was ended. If $i_{ox} = |i_{red}|$ at E_{corr} , why is $|i_{meas-PD}| \neq 0$ at $E_{elec} = E_{corr}$? Instead, $|i_{meas-PD}| = 0$ at $E_{elec} < E_{corr}$ at all t_{corr} , independent of pH or I_s . This cannot be attributed to metal oxidation product(s) that have been accumulated in the interfacial region being reduced at $E_{elec} < E_{corr}$ during the PD scan prior to reaching E_{corr} . If so, $E_{i=0,PD}$ should be higher, not lower than E_{corr} . As far as we are aware none of the existing corrosion rate formula or models can adequately address these observations.

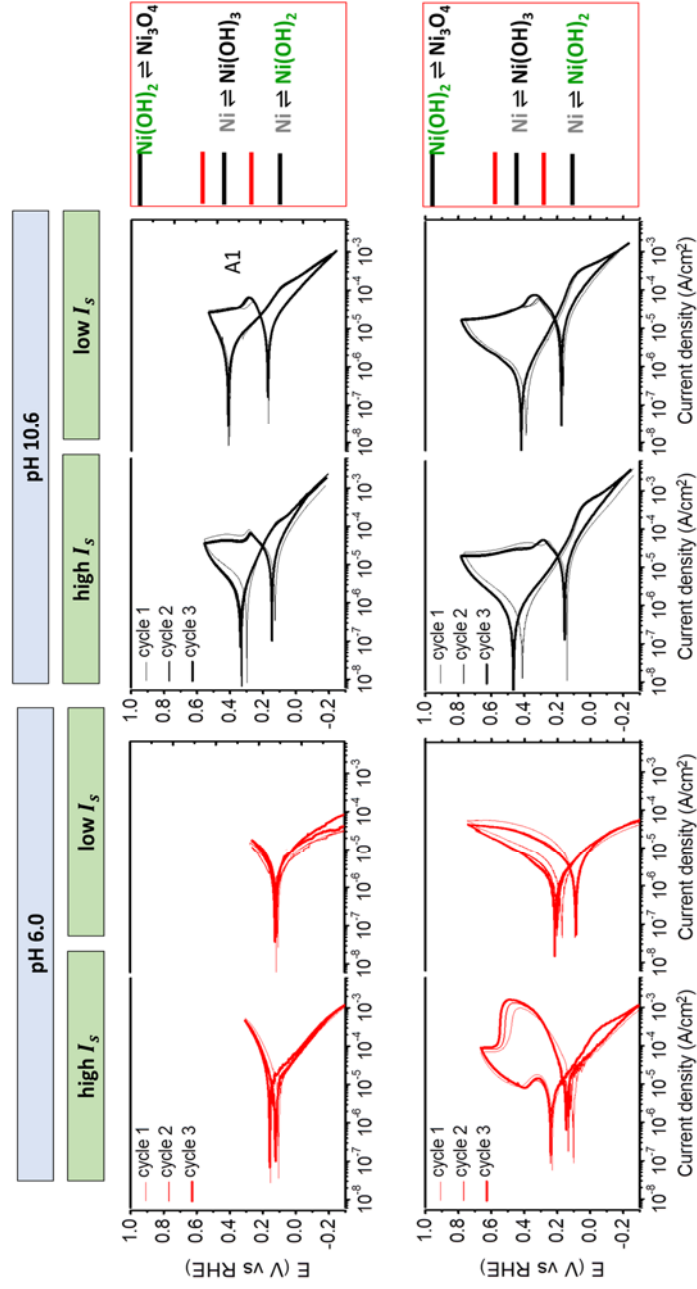
The observed changes in E_{corr} , $E_{i=0,PD}$ and the $\log|i_{meas-PD}|$ vs E_{elec} relationship with t_{corr} collectively indicate that the elementary reaction and transport steps that comprise the overall metal oxidation process evolve as corrosion progresses. Because pH and I_s affect the kinetics of different steps differently, the effect of I_s on overall metal oxidation rate (or metal oxidation current) is different at different pH, and vice versa.

The combined effect of pH and I_s on the $\log|i_{meas-PD}|$ vs E_{elec} relationship was further examined by comparing the PD polarization results with those observed during cyclic voltammetry (CV) and potentiostatic (PS) polarization tests.

5.3.3. The $\log|i_{meas}|$ vs E_{elec} Relationship During PD vs CV

The $\log|i_{meas-CV}|$ as a function of E_{elec} observed during CV are presented in **Figure 5.5**. At each pH and I_s , multiple cycles of CV with a specific upper vertex potential were performed, and three different upper vertex potentials were used. Only the first 3 cycles are shown in the figure. The potential scan rate used was 5 mV/s, the same rate used for the PD scan as a function of t_{corr} .

Figure 5.5: Cyclic voltammograms obtained for Ni electrodes in either high or low I_s solutions at pH 6.0 and pH 10.6. The CVs of up to 3 consecutive cycles (from thinnest to thickest lines with cycling) are shown and different graphs are those with different upper vertex potentials. Also shown are the equilibrium potentials of metal redox half-reactions (black bars) and mid potentials of two E_{rxn}^{eq} values (red bars).



At each pH and I_s , the $\log|i_{meas-CV}|$ vs E_{elec} relationship observed during the reverse CV scan was different from that observed during the forward scan. The difference depended on the upper vertex potential. The different effects of pH and I_s on the $\log|i_{meas-CV}|$ vs E_{elec} relationship depending on the upper vertex potential can be better appreciated from **Figure 5.6**. Despite the difference in the voltammograms of the forward and reverse scans, multiple cycling had a negligible effect on the $\log|i_{meas}|$ vs E_{elec} relationship. That is, each full scan cycle did not induce any significant chemical change in the interfacial region. Hence, the $\log|i_{meas-CV}|$ vs E_{elec} relationship is thus considered as the $\log|i_{meas-PD}|$ vs E_{elec} relationship at $t_{corr} = \tau_0$.

The elementary steps that are responsible for the observed $\log|i_{meas-CV}|$ vs E_{elec} relationship, and the effect of pH on the relationship in the high I_s solution, are discussed in detail in Chapter 4. In this chapter discussion will focus on the different effects of pH and I_s on the $\log|i_{meas-CV}|$ vs E_{elec} relationship.

The key observations from **Figures 5.5** and **5.6** are:

- The current observed on the forward scan, $|i_{meas-CV_f}|$, in the cathodic potential range ($< E_{i=0,CV_f}$) varied considerably with pH and I_s . Despite the large variation in $|i_{meas-CV_f}|$, the potential of zero current during the forward CV scan, $E_{i=0,CV_f}$ was near $E_{Ni^0 \rightleftharpoons Ni(OH)_2}^{eq}$, independent of pH and I_s . Recall that $E_{Ni^0 \rightleftharpoons Ni(OH)_2}^{eq}$ was also the initial E_{corr} at pH 6.0 in both low and high I_s solutions, and $E_{i=0,PD}$ at $t_{corr} = 0.5 \text{ h}$ observed at both pHs and both I_s .

- The $\left| i_{meas-CV_f} \right|$ at $E_{elec} < E_{i=0,CV_f}$ was not significantly affected by repeated cycling or upper vertex potential used. The effect of pH on the cathodic current was negligible in the higher I_s solution, but significant in the lower I_s solution. The effect of I_s was significant at pH 6.0 but negligible at pH 10.6.
- At $E_{elec} > E_{i=0,CV_f}$, the $\log \left| i_{meas-CV_f} \right|$ vs E_{elec} relationship changed from interfacial charge-transfer limiting behaviour (smaller Tafel slope) to mass-transport limiting behaviour (larger Tafel slope). The change occurred at a higher E_{elec} at pH 6.0 than at pH 10.6 in the higher I_s solution, but a lower E_{elec} at pH 6.0 than at pH 10.6 in the lower I_s solution.
- The $\log |i_{meas-CV}|$ vs E_{elec} relationship at anodic potentials on the reverse scan deviated from that observed on the forward scan. The difference was significant when the upper vertex potential was higher than the first anodic peak potential. Although the peak potential of A1 varied considerably depending on pH, the potential of zero current during the reverse CV scan, $E_{i=0,CV_r}$ was near either $E_{Ni^0 \rightleftharpoons Ni(OH)_2/Ni(OH)_3}^{mid}$ or $E_{Ni^0 \rightleftharpoons Ni(OH)_3}^{eq}$ depending on the vertex potential, independent of pH and I_s .

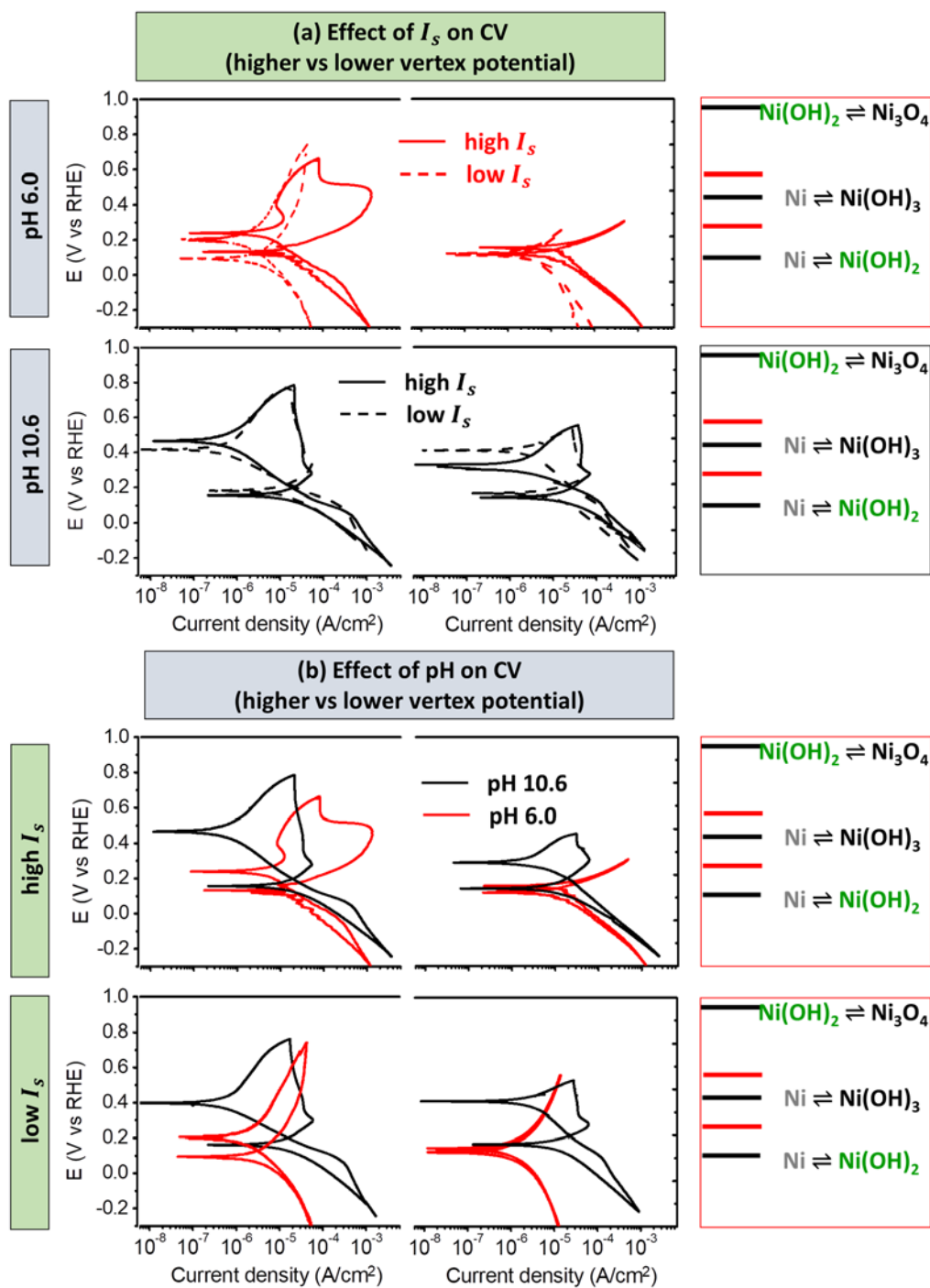


Figure 5.6: Comparison of the 3rd cycle CVs obtained, (a) in high vs low I_s solution at pH 6.0 and pH 10.6, and (b) at pH 6.0 vs pH 10.6 in the high and low I_s solutions. The CVs with two different upper vertex potentials are shown. Also shown are the equilibrium potentials of metal redox half-reactions (black bars) and mid potentials of two E_{rxn}^{eq} values (red bars).

These observations are consistent with the claims that pH has a negligible effect on the rate of (M1) and hence, on the i_{ox} or $|i_{red}|$ as a function of E_{elec} on the V_{RHE} scale. However, pH has a significant effect on the reaction yield of (M1), i.e., the maximum $(a_{Ni^{2+}})_{int}$ can reach. On the other hand, I_s affects the transport of ions, Ni^{2+} and H^+ .

Earlier we have argued that because of the effect of pH on the Ni^{2+} saturation capacity of the interfacial region, the overall metal oxidation moves through different dynamic phases faster at pH 10.6. Hence, while (M1) and (trans) are the main RDS for a long time at pH 6.0, (hyd), (gel) and (M2), in addition to (M1) and (trans), begin to occur at very early stages of corrosion at pH 10.6 (see Eqs.5.6a). As a result, $E_{corr}(\tau_0)$ reaches a value near $E_{Ni^0 \rightleftharpoons Ni(OH)_2}^{eq}$ at pH 6.0, but a value near $E_{Ni^0 \rightleftharpoons Ni(OH)_3}^{eq}$ at pH 10.6. (Note that the initial rapid transition at pH 10.6 occurred stepwise, passing through $E_{Ni^0 \rightleftharpoons Ni(OH)_2}^{eq}$, $E_{Ni^0 \rightleftharpoons Ni(OH)_2/Ni(OH)_3}^{mid}$ to $E_{Ni^0 \rightleftharpoons Ni(OH)_3}^{eq}$).

The pH-dependent metal oxidation mechanism at early stages of corrosion is consistent with the CV results. Under naturally corroding conditions, $i_{ox}(t) = |i_{red}(t)|$ and this mass and charge conservation law dictates $E_{corr}(t)$. During the CV scan, E_{elec} is controlled externally and $|i_{meas-CV}| = i_{ox}(t) - |i_{red}(t)|$.

At pH 6.0, $E_{corr}(\tau_0) \approx E_{Ni^0 \rightleftharpoons Ni^{2+}(sat)}^{eq}$, and $E_{i=0 CV_f} \approx E_{Ni^0 \rightleftharpoons Ni^{2+}(sat)}^{eq}$. When the potential scan was reversed before peak A1/A2 was observed on the forward scan, the current-potential relationship during the reverse scan did not deviate from that observed on the forward scan. (The assignment of current peaks and the processes responsible for

the peaks are discussed in detail in Chapter 4. The anodic peak(s) is associated with the precipitation of mixed Ni^{II}/Ni^{III} hydroxide (gel.) As discussed in more detail later, the small difference in $|i_{meas-CV}|$ near $E_{Ni^{0} \rightleftharpoons Ni^{2+}}^{eq}{}_{(sat)}$ is due to small difference in $(a_{Ni^{2+}})_{int}$ due to small change in $v_{ox} = v_{M1} - v_{trans}$ (see Eq 5.5a). When the potential scan was reversed at the higher potential, the current-potential relationship during the reverse scan deviated considerably from that observed on the forward scan.

These observations indicate that at pH 6.0 in Ar-purged solution metal oxidation at early times progresses only to production of Ni²⁺. However, even at this pH, in more oxidizing solution or at a higher E_{elec} under polarization, v_{M1} and i_{M1} become sufficiently large to saturate the interfacial region and induce (gel) and (M2). The change in the RDS at the higher E_{elec} or under more oxidizing conditions results in $E_{i=0,CV_r}$ different from $E_{i=0,CV_f}$ and the potential dependence of $|i_{meas-CV_r}|$ different from that of $|i_{meas-CV_f}|$.

At pH 10.6, $E_{corr}(\tau_0) \approx E_{Ni^{0} \rightleftharpoons Ni(OH)_3}^{eq}$, but $E_{i=0,CV_f} \approx E_{Ni^{0} \rightleftharpoons Ni(OH)_2}^{eq}$. During CV, E_{elec} was scanned at a controlled rate from the cathodic cleaning potential. At the low E_{elec} the $|i_{meas-CV_f}|$ is determined by $i_{ox} \approx i_{M1}$ and $|i_{H^+ red}|$. Hence, $E_{i=0,CV_f} \approx E_{Ni^{0} \rightleftharpoons Ni(OH)_2}^{eq}$, different from $E_{corr}(\tau_0)$, but same as $E_{i=0,CV_f}$ at pH 6.0, and the i_{ox} at $E_{i=0,CV_f}$ is similar at both pHs in the high I_s solutions. However, at $E_{elec} > E_{i=0,CV_f}$, $|i_{meas-CV_f}|$ increased with E_{elec} only over a narrow potential range before it decreased with E_{elec} . That is, peak A1 appeared at a much lower potential at pH 10.6 than at pH 6.0, because saturation and the precipitation of mixed Ni^{II}/Ni^{III} hydroxide occurs at the

lower E_{elec} and under the less oxidizing conditions at pH 10.6. The peak potential was also far below $E_{corr}(\tau_0)$.

At pH 10.6, when the potential scan was reversed at $E_{elec} > E_{corr}(\tau_0)$ ($\approx E_{Ni^0 \rightleftharpoons Ni(OH)_3}^{eq}$), $E_{i=0,CV_r}$ was very different from $E_{i=0,CV_f}$. Instead, $E_{i=0,CV_r} \approx E_{corr}(\tau_0)$.

The potential dependence of $|i_{meas-CV_r}|$ was very different from that of $|i_{meas-CV_f}|$.

The observed effects of pH on the $\log|i_{meas-CV}|$ vs E_{elec} relationship further support the proposed metal oxidation mechanisms of Dynamic Phases I and II, and the dynamic conditions the transition occurs. In Ar-purged solutions and at 80 °C, it does not take long to reach Dynamic Phase II at pH 10.6.

The effect of I_s on the overall metal oxidation rate is primarily through its effect on (trans). The slower (trans) is, the slower (M1) and the slower overall oxidation rate are (see Eq. 5.5a). Similarly, I_s affects the transport of H^+ and can influence the overall proton reduction rate. Accordingly, at pH 6.0, I_s has a negligible effect on $E_{i=0,CV_f}$, but a significant effect on $|i_{meas-CV_f}|$ at E_{elec} near $E_{i=0,CV_f} \approx E_{corr}(\tau_0) \approx E_{Ni^0 \rightleftharpoons Ni(OH)_2}^{eq}$. The $|i_{meas-CV_f}|$ values were significantly smaller, and the anodic and cathodic Tafel slopes were significantly larger, in the lower I_s solution.

On the other hand, the effect of I_s on the overall metal oxidation rate is diminished when (hyd), (gel) and (M2) occur at substantial rates. Accordingly, at pH 10.6, I_s has a negligible effect on $E_{i=0,CV_f}$, and has only a minor effect on $E_{i=0,CV_r}$; despite the large hysteresis in the anodic current in each I_s solution, the $|i_{meas-CV_f}|$ and

$|i_{meas-CV_r}|$ values at E_{elec} near $E_{i=0,CV_r} \approx E_{corr}(\tau_0) \approx E_{Ni^0 \rightleftharpoons Ni(OH)_3}^{eq}$ were not affected significantly by I_S .

The CV results provide the information on the metal oxidation kinetics as a function of E_{elec} on the metal surface at early stages of corrosion. Initially, E_{corr} increased very rapidly to reach $E_{corr}(\tau_0)$ and the value of $E_{corr}(\tau_0)$ depended strongly on pH. The subsequent change in E_{corr} with t_{corr} was much slower, indicating no further changes in metal oxidation mechanism in a given pH. Instead, the long-term changes in E_{corr} are mostly due to slow changes in the chemical/electrochemical environments of the interfacial region as metal oxidation products precipitate and grow (steps (gel) and (oxide) in **Table 5.1**).

The growth of solid hydroxides/oxides is a very slow process and hence, it does not directly contribute to the overall metal oxidation current during potentiodynamic polarization. That is, the rate of hydroxide/oxide growth cannot be extracted from a CV or a PD scan performed at one specific time. However, the precipitates on the surface can affect the kinetic parameters, the pseudo 1st order rate coefficients, of the other elementary steps over long-term corrosion. The effect of the change in the chemical /electrochemical environment of the interfacial region due to slow processes can be obtained by comparing the $\log|i_{meas}|$ vs E_{elec} relationships during CV and PD polarization scans performed at different t_{corr} .

Figure 5.7 compares the $\log|i_{meas-CV}|$ vs E_{elec} relationship with the $\log|i_{meas-PD}|$ vs E_{elec} relationship observed as a function of t_{corr} . As stated earlier, the CV scans can be considered as the PD scans at τ_0 . The solution conditions and the potential scan rates were the same in both CV and PD polarization tests. Hence, the

progression of the $\log|i_{meas}|$ vs E_{elec} relationship with t_{corr} can be attributed to the chemical change in the interfacial region over t_{corr} and, as a result, the change in metal oxidation kinetics as a function of E_{elec} . The comparison shows that:

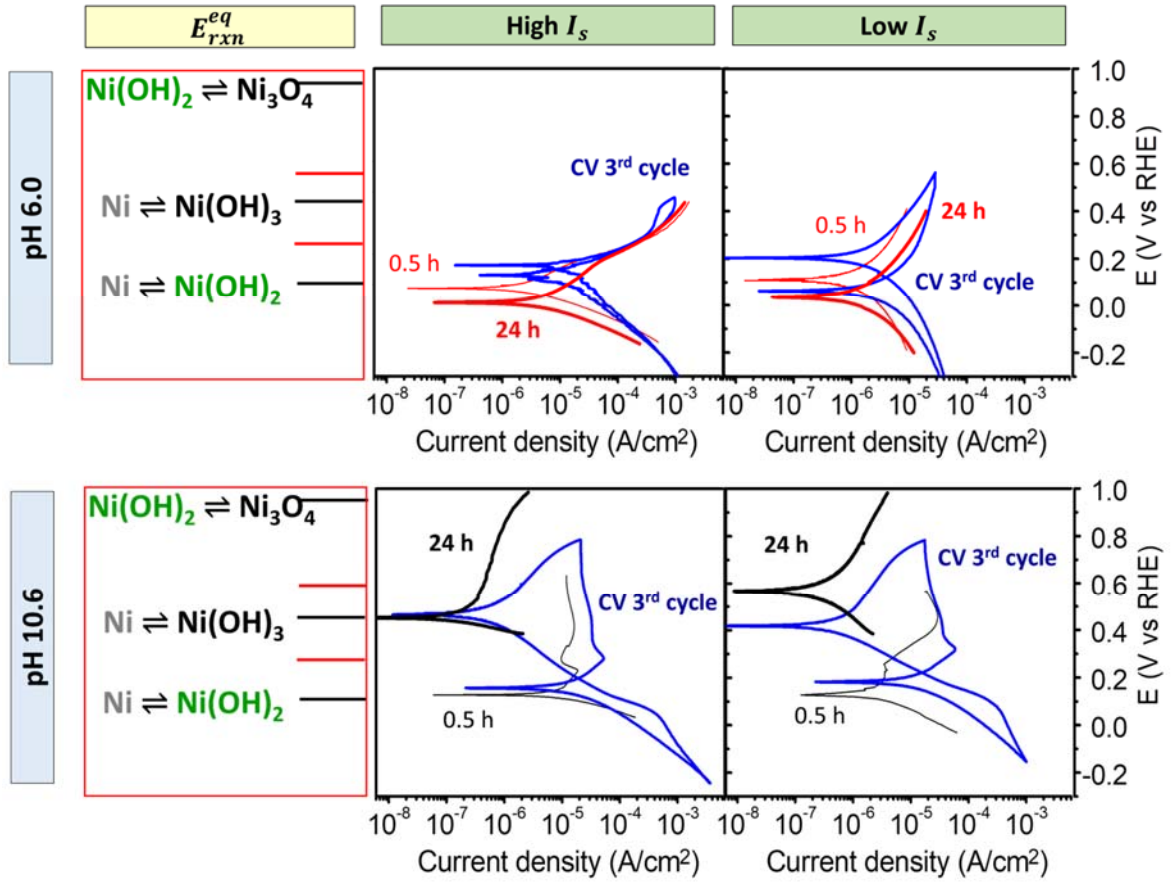


Figure 5.7: Comparison of the $\log|i_{meas-CV}|$ vs E_{elec} relationship with the $\log|i_{meas-PD}|$ vs E_{elec} relationship observed as a function of t_{corr} .

At pH 6.0 and in the high I_s solution,

- E_{corr} increased from $E_{corr}(\tau_0) \approx E_{Ni^0 \rightleftharpoons Ni(OH)_2}^{eq}$ to an intermediate steady state in 10 min and stayed there for a couple of hours before decreasing very slowly to the final steady state near $E_{Ni^0 \rightleftharpoons Ni(OH)_2}^{eq}$. On the other hand, $E_{i=0}$ during polarization

decreased steadily with t_{corr} , from $E_{Ni^0 \rightleftharpoons Ni(OH)_2}^{eq}$ to near 0.0 V_{RHE} (i.e., $E_{H^+ \rightleftharpoons H_2}^{eq}$).

The change in $E_{i=0}$ with t_{corr} was also slow.

- Despite these changes with t_{corr} , the $\log|i_{meas}|$ value and its E_{elec} dependence in potential range R3 ($E_{elec} > E_{Ni^0 \rightleftharpoons Ni(OH)_2/Ni(OH)_3}^{mid}$) did not change with t_{corr} .
- These observations indicate that when E_{elec} is scanned to the mid-potential, the interfacial region becomes fully saturated and the potential dependences of (M1) and (M2) become the same, irrespective of any changes in the interfacial region over t_{corr} .
- The main changes in $|i_{meas}|$ with t_{corr} occurred in potential range -200 mV_{RHE} to 200 mV_{RHE}. Interestingly, the $|i_{meas}|$ value at a given E_{elec} in the cathodic potential range decreased with t_{corr} whereas the cathodic Tafel slope was -120 mV/dec at all t_{corr} except at $t_{corr} = 0$ h.
- On the other hand, the $|i_{meas}|$ value at a given E_{elec} in the anodic potential range below 200 mV_{RHE} increased with t_{corr} and the anodic Tafel slope increased with t_{corr} , approaching 180 mV/dec at 24 h.

At pH 6.0 and in the low I_s solution,

- E_{corr} did not increase to the intermediate steady state observed in the high I_s solution, but decreased slowly from $E_{corr}(\tau_0) \approx E_{Ni^0 \rightleftharpoons Ni(OH)_2}^{eq}$ to the final steady state slightly below $E_{Ni^0 \rightleftharpoons Ni(OH)_2}^{eq}$. The $E_{i=0}$ during polarization also decreased with t_{corr} , but the decrease occurred in the first 1 h after which no further change was

observed. In comparison, the change was more gradual in the high I_s solution (Figure 5.2).

- The main changes in $|i_{meas}|$ with t_{corr} occurred primarily in the anodic potential range. In the anodic range, the $|i_{meas}|$ value at a given E_{elec} increased with t_{corr} while the anodic Tafel slope was ~ 350 mV/dec at all t_{corr} except at $t_{corr} = 0$ h. Interestingly, the $|i_{meas}|$ value at 0.5 h was similar to that observed on the reverse CV scan.
- The $|i_{meas}|$ value at E_{elec} in the cathodic potential range (away from $E_{i=0}$) did not change with t_{corr} . The cathodic Tafel slope was also ~ 350 mV/dec.

At pH 10.6, the change in the $\log|i_{meas}|$ vs E_{elec} relationship with t_{corr} is similar in both low and high I_s solutions:

- E_{corr} was initially at $E_{Ni^0 \rightleftharpoons Ni(OH)_3}^{eq}$ and continued to increase to the final steady state near or above the mid-potential between $E_{Ni^0 \rightleftharpoons Ni(OH)_2}^{eq}$ and $E_{Ni(OH)_2 \rightleftharpoons Ni_3O_4}^{eq}$, denoted as $E_{Ni^0 \rightleftharpoons Ni(OH)_2/Ni_3O_4}^{mid}$ hereafter.
- The $E_{i=0}$ during polarization also increased with t_{corr} . Interestingly, the $E_{i=0}$ at short corrosion time ($t_{corr} = 0.5$ h) was near the $E_{i=0,f-CV}$ whereas the $E_{i=0}$ at $t_{corr} = 24$ h was near the $E_{i=0,r-CV}$.
- In the higher I_s solution, the main change in the $\log|i_{meas}|$ vs E_{elec} relationship with t_{corr} occurred primarily in the anodic potential range. The relationship in the cathodic potential range also changed with t_{corr} . However, the $\log|i_{meas}|$ vs E_{elec}

relationship at $t_{corr} = 0.5$ h was the same as that of the forward CV scan, whereas that at $t_{corr} = 24$ h was the same as that of the reverse CV scan.

- Similar changes were observed in the lower I_s solution. The main differences were that the $E_{i=0}$ at $t_{corr} = 0.5$ h was slightly below the $E_{i=0,f-CV}$ and $E_{i=0}$ at $t_{corr} = 24$ h was above the $E_{i=0,r-CV}$. As the concentration of solution oxidant at the interface was depleted, the $|i_{meas}|$ in the cathodic polarization range decreased in the first 0.5 h. The $|i_{meas}|$ in the anodic polarization range below $E_{Ni^{0} \rightleftharpoons Ni(OH)_2 / Ni(OH)_3}^{mid}$ also decreased in the first 0.5 h.

These observations further support the metal oxidation mechanisms discussed to explain the combined effects of pH and I_s on the time-dependent behaviour of E_{corr} and the potential dependence of $|i_{meas}|$ observed during the forward and reverse CV scans.

At pH 6.0 the overall metal oxidation rate is primarily determined by the kinetics of (M1) and (trans). The slower (trans) is, the slower (M1) and the slower overall oxidation rate are (see Eq. 5.5a). I_s affects ion mobility and hence, the pseudo 1st-order rate coefficient for (trans) (k_{trans} in **Table 5.1**). Similarly, I_s also affects the transport of H^+ .

At pH 6.0, decreasing I_s decreases both metal oxidation and proton reduction currents similarly. Hence, I_s has a minor effect on E_{corr} , but a significant effect on i_{ox} or $|i_{red}|$ at E_{elec} near E_{corr} . At this pH, I_s has only a small effect on the time-dependent behaviours of E_{corr} or on i_{ox} or $|i_{red}|$ at E_{elec} near E_{corr} .

The small difference observed for the evolution of the $|i_{meas}|$ vs E_{elec} relationship with t_{corr} can then be attributed to the further changes in k_{M1} and k_{trans} as a result of the products of (M1) and (trans) accumulated over t_{corr} . Step (hyd) occurs all

throughout t_{corr} . However, this reaction has a negligible effect on the overall metal oxidation rate when $(a_{Ni^{2+}})_{int}$ remains near or below the saturation capacity. The slow (hyd) leads to slow precipitation of mixed Ni^{II}/Ni^{III} hydroxide (gel) and slow oxidation of Ni²⁺/Ni(OH)₂ to Ni(OH)₃ (M2). Their rates still cannot compete with the rate of (trans). However, the mixed hydroxide colloids and/or oxides can accumulate in the interfacial region over long corrosion duration. Thus, although the overall production rate of the precipitates is slow, the precipitates accumulated can affect the rate coefficient of (trans) and hence, the overall metal oxidation rate.

At pH 10.6 because Ni²⁺ concentration in the interfacial region reaches its saturation limit nearly instantly, not only (M1), (trans) and (hyd), but also (M2) and (gel), contribute significantly to determination of the overall metal oxidation rate (see Eq 5.6a). The i_{ox} or $|i_{red}|$ at E_{elec} near E_{corr} is smaller at this pH than at pH 6.0. Because of the smaller contribution of (trans) compared to other competing Ni²⁺ removal steps, I_s has a smaller effect on i_{ox} or $|i_{red}|$ at E_{elec} near E_{corr} . At this pH, the mixed hydroxide and oxide precipitates also accumulate faster with t_{corr} . Their effects on in k_{M1} and k_{trans} can become progressively more important with t_{corr} . Hence, the $E_{i=0}$ and the $|i_{meas}|$ vs E_{elec} relationship during polarization changes more rapidly with t_{corr} , but the effect of I_s on the time-dependent behaviour of i_{ox} or $|i_{red}|$ at $E_{corr} \geq E_{Ni^0 \rightleftharpoons Ni(OH)_3}^{eq}$ is negligible.

The CV and PD polarization results provide information on the E_{elec} dependence of the overall metal oxidation rate in specific chemical and electrochemical environment of the interfacial region at t_{corr} . The comparison of the polarization curves obtained at different t_{corr} indicate that the change in the chemical environment with t_{corr} although E_{corr} does not change significantly. Hence, the effect of the change in interfacial

chemistry with t_{corr} under near constant E_{corr} conditions was investigated by performing potentiostatic polarization tests.

5.3.4. Time-Dependent Behaviour of $|i_{meas-PS}|$ During Potentiostatic Polarization

The $|i_{meas-PS}|$ as a function of time observed at various E_{elec} during potentiostatic polarization are presented in **Figure 5.8**. In the figure, the data were grouped according to the potential ranges defined earlier: (R1) $E_{elec} < E_{Ni^{0} \rightleftharpoons Ni(OH)_2}^{eq}$;

$$(R2) \quad E_{Ni^{0} \rightleftharpoons Ni(OH)_2}^{eq} < E_{elec} < E_{Ni^{0} \rightleftharpoons Ni(OH)_2 / Ni(OH)_3}^{mid}; \quad (R3) \quad E_{Ni^{0} \rightleftharpoons Ni(OH)_2 / Ni(OH)_3}^{mid} < E_{elec} <$$

$$E_{Ni^{0} \rightleftharpoons Ni(OH)_3}^{eq}; \quad (R4) \quad E_{Ni^{0} \rightleftharpoons Ni(OH)_3}^{eq} < E_{elec}.$$

In Chapter 4, we have discussed the combined effect of E_{elec} and pH on the time-dependent behaviour of $|i_{meas-PS}|$ in high I_s solutions. In this chapter, we will focus on the combined effect of I_s with E_{elec} and pH.

Figure 5.8 shows that at specific pH, I_s and E_{elec} , the $\log|i_{meas-PS}|$ vs $\log t$ plot showed distinct periods of characteristic time dependences. These periods, which are referred to as kinetic stages hereafter, are illustrated for an E_{elec} in R3 in **Figure 5.9**.

They are:

- (S1) in which $|i_{meas-PS}|$ is nearly constant with t ,
- (S2) in which $|i_{meas-PS}|$ decreases with t , and
- (S3) in which $|i_{meas-PS}|$ fluctuates with t about an average value that remains nearly constant with t .

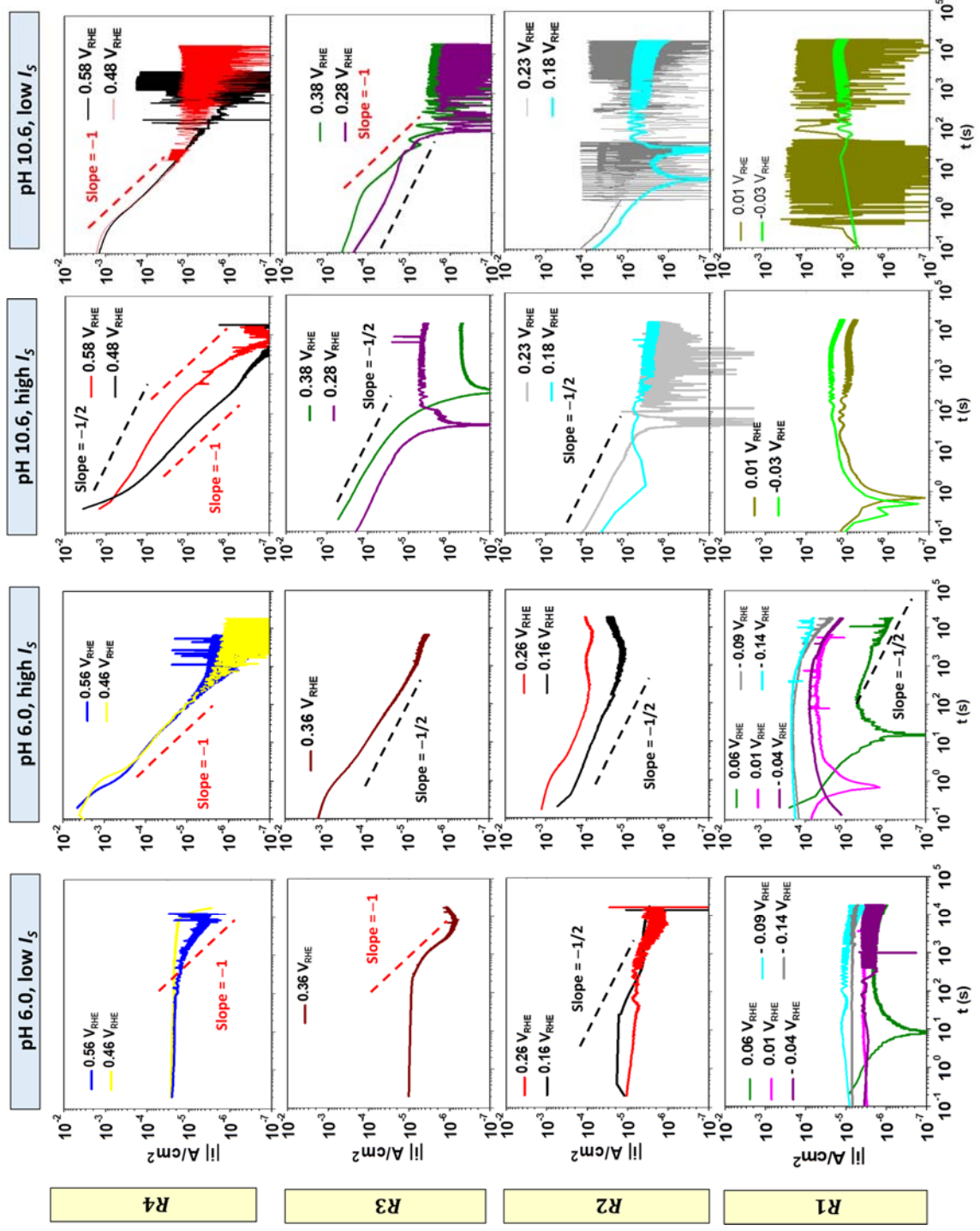


Figure 5.8: Time-dependent behaviours of $|l_{meas-ps}|$ observed at various E_{eltec} under potentiostatic polarization at pH 6.0 and pH 10.6 in low versus high I_s solutions. The data are grouped together according to potential ranges. Dashed lines with slopes of -0.5 (black) and -1.0 (red)

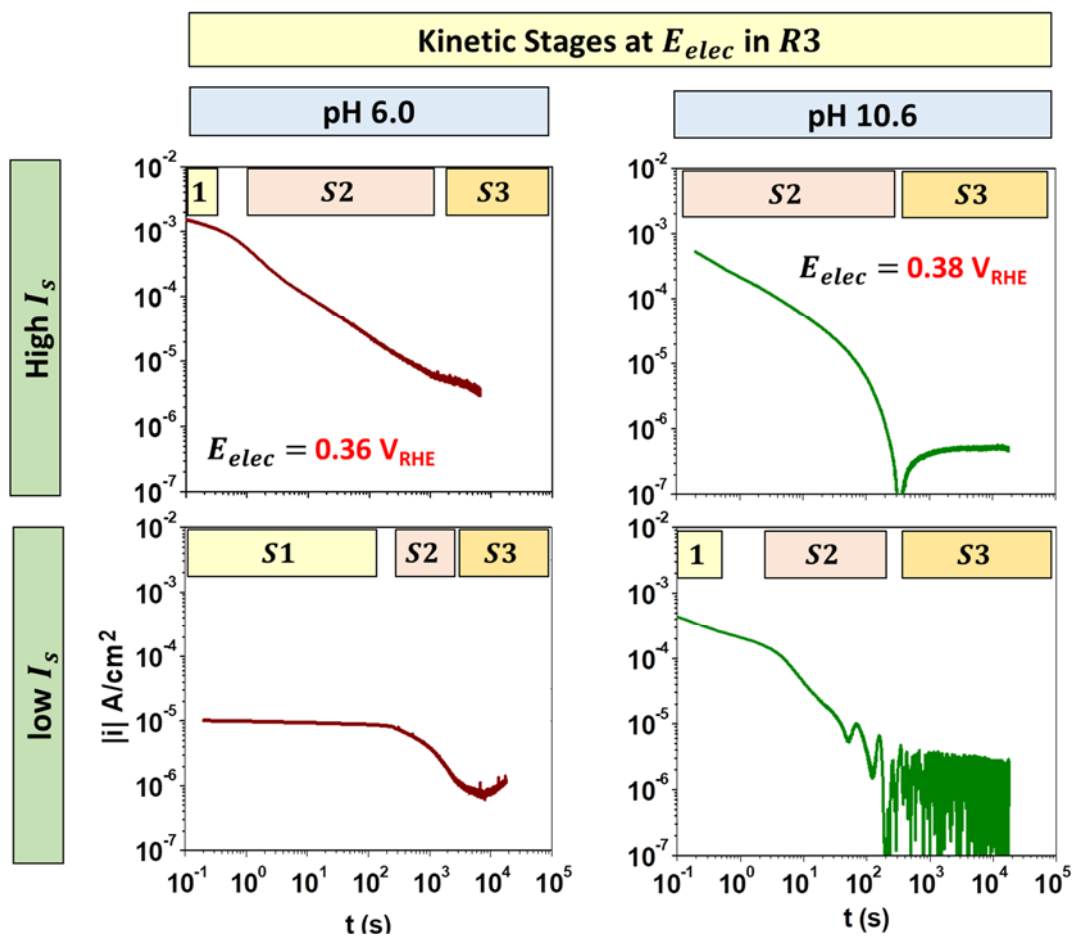


Figure 5.9: Illustration of the periods of metal oxidation kinetic stages observed during potentiostatic polarization at an E_{elec} in potential range R3.

The duration and the value of $|i_{meas-PS}|$ of each stage varied with pH, I_s and E_{elec} . The effects of pH and I_s on the time-dependent behaviour of $|i_{meas-PS}|$ at E_{elec} in different anodic potential regions (R2, R3 and R4) can be better appreciated from **Figure 5.10**. The observed effects are:

- The duration of (S1) was shorter in higher I_s solutions and at higher pHs. In the high I_s solutions, the duration was shorter than 0.1 s (hence not detected) at pH 10.6 and shorter than 1 s at pH 6.0. The duration was longer in the lower I_s

solutions, but the effect of I_s was more significant at the lower pH. At pH 10.6 (S1) was detected only at high E_{elec} .

- The $|i_{meas-PS}|$ in (S1) was larger at higher E_{elec} and in higher I_s solutions. The E_{elec} dependence of $|i_{meas-PS}|$ was much weaker in the low I_s solutions.
- The time-dependence of $|i_{meas-PS}|$ in (S2) depended on the potential range of E_{elec} independent of pH or I_s . The current decreased approximately proportionally to \sqrt{t} (the slope of $\log|i_{meas-PS}|$ vs $\log t$ is -0.5) when E_{elec} was in R2, while it decreased nearly linearly in R4. The time-dependent behaviour switched from the square-root to linear dependence at an E_{elec} in R3.
- The $|i_{meas-PS}|$ in (S3) fluctuated with time, about the near constant average value. The amplitude of high frequency fluctuation was largest at E_{elec} in R2 at pH 10.6 while in R4 at pH 6.0 indicate that these fluctuations were due to constant nucleation-desorption of mixed Ni^{II}/Ni^{III} hydroxide and associated changes in transport of H^+ and Ni^{2+} . The low frequency fluctuation observed at pH 6.0 is due to change in the strength of systemic feedback between different elementary steps.
- The average $|i_{meas-PS}|$ in (S3) increased with E_{elec} within each potential range. However, the E_{elec} dependence of $|i_{meas-PS}|$ changed when the potential range was changed.

Both pH and I_s affected the average $|i_{meas-PS}|$ in (S3). However, the combined effect was not additive. The anodic current was significantly lower at pH 10.6 than at pH 6.0 in higher I_s solutions. Lowering I_s decreased the anodic current

significantly at pH 6.0, but it had a negligible effect at pH 10.6. (Lowering I_s actually increased the i_{ox} at E_{elec} in R2 and R3 at pH 10.6).

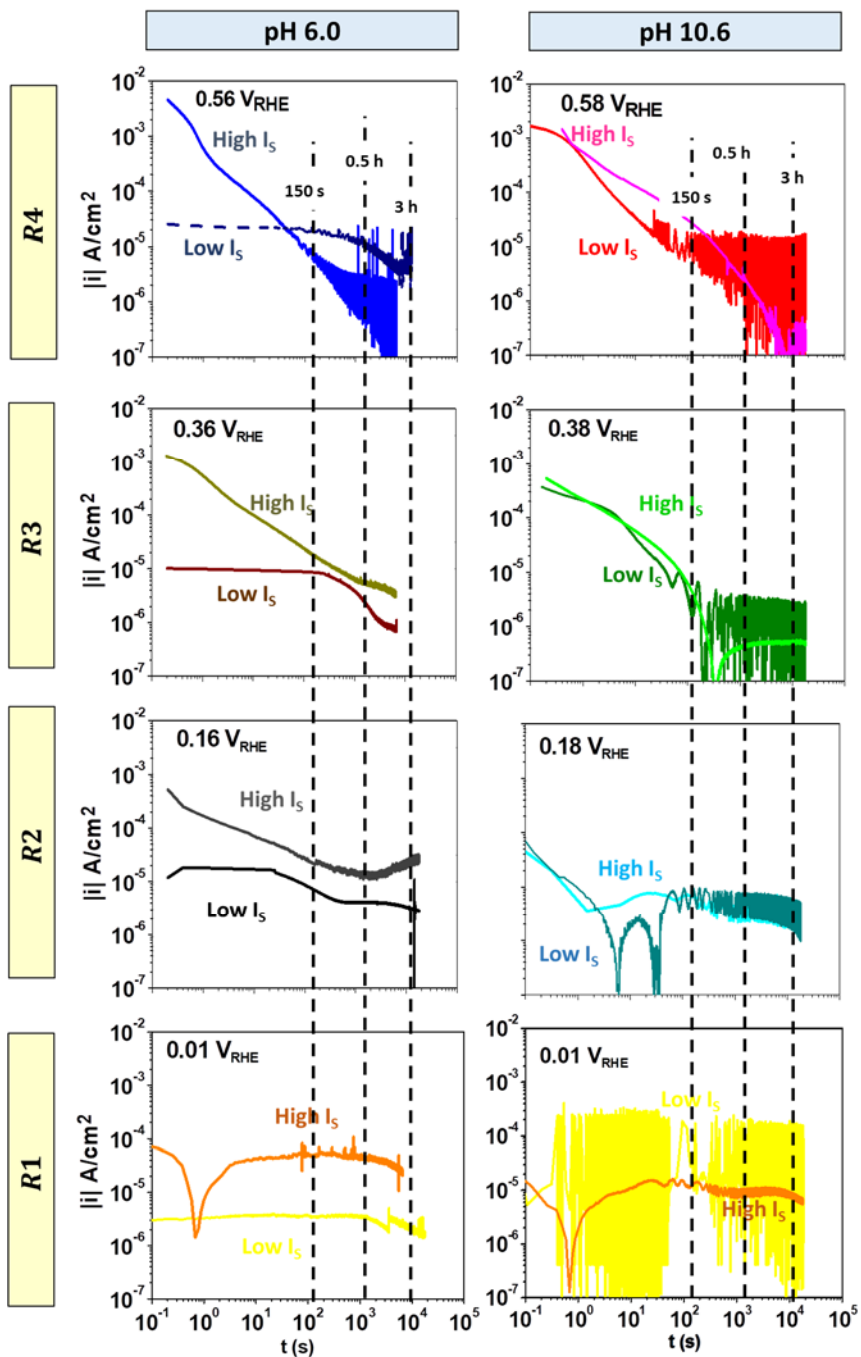


Figure 5.10: Effect of I_s on time-dependent behaviour of $|i_{meas-PS}|$ at an E_{elec} in each anodic potential range at pH 6.0 versus at pH 10.6. The data are grouped together according to potential ranges. The vertical lines indicate 150 s, 0.5 h and 3 h on the log t scale.

The observed time-dependent behaviour of $|i_{meas-PS}|$ as a function of pH, I_s and E_{elec} are also consistent with the proposed metal oxidation mechanisms presented in **Table 5.1** and **Figure 5.1**.

At E_{elec} in R2 where the E_{corr} values at pH 6.0 in Ar-purged solution were observed, the overall metal oxidation is controlled mainly by (M1) and (trans) (Dynamic Phase I). The slower (trans) is, the slower (M1) and the slower overall oxidation rate (ν_{ox}), are: $\nu_{ox} \approx \nu_{M1} \approx \nu_{trans}$ (see Eq. 5.5a). (M1) is a reversible process, consisting of the forward and reverse reactions and hence, $\nu_{M1} \approx \nu_{M1f} - \nu_{M1r}$. The concentration of the oxidation product in the interfacial region $(a_{Ni^{2+}})_{int}$ is controlled by ν_{M1} and ν_{trans} . However, while ν_{M1f} is independent of $(a_{Ni^{2+}})_{int}$, ν_{M1r} and ν_{trans} increases with $(a_{Ni^{2+}})_{int}$. Because of the interdependence of $(a_{Ni^{2+}})_{int}$ and ν_{ox} , the overall oxidation kinetics change with time. At E_{elec} in R2, the metal oxidation kinetics at different stages and the effects of pH and I_s on the kinetics are:

- Kinetic stage (S1) represents the period in which $(a_{Ni^{2+}})_{int}$ is below the Ni^{2+} saturation limit. Because $\nu_{M1f} > \nu_{M1r}$, ν_{ox} is mainly controlled by ν_{M1f} and ν_{trans} and is nearly constant with time.
- Ionic strength has a considerable effect on ion mobility and hence, ν_{trans} . Accordingly, the overall metal oxidation current ($i_{ox} = 2F \cdot \nu_{ox}$) in (S1) is lower in lower I_s solutions.

- As the net oxidation continues, $(a_{\text{Ni}^{2+}})_{int}$ increases, albeit slowly, reaching near saturation limit. v_{M1r} is no longer negligible and increases with $(a_{\text{Ni}^{2+}})_{int}$. The net rate of (M1) is no longer constant with time but decreases with time.
- Kinetic stage (S2) represents the period in which $(a_{\text{Ni}^{2+}})_{int}$ increases and v_{ox} decreases with time. At E_{elec} in R2 they change at parabolic rates ($\propto \sqrt{t}$) because v_{trans} depends not on $(a_{\text{Ni}^{2+}})_{int}$ but its gradient.
- The slower the v_{ox} in (S1) is and the higher the Ni^{2+} saturation capacity is, the longer the duration of (S1). Hence, the duration of (S1) is longer at lower pHs and in lower I_s solutions.
- Kinetic stage (S3) represents the period in which $(a_{\text{Ni}^{2+}})_{int}$ is at or slightly above the Ni^{2+} saturation capacity and hence, becomes constant with time again.
- v_{trans} is approximately proportional to $\sqrt{(a_{\text{Ni}^{2+}})_{int}}$ when the bulk concentration is negligible. The Ni^{2+} saturation capacity decreases exponentially with pH. Hence, in (S3), the overall metal oxidation current ($i_{ox} = 2F \cdot v_{ox}$) in (S1) is lower at higher pHs and in lower I_s solutions.

At E_{elec} in R4, where the E_{corr} values at pH 10.6 in Ar-sparged solution were observed, the contributions of elementary steps other than (M1) and (trans) to rate determining are not negligible (Dynamic Phase II). As discussed earlier, in Phase II, the relationship between the overall oxidation rate and current with those of elementary steps are (Eq. 5.6a and Eq. 5.6b)

Compared to those at E_{elec} in R2, the kinetics of different stages at E_{elec} in R4 are,

- In (S1), ν_{M2} and ν_{gel} are zero. Hence, the kinetics of the overall metal oxidation are the same as that at the lower potentials. Except for the difference due to higher rate of (M1) at higher E_{elec} (on the V_{RHE} scale) in high I_s solutions.
- In (S2), ν_{M1} decreases nearly linearly with time because of precipitation of mixed Ni^{II}/Ni^{III} hydroxide (gel) and its conversion to solid oxide (oxide) which suppresses (M1) and (M2).
- In (S3), the surface is covered with hydroxide and oxide precipitates and ν_{M1} and ν_{M2} are very small and fluctuate depending on precipitation-dissolution dynamics of the mixed hydroxide and its conversion to solid oxide [33,34].

The pH and I_s affect the kinetics at E_{elec} in R4 via the same mechanism as for those at E_{elec} in R2, pH via its effect on saturation capacity and I_s via its effect on ion mobility of Ni^{2+} .

The time-dependent behaviour of $|i_{meas-PS}|$ as a function of E_{elec} , and the potential dependent behaviours of $|i_{meas-CV}|$ and $|i_{meas-PD}|$ obtained as a function of t_{corr} can be used to extract different metal oxidation rate parameters and their dependences on solution environmental parameters. These parameters are required to develop corrosion dynamic models that can evaluate the overall corrosion damage of Ni as a function of service environments. It is important to mention that the PS tests were done only for 5 h, and by 5 h the other processes start affecting the overall metal oxidation rate. The dynamic model development is underway and will be reported elsewhere.

5.3.5. Time-Dependent Behaviour of Metal Oxidation Products

Figure 5.11 shows the amount of nickel ions dissolved in the solution ($[\text{Ni}^{2+}]_{\text{bulk}}$) during coupon exposure tests after 30 mins to 24 h of nickel corrosion. For the electrochemical tests conducted in large solution volumes the bulk concentration would be negligible over long duration, but in small solution volumes it may increase to a significant level potentially affecting (trans) in stage (S3). Similar to (trans) the rates of hydroxide, gel and solid oxides cannot be directly determined from $i_{(ox)} - E$ relationship, but the change in the relationship with t_{corr} provides information about their growth with time which is further explained in chapters 6 and 7.

To investigate the effect of ionic strength and pH on Ni^{2+} diffusion rate versus oxide precipitation, the amount of $[\text{Ni}^{2+}]_{\text{bulk}}$ is plotted vs \sqrt{t} . As observed during the first few hour of nickel corrosion for all solution conditions, $[\text{Ni}^{2+}]_{\text{bulk}}$ linearly increased with \sqrt{t} . This indicates that the corrosion mainly undergoes metal dissolution with constant dissolution rate. The rate of ion dissolution and the maximum amount of nickel dissolved during this time strongly depend on solution pH and ionic strength. At pH 6.0, the rate of dissolution and the maximum $[\text{Ni}^{2+}]_{\text{bulk}}$ dissolved during this period are higher than at pH 10.6. Moreover, at pH 6.0 by decreasing ionic strength the $[\text{Ni}^{2+}]_{\text{bulk}}$ and the dissolution rate also decreased by a factor of 10. Albeit at pH 10.6, the $[\text{Ni}^{2+}]_{\text{bulk}}$ and the dissolution rate are higher at lower ionic strength. The dissolved concentration is related to (trans) which is not always the same as $i_{(ox)}$, particularly at pH 10.6 and also at longer times at pH 6.0.

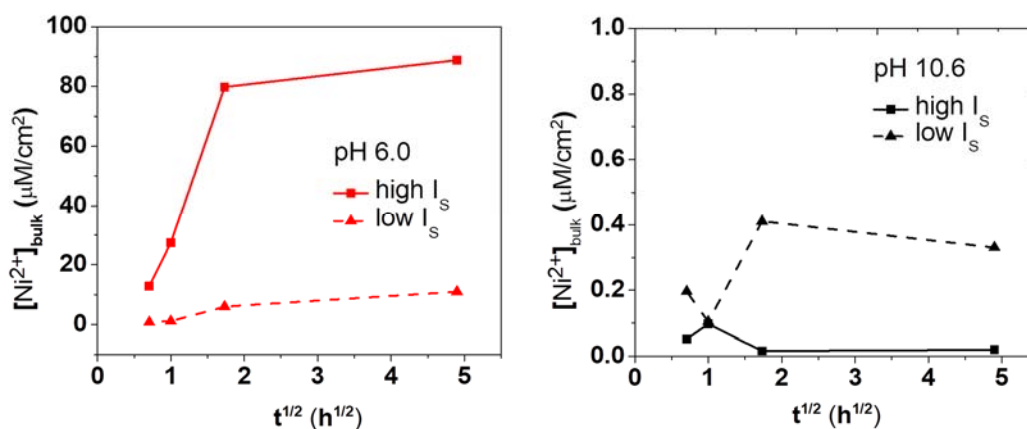


Figure 5.11: The amount of nickel ions dissolved in the solution vs \sqrt{t} at pH 6.0 and 10.6 for low and high ionic strength.

At longer times, at all conditions the trend of $[\text{Ni}^{2+}]_{\text{bulk}}$ vs \sqrt{t} is different. At pH 6.0 in both ionic strengths, the nickel concentration continuously increased over longer times, however the slope is significantly smaller than at the beginning. This indicates that the rate of metal dissolution is limited by mass transport processes and/or the gradual formation of an oxide layer on the surface. At pH 10.6, this value remained constant and/or slightly decreased over time. This indicates that there is no more nickel ion dissolution at this time and the saturated nickel ions at the interface can precipitate on the surface to form an oxide layer.

5.4. CONCLUSIONS

In this chapter, the combined effect of pH and ionic strength (I_s) on the evolution of Ni oxidation was investigated under Ar-purged conditions at pH 6.0 or pH 10.6 at 80 °C using electrochemical technique. The electrochemical analyses performed included E_{corr} as a function of corrosion time, potentiodynamic (PD) polarization measurement, multiple cycles of CV with different vertex potentials, and potentiostatic (PS) polarization measurements as a function of time at various E_{elec} .

The time-dependent behaviours of E_{corr} showed that Ni⁰ is oxidized to Ni(OH)₂ and Ni(OH)₃ in Ar-purged solutions. The E_{corr} coincided with the E_{rxn}^{eq} of metal redox half-reactions, $E_{Ni^0 \rightleftharpoons Ni(OH)_2}^{eq}$ at pH 6.0 and $E_{Ni^0 \rightleftharpoons Ni(OH)_3}^{eq}$ at pH 10.6. The overall effects of pH and I_s on E_{corr} depends on their effects on the kinetics of the elementary steps and the saturation capacity for Ni²⁺ at the interfacial region. The saturation capacity of metal cation depends strongly on pH. At pH 6.0, the solubility of Ni²⁺ is about four orders of magnitude higher than at pH 10.6. Hence, the Ni²⁺ concentration in the interfacial region remains below its saturation limit, and the overall metal oxidation does not progress beyond the oxidation of Ni⁰ to Ni²⁺/Ni(OH)₂. The overall rate of metal oxidation consists of interfacial charge (electron/metal atom) transfer (M1) and transport of Ni²⁺ (trans) (Dynamic Phase I). At pH 10.6, the solubility of Ni²⁺ is very low and therefore, the Ni²⁺ concentration in the interfacial region reaches its saturation limit nearly instantly. Once the interfacial region becomes saturated with Ni²⁺, metal atoms cannot be transferred from the metal to the solution, and the hydrolysis equilibrium (hyd) leads to the formation of Ni(OH)₂. Ni(OH)₂ precipitates as hydroxide salt (gel) and is oxidized to Ni(OH)₃. The overall metal oxidation consists of not only (M1), (trans) and (hyd), but

also (M2) and (gel) (Dynamic Phase II). The effect of I_s on the overall metal oxidation rate is through its effect on the transport of Ni^{2+} (trans), which is coupled strongly with other elementary steps. Due to systemic feedback between different elementary steps, the rates of individual steps change with time. At pH 10.6, (M2) becomes an important RDS even at early stages of corrosion, and $E_{corr}(\tau_0)$ reaches a value near $E_{\text{Ni}^{2+} \rightleftharpoons \text{Ni}(\text{OH})_3}^{eq}$.

The observed changes in E_{corr} , $E_{i=0,PD}$, and the $\log|i_{meas-PD}|$ vs E_{elec} relationship with t_{corr} collectively indicate that the elementary reaction and transport steps that comprise the overall metal oxidation process evolve as corrosion progresses. Because pH and I_s affect the kinetics of different steps differently, the effect of I_s on overall metal oxidation rate is different at different pH. The time-dependent behaviour of $|i_{meas-PS}|$ as a function of E_{elec} , and the potential dependent behaviours of $|i_{meas-CV}|$ and $|i_{meas-PD}|$ obtained as a function of t_{corr} further supports the elementary steps that control the overall corrosion behaviour at pH 6.0 (Dynamic Phase I) and pH 10.6 (Dynamic Phase II).

The results presented in this chapter show that the overall metal oxidation occurs through a series of elementary rate-determining steps (RDS) with some steps occurring in parallel. Because metal oxidation involves interfacial transfer of metal atoms and the intermediate oxidation products can undergo their own chemical processes, the rate determining step (RDS) that comprises the overall oxidation process can evolve as the intermediate products accumulate in the interfacial region. The composition of the RDS, that determines the steady state of the reaction system, can change with corrosion time even under specific corrosion conditions. The metal oxidation dynamic system may transition from one (pseudo-) steady state to another before it reaches the final steady

state. The final steady state (dynamic phase) the system reaches, and how fast the system passes through intermediate steady states (kinetic stages) to reach the final steady state, depend on solution reaction environments in the interfacial region.

Our results show that the kinetics of interfacial charge (electron/metal atom) transfer (M1) and transport of Ni^{2+} (trans), and the saturation capacity of the solution for Ni^{2+} , are very important parameters that determine whether the metal oxidation can progress beyond Dynamic Phase I. In Dynamic Phase I the kinetics of both (M1) and (trans), that contribute to determination of the overall rate of metal oxidation, are independent of each other, because the net rate of (M1), consisting of (M1f) and (M1r), depends on the Ni^{2+} concentration (activity) in the interfacial region ($(a_{\text{Ni}^{2+}})_{int}$) while $(a_{\text{Ni}^{2+}})_{int}$ accumulates at a rate determined by both (M1) and (trans).

At pH 6.0 when the solubility of Ni^{2+} is large $(a_{\text{Ni}^{2+}})_{int}$ is not accumulated above its saturation capacity. The chemical reactions of Ni^{2+} , (hyd), (gel) and (M2), in Ar-sparged environment are too slow to compete with (trans). Consequently, the metal oxidation dynamic system does not progress beyond Phase I, i.e., the RDS of the final steady state are (M1) and (trans). Ionic strength (I_s) affects ion mobility and has a significant effect on the rate of (trans). At pH 10.6, when the solubility of Ni^{2+} is significantly reduced, $(a_{\text{Ni}^{2+}})_{int}$ quickly reaches its saturation capacity. The hydrolysis equilibrium quickly shifts to $\text{Ni}(\text{OH})_2$ formation, accelerating (gel) and (M2). The metal oxidation system quickly progresses beyond Phase I and into Phases II (and perhaps Phase III at longer times). I_s does not affect the kinetics of (gel) and (M2) directly. However, the kinetics of (gel) and (M2) strongly influence the rate of (trans). Hence, in

large volume Ar-purged solutions, the effect of I_s on the overall oxidation rate is diminished at pH 10.6, compared to that at pH 6.0.

5.5. REFERENCES

- [1] Y. Wang, C. Yin, Q. Zhuang, An electrochemical sensor modified with nickel nanoparticle/nitrogen-doped carbon nanosheet nanocomposite for bisphenol A detection, *J. Alloys Compd.* 827 (2020) 154335. <https://doi.org/10.1016/j.jallcom.2020.154335>.
- [2] D. Wang, W. Yan, G.G. Botte, Exfoliated nickel hydroxide nanosheets for urea electrolysis, *Electrochem. Commun.* 13 (2011) 1135–1138. <https://doi.org/10.1016/j.elecom.2011.07.016>.
- [3] C. Daniel, J.O. Besenhard, *Handbook of battery materials*, Wiley, 2012.
- [4] X. Li, F.C. Walsh, D. Pletcher, Nickel based electrocatalysts for oxygen evolution in high current density, alkaline water electrolyzers, *Phys. Chem. Chem. Phys.* 13 (2011) 1162–1167. <https://doi.org/10.1039/c0cp00993h>.
- [5] Y. Miao, L. Ouyang, S. Zhou, L. Xu, Z. Yang, M. Xiao, R. Ouyang, Electrocatalysis and electroanalysis of nickel, its oxides, hydroxides and oxyhydroxides toward small molecules, *Biosens. Bioelectron.* 53 (2014) 428–439. <https://doi.org/10.1016/j.bios.2013.10.008>.
- [6] W. Xia, X. Zhao, L. Yue, Z. Zhang, A review of composition evolution in Ni-based single crystal superalloys, *J. Mater. Sci. Technol.* 44 (2020) 76–95. <https://doi.org/10.1016/j.jmst.2020.01.026>.
- [7] M. Dodaran, A.H. Etefagh, S.M. Guo, M.M. Khonsari, W.J. Meng, N. Shamsaei, S. Shao, Effect of alloying elements on the γ' antiphase boundary energy in Ni-base superalloys, *Intermetallics.* 117 (2020) 106670. <https://doi.org/10.1016/j.intermet.2019.106670>.
- [8] M. Behazin, Radiation induced corrosion of Stellite-6, *Electron. Thesis Diss. Repos.* 2432, University of Western Ontario (2014).
- [9] J. Wang, J. Wang, E.H. Han, Influence of Conductivity on Corrosion Behavior of 304 Stainless Steel in High Temperature Aqueous Environment, *J. Mater. Sci. Technol.* 32 (2016) 333–340. <https://doi.org/10.1016/j.jmst.2015.12.008>.
- [10] D. Guo, Corrosion Dynamics of Carbon Steel in Used Fuel Container Environments, *Electron. Thesis Diss. Repos.* 5897, University of Western Ontario (2018).

- [11] Y. Liu, Z. Zhang, N. Bhandari, Z. Dai, F. Yan, G. Ruan, A.Y. Lu, G. Deng, F. Zhang, H. Al-Saiari, A.T. Kan, M.B. Tomson, New Approach to Study Iron Sulfide Precipitation Kinetics, Solubility, and Phase Transformation, *Ind. Eng. Chem. Res.* 56 (2017) 9016–9027. <https://doi.org/10.1021/acs.iecr.7b01615>.
- [12] M. Semmler, E.K. Mann, J. Rička, M. Borkovec, Diffusional deposition of charged latex particles on water - Solid interfaces at low ionic strength, *Langmuir*. 14 (1998) 5127–5132. <https://doi.org/10.1021/la9801559>.
- [13] A. Persat, R.D. Chambers, J.G. Santiago, Basic principles of electrolyte chemistry for microfluidic electrokinetics. Part I: Acid-base equilibria and pH buffers, *R. Soc. Chem.* 9 (2009) 2437–2453. <https://doi.org/10.1039/b906465f>.
- [14] H.S. Harned, B.B. Owen, *The Physical Chemistry of Electrolytic Solutions*, American Chemical Society Monograph Series, New York, 1964.
- [15] M. Xu, K. Sullivan, G. Vanness, K.G. Knauss, S.R. Higgins, Dissolution kinetics and mechanisms at dolomite-water interfaces: Effects of electrolyte specific ionic strength, *Environ. Sci. Technol.* 47 (2013) 110–118. <https://doi.org/10.1021/es301284h>.
- [16] L. Arnaut, Hugh Burrows, *Elementary Reactions in Solution*, in: *Chem. Kinet.*, Elsevier Science, 2006.
- [17] H. Strathmann, *Electromembrane Processes: Basic Aspects and Applications*, in: *Compr. Membr. Sci. Eng.*, Elsevier Ltd., 2017: pp. 355–392. <https://doi.org/10.1016/b978-0-12-409547-2.12257-7>.
- [18] J. Owen, *Ionic Conductivity*, in: *Compr. Polym. Sci. Suppl.*, Pergamon Press, 1989.
- [19] B. Beverskog, I. Puigdomenech, Revised Pourbaix diagrams for nickel at 25–300°C, *Corros. Sci.* 39 (1997) 969–980. [https://doi.org/10.1016/S0010-938X\(97\)00002-4](https://doi.org/10.1016/S0010-938X(97)00002-4).
- [20] P. Oliva, J. Leonardi, J.F. Laurent, C. Delmas, J.J. Braconnier, M. Figlarz, F. Fievet, A. de Guibert, Review of the structure and the electrochemistry of nickel hydroxides and oxy-hydroxides, *J. Power Sources.* 8 (1982) 229–255. [https://doi.org/10.1016/0378-7753\(82\)80057-8](https://doi.org/10.1016/0378-7753(82)80057-8).
- [21] C.F.B. Jr., R.E. Mesmer, *The Hydrolysis of Cations*, Krieger Publishing Company, 1976.
- [22] F. Xue, X. Wei, J. Dong, I.I.N. Etim, C. Wang, W. Ke, Effect of residual dissolved oxygen on the corrosion behavior of low carbon steel in 0.1 M NaHCO₃ solution, *J. Mater. Sci. Technol.* 34 (2018) 1349–1358. <https://doi.org/10.1016/j.jmst.2017.11.004>.
- [23] Y. Lu, J. Dong, W. Ke, Corrosion evolution of low alloy steel in deaerated bicarbonate solutions, *J. Mater. Sci. Technol.* 31 (2015) 1047–1058. <https://doi.org/10.1016/j.jmst.2014.10.013>.

- [24] Y.G. Shin, Nonlinear Dynamics of Carbon Steel Corrosion under Gamma Radiation, Electron. Thesis Diss. Repos. 7339, University of Western Ontario (2020).
- [25] A. J. Bard Larry R., Faulkner, Electrochemical Methods Fundamentals and Applications, second, Wiley , 2001.
- [26] Nestor Perez, Electrochemistry and Corrosion Science, 1st ed., KluwerAcademic Publishers, 2004.
- [27] Z. Nagy, D.A. Thomas, Effect of Mass Transport on the Determination of Corrosion Rates From Polarization Measurements., Electrochem. Soc. Ext. Abstr. 85–2 (1985) 230–231. <https://doi.org/10.1149/1.2108331>.
- [28] L. Wang, X. Wei, D. Choi, X. Lu, G. Yang, C. Sun, Electrochemical cells for medium- and large-scale energy storage: fundamentals, in: Adv. Batter. Mediu. Large-Scale Energy Storage, Woodhead Publishing, Cambridge, 2015.
- [29] M. Momeni, Gamma-Radiation Induced Corrosion of Alloy 800, Electron. Thesis Diss. Repos. 5011, University of Western Ontario (2017). <https://doi.org/10.1016/j.psychres.2013.12.014>.
- [30] E. McCafferty, Validation of corrosion rates measured by the Tafel extrapolation method, Corros. Sci. 47 (2005) 3202–3215. <https://doi.org/10.1016/j.corsci.2005.05.046>.
- [31] K. Kakaei, M.D. Esrafil, A. Ehsani, Graphene and Anticorrosive Properties, in: Graphene Surfaces, 1st ed., Academic Press, 2019: pp. 303–337. <https://doi.org/10.1016/B978-0-12-814523-4.00008-3>.
- [32] R.A. Buchanan, E.E. Stansbury, Electrochemical Corrosion, in: Handb. Environ. Degrad. Mater., 2nd Editio, William Andrew, Tennessee, 2012: pp. 87–125. <https://doi.org/10.1016/B978-1-4377-3455-3.00004-3>.
- [33] T.I. Sutherland, C.J. Sparks, J.M. Joseph, Z. Wang, G. Whitaker, T.K. Sham, J.C. Wren, Effect of ferrous ion concentration on the kinetics of radiation-induced iron-oxide nanoparticle formation and growth, Phys. Chem. Chem. Phys. 19 (2017) 695–708. <https://doi.org/10.1039/c6cp05456k>.
- [34] A.Y. Musa, M. Behazin, J.C. Wren, Potentiostatic Oxide Growth Kinetics on Ni-Cr and Co-Cr Alloys: Potential and pH Dependences, Electrochim. Acta. 162 (2015) 185–197. <https://doi.org/10.1016/j.electacta.2015.02.176>.

CHAPTER 6

COMBINED EFFECTS OF pH, IONIC STRENGTH AND γ -RADIATION ON NICKEL OXIDATION IN SOLUTIONS OF SMALL STAGNANT VOLUMES AT 150 °C

6.1. INTRODUCTION

Nickel is an important element in many superalloys that exhibit superior mechanical properties and corrosion resistance [1]. The high corrosion resistance of these alloys is attributed to the preferential formation of passive oxide films on the alloy surfaces. For this reason, nickel-chromium-iron alloys are used in nuclear power plant components and corrosion-resistant materials for nuclear waste repositories [2,3]. In these applications, the nickel alloys are exposed to γ -radiation at high temperatures and in different solution environments. The presence of highly ionizing radiation can decompose water to a range of highly oxidizing (\bullet OH, H₂O₂, O₂) species. These species can participate in the corrosion process and affect the long term corrosion behaviour of these alloys [2,4].

In nuclear power plants, corrosion of these alloys can release corrosion products into the reactor coolant that can be transported to the reactor core. These products can

then be neutron activated, transported outside of the reactor core and redeposit on piping and components located outside the biological shield of the reactor core, posing a radiological hazard to plant workers [2,4,5].

To predict the corrosion behaviour of nickel-based alloys, it is important to understand the long-term corrosion behaviour of nickel metal under similar conditions. The corrosion behaviour of Ni, and particularly under radiation, is not well understood. The effect of solution parameters on nickel corrosion has also not been studied in detail [2].

Corrosion is an electrochemical process involving a series of elementary processes which include electrochemical redox reactions, solution reactions, transport processes and oxide particle nucleation and growth. The effect of the solution environment on corrosion is through its effect on elementary processes. Therefore, to predict the long-term behaviour of nickel alloys, it is important to identify the key elementary processes that control the overall corrosion rate [4,6].

One important factor influencing elementary processes in corrosion is the ionic strength (I_S) and conductivity of the electrolyte. The conductivity or ionic strength of the solution can affect ion mobility, and consequently the distribution of redox-active species near the electrode surface [7]. As described in Chapter 5, the overall metal oxidation occurs through a series of elementary rate-determining steps (RDS) with some steps occurring in parallel. Because metal oxidation involves interfacial transfer of metal atom and the intermediate oxidation products can undergo their own chemical processes, the RDS that comprise the overall oxidation process can evolve as the intermediate products accumulate in the interfacial region. That is, the composition of RDS, that determines the

steady state of the reaction system, can change with corrosion time even under specific corrosion conditions. The metal oxidation dynamic system may transition from a (pseudo-) steady state to another before it reaches the final steady state. In the previous studies presented in Chapters 4 and 5, the final steady state (dynamic phase) the system reaches, and how fast the system passes through intermediate steady states (kinetic stages) to reach the final steady state, depend on solution reaction environments in the interfacial region. The RDS that comprise the overall Ni oxidation process occurring in Ar-purged solutions of large volumes are listed in **Table 6.1** and schematically illustrated in **Figure 6.1** (reproduced from **Table 5.1** and **Figure 5.1**).

The previous studies have shown that the kinetics of interfacial charge (electron/metal atom) transfer (M1) and transport of Ni^{2+} (trans), and the saturation capacity of the solution for Ni^{2+} , are very important parameters that determine whether the metal oxidation can progress beyond Dynamic Phase I. We have shown that in Dynamic Phase I the kinetics of both (M1) and (trans), that contribute to determination of the overall rate of metal oxidation, are independent of each other, because the net rate of (M1), consisting of (M1f) and (M1r), depends on the Ni^{2+} concentration (activity) in the interfacial region ($(a_{\text{Ni}^{2+}})_{int}$) while $(a_{\text{Ni}^{2+}})_{int}$ accumulates at a rate determined by both (M1) and (trans).

Hence, in large volume and Ar-purged solutions, we observed that at pH 6.0 when the solubility of Ni^{2+} is large $(a_{\text{Ni}^{2+}})_{int}$ does not accumulate above its saturation capacity. The chemical reactions of Ni^{2+} , (hyd), (gel) and (M2), in Ar-purged environment are too slow to compete with (trans). Consequently, the metal oxidation dynamic system does not

progress beyond Phase I, i.e., the RDS of the final steady state are (M1) and (trans). Ionic strength (I_s) affects ion mobility and has a significant effect on the rate of (trans). At this pH, I_s affects the overall metal oxidation rate initially (kinetic stage (S1)) when $(a_{\text{Ni}^{2+}})_{int}$ remains low and hence, the overall metal oxidation rate is primarily controlled by (M1f) and (trans), and $v_{M1} \approx v_{M1f} \approx v_{trans}$. When $(a_{\text{Ni}^{2+}})_{int}$ is high, $v_{M1} \approx v_{M1f} - v_{M1r} \approx v_{trans}$. Hence, I_s affects the overall metal oxidation current initially and at the final steady state, and the time to reach the final steady state. At pH 10.6, when the solubility of Ni^{2+} is significantly reduced $(a_{\text{Ni}^{2+}})_{int}$ quickly reach its saturation capacity. The hydrolysis equilibrium quickly shifts to $\text{Ni}(\text{OH})_2$ formation, accelerating (gel) and (M2). The metal oxidation system quickly progresses beyond Phase I and into Phases II (and perhaps Phase III at longer times). I_s does not affect the kinetics of (gel) and (M2) directly. However, the kinetics of (gel) and (M2) strongly influence the rate of (trans). Hence, in large volume Ar-purged solutions, the effect of I_s on the overall oxidation rate is diminished at pH 10.6, compared to that at pH 6.0.

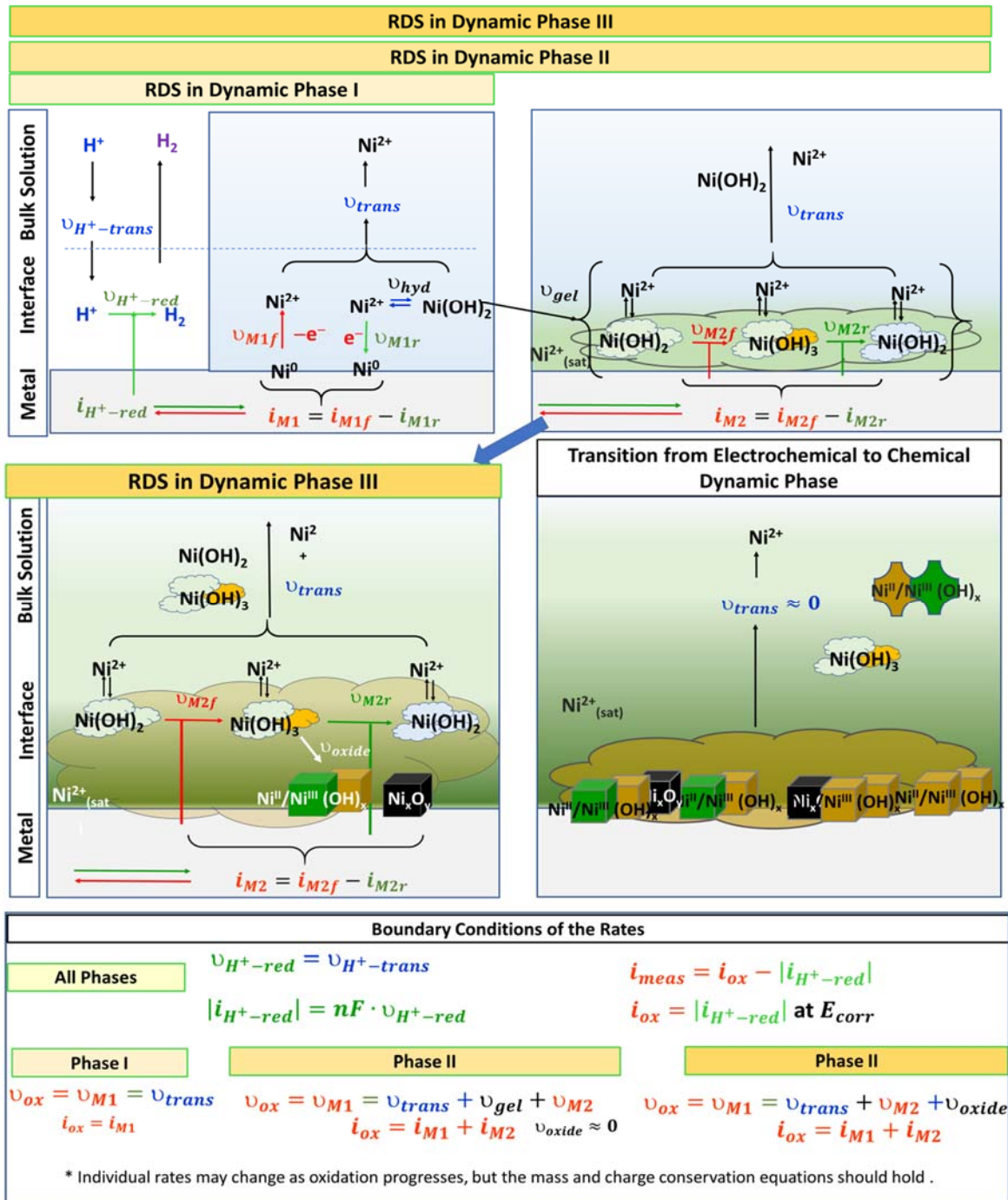


Figure 6.1: The Rate Determining Steps (RDS) arising during the corrosion process. For metal oxidation, the v_{M1f} is forward nickel oxidation rate of $Ni \rightleftharpoons Ni^{2+}$ and v_{M1r} is the rate of reverse reaction, v_{M2f} is the forward nickel oxidation rate of $Ni^{2+} \rightleftharpoons Ni^{3+}$ and v_{M2r} is the reverse reaction. v_{gel} , v_{oxide} and v_{trans} are the rate of gel, oxide formation and nickel cation transport to bulk respectively. For the solution species half-reaction v_{H^+-red} is the H^+ reduction rate and $v_{H^+-trans}$ is the rate of H^+ transfer from the bulk solution to the interface.

Table 6.1: Elementary Reactions Involved in the Overall Metal Oxidation Process

Rxn ID	Reaction Type	Chemical Equation	Rate ID
M1	Electron/metal-atom transfer	$\text{Ni}^0 _{\text{int}} \rightleftharpoons \text{Ni}^{2+} _{\text{int}} + 2 e^-$	$\frac{\nu_{\text{M1}}}{i_{\text{M1}}} = nF \cdot \nu_{\text{M1}}$
	<p>This is a reversible process, consisting of two reaction steps ($\nu_{\text{M1}} = \nu_{\text{M1f}} - \nu_{\text{M1r}}$):</p> <p>(M1f): $\text{Ni}^0 \rightarrow \text{Ni}^{2+} + 2 e^-$ $\nu_{\text{M1f}} = k_{\text{M1f}} \cdot (a_{\text{Ni}^0})_{\text{int}} \approx k_{\text{M1f}}$</p> <p>(M1r): $\text{Ni}^{2+} + 2 e^- \rightarrow \text{Ni}^0$ $\nu_{\text{M1r}} = k_{\text{M1r}} \cdot (a_{\text{Ni}^{2+}})_{\text{int}}$</p> <p>where $(a_{\text{Ni}^{2+}})_{\text{int}}$ represents the chemical activity of Ni^{2+} in the interfacial region.</p>		
trans	Ion diffusion	$\text{Ni}^{2+} _{\text{int}} \rightarrow \text{Ni}^{2+} _{\text{bulk}}$	ν_{trans}
M2	Electron transfer	$\text{Ni}^{2+}/\text{Ni}(\text{OH})_2 + \text{OH}^- \rightleftharpoons \text{Ni}(\text{OH})_3 + e^-$	$\frac{\nu_{\text{M2}}}{i_{\text{M2}}} = nF \cdot \nu_{\text{M2}}$
	<p>This is a reversible process, consisting of two reaction steps ($\nu_{\text{M2}} = \nu_{\text{M2f}} - \nu_{\text{M2r}}$):</p> <p>(M2f): $\text{Ni}^{2+}/\text{Ni}(\text{OH})_2 + \text{OH}^- \rightarrow \text{Ni}(\text{OH})_3 + e^-$ $\nu_{\text{M2f}} \approx k_{\text{M2f}} \cdot (a_{\text{Ni}^{\text{II}}})_{\text{int}}$</p> <p>(M2r): $\text{Ni}(\text{OH})_3 + e^- \rightarrow \text{Ni}^{2+}/\text{Ni}(\text{OH})_2 + \text{OH}^-$ $\nu_{\text{M2r}} = k_{\text{M2r}} \cdot (a_{\text{Ni}^{\text{III}}})_{\text{int}}$</p> <p>where $(a_{\text{Ni}^{\text{II}}})_{\text{int}}$ and $(a_{\text{Ni}^{\text{III}}})_{\text{int}}$ represent the overall redox activities of Ni^{II} and Ni^{III} species (dissolved & colloidal) in the interfacial region.</p>		
hyd	Hydrolysis	$\text{Ni}^{2+} + n \text{OH}^- \rightleftharpoons \text{Ni}(\text{OH})_x^{2-x} + (n-x) \text{OH}^-$	ν_{hyd}
gel	Hydrogel formation	$\text{Ni}(\text{OH})_2 + \text{Ni}(\text{OH})_3 \rightarrow x\text{Ni}(\text{OH})_2 \cdot y\text{Ni}(\text{OH})_3(\text{gel})$	ν_{gel}
oxide	Crystalline oxide growth	$\text{Ni}(\text{OH})_2 \cdot 2\text{Ni}(\text{OH})_3(\text{gel}) \rightarrow \text{Ni}_3\text{O}_4(\text{cryst}) + 4 \text{H}_2\text{O}$	ν_{oxide}

In this chapter, we explore the combined effect of pH and I_s in small volume and stagnant solutions under Ar saturated conditions, either in the absence or presence of a continuous flux of γ -radiation.

The convective solution flow under the stagnant conditions is negligible and hence, the rate of (trans) will be further affected. In a smaller solution volume the bulk concentration of Ni^{2+} ($[\text{Ni}^{2+}]_{\text{bulk}}$) increases faster at the same metal oxidation rate. Because the rate of (trans) depends on concentration gradient, the faster increase in $[\text{Ni}^{2+}]_{\text{bulk}}$ will decelerate (trans). The overall metal oxidation progresses quickly to Phase III. At long times, the overall metal oxidation may be very slow but the chemical processes of corrosion products, (trans), (gel) and (oxide), can continue. Ionic strength affects the oxide growth by Ostwald ripening from precipitation-redissolution of dissolved species [8].

In Dynamic Phase III, the overall metal oxidation current corresponds to the sum of the rates of (M1) and (M2). These rates are very small and the change in current is even more difficult to observe. In these slow dynamic stages the overall metal oxidation rate can be obtained from the overall yields of metal oxidation products over different durations. Hence, in this study we studied the long-term corrosion dynamics by examining the changes in oxide composition and morphology and the dissolved (and dispersed) Ni^{2+} concentration as a function of t_{corr} . In this study, dissolved metal concentration was analyzed by ICP-OES and the morphology of surface using optical microscopy and SEM and elemental composition of surface layer as a function of depth using AES.

6.2. EXPERIMENTAL

6.2.1 Materials and Solutions

A pure Ni rod 6.20 mm in diameter was cut into 3 mm thick circular flat coupons. For the coupon studies both flat sides of the sample (with a total surface area of 1.187 cm²) were exposed to the solution. Before each experiment, the flat coupon surfaces were mechanically abraded successively with 400, 600, 800, and 1200 grit silicon carbide papers, and then mirror-polished on a Texmet microcloth (Buehler) with the 1 μm MetaDi Supreme diamond paste suspension (Buehler). The samples were rinsed in a 1:1 acetone/ethanol mixture in an ultrasonic bath for 5 min to remove surface residues, and then rinsed with Type 1 water and dried with Ar.

All solutions were prepared using Type 1 water (purified using a NANO pure Diamond UV ultra-pure water system from Barnstead International) with a resistivity of 18.2 MΩ·cm. Solutions were prepared using sodium borate (Na₂B₄O₇·10H₂O), boric acid (H₃BO₃) and sodium hydroxide (NaOH), all purchased from Caledon Laboratories Ltd. The test solutions used were buffer solutions at pH 6.0, 8.4 and 10.6 and three different ionic strengths (**Table 6.2**). The pH of the solution was measured using an Accumet[®] Basic AB15 pH meter with an Ag/AgCl electrode. Different ionic strengths were obtained by the addition of different amounts of sodium borate and boric acid to the electrolyte solution.

Table 6.2: Solution preparation method, ionic strengths (I_s) and conductivity (κ)

pH	Low I_s	Mid I_s	High I_s
6.0	10 mM Boric Acid + Drops of NaOH $I_s=6.2 \times 10^{-6}$ M $\kappa= 12.34 \mu\text{S/cm}$	1 mM Sodium Borate + 25 mM Boric Acid $I_s=0.0020$ M $\kappa= 158.32 \mu\text{S/cm}$	10 mM Sodium Borate + 500 mM Boric acid $I_s=0.020$ M $\kappa=1295.17 \mu\text{S/cm}$
8.4	10 mM Boric Acid + Drops of NaOH $I_s=0.0013$ M $\kappa= 20.61 \mu\text{S/cm}$	1 mM Sodium Borate + 5mM Boric Acid $I_s=0.0021$ M $\kappa=166.60 \mu\text{S/cm}$	10 mM Sodium Borate + 50mM Boric Acid $I_s=0.021$ M $\kappa=1429.31 \mu\text{S/cm}$
10.6	10 mM Boric Acid + Drops of NaOH $I_s=0.001$ M $\kappa=39.57 \mu\text{S/cm}$	1 mM Sodium Borate + 0.00015mM NaOH $I_s= 0.0043$ M $\kappa=372.16 \mu\text{S/cm}$	10 mM Sodium Borate + 0.0015mM NaOH $I_s=0.039$ M $\kappa=2333.31 \mu\text{S/cm}$

6.2.2. Coupon Exposure Tests

The test vials were prepared in an Ar-filled glove box. The freshly polished coupons were placed in individual Pyrex/quartz vials and both sides of the coupon with a total surface area of 1.187 cm^2 were exposed to the test solution. Quartz was chosen since it has a low solubility at $150 \text{ }^\circ\text{C}$, and therefore less silica is expected to dissolve into the solution and interfere with the experiment. The Ar-purged test solutions (buffer solutions) were added to each vial and the vials were sealed using aluminum crimp caps fitted with PTFE silicone septa (Agilent Technologies). The crimp caps provided a vacuum seal to prevent solution evaporation and any ingress/egress of gas during the test duration. The sample vials were then placed in a 300 mL AISI 316 stainless steel autoclave (Parr Instrument Company) as shown in **Figure 6.2**.

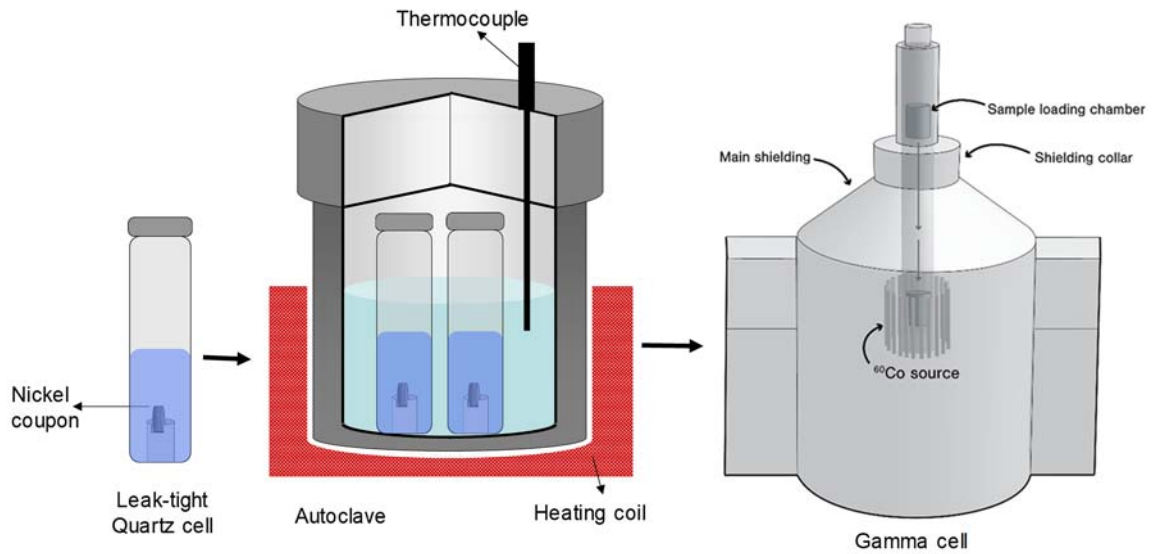


Figure 6.2: Experimental setup for coupon exposure tests in the presence and absence of gamma radiation.

6.2.3 Irradiation

All irradiation experiments were conducted in an MDS Nordion Gammacell 220 Excel Cobalt-60 irradiator, which provided an absorbed radiation dose of 2.5 kGyh^{-1} at the time of these experiments. The autoclave was heated to the desired temperature ($150 \text{ }^\circ\text{C}$) before being lowered into the irradiation zone, a cylindrical cavity surrounded by 11 tubular pencils containing ^{60}Co . Coupon exposure tests were conducted as a function of time.

For experiments in the absence of radiation, samples were prepared in similar manner and heated using the autoclave on the laboratory bench top.

6.2.4. Post-Test Analyses

After the test duration the nickel coupons were removed from the vials, washed with water, and dried with flowing argon. They were then stored in a vacuum chamber to await surface analysis. The solutions were transferred into glass vials and allowed to cool to room temperature before measuring the pH. These solutions were then digested using TraceMetal™ grade nitric acid (Fisher Chemical) and analyzed using a PerkinElmer Avio 200 ICP-OES instrument to determine the concentration of dissolved nickel ions in solution.

The morphology and composition of the oxide layer formed on the surface were investigated using optical microscopy, scanning electron microscopy (SEM) and Auger emission spectroscopy (AES). Optical images were obtained using a Leica DVM 6A digital microscope. The same lighting settings were used to image each sample. A LEO 1540XB field emission SEM was used in the high-resolution mode for analyzing the surface morphology. AES analysis was performed to measure the chemical composition of the first few monolayers of a given surface.

6.3. RESULTS AND DISCUSSION

The effect of ionic strength (I_s) on nickel corrosion was studied at 150 °C in de-aerated buffered solutions at three different pHs (6.0, 8.4 and 10.6) in the presence (RAD) and absence of radiation (No RAD). These pHs were chosen since the solubility of Ni ions changes by several orders of magnitude from pH 6.0 to 10.6, as shown in **Figure 6.3**.

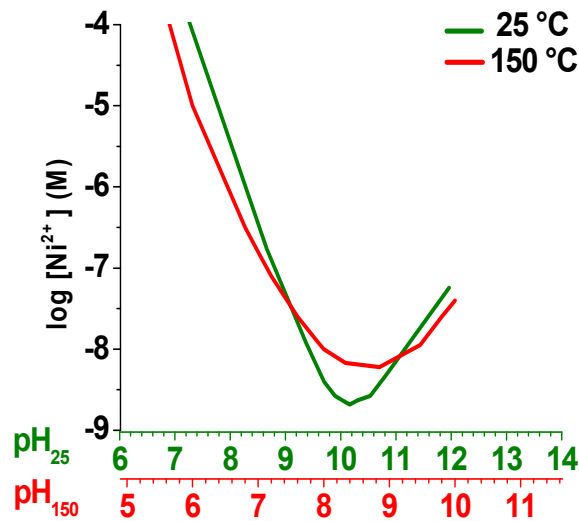


Figure 6.3: The solubility of Ni²⁺ in water at 25 and 150 °C [9,10].

6.3.1. Effect of Ionic Strength in the Absence of Radiation (No RAD)

The results obtained from the coupon exposure tests in deaerated buffered solutions at 150 °C in the absence of radiation for pHs 6.0, 8.4 and 10.6 and for test durations of 0 - 144 h are discussed first. The pH of the test solutions was measured prior to and after each corrosion test and the pH remained stable during the test durations.

6.3.1.1. Effect of Ionic Strength at pH 6.0 (No RAD)

In the work presented here, the morphology of corroded metal surface and the concentration of dissolved nickel ($[\text{Ni}^{2+}]_{\text{bulk}}$) were examined as a function of corrosion time (t_{corr}). The low-magnification optical micrographs and $[\text{Ni}^{2+}]_{\text{bulk}}$ observed for three different ionic strengths at pH 6.0 are shown in **Figure 6.4A** and the solution analysis of the same experiment is shown in **Figure 6.4B**.

As the solution analysis illustrates the evolution of $[\text{Ni}^{2+}]_{\text{bulk}}$ during the test duration (0 -144 h) occurs in a non-linear manner. This concentration at individual times shows fluctuation from its average value over time. Corrosion is an interfacial process involving both the metal and the solution electrochemical reactions (M1 and M2) and trans processes. There can be a strong feedback between electrochemical reactions, solution transport, dissolution and precipitation of corrosion products [8]. Hence, these fluctuations are expected for a process involving a phase transition (unlike for homogeneous solution reactions). These fluctuations and non-linear dynamic behaviours are influenced by changing the solution ionic strength and applying γ -radiation (see further discussion in this section and section 6.3.2).

In low and mid I_s solution the nickel concentration remained low, well below the solubility of nickel ions at pH 6.0, and fluctuated, within the test duration. For low I_s , during the first 48 h the $[\text{Ni}^{2+}]_{\text{bulk}}$ increased, followed by a decrease and an increase again after 120 h. For mid I_s , the $[\text{Ni}^{2+}]_{\text{bulk}}$ increased until 72 h followed by a decrease until 144 h. For high I_s , similar fluctuations were observed, with the $[\text{Ni}^{2+}]_{\text{bulk}}$ increasing during the first 24 h of nickel corrosion followed by a decrease, and an increase again after 72 h.

In all cases, the nickel concentration increased in the initial few hours of corrosion (low I_s (48 h), mid I_s (72 h) and high I_s (24 h)). This indicates that initially corrosion predominantly involves nickel cation dissolution (the slope of $[\text{Ni}^{2+}]_{\text{bulk}}$ represents the rate of nickel ion dissolution) along with minimal oxide precipitation on the surface (**Figure 6.6**). This slope is ~ 5 -6 times steeper for high I_s solution (slope $\approx 5.6 \times 10^{-7} \text{ M}\cdot\text{h}^{-1}$) compared to low (slope $\approx 1.45 \times 10^{-7} \text{ M}\cdot\text{h}^{-1}$) and mid I_s (slope $\approx 8.93 \times 10^{-8} \text{ M}\cdot\text{h}^{-1}$). At longer times precipitation on the surface can lead to a decrease in $[\text{Ni}^{2+}]_{\text{bulk}}$, and the slope associated with this process is ~ 2 times higher for high I_s ($1.67 \times 10^{-7} \text{ M}\cdot\text{h}^{-1}$) than for low ($9.04 \times 10^{-8} \text{ M}\cdot\text{h}^{-1}$) and mid I_s ($6.62 \times 10^{-8} \text{ M}\cdot\text{h}^{-1}$) (more discussion about these fluctuations is provided in section 6.3.2).

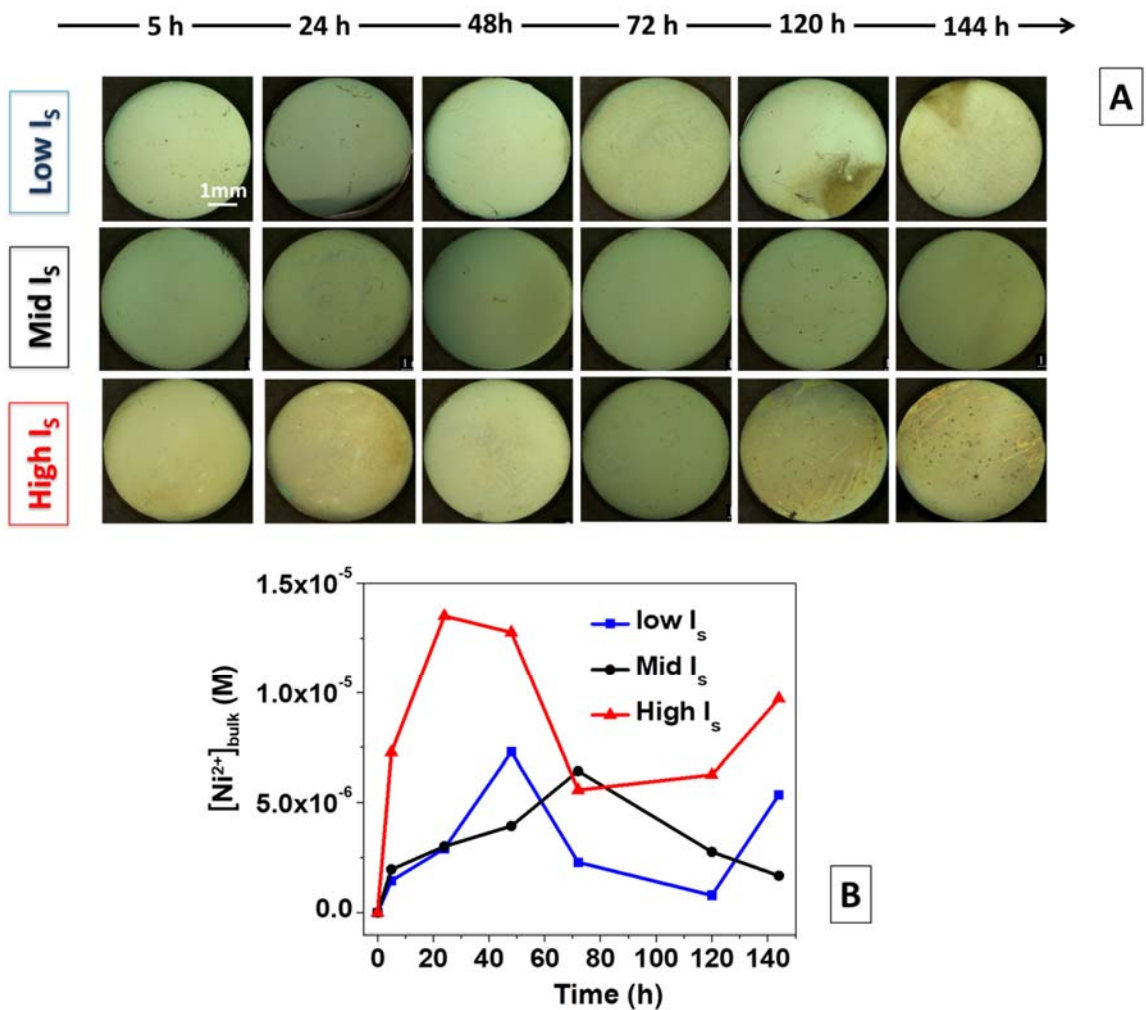


Figure 6.4: Nickel samples corroded at pH 6.0 at three ionic strengths in the absence of γ -radiation for test durations of 5-144 h: A) Low magnification optical micrographs of the entire coupon surfaces, B) Concentration of dissolved nickel ions in solution.

Optical microscopy provides information about the general surface topography through the colour and morphology of oxides formed on the surface (Figure 6.4A). Depending on the oxidation state, nickel oxides/hydroxides have characteristic colours. Nickel hydroxide (Ni(OH)₂) is green [11–13], NiO is green [14,15], Ni(OH)₃ is expected

to be brownish [12], and Ni_3O_4 and Ni_2O_3 are black in colour [16,17]. The colours of standard nickel oxide/hydroxide powder samples (Alfa Aesar) seen under the optical microscope are presented in **Figure 6.5**.

In general, the colour of the general area of coupon surface changed from light green to darker green. On the thin greenish layer, brownish spots were uniformly distributed across the surface and the number density and the average size of the brownish spots varied with time and I_s . As shown and discussed later, the changes in colour and its distribution across the surface represent those of hydroxide/oxide composition and morphology, the uniformly distributed greenish colour representing the gel-like layer consisting of $\text{Ni}^{2+}/\text{Ni}(\text{OH})_2$ with small amounts of $\text{Ni}(\text{OH})_3$ and the brownish spots representing $\text{Ni}(\text{OH})_3$ particles.

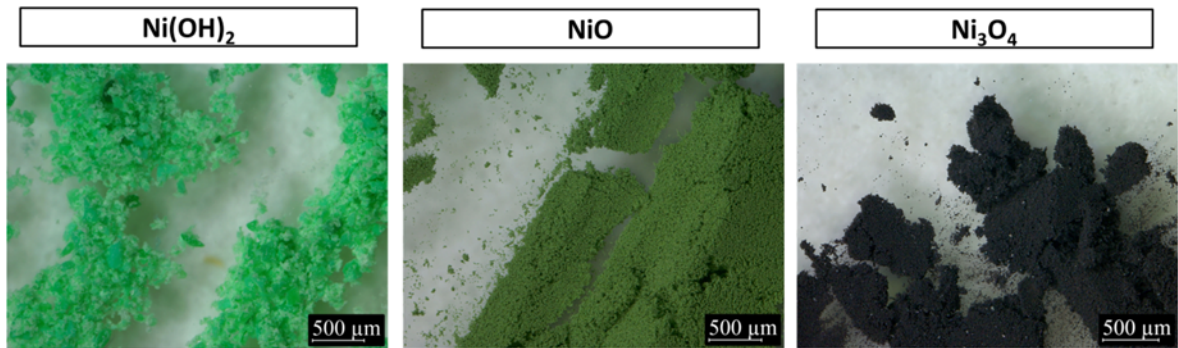


Figure 6.5: The colours of standard Ni hydroxide/oxide samples (Alfa Aesar) observed by optical microscopy.

This greenish colour could be due to the formation of a thin layer of $\text{Ni}(\text{OH})_2$ / NiO on the surface [11,14,15] and the darker layer due to formation of a higher oxidation state nickel hydroxide/oxide layer on the surface [12] (see further discussion in Chapter 7). Although during corrosion the formation of a pure single-phase oxide is not

expected, the oxide colour (as shown in **Figure 6.5**) can provide qualitative information on the main oxidation state of nickel and the extent of hydration and hydroxylation (i.e., hydroxide, oxyhydroxide or oxide) of the corrosion products.

High magnification optical and SEM images were taken to get a closer look at the physical features of the oxides formed on the metal surface. The high-resolution optical images and SEM images of nickel surfaces corroded in different I_s solutions are shown in **Figure 6.6**. Similar to the low magnification images, in general the surface remained uniform and greenish in colour, later developing a darker green layer (greenish-brown) on the surface. For high I_s solutions more of the brown oxide layer was observed on the surface.

The SEM images provide information about the morphology and distribution of the oxide layer formed on the surface. The SEM images of the coupons corroded in low and mid I_s solutions show a smooth surface with remnants of polishing lines visible, and there are some discrete areas of a thin filament-like oxide formed on the surface. The presence of polishing lines suggests that the oxide layer present on the surfaces is very thin. Filament-like nickel oxides were observed on the surface during the first 5 h (low I_s and mid I_s) of the experiment and at longer times ($t_{corr} \geq 72\text{h}$). This indicates that the dissolved nickel concentration evolution is consistent with the evolution of the surface morphology and the formation and growth of the oxide layer on the surface. The production of nickel ions during nickel oxidation is strongly coupled with precipitation/re-dissolution of nickel ions which causes the continuous evolution of $[\text{Ni}^{2+}]_{\text{bulk}}$ during nickel corrosion.

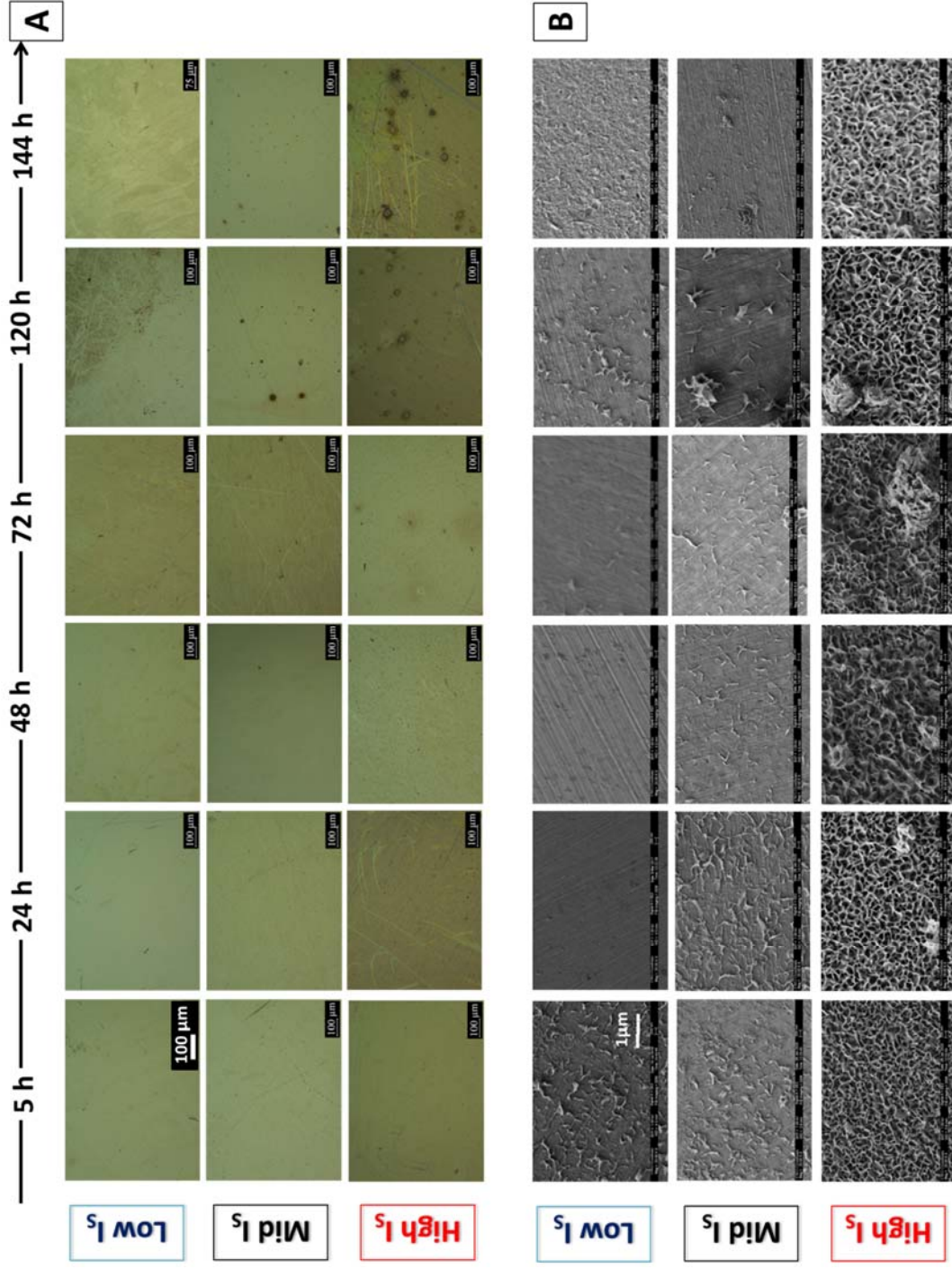


Figure 6.6: Nickel samples corroded at pH 6.0 at three ionic strengths and in the absence of γ -radiation (same samples as presented in Figure 6.5):
A) High magnification

optical micrographs, **B)** SEM images of the general oxide morphology of nickel samples.

For high I_s solutions, the filament-like oxide layer forms earlier on the surface and more surface coverage is observed. A filament-like morphology is a common feature associated with the more soluble form of many transition metal hydroxides (such as Co^{II} , Fe^{II} and Ni^{II} hydroxides) [2,5,18,19]. This oxide forms via hydroxide dehydration on the surface.

A comparison of both solution and surface analyses indicates that increasing the I_s increases the corrosion rate. This leads to dissolution of more nickel ions into solution (**Figure 6.4 B**) and the formation of more oxide on the surface (AES results in **Figure 6.16**). Moreover, the non-linear behaviour of nickel corrosion is more pronounced at higher I_s . This indicates that as continual evolution of $[\text{Ni}^{2+}]_{\text{bulk}}$ occurs during nickel oxidation it can be strongly coupled with precipitation/re-dissolution of nickel ions on the surface.

Generally, corrosion of metals involves several consecutive elementary steps in which the rate of each elementary process is critical in the overall corrosion process and corrosion rates [4,6]. The sequential elementary steps consist of nickel oxidation/solution reduction reactions at the metal surface, Ni^{2+} dissolution and ion transfer from/toward the solution phase, solution saturation at the interface and oxide formation.

The results presented in Chapter 5 and the results shown in **Figure 6.4** and **6.6**, illustrate that a change in solution ionic strength can change the rate of nickel corrosion, and this is due to an effect on the ion mobility and mass transport process of the ions [20–23]. The different mass transport conditions and concentration of charged species result in different time-dependent behaviours [8].

Nickel cations are produced during corrosion, and the solution near the surface (interfacial region) becomes saturated with nickel cations, since the rate of ion diffusion is lower than the rate of nickel oxidation (**Figure 6.1**). Saturation of Ni^{2+} at the interface influences the rate of redox electron transfer process and decreases the rate of corrosion. In dilute solutions, increasing the ionic strength or solution conductivity increases ion mobility [20], which can increase the rate of ion transfer [24]. Thus, Ni ions can move more rapidly from the interfacial region to the bulk solution and the higher the ionic strength, the thinner the saturation layer at the interface (Debye length) [25]. So, as the rate of ion mass transport (v_{trans}) increases, more nickel can be oxidized during corrosion and this increases the total rate of nickel ion production in high I_s solutions.

For high I_s solutions, circular features were observed on the coupon surface. The shapes of the circular patterns and depth profiles are shown in high magnification optical images in **Figure 6.7**. The mechanism for the formation and propagation of these surface features is discussed in more detail in Chapter 7 but will be briefly explained here. These patterns result from chemical waves caused by chemical oscillation and are known as Liesegang rings [8,26,27]. This phenomenon occurs in conditions where the solution reactions and mass transport processes are strongly coupled, which is a further confirmation of the presence of systemic feedback and non-linear dynamic behaviour during nickel corrosion [8,28]. The results presented in this chapter show that these features are amplified in higher ionic strength solutions (and/or in the presence of γ -radiation – see section 6.3.2). Non-linear corrosion dynamics occur in systems where there is strong coupling between elementary processes [6]. This coupling may occur between the redox reactions (M1 and M2) and trans processes and can be influenced by

solution ionic strength. Since the ion diffusion is faster in high I_s solution, the Liesegang ring spreads wider and the different oxide bands are not as well separated. In addition, the depth to width ratio of the pit is lower, in the high I_s solution, compared to the lower I_s solution.

The Liesegang banding consists of parallel bands of precipitated materials (metal hydroxide/oxide) which form in periodic patterns on the surface [6]. The results obtained from the surface profiles of these features (**Figure 6.7**) show a drop in the surface height in the middle of the ring due to metal dissolution in this region, resulting in lower elevation than the surrounding area where the oxide has precipitated. In the optical image surface profiles (**Figure 6.7**) this drop is about 0.3-0.6 μm ; however, the FIB cuts of the rings show that the cross section of this region is deeper. Results from FIB cuts and discussion of the propagation mechanism are provided in section 6.3.2.2.

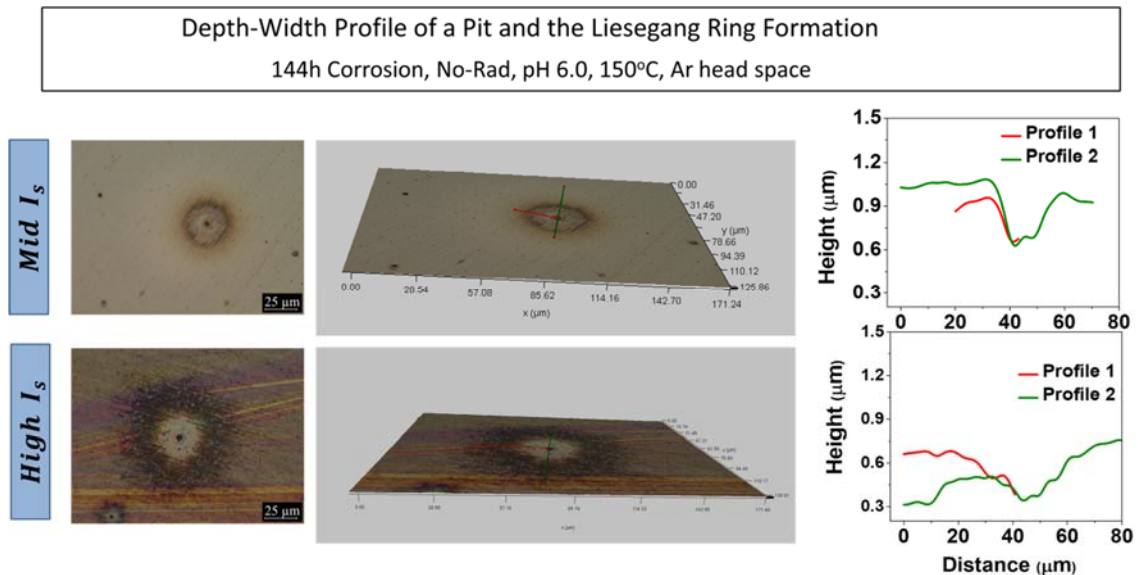


Figure 6.7: Surface profiles of Liesegang rings formed on nickel surfaces corroded for 144 h in the absence of radiation in mid and high I_s pH 6.0 solutions.

In order for coupling between solution reactions and mass transport to occur, resulting in the formation of concentric circular patterns, it is essential to have a slow trans medium such as a gel network on the surface [8,26,27,29]. So, the existence of these rings indicates that over long periods there is a layer present near the surface which inhibits mass transport, in the form of a gel and/or porous medium. The observation of the Liesegang rings further support the mechanism involving hydrogel formation.

As a result of the gelatinous layer inhibiting diffusion in this region, nickel ions are not easily transferred to the bulk solution. Hence, the amount of nickel ions in solution decreases after a period of 24-72 h, depending on solution ionic strength. The interfacial region becomes supersaturated, and nickel ions precipitate on the surface in specific concentric circular shapes. Nickel continuously dissolves from the central

region, but since ion transport is inhibited by the gelatinous layer it continuously precipitates in a circular pattern around the middle dissolving region.

6.3.1.2. Effect of Ionic Strength at pH 8.4 and 10.6 (No RAD)

The effect of ionic strength at pH 8.4 and pH 10.6 in the absence of γ - radiation is discussed here. The solution analysis results for nickel coupons corroded for duration of 144 h for three different I_s solutions at pH 8.4 and pH 10.6 are compared with that of pH 6.0 in **Figure 6.8**.

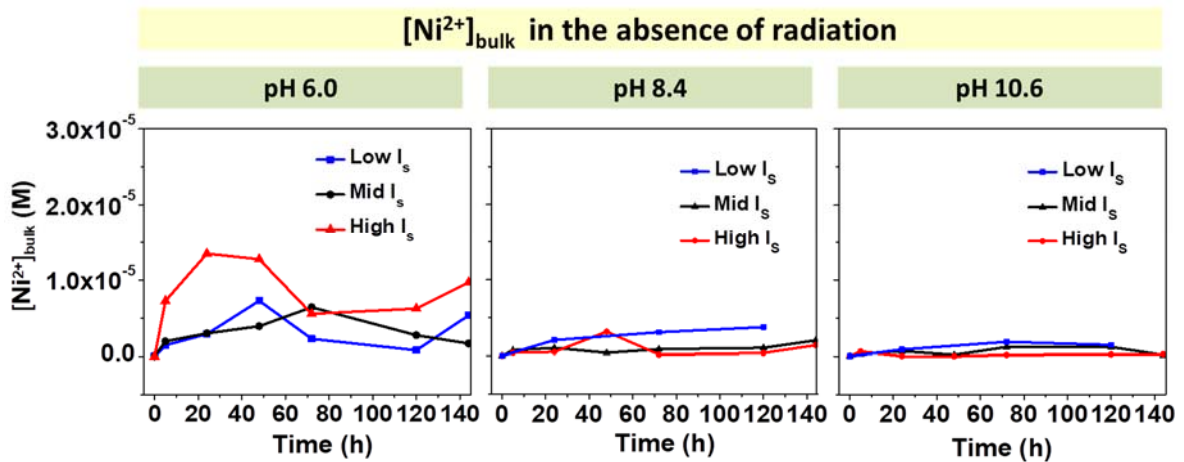


Figure 6.8: Concentration of dissolved nickel ions for nickel samples corroded at pH 8.4 and 10.6 at three ionic strengths compared to that of pH 6.0 shown in **Figure 6.4B**, in the absence of γ -radiation for test durations of 144 h.

As the results show the dissolved nickel concentrations are an order of magnitude lower for pH 8.4 and 10.6 than for pH 6.0. This observation is consistent with the pH-dependence of the solubility of Ni^{2+} , as shown in **Figure 6.3**. At pH 6.0, Ni^{2+} ions are highly soluble, and therefore dissolution dominates over oxide formation. At higher pH the solubility of Ni^{2+} is near minimum and less metal dissolution is observed over the

time studied. The effect of I_s on the $[\text{Ni}^{2+}]_{\text{bulk}}$ is very minimal at both pH 8.4 and 10.6 and shows an opposite trend to that observed at pH 6.0. At both pH 8.4 and 10.6, the $[\text{Ni}^{2+}]_{\text{bulk}}$ follow the following order: low $I_s >$ mid $I_s >$ high I_s .

The dissolution rate is initially affected by both pH and I_s . Solvation of metal cation increases with decreasing pH and increasing I_s initially and increases dissolution rate. Thus, increasing pH has a considerable effect on the maximum concentration, and diffusion rate at longer times. Hence, the overall effect of pH on dissolution is not linear. The fluctuations in the $[\text{Ni}^{2+}]_{\text{bulk}}$ are still with a factor of 2 which is consistent for a dynamic system when mass (metal atoms) is moving in and out of the solution phase. The fluctuation of dissolved nickel concentration indicates the precipitation/re-dissolution process (the Ostwald ripening – Liesegang phenomena) which indicate a cyclic feedback loop between different elementary steps. Such cyclic feedback only occurs when the overall system does not stay at one stable steady state but oscillate between two unstable steady states.

The low magnification optical micrographs of the coupon surface and the corresponding SEM images as a function of time for three different ionic strengths for pH 8.4 and 10.6 are shown in **Figure 6.9** and **Figure 6.10**. Since the results obtained for the low I_s solution was consistent, the coupon exposure test was performed only for 24, 72 and 120 h for pH 8.4 and pH 10.6. The low magnification optical micrographs of the coupon surfaces at both pH 8.4 and 10.6 show that the surface remains green and uniform within the test duration (0-144 h). The surface of the coupon corroded in low and mid I_s solutions is greenish in colour, whereas a greenish-brown colour is observed on the surface for high I_s solutions.

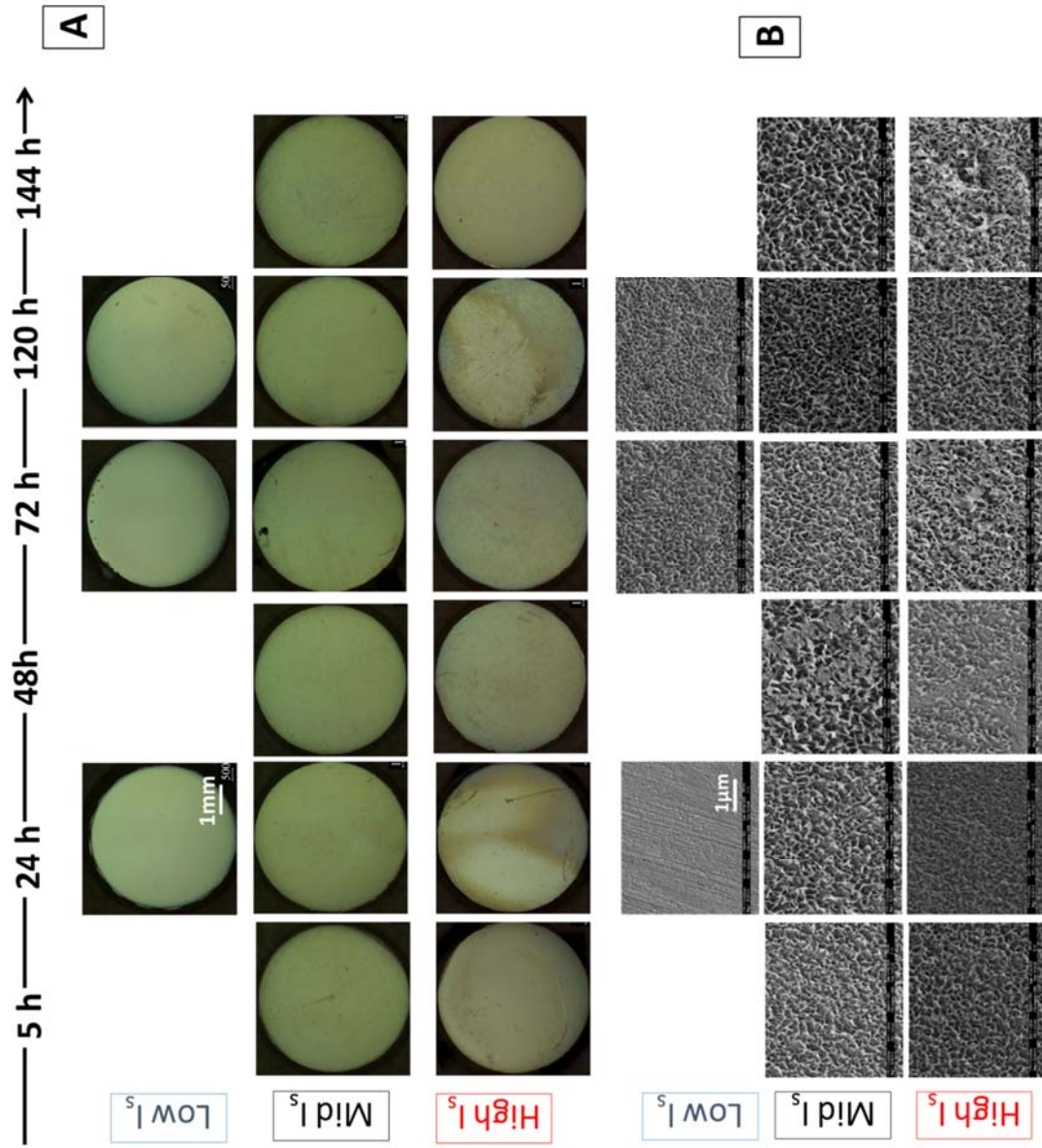


Figure 6.9: Nickel samples corroded at pH 8.4 at three ionic strengths and in the absence of γ -radiation for test durations of 5, 24, 48, 72, 120 and 144 h (for low I_S results are shown for only 24, 72 and 120 h): A) Low magnification optical micrographs of the entire coupon surfaces, B) SEM images of the general oxide morphology of nickel samples.

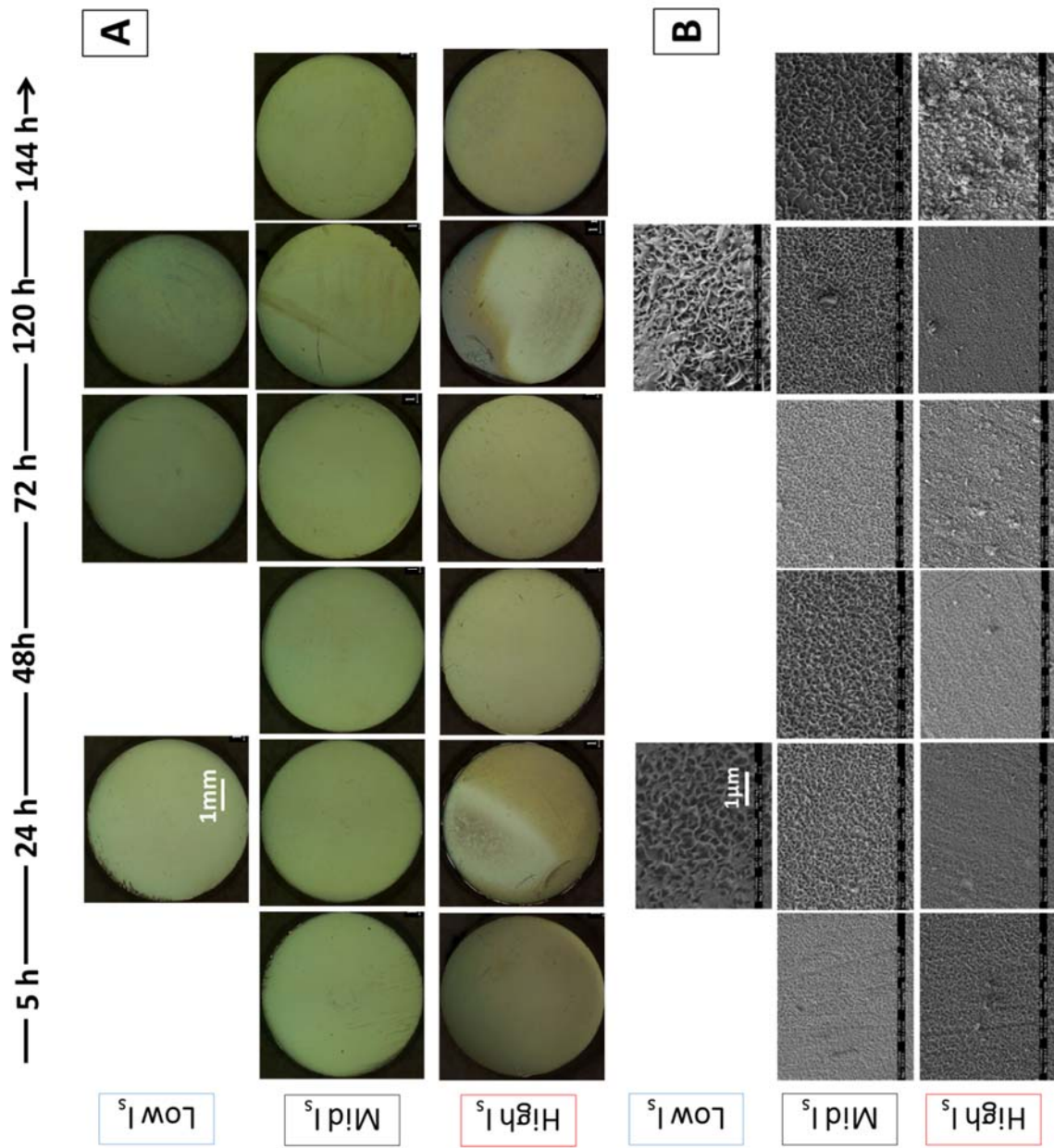


Figure 6.10: Nickel samples corroded at pH 10.6 at three ionic strengths and in the absence of γ -radiation for test durations of 144 h (for low I_s results are shown for only 24, 72 and 120 h): A) Low magnification optical micrographs of the entire coupon surfaces, B) SEM images of the general oxide morphology of nickel samples.

To better understand this behaviour, SEM images were taken to get a closer look at the physical features of the oxides formed on the metal surface. The SEM images show the presence of more filament-like oxide at pH 8.4, whereas a more compact oxide film was observed at pH 10.6. At high pH (8.4 and 10.6) oxide formation predominates. As a protective oxide layer forms on the surface, v_{trans} controls the rate of oxidation, and the concentration of nickel ions in solution is lower. Higher nickel concentrations were observed for solutions with low I_S . The SEM images in **Figure 6.11** and **6.12** are consistent with this observation, showing that for high I_S solution the surface is covered from the beginning of the test with more compact oxide with finer particle size (more evident at pH 10.6).

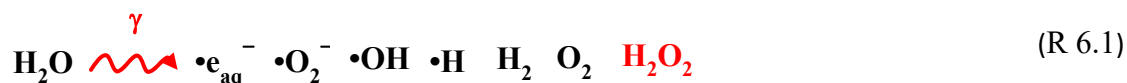
The results obtained for the effect of solution ionic strength at both pH 10.6 and 8.4 are consistent with those observed at pH 6.0. The results indicate that at all pHs the corrosion rate of nickel increases with solution ionic strength. However, whether the corrosion pathway leads to more metal cation dissolution or oxide formation depends on solution pH. This is due to the different solubility of nickel cations at different solution pHs.

At pH 8.4 and 10.6 the non-linear evolution of $[Ni^{2+}]_{bulk}$ occurs in a smaller range compared to that observed at pH 6.0. Moreover, the coupon surfaces do not exhibit any surface features indicating nonlinear behaviour, such as Liesegang rings, at any ionic strengths. As mentioned before, an important requirement for Liesegang ring formation is the presence of a gelatinous layer on the surface which can facilitate systemic feedback and coupling of solution reaction and mass transport processes. At both high solution pHs, due to the low nickel solubility, the gel layer transforms to a solid oxide layer

earlier, and solution feedback processes do not occur in the solution. Hence, at pH 8.4 and 10.6 Liesegang rings are not observed on the nickel surface and the surface is covered by a uniform solid green layer of Ni(OH)₂/NiO during nickel corrosion. At high I_S the formation of a darker brown layer of high oxidation state nickel oxide is also observed.

6.3.2. Effect of Ionic Strength in The Presence of Radiation (RAD)

The results obtained in the presence of radiation for different I_S at pH 6.0, 8.4 and 10.6 are discussed here. The progression of corrosion was studied by analyzing the changes in surface morphology and measuring the dissolved nickel concentration as a function of time. Comparing these results with results from absence of radiation will allow for a better understanding of the effect of radiation on different ionic strengths. Gamma radiation makes the solution more oxidizing by decomposing water and producing a number of oxidizing species. The water radiolysis products (notably H₂O₂) change the primary redox reactions which are involved in the corrosion process.



6.3.2.1 Effect of Ionic Strength at pH 6.0 (RAD)

Figure 6.11 B show the evolution of the surface morphology and dissolved nickel ($[\text{Ni}^{2+}]_{\text{bulk}}$), for three different ionic strengths in the presence of γ -radiation at pH 6.0. The trend in the evolution of the surface morphology and dissolved nickel concentration is opposite to that observed in the absence of radiation (section 6.3.1.1). The pH of the

test solution was measured prior to and after irradiation for each set of test conditions. The pH of the solution measured after irradiation was in the range of 5.8.

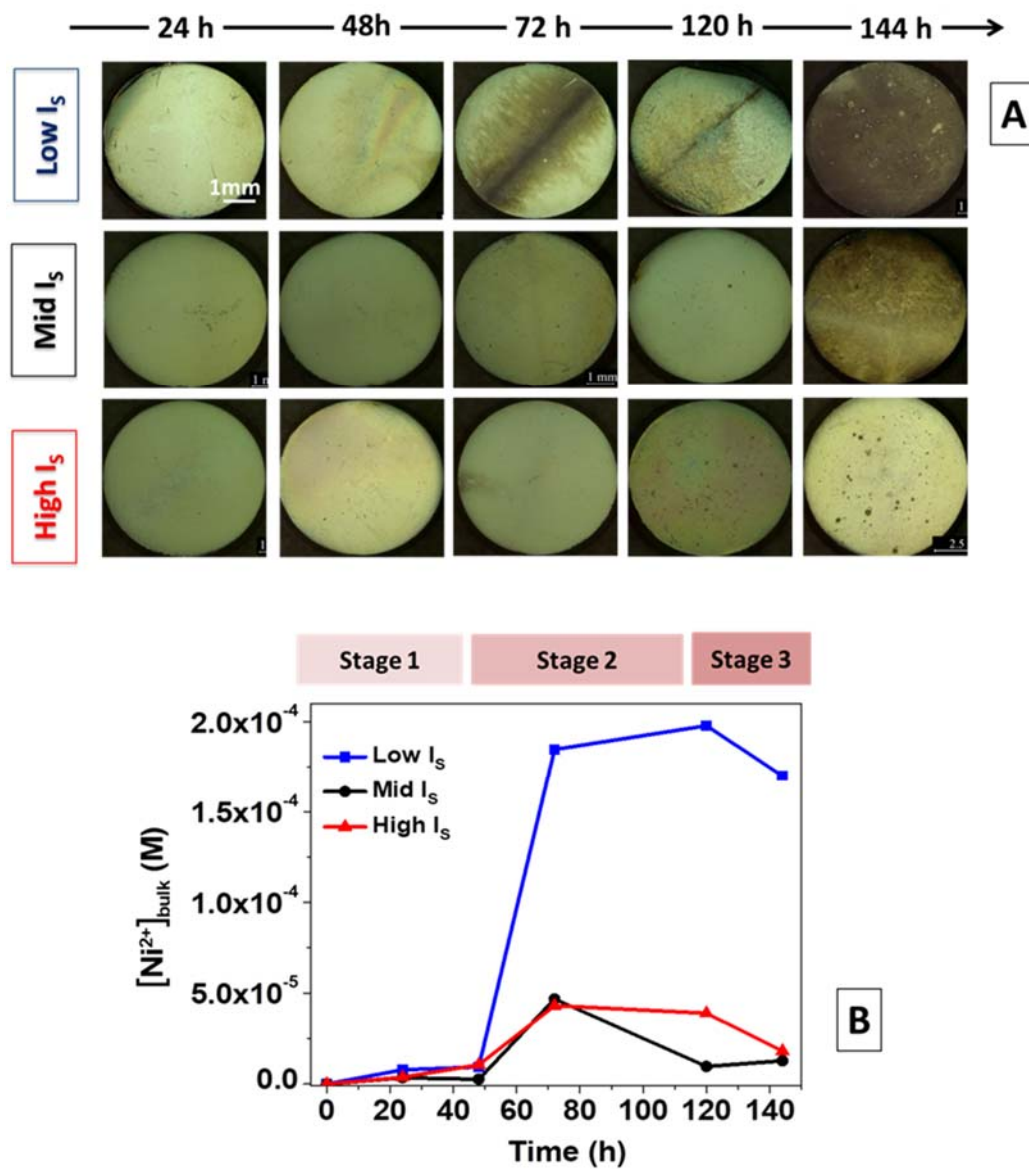


Figure 6.11: Nickel samples corroded at pH 6.0 at three ionic strengths and in the presence of γ -radiation (dose rate $1.8 \text{ kGy}\cdot\text{h}^{-1}$) for test durations of 5-144 h: A) Low magnification optical micrographs of the entire coupon surfaces, and B) Concentration of dissolved nickel ions in solution.

The solution analysis shows three distinct characteristic stages (clearly observed for low I_S). At early times ($t_{corr} \leq 48$ h) (**Stage 1**), the dissolved nickel concentration increases linearly with time with a slope of $1.9 \times 10^{-7} \text{ M}\cdot\text{h}^{-1}$. This slope is similar for mid and high I_S : $1.4 \times 10^{-7} \text{ M}\cdot\text{h}^{-1}$ and $2.2 \times 10^{-7} \text{ M}\cdot\text{h}^{-1}$ respectively. Similar concentrations were observed for all I_S solutions in **Stage 1**.

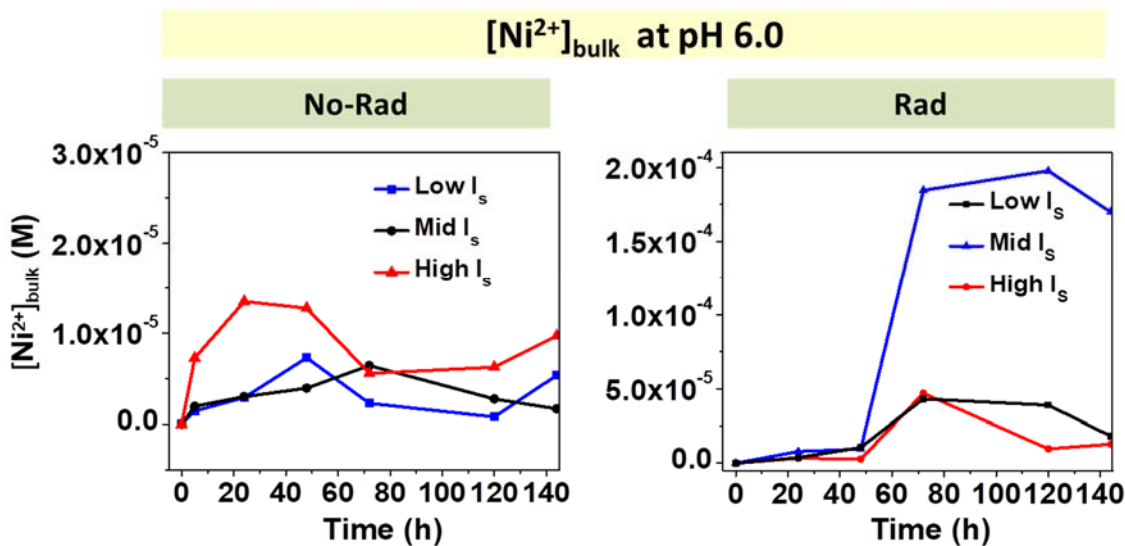


Figure 6.12: Concentration of dissolved nickel ions for nickel samples corroded at pH 6.0 at three ionic strengths in the presence and absence of γ -radiation for test durations of 144 h.

The nickel concentration observed during **Stage 1** was in a similar range to that observed for the no RAD case as shown in **Figure 6.12**. The fluctuations in the $[\text{Ni}^{2+}]_{\text{bulk}}$ were amplified in the presence of γ -radiation, and particularly for low I_S , where the $[\text{Ni}^{2+}]_{\text{bulk}}$ is ~ 10 times higher than for high I_S ($t > 48$ h). Also, this value is ~ 10 - 100

times higher than the $[\text{Ni}^{2+}]_{\text{bulk}}$ observed for low I_S in the absence of radiation. The time to reach the maximum under No RAD is similar to the time when the concentration increases abruptly under RAD. This change signals the transition from the kinetic **Stage 1** to **Stage 2** and beyond.

The low magnification optical images of the coupon surface, are shown in **Figure 6.10A**. The coupons exposed to high and mid I_S solutions are more greenish in colour, while in low I_S solution the surface are greenish-brown with localized black areas (72 to 144 h). The solid black hydroxide/oxide observed on the coupons irradiated for 72 to 144 h coincide with the increase in dissolved metal concentration, possibly due to hydrogel layer converting to solid products and $\text{Ni}(\text{OH})_2$ colloid formation in solution as described later in **Stage 3**. As described earlier, nickel hydroxide/oxides have different characteristic colours: NiO is green, $\text{Ni}(\text{OH})_3$ is expected to be brownish [12] and Ni_3O_4 and Ni_2O_3 are black [16,17]. The presence of mixed Ni^{2+} and Ni^{3+} oxides is expected under gamma radiation due to the more oxidizing conditions.

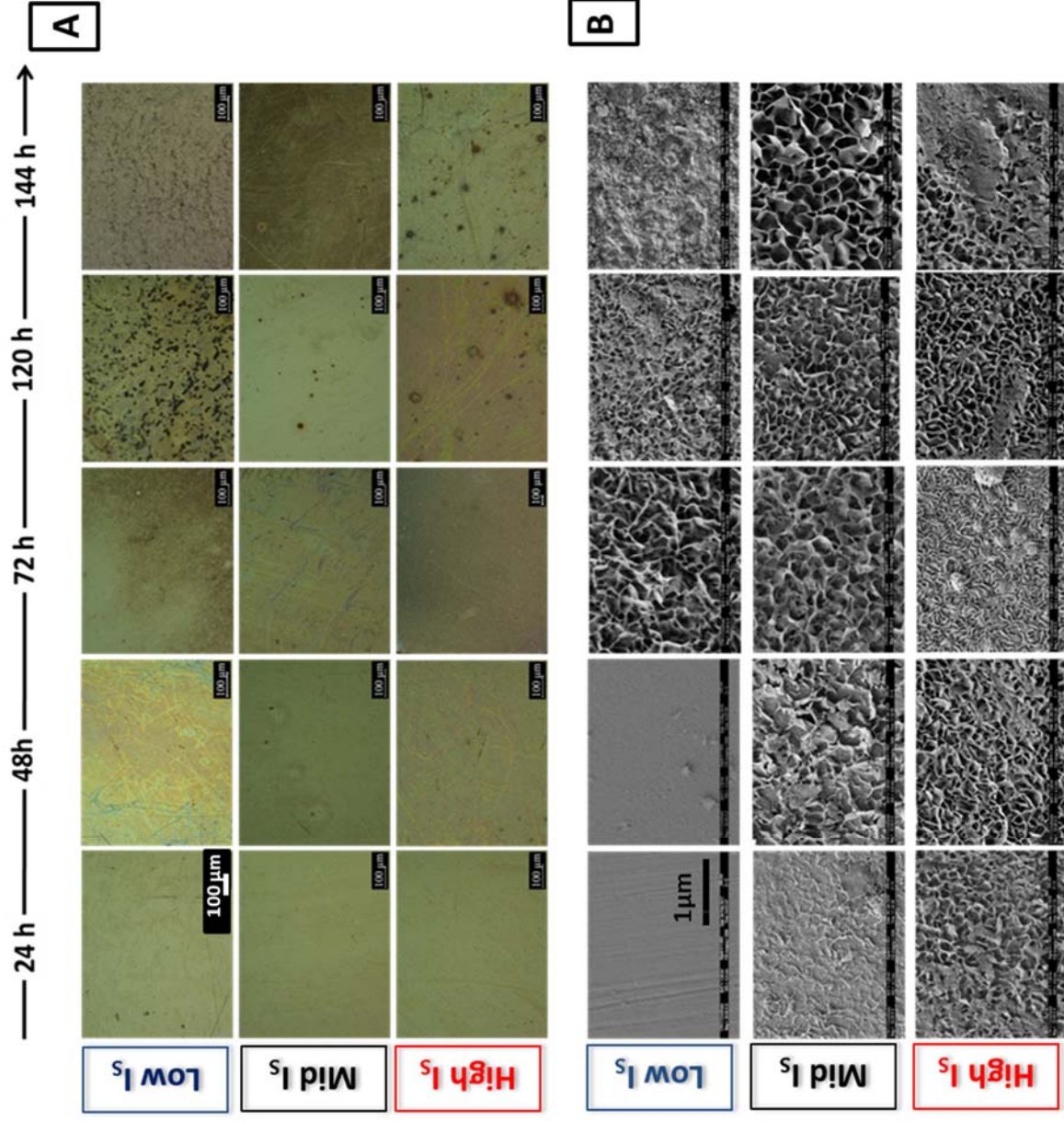
The surface morphology during **Stage 1** was analysed using the high magnification optical and SEM images as shown in **Figures 6.13**. The surfaces are greenish-brown in all cases, with localized brown areas observed for the low I_S samples. The SEM images (0- 48 h) for low I_S show a smooth surface and no filament-like oxide. For mid and high I_S the surface is covered by filament-like oxides. The density of the filament-like oxide was higher for high I_S solution than for mid I_S .

At longer times ($t_{\text{corr}} > 48$ h, **Stage 2**), the amount of nickel in solution increases at a faster rate for all solutions with slopes of $7.3 \times 10^{-6} \text{ M}\cdot\text{h}^{-1}$ for low I_S , 1.8×10^{-6} for mid I_S and $1.3 \times 10^{-6} \text{ M}\cdot\text{h}^{-1}$ for high I_S . The increase relative to **Stage 1** is most prominent for

low I_s . The mid and high I_s were similar in their behaviour. During this stage a brownish layer forms on the surface which becomes blacker due to the presence of higher oxidation state Ni oxides (Ni_3O_4 and Ni_2O_3). The oxide that forms on the surface at higher ionic strength is thicker than low I_s solution (observed in AES analysis in **Figure 6.16**). It is believed that this oxide can quickly inhibit metal oxidation on the surface. During this stage, the oxide layer (or the hydrogel layer) formed on the surface (or interface) at higher I_s can slow down the dissolution of nickel cations. Consequently, the maximum $[\text{Ni}^{2+}]_{\text{bulk}}$ during this stage is ~ 5 times lower at higher ionic strengths. Also, the number of concentric circular patterns observed on the nickel surface was higher for high I_s solutions (**Figure 6.13A** and **Figure 6.14**). This can be explained by the more rapid formation of the hydrogel layer that can act a mass transport barrier layer.

Also to have a better understanding about the corrosion evolution observed for the low ionic strength pH 6.0 solutions, non-buffered solution results are discussed in Chapter 7.

Figure 6.13: Nickel samples corroded at pH 6.0 at three ionic strengths and in the presence of γ -radiation (same samples as presented in Figure 6.10):
 A) High magnification optical micrographs, B) SEM images of general oxide morphology. All images have the same scales as indicated by 100 μm bar for optical images and 1 μm bar for SEM images.



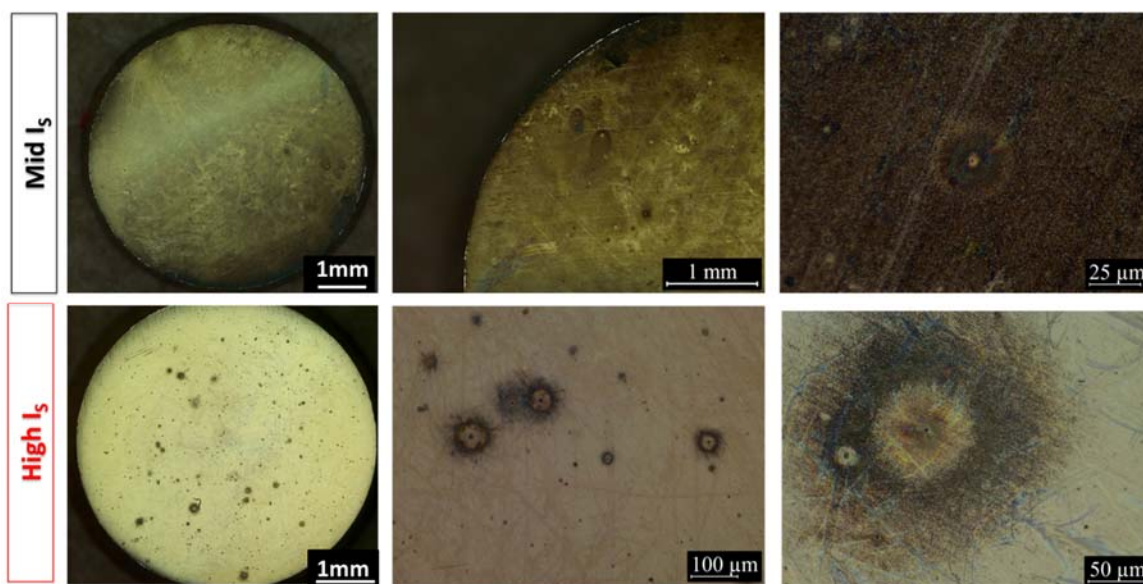


Figure 6.14: Distribution and size of circular patterns on corroded nickel surfaces after 144 h in the presence of γ -radiation at mid and high I_s .

In Stage 3 ($t_{corr} > 120$ h), the amount of dissolved nickel decreased for low and high I_s . For the low I_s solution, after 120 h more black oxide was observed on the surface and after 144 h the surface was completely covered by this black oxide layer. During this stage once the nickel ions in bulk solution become supersaturated, they can undergo hydrolysis forming $\text{Ni}(\text{OH})_2$ colloids. The nucleation and formation of colloid particles in the bulk solution is possible in irradiated solution due to the production of $\bullet\text{OH}$ [30,31]. The precipitation of $\text{Ni}(\text{OH})_2$ colloids particles can result in decrease in Ni^{2+} concentration in solution. The presence of nickel oxide nanoparticle clusters in the solution phase was further confirmed by transmission electron microscopy (TEM) analysis. The TEM samples were prepared by dipping a carbon-coated copper grid into the test solution and then drying the sample grid in air. The TEM images were obtained

with a Philips Electronics instrument with the electron microscope operating at 80 keV. The TEM images of the nickel oxide nanoparticles are shown in **Figure 6.15**.

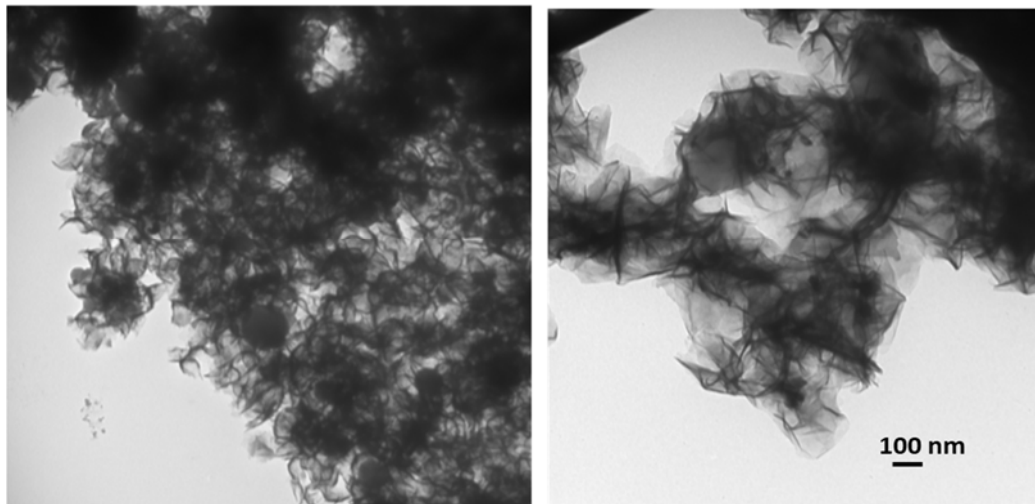


Figure 6.15: TEM image showing the presence of nanoparticle clusters in low I_s solution after 120 h of corrosion in the presence of γ -radiation.

Comparing the results of different I_s in this stage indicates that at higher I_s , the formation of the darker brown oxide layer on the surface is less prevalent. However, at high I_s more circular surface features (Liesegang rings) are present on the surface and darker brown oxide forms, and particularly in the circular bands of the Liesegang rings (**Figure 6.13** and **6.14**). Although the formation of these features is most prevalent in high I_s solutions, they were also observed on the surfaces for lower ionic strengths, but the number and size of these features are lower than for high I_s . (Liesegang rings in low I_s pH 6.0 solutions are discussed more fully in Chapter 7).

The elemental composition of the surface oxide layer as a function of depth was further investigated by AES depth profiling. The atomic percentage distribution (At %) in

the AES depth profile shows the concentration ratio for each element at a given depth. In low I_S , the oxide layer formed on the surface in both the no RAD and RAD cases is thinner than for the high I_S solution. In the presence of radiation, thicker oxide films formed on the surfaces. The different ratios observed indicate different compositions of the oxide layer on the surface. An O/Ni ratio of 1.0 is the stoichiometric point in the oxide layer, where the concentration of main metal atoms is equal that of oxygen atoms. This point in the AES graphs is the intersection of the Ni and O lines and indicates that at this depth the main oxide chemical composition is NiO. A ratio less than 1.0 is observed in deeper layers and indicates an oxide in which some fraction of the Ni has not yet been oxidized. A ratio higher than 1.0 indicates an oxide with a lower concentration of Ni atoms, which suggests the presence of metal hydroxide at the given depth.

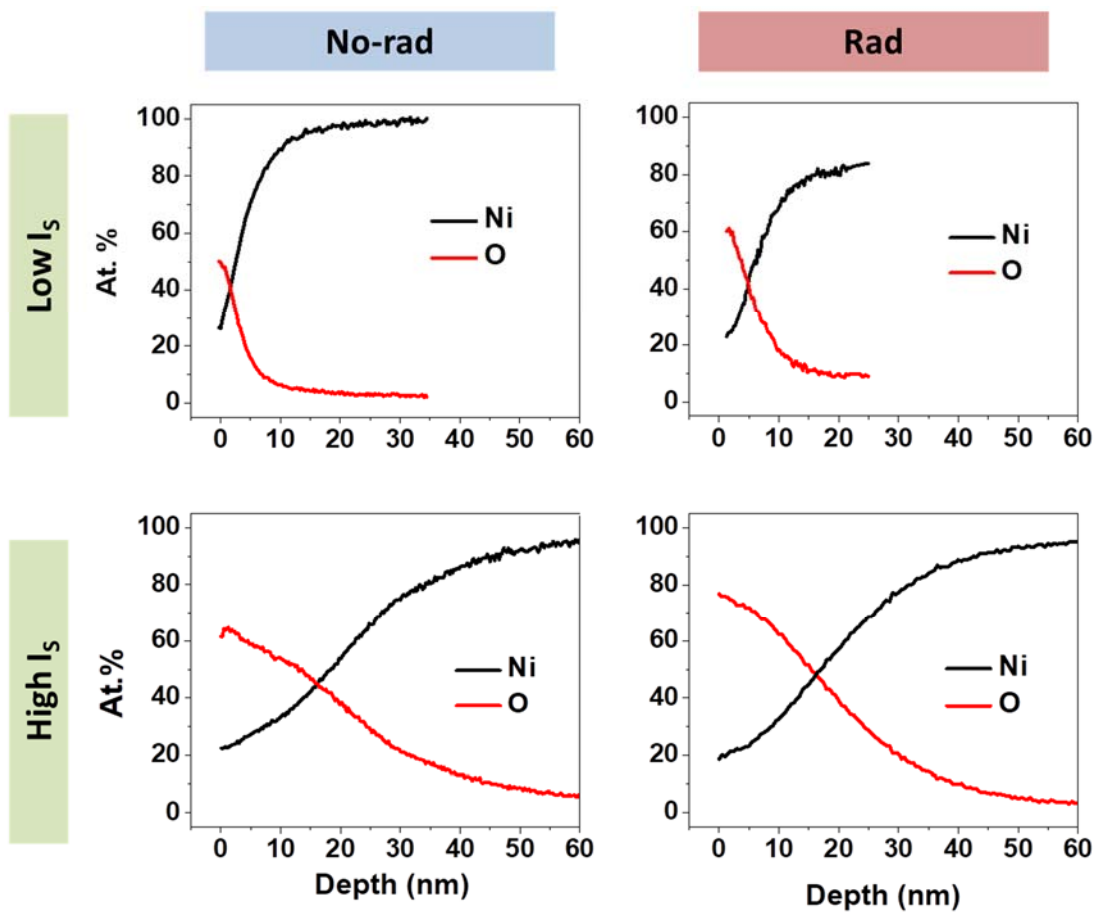


Figure 6.16: Depth profiles for Ni and O determined by AES, of nickel coupons corroded for 120 h in the presence and absence of γ -radiation at pH 6.0 with high and low ionic strengths.

The solution analysis results, and the evolution of the surface morphology clearly show that the corrosion kinetics evolve over time in the presence of γ -radiation. A schematic of the mechanism of the three distinct stages involved in nickel corrosion is presented in **Figure 6.17, 6.18, 6.19**. The predominant corrosion processes occurring in each stage are described below.

Stage 1:

Stage 1 is the early stage of nickel corrosion where the overall corrosion process consists mainly of oxidation of $\text{Ni}^0_{(m)}$ to $\text{Ni}^{2+}_{(aq)}$ at the metal surface (coupled with the reduction of oxidant present in the solution) (M1), and the transport of $\text{Ni}^{2+}_{(aq)}$ from the metal surface to the bulk solution (trans). In presence of γ -radiation, the main oxidant that can affect the corrosion of metals is the H_2O_2 [4,32]. In the presence of a continuous flux of γ -radiation, the concentration of H_2O_2 remain in a steady state level during the exposure time. H_2O_2 is more powerful and kinetically facile oxidant than O_2 . The schematics of the H_2O_2 half reaction on metal oxidation in **Stage 1** is shown in **Figure 6.17**. Proton reduction is not included for simplicity as its contribution as an oxidant is negligible in the presence of H_2O_2 . H_2O_2 can either reduce to H_2O and OH^- or oxidize to O_2 , depending on what the other half-reaction it can couple with. In kinetic **Stage 1**, when the concentrations of metal oxidation products in the interfacial region are low, H_2O_2 acts primarily as an oxidant. In later stages, the oxidation and reduction of H_2O_2 can couple with the reduction of the metal oxidation product and the oxidation of metal or metal cation with a lower oxidation state. The main difference between chemically added H_2O_2 and radiolytically produced H_2O_2 is that in the former case $[\text{H}_2\text{O}_2]$ is not constant with

time as it is consumed during metal oxidation but not replenished by other processes such as radiolysis.

For redox half-reactions of dissolved species, when its concentration in the bulk solution is constant, its concentration in the interfacial region remains also constant with reaction time. This is not the case with metal oxidation. In corrosion, metal atoms are continuously transferred into the bulk solution volume via the interfacial region. In **Stage 1**, the overall metal oxidation kinetics can be simplified using the kinetics of two redox half-reactions, oxidation half-reaction of Ni^0 to Ni^{2+} (M1) coupled with the reduction half-reaction of H_2O_2 to OH^- . During this Stage, $[\text{Ni}^{2+}]_{\text{int}}$ stays below its saturation capacity and therefore the rate of (M1r) is negligible and does not affect the net rate of (M1).

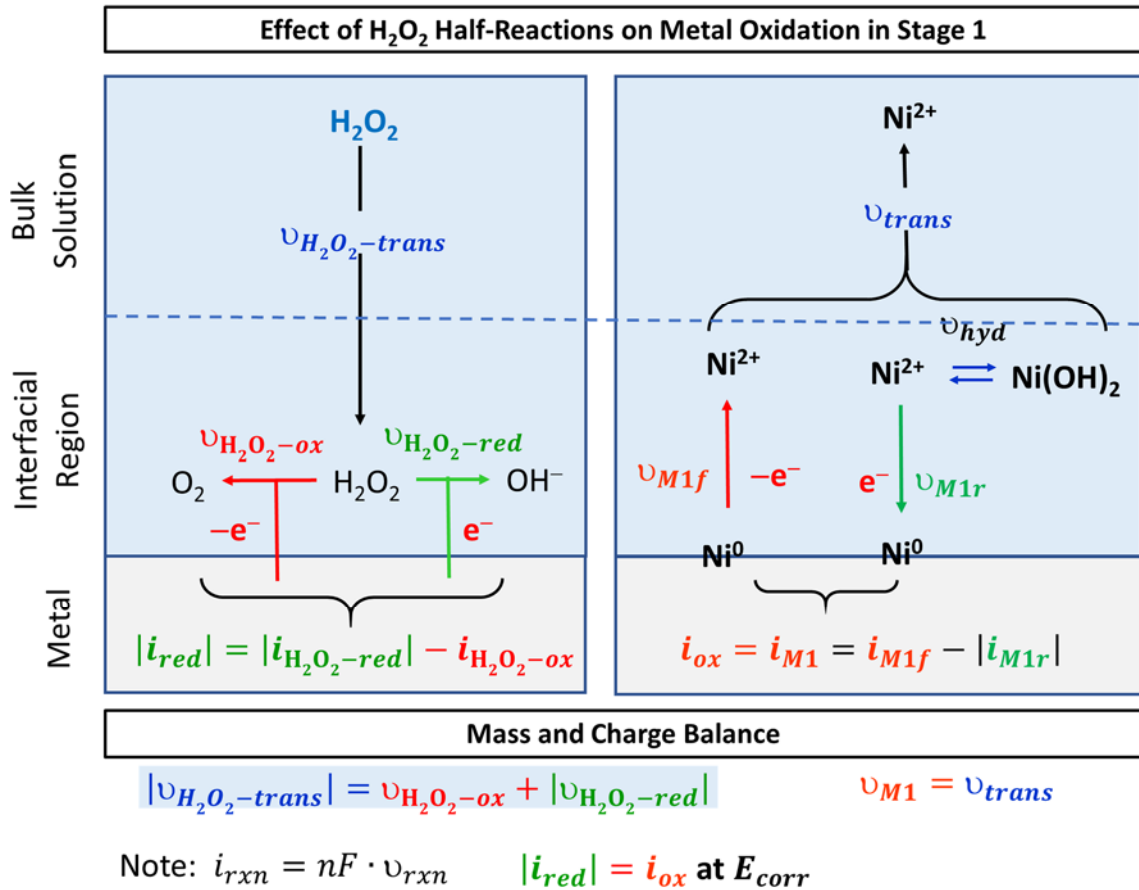


Figure 6.17: The schematics of the H₂O₂ half reaction on metal oxidation occurring during Stage 1 of the corrosion process. For metal oxidation, the ν_{M1f} is forward nickel oxidation rate of $Ni \rightleftharpoons Ni^{2+}$ and ν_{M1r} is the rate of reverse reaction, and ν_{trans} is the rate of nickel cation transport to bulk solution. For the solution species half-reaction $\nu_{H_2O_2-red}$ is the H₂O₂ reduction rate and $\nu_{H_2O_2-trans}$ is the rate of H₂O₂ transfer from the bulk solution to the interface.

For metal oxidation, i_{M1} is not controlled by electron transfer but the transfer of metal atom from the solid metal phase to the solution in the interfacial region. The dissolved metal concentration in **Stage 1** in the presence of RAD was in a similar range to that observed for the no RAD case, before the transition to **Stage 2** occurs when the

concentration increases abruptly in the presence of RAD. Before the transition, the effect of radiation on dissolution is negligible or slightly to suppress it. This is consistent with our understanding that (M1) is mostly controlled by solvation of Ni^{2+} , not by the reduction of oxidant present in the solution, nor (trans) and (gel). The solution redox environment is more important for (M2). Hence, if the system can progress to gel formation and (M2), it can start having more impact on metal dissolution rate.

The solvation properties of the solution, such as $[\text{OH}^-]$ and ionic strength, can affect the rate of metal oxidation and the maximum yield of metal cation. The pH has a negligible effect on electron transfer reaction rates. However, it can have a significant effect on the maximum yield (saturation capacity) for $[\text{Ni}^{2+}]_{\text{int}}$. The trans process of metal cations from the interfacial region to the bulk solution is affected by the pH and the ionic strength of the solution. Depending on the solution pH, the metal cations in the interfacial region can have two pathways: they can be transported into the bulk solution (at lower pH) or reach their saturation limit at the interface (at higher pH). When it reaches its saturation limit the Ni^{2+} undergoes hydrolysis (hyd) forming metal hydroxide $\text{Ni}(\text{OH})_2$. Thus, the duration of **Stage 1** is shorter at a higher pH. Radiation lowers the pH over time (as described in Chapter 7). It will not affect the corrosion rate in **Stage 1**, but it can prolong **Stage 1** and transition from **Stage 1** to **Stage 2**. During **Stage 1**, the surface looked relatively clean and uniform and with minimum amount of Ni hydroxide/oxide present on the surface.

Stage 2:

As corrosion progresses, in the presence of radiation, continuous production of oxidizing agents can facilitate this stage particularly at the low solution pH. The schematics of the corrosion process occurring during stage 2 is shown in **Figure 6.18**. In Stage 2, depending on the solution pH, dissolution of Ni^{2+} from the interfacial region or the hydroxide layer to the bulk solution can occur and the concentration of Ni^{2+} in the solution increases at a faster rate. At lower pH the metal ion solubility is higher and mass transport of nickel cations to the solution phase occur at a faster rate compared to that at higher pH, and the presence of radiation can increase the rate of mass transport. During stage 2, the $(a_{\text{Ni}^{2+}})_{int}$ and $[\text{Ni}^{2+}]_{bulk}$ approaches $\approx [\text{Ni}^{2+}]_{(sat)}$ faster. And gradually the net rate of (M1) decreases with t_{corr} , and the hydrolysis equilibrium (hyd) shifts to $\text{Ni}(\text{OH})_2$ formation, and $\text{Ni}^{2+}/\text{Ni}(\text{OH})_2$ starts oxidizing. The presence of a small amount of $\text{Ni}(\text{OH})_3$ (from (M2)) can accelerate the condensation/nucleation of mixed $\text{Ni}^{\text{II}}/\text{Ni}^{\text{III}}$ hydroxide, initially as colloids and then aggregates forming a hydrogel network. Depending on the redox activities of dissolved species that can couple with the forward and reverse reactions of (M2), the rate of each direction can be very fast, but the net oxidation rate can be negligible: $v_{M2f}, v_{M2r} \gg v_{M2} \approx 0$. Due to fast hydrolysis equilibrium in the hydrogel network, v_{trans} is primarily determined by the concentration gradient between saturation capacity and the bulk concentration. Hence, $v_{trans}, v_{gel} \approx \text{decreases} \propto \sqrt{t_{corr}}$. Over time, the content of $\text{Ni}(\text{OH})_3$ (yield of (M2)) increases with t_{corr} . This affects the overall transport of $\text{Ni}^{2+}/\text{Ni}(\text{OH})_2$ (trans). With a sufficient amount of $\text{Ni}(\text{OH})_3$ the aggregates or precipitates can start to grow mixed hydroxide/oxide crystals (into Stage 3). During stage 2, the surface is covered with green/brownish hydroxide/oxide

layer and SEM images shows the presence of a filament liked oxide on the coupon surface. In the presence of γ -radiation, the brownish layer is formed on the surface which becomes blacker due to the presence of higher oxidation state Ni oxides (Ni_3O_4 and Ni_2O_3).

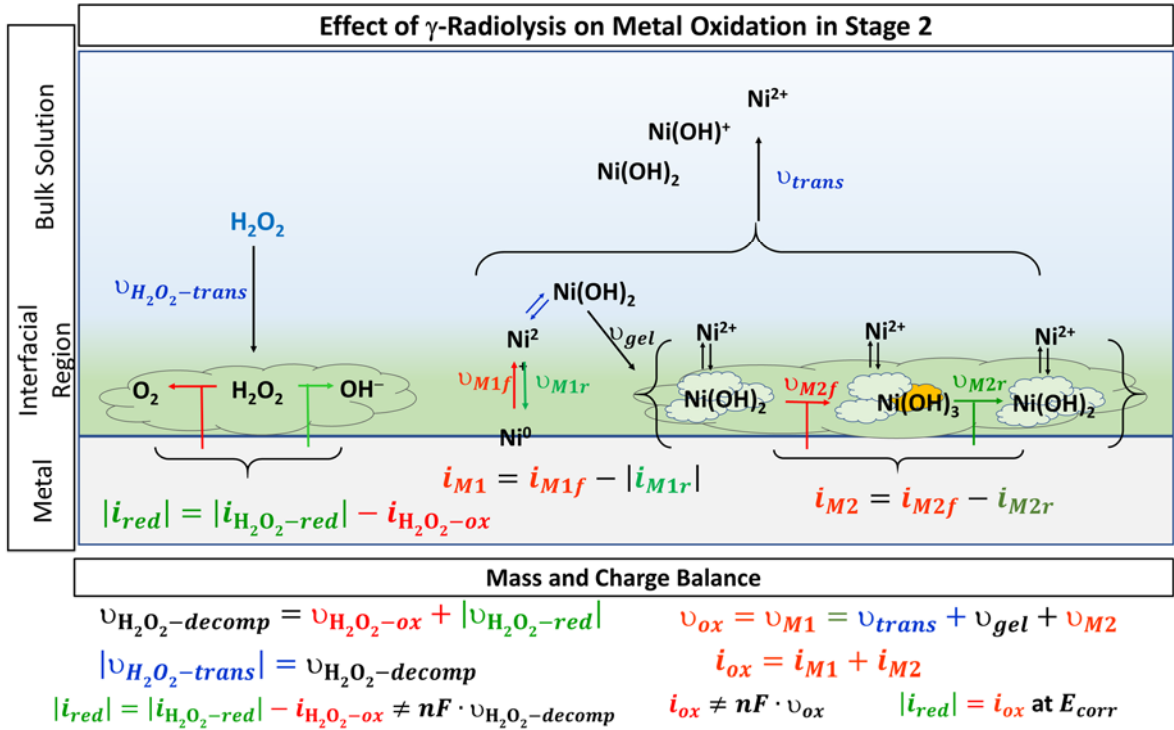


Figure 6.18: The schematics of the effect of γ -radiation on Stage 2 of the corrosion process. The Rate Determining Steps (RDS) arising during the corrosion process include metal oxidation, the v_{M1f} is forward nickel oxidation rate of $\text{Ni} \rightleftharpoons \text{Ni}^{2+}$ and v_{M1r} is the rate of reverse reaction, v_{M2f} is the forward nickel oxidation rate of $\text{Ni}^{2+} \rightleftharpoons \text{Ni}^{3+}$ and v_{M2r} is the reverse reaction. v_{gel} , v_{hyd} and v_{trans} are the rate of gel, hydrolysis and nickel cation transport to bulk respectively.

Stage 3:

The schematics of the effect of γ -radiation on **Stage 3** of the corrosion process are shown in **Figure 6.19**. Once the bulk solution becomes supersaturated, the Ni^{2+} undergoes hydrolysis and achieves phase equilibrium with solid metal hydroxide $\text{Ni}(\text{OH})_{2(\text{solid})}$ which can precipitate on the metal surface. With the formation of the hydrogel layer the possibility of oxidizing Ni^{2+} ions to higher oxidation states (Ni^{3+}) also increases. As the content of $\text{Ni}(\text{OH})_3$ (yield of (M2)) increases with t_{corr} , the mixed hydroxide aggregates or precipitates can start to grow as mixed hydroxide/oxide crystals. The kinetics of the overall metal oxidation in **Stage 3** are similar to that of **Stage 2**. In **Stage 3**, when the surface is not extensively covered by the crystals the net rate of crystal growth is proportional to v_{gel} .

In **Stage 3**, the overall metal oxidation to produce Ni^{II} & Ni^{III} becomes smaller and the changes in the metal oxidation products (dissolved or precipitated) are more due to the metal atom transfer between the solution and solid-oxide phases. The overall metal oxidation becomes negligible with time. With no more net production of Ni^{II} and Ni^{III} , the overall production of oxide crystals (in number density and size) stops. However, the interaction between the dissolved metal cations and oxide precipitates can continue via the dissolution and reprecipitation of the hydroxide/oxide particles – Ostwald ripening (detailed description provided in Chapter 7). The SEM images of the 144 h low I_s surface show the dissolution and reprecipitation process as shown in **Figure 6.20**. The surface looks rougher and crystals can be observed. Because γ -radiation continuously produces H_2O_2 , it can have a considerable impact on Ostwald-ripening and Liesegang band formation.

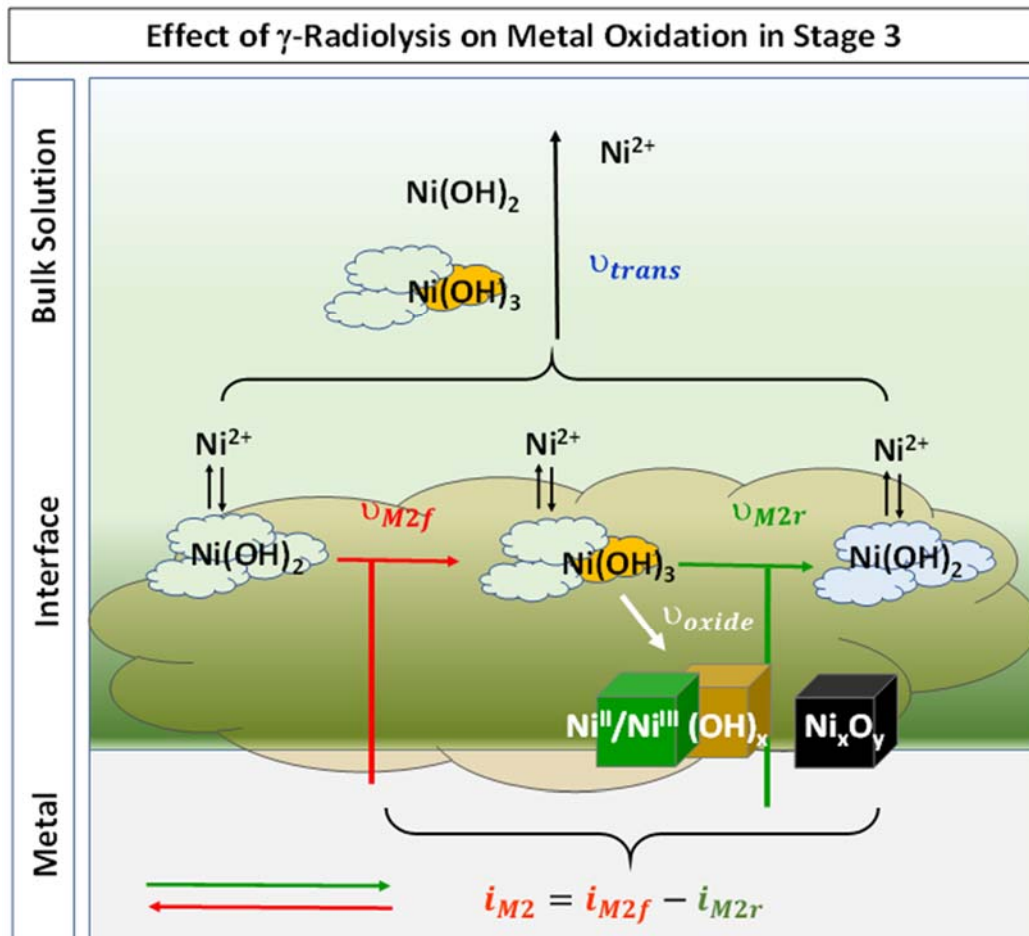


Figure 6.19: The schematics of the effect of γ -radiation on Stage 3 of the corrosion process. The Rate Determining Steps (RDS) arising during the corrosion process include for metal oxidation, the v_{M1f} is forward nickel oxidation rate of $\text{Ni} \rightleftharpoons \text{Ni}^{2+}$ and v_{M1r} is the rate of reverse reaction, v_{M2f} is the forward nickel oxidation rate of $\text{Ni}^{2+} \rightleftharpoons \text{Ni}^{3+}$ and v_{M2r} is the reverse reaction. v_{gel} , v_{trans} , v_{hyd} v_{oxide} are the rate of gel, hydrolysis, nickel cation transport to bulk and oxide formation respectively.

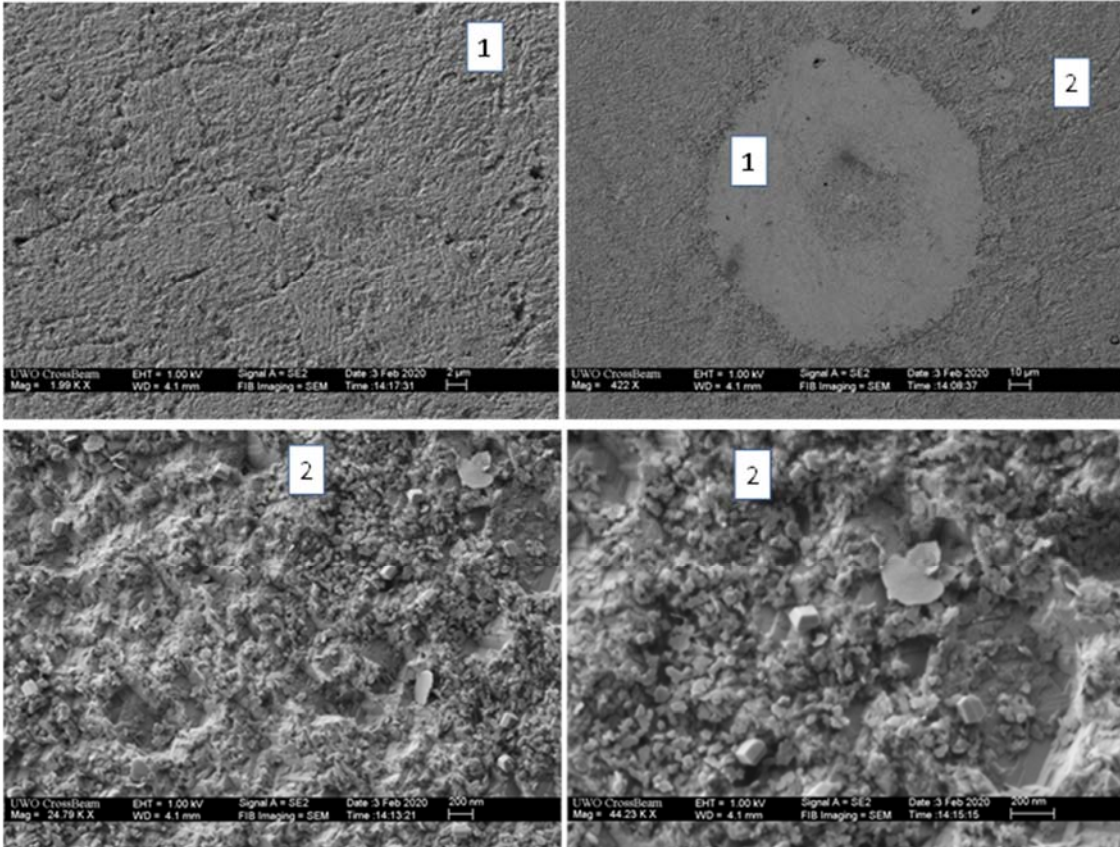


Figure 6.20: SEM image showing the surface morphology of the 144 h, pH 6.0 low ionic strength sample.

6.3.2.2. Mechanism of Formation of Nickel Surface Features

The mechanism of formation of the surface features known as Liesegang rings is briefly discussed here, but a more detailed discussion is provided in Chapter 7. As mentioned earlier, Liesegang rings result from chemical waves that occur under particular conditions when strong systemic feedback has developed [29]. A Liesegang feature consists of concentric rings of precipitated oxide that form periodically when co-precipitating ions inter-diffuse through a gel medium. The most important condition for ring formation is the presence of a hydrogel network on the surface [8,26,27,29].

In the presence of this layer, net metal oxidation, metal dissolution, and oxide growth and conversion are all strongly coupled. This can result in strong systemic feedback, resulting in oscillatory behaviours. These behaviours are only observed under certain solution conditions in which the chemical and physical properties of the solution can affect the nature and the strength of this systemic feedback. These solution properties include dissolved metal ion concentration, pH, types and concentrations of oxidants, temperature, solution flow rate, and solution volume to surface area ratio. Each of these parameters affects the rates of the elementary processes and consequently affects the strength of the systemic feedback [6].

Ni ions produced during oxidation gradually accumulate in the solution near the surface, and so this region becomes saturated within the diffusion layer. This layer mainly acts as a trans barrier layer in the form of a gel and/or porous medium [9,33]. The diffusion of metal cations through a viscous network (such as a hydrogel) to the bulk solution is significantly more difficult than the diffusion of ions through the solution, so ion transport to the bulk solution becomes the rate-determining step. After this hydrogel network has been generated, the diffusion layer thickness increases as the saturation front moves further from the surface of the bulk solution.

Hence in the presence of gel layer, the nickel cations cannot move easily from the interfacial region to the bulk solution. Therefore, the dissolved nickel cations diffuse within the gel layer and precipitate as specific features such as concentric circular shapes. In these features, there is usually more dissolution at the center of the rings which are typically close to inclusion sites, and nickel oxides continuously precipitate in a circular pattern around the dissolving region.

Figure 6.21 presents the SEM and cross-sectional (FIB cut) images of a Liesegang ring on a nickel sample corroded for 144 h in a high I_s pH 6.0 solution. The SEM images show a localized dissolving pit area in the centre of the ring. However, this area is covered with the precipitated oxide layer. The FIB cut performed at the center of the ring illustrates that metal dissolution is propagating into the metal. Dissolution in this pit has occurred to a diameter of 4.13 μm and a depth of 14.37 μm in the center of the ring after 144 h of nickel corrosion in the presence of γ -radiation. Nickel ions produced in this region can remain in the channel and/or diffuse out to the nickel surface and precipitate in a circular pattern around the central region as described in section 6.3.1.1 (**Figure 6.7**).

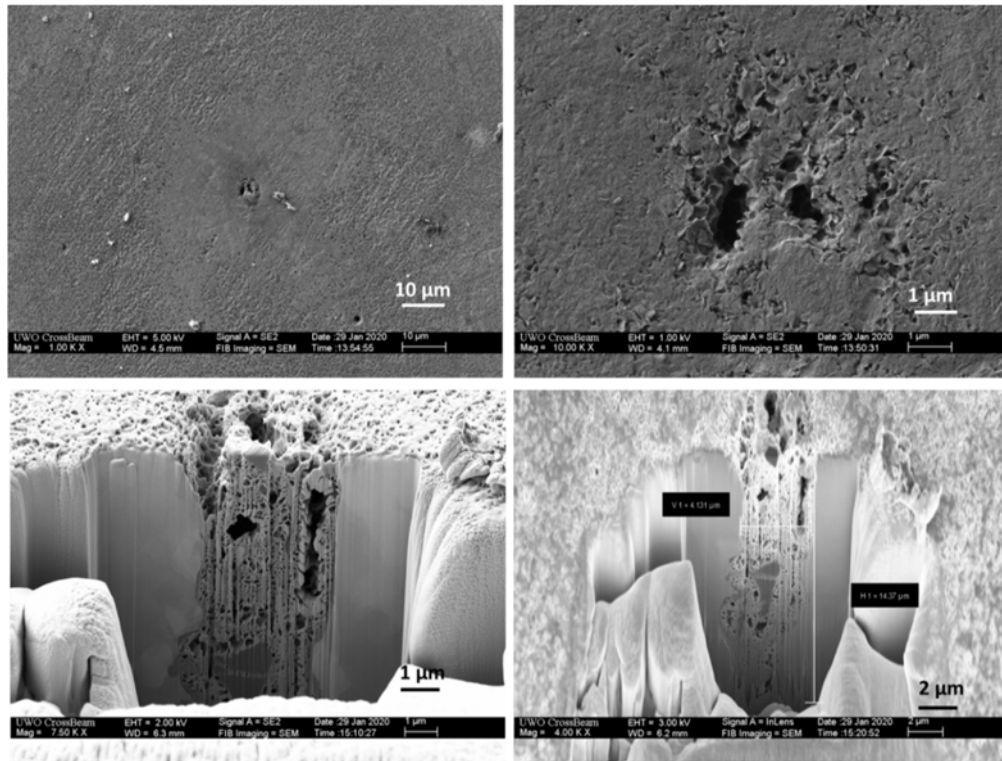


Figure 6.21: SEM and FIB cut image of the center of a Liesegang ring observed on a nickel surface corroded for 144 h in high ionic strength pH 6.0 solution in the presence of γ -radiation.

According to the EDX (energy-dispersive X-ray spectroscopy) results obtained from the Liesegang surface and cross-sectional area, **Figure 6.22** and **Figure 6.23**, there is an evidence of the presence of inclusion sites in the central areas of these features. We assume that the presence of inclusions, particularly in this case titanium, can initiate localized metal dissolution (Intergranular dissolution); however, the propagation of Liesegang features is due to solution conditions and solution systemic feedback in the presence of the gel layer on the surface, and autocatalytic cycles.

Intergranular dissolution usually occurs earlier near the inclusion area due to the weakest metallic bonding between different metals (Ti- Ni) and the pit starts propagating.

As metal dissolution is faster from the localized site than from the surrounding area, the saturation of Ni cations at the interface occurs faster near the surface of the pit area. The metal surface provides the adsorption & nucleation sites for the mixed hydroxide colloids and the hydrogel network starts to spread horizontally and the hydroxide/oxide particles start precipitating early. The formation of hydrogel further slows down the metal dissolution from the surrounding areas of the pit. The metal dissolution from the pit continues but at a progressively slower rate and the mixed hydroxide starts condensing/precipitating earlier near the mouth of the pit. The continued production of Ni^{2+} from the pit creates the concentration gradient of Ni^{2+} within the 2-D Hydrogel network. Liesegang banding, which is a phenomenon arising from the 2-D diffusion of Ni^{2+} combined with adsorption/desorption of Ni^{2+} coupled with oxidation-reduction between $\text{Ni}(\text{OH})_2$ and $\text{Ni}(\text{OH})_3$ (redox assisted Ostwald ripening). Liesegang bands are formed when the diffusion of dissolved species can effectively coupled with precipitation and redissolution of the species (see discussion in Chapter 7).

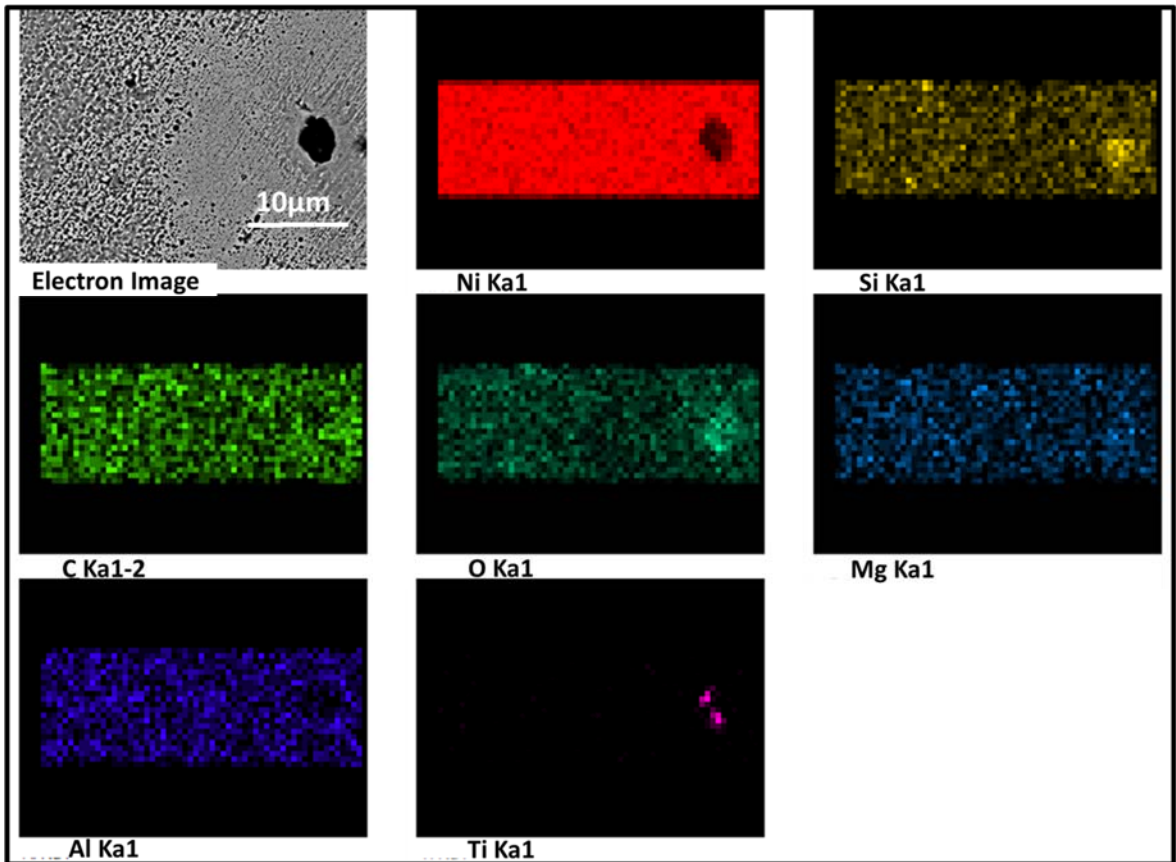


Figure 6.22: EDX analysis of the center of the Liesegang region illustrates the presence of inclusion sites in this area.

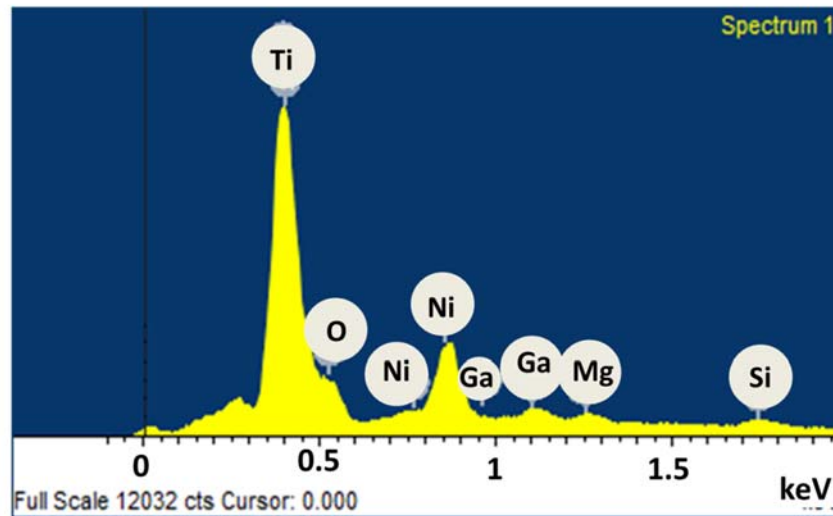
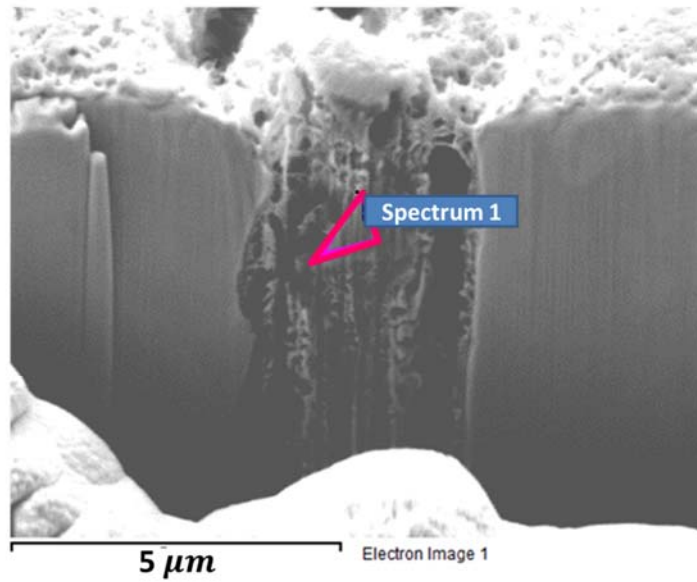


Figure 6.23: EDX analysis of a cross-section of the central area of a Liesegang ring on nickel corroded for 144 h in the presence of γ -radiation in a high I_s pH 6.0 solution. The analysis illustrates the presence of titanium in the localized corroded area.

One of the main processes involved in systemic feedback is autocatalytic cycles accompanied by the formation of a gel layer. Autocatalytic cycles occur as a result of continuous oxidation and reduction reactions between Ni^{2+} and Ni^{3+} . Under radiation, H_2O_2 is continuously produced and reaches a steady-state concentration. Once enough Ni^{3+} has formed on the surface, H_2O_2 can effectively couple with the redox reactions of Ni^{2+} and Ni^{3+} . This phenomenon is facilitated in the presence of a gelatinous layer, and the strength of the feedback or coupling of different processes can be enhanced in the presence of γ -radiation.

Generally, in the presence of a gelatinous layer, transport of oxidants to the pit region and metal cations to the bulk solution is limited. It is assumed that the metal dissolution process generates pores through which solution along with oxidants can pass. The produced $\text{Ni}^{2+}/\text{Ni}^{3+}_{(\text{aq})}$ can diffuse out from the pit region and precipitate in circular patterns due to the presence of the gel layer, but for the most part their diffusion is limited, and these ions remain in the pit and cause autocatalytic cycles, propagating the corrosion in this localized area (**Figure 6.24**).

The presence of radiation can facilitate this process by the continuous production of oxidants (H^+ and H_2O_2) in the diffusion-limited region and providing a more oxidizing environment in the localized deep region (the rate of this propagation would depend on nickel ions diffusing out, not solution diffusion into the pores).

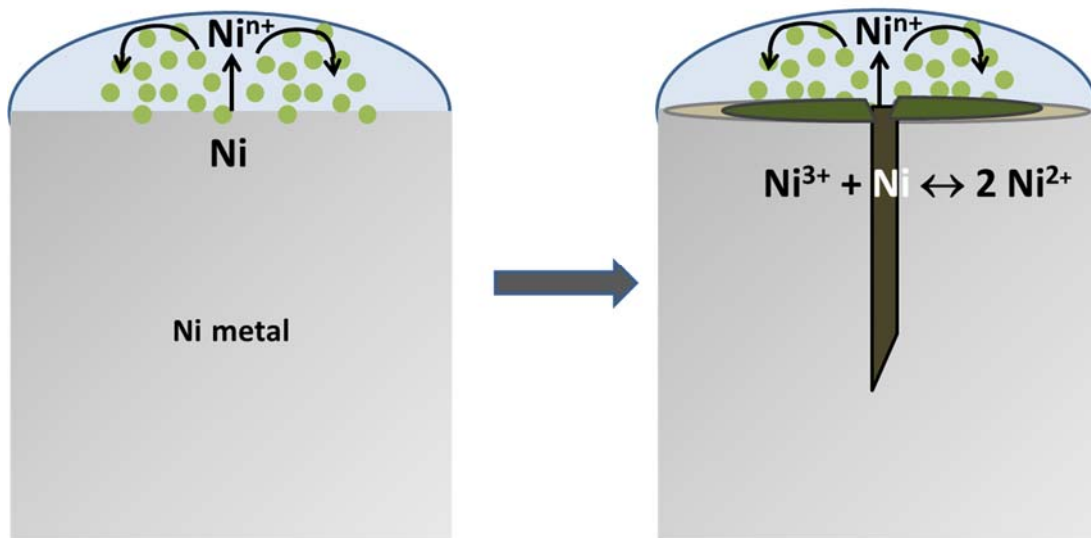


Figure 6.24: Schematic of formation of the Liesegang rings and the hole in the center of the ring. The formation of the gel layer on the surface restricts Ni ion movement toward the bulk solution. Coupling of solution transport and nickel autocatalytic cycles (reduction of Ni^{3+} to Ni^{2+} (M2r)) results in the formation of a hole on the surface.

6.3.2.3. Effect Ionic Strength at pH 8.4 and 10.6 (RAD)

The effect of ionic strength in the presence of γ -radiation at pH 8.4 and pH 10.6 is compared with that of pH 6.0 in **Figure 6.25**.

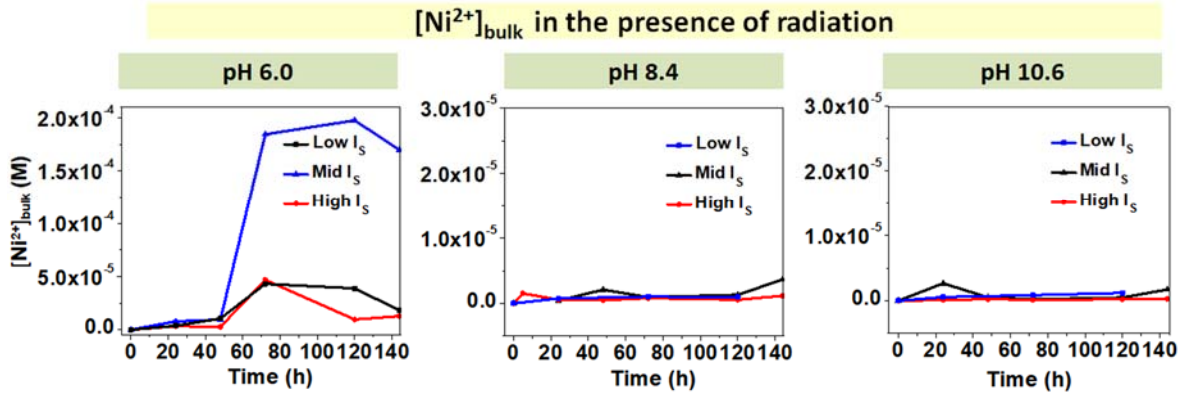


Figure 6.25: Concentration of dissolved nickel ions for nickel samples corroded at pH 8.4 and 10.6 at three ionic strengths compared to that of pH 6.0 shown in Figure 6.11B, in the presence of γ -radiation for test durations of 144 h.

At both pH 8.4 and 10.6 the dissolved nickel concentration remained in a similar range for all I_s , and remained very low compared to at pH 6.0 conditions. At higher pH the evolution of $[Ni^{2+}]_{bulk}$ in the presence of γ -radiation is almost the same as that observed in the absence of radiation. The effect of ionic strength at pH 8.4 and 10.6, in the presence of γ -radiation is similar to that observed in the absence of radiation (section 6.3.1.2). The results show that at higher pH the effect of ionic strength is minimal.

This behaviour is consistent with the low solubility of Ni ions as shown in **Figure 6.3**. At higher pH the solubility of nickel ion is near its minimum and at this pH oxide formation is preferred over dissolution as opposed to the pH 6.0 case, where nickel species are highly soluble, and dissolution dominates over oxide formation. Hence the

chemical activity of $\text{Ni}^{2+}/\text{Ni}(\text{OH})_2$ in the interfacial region stays constant and the net rates of (M1) and (M2) are constant with time. For this reason, the three kinetic corrosion stages observed at pH 6.0 in the presence of γ -radiation (6.3.2.1) are not observed in corrosion systems with high pHs. At higher pH formation of hydroxide/ oxide layer on the surface is faster as shown in the SEM images **Figure 6.26** and **Figure 6.27**

The low magnification optical micrographs of the coupon surface and SEM images showing the surface morphology for pH 8.4 and 10.6 is shown in **Figure 6.26** and **Figure 6.27**. The optical images show that at both pH 8.4 and 10.6 the surface remains relatively uniform during the test duration of 144 h. The coupon surface corroded in low and high I_S solution is greenish in colour whereas a browner colour is observed on the surface for mid I_S solution. The SEM images shows that at low I_S the oxide formed is less compact and uniform than for high I_S samples. At pH 8.4 and low I_S the surface looks clean and no oxide is observed on the surface after 24 h of corrosion, but once it has formed the oxide particle size is large and the oxide is less protective (**Figure 6.26**). At higher ionic strengths the oxide layer forms faster and is more compact. This behaviour is more evident at pH 10.6. Due to the formation of a protective oxide layer on the surface at high I_S , further dissolution of nickel is impeded after 144 h. The AES depth profiling results (**Figure 6.28**) are consistent with this observation. For both pH 8.4 and pH 10.6 a thicker oxide layer forms on the nickel samples corroded in high I_S solutions.

By comparing SEM images obtained at pH 8.4 and 10.6 (**Figure 6.26 and 6.27**) it is evident that the morphologies of the oxide layers that form on the surfaces at these two pHs are different, particularly for high I_S samples. Although at both pHs at higher I_S the filament-like oxides are more compact and coherent, at pH 10.6, the oxide particles are

finer than at pH 8.4, are more integrated into each other and uniformly cover the nickel surface. Although the solubility of nickel cations at pH 8.4 is low, it is still higher than at pH 10.6 [18] and a thicker oxide can form on the nickel surface at pH 8.4 at high I_S , as shown in the AES analysis in **Figure 6.28**. At pH 10.6, due to the formation of a more protective oxide layer on the nickel surface, the total rate of nickel corrosion is lower.

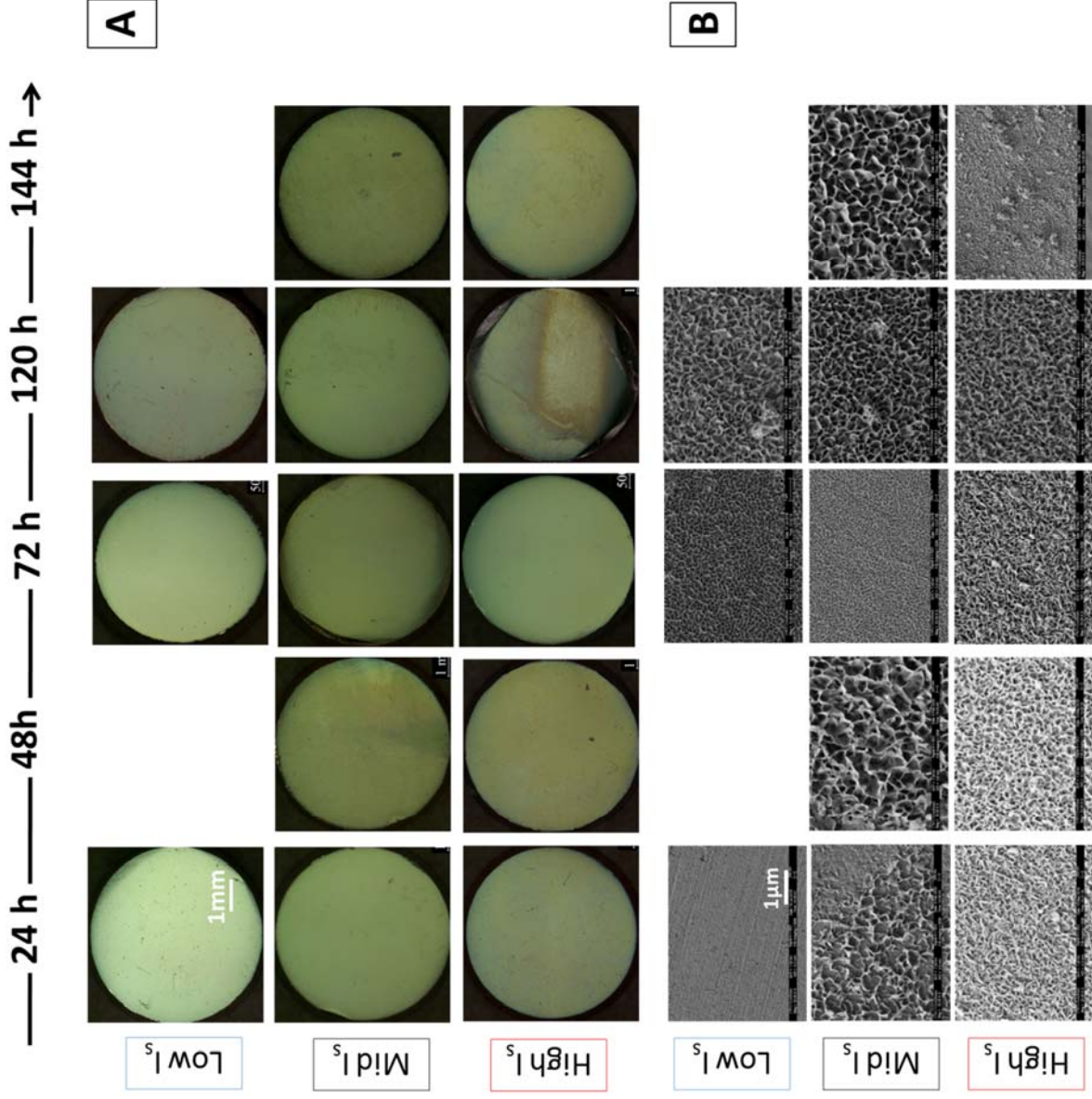


Figure 6.26: Nickel coupons corroded in de-aerated buffered solutions with three different ionic strengths at pH 8.4 in the presence of γ -radiation (at dose rate of $1.8 \text{ kGy}\cdot\text{h}^{-1}$) for test durations of 144 h (for low I_s the results for 24, 72 and 120 h are shown in the Figure): A) Low magnification optical micrographs of the entire surfaces B) SEM images of the general oxide morphology of nickel samples. All images have the same scales (1 μm bar

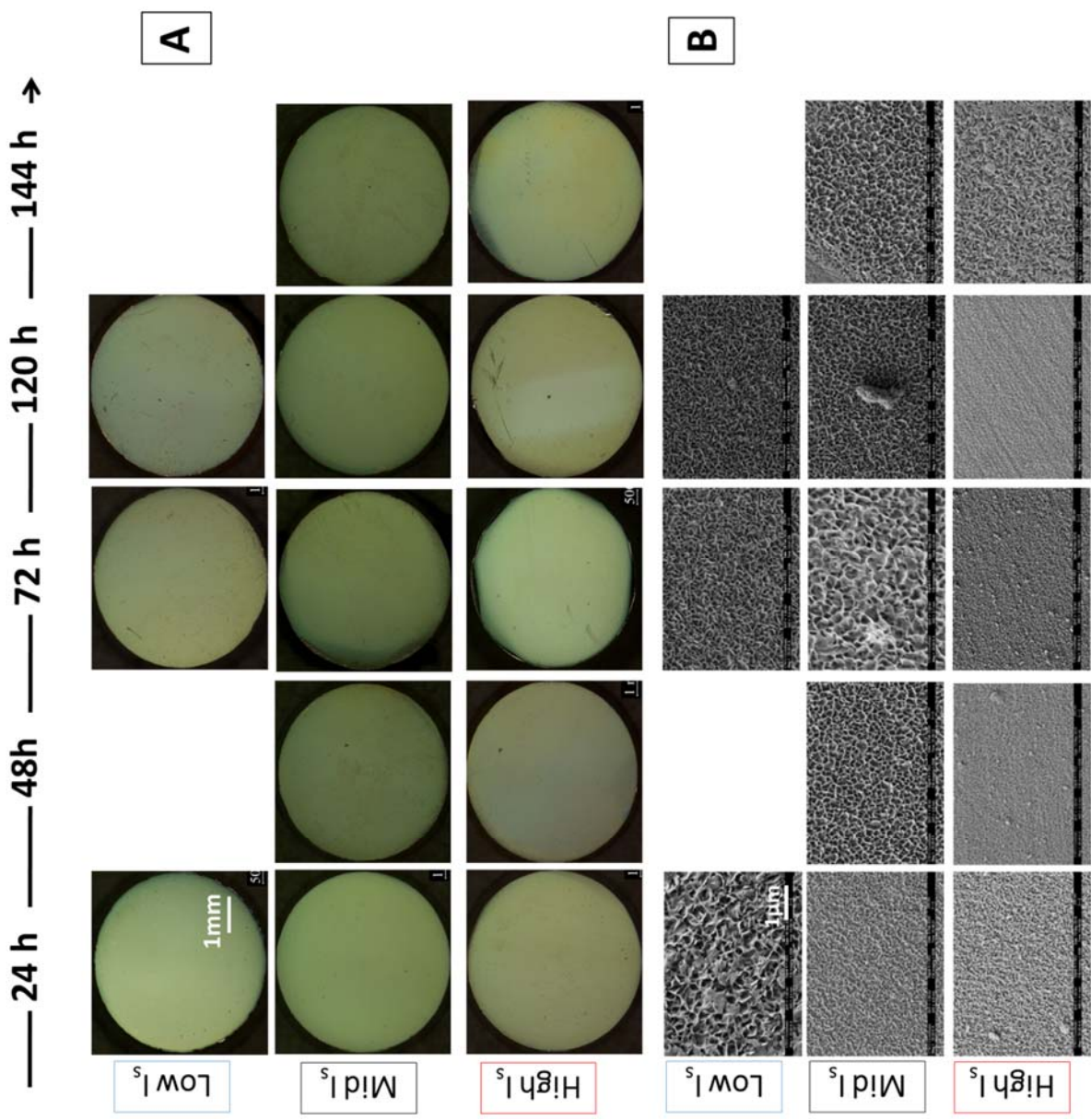


Figure 6.27: Nickel coupons corroded in de-aerated buffered solutions with three different ionic strengths at pH 10.6 in the presence of γ -radiation (at dose rate of $1.8 \text{ kGy}\cdot\text{h}^{-1}$) for test durations of 5-144 h (for low I_s the results for 24, 72 and 120 h are shown in the Figure): A) High magnification optical micrographs of the entire surfaces B) SEM images of the general oxide morphology of nickel samples. All images have the same scales ($1 \mu\text{m}$ bar

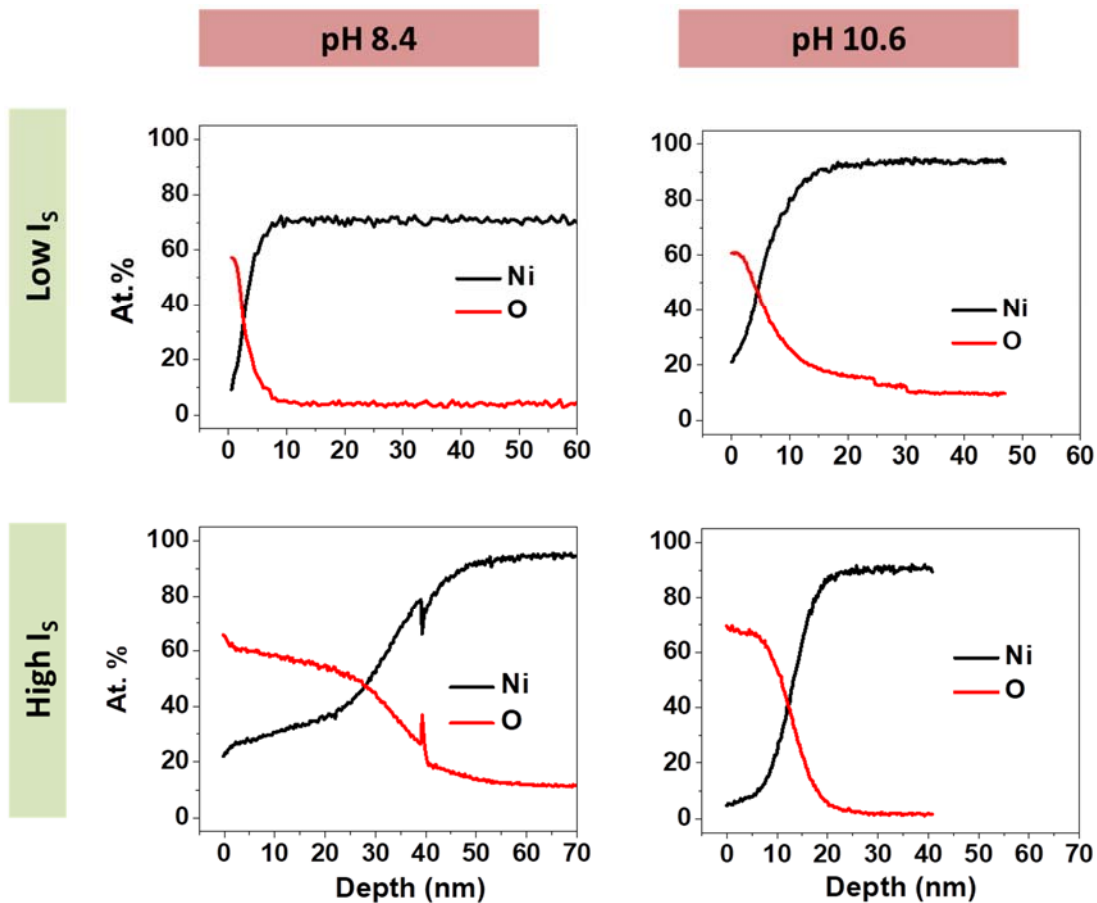


Figure 6.28: Ni and O Depth Profiles determined by AES, of nickel coupons corroded for 120 h in the presence of γ -radiation at pH 8.4 and 10.6 in both high and low ionic strength solutions.

The results show that in the presence of γ -radiation the Ni oxidation rate increases, which increases both Ni dissolution and Ni oxide growth. At pH 6.0, this increase primarily appears as an increase in dissolution. However, at pH 10.6 metal oxide growth increases and subsequently impedes nickel oxidation. At the intermediate pH (8.4), the nickel dissolution rate is higher than pH 10.6 and less than pH 6.0 (which is

similar in both the presence and absence of radiation). At pH 8.4 oxide formation and metal dissolution are competing, which is why the oxide on the surface at pH 8.4 is thicker than the oxide at pH 6.0 and more porous than the oxide at pH 10.6.

Unlike for pH 6.0, for pH 8.4 and 10.6 the non-linear trend of $[\text{Ni}^{2+}]_{\text{bulk}}$ over the test duration is in the same range in both the presence and absence of γ -radiation, and γ -radiation has only a minor effect on the $[\text{Ni}^{2+}]_{\text{bulk}}$ behaviour. This is an indication that redox/mass transport coupling is not a predominant process during nickel corrosion for high solution pHs, regardless of the ionic strength. As a result, despite the fact that γ -radiation leads to the formation of more surface features (as described in 6.3.2.2), Liesegang rings are not present on the nickel surfaces corroded at higher pHs.

6.4. CONCLUSIONS

Corrosion is an interfacial charge and mass transfer process in which solid metal atoms are oxidized to soluble cations, coupled with reduction of solution species at the interfacial region. Depending on the corrosion conditions, the initially dissolved metal cations can diffuse from the surface to the bulk solution or can precipitate on the surface and grow as stable oxides over time. The ionic strength of the solution does not directly affect interfacial charge transfer processes (metal oxidation and solution reduction occurring near the metal surface) but can affect the transport of ionic species (Ni^{2+} and H^+) into and from the bulk solution. This can subsequently influence the chemistry of the oxide (morphology and thickness) formed on the surface and the general trend of the overall corrosion process.

In this Chapter, the effect of solution ionic strength on nickel corrosion was investigated by performing coupon exposure test at three different solution pHs in the absence and presence of γ -radiation. The effect of ionic strength was studied by keeping the pH constant during the test duration (using buffered solutions) while varying the ionic strength of the solution.

In the absence of radiation at pH 6.0, the main corrosion process is metal ion dissolution, and the concentration of nickel ions dissolved in solution increases with increasing ionic strength. At higher pH (8.4 and 10.6) oxide formation predominates. As a protective oxide layer forms on the surface, v_{trans} controls the rate of oxidation, and the concentration of nickel ions in solution is lower. However, at higher solution pHs, an increase in I_S leads to the formation of a more protective oxide which can impede nickel oxidation over longer time periods.

The presence of γ -radiation affects the overall metal oxidation rate primarily via production of H_2O_2 . Radiation also alters the oxide film composition, thickness and morphology at all pHs. In the presence of γ -radiation at pH 6.0, more nickel dissolution was observed for the low I_S solution, a behaviour that is opposite to that observed in the absence of radiation. For the high I_S solutions at pH 6.0 in the presence of radiation, the high concentration of nickel ions at the interface results in the formation of a gelatinous oxide layer on the surface, decreasing the rate of metal ion dissolution.

In the presence of γ -radiation, the fluctuations in dissolved nickel ion concentration were amplified, and particularly for low I_S , and the concentration of dissolved ions was about 10 times higher than for high I_S . Also, this value was about 100

times higher than that observed for low I_S in the absence of radiation. The evolution of dissolved ion concentration and surface morphology for low I_S , shows that the corrosion progress through three kinetic stages. In Stage 1, the overall corrosion process is the oxidation of $\text{Ni}^0_{(m)}$ to $\text{Ni}^{2+}_{(aq)}$, and the trans of $\text{Ni}^{2+}_{(aq)}$ from the metal surface to the bulk solution. In Stage 2, as the concentration of Ni^{2+} in the solution reaches its saturation limit, the Ni^{2+} undergoes hydrolysis and phase-partitioning equilibrium forming $\text{Ni}(\text{OH})_2$ colloids that can precipitate as a hydrogel network on the surface. In Stage 3, the overall oxidation of $\text{Ni}^0_{(m)}$ becomes negligible, but redox assisted Ostwald ripening continues, forming $\text{Ni}^{\text{II}}/\text{Ni}^{\text{III}}$ hydroxide/oxides on the surface.

This study has also revealed the non-linear nature of nickel corrosion dynamics over long time periods. These non-linear dynamics can be influenced by changing the solution ionic strength and applying γ -radiation. The results presented here have shown that this behaviour is amplified in the presence of γ -radiation and at low solution pHs; at higher solution pHs this effect is reduced in both the presence and absence of radiation. The non-linear behaviour occurs as a result of coupling between the redox reactions and transport processes. Chemical oscillation resulting in periodic ion precipitation and dissolution is one consequence of this coupling, which leads to the formation of surface features such as Liesegang rings on the nickel surface at pH 6.0, and particularly at high I_S and in the presence of γ -radiation.

Based on the results obtained from this study it can be concluded that ionic strength increases the ion transport and thus increases the rate of the nickel corrosion process. However, the predominant corrosion pathway is determined by the solution pH. The dissolution rate is initially affected by both pH and I_S . At near-neutral pH (6.0),

nickel species are highly soluble and therefore the main corrosion pathway is dissolution. At higher pHs (8.4 and 10.6), the solubility of nickel species is lower, oxide formation dominates over dissolution, and a thicker oxide layer forms on the surface. Solvation of metal cation increases with pH and I_S initially increases dissolution rate. But increasing pH has a considerable effect of the maximum concentration, and diffusion rate at longer times. Hence, the overall effect of pH on dissolution is not linear.

The systematic studies presented in this chapter have produced many unusual observations that have not previously been reported in nickel corrosion studies. These observations are very different from what is expected, given the high corrosion resistance of nickel. These results presented in this chapter demonstrate that nickel corrosion depends strongly on the solution pH. The ionic strength of the solution can affect the overall corrosion rate at lower pH by increasing the ion mobility which increases the rate of ion transfer from the metal surface to the bulk solution.

6.5. REFERENCES

- [1] D.S. Hall, An Electrochemical and Spectroscopic Investigation of Nickel Electrodes in Alkaline Media for Applications in Electro-Catalysis An Electrochemical and Spectroscopic Investigation of Nickel, Thesis Diss Univ. Ottawa. (2014).
- [2] A.Y. Musa, J.C. Wren, Combined effect of gamma-radiation and pH on corrosion of Ni-Cr-Fe alloy inconel 600, *Corros. Sci.* 109 (2016) 1–12. <https://doi.org/10.1016/j.corsci.2016.03.015>.
- [3] R.B. Rebak, Corrosion testing of nickel and titanium alloys for nuclear waste disposition, *Corros. Sci.* 65 (2009) 252–271. <https://doi.org/10.5006/1.3319132>.
- [4] M. Momeni, Gamma-Radiation Induced Corrosion of Alloy 800, *Electron. Thesis Diss. Repos.* 5011, University of Western Ontario (2017). <https://doi.org/10.1016/j.psychres.2013.12.014>.
- [5] M. Behazin, Radiation induced corrosion of Stellite-6, *Electron. Thesis Diss. Repos.* 2432, University of Western Ontario (2014).
- [6] D. Guo, Corrosion Dynamics of Carbon Steel in Used Fuel Container Environments, *Electron. Thesis Diss. Repos.* 5897, University of Western Ontario. (2018).
- [7] P.H. Tewari, A.B. Campbell, Temperature dependence of point of zero charge of cobalt and nickel oxides and hydroxides, *J. Colloid Interface Sci.* 55 (1976) 531–539. [https://doi.org/10.1016/0021-9797\(76\)90063-1](https://doi.org/10.1016/0021-9797(76)90063-1).
- [8] Y.G. Shin, Nonlinear Dynamics of Carbon Steel Corrosion under Gamma Radiation, *Electron. Thesis Diss. Repos.* 7339, University of Western Ontario (2020).
- [9] C.F. Baes, R.E. Mesmer., *Hydrolysis of Cations*, Wiley, 1976.
- [10] B. Beverskog, I. Puigdomenech, Revised Pourbaix diagrams for nickel at 25–300°C, *Corros. Sci.* 39 (1997) 969–980. [https://doi.org/10.1016/S0010-938X\(97\)00002-4](https://doi.org/10.1016/S0010-938X(97)00002-4).
- [11] E. Cattaneo, B. Riegel, Chemistry, Electrochemistry, And Electrochemical Applications | Nickel, in: *Encycl. Electrochem. Power Sources*, Elsevier, 2009 https://doi.org/10.1063/9780735421578_app1.
- [12] Y. Miao, L. Ouyang, S. Zhou, L. Xu, Z. Yang, M. Xiao, R. Ouyang, Electrocatalysis and electroanalysis of nickel, its oxides, hydroxides and oxyhydroxides toward small molecules, *Biosens. Bioelectron.* 53 (2014) 428–439. <https://doi.org/10.1016/j.bios.2013.10.008>.
- [13] A.M. Gadalla, T.W. Livingston, Thermal behavior of oxides and hydroxides of

iron and nickel, *Thermochim. Acta.* 145 (1989) 1–9. [https://doi.org/10.1016/0040-6031\(89\)85121-4](https://doi.org/10.1016/0040-6031(89)85121-4).

- [14] B. Subramanian, M. Mohamed Ibrahim, V. Senthilkumar, K.R. Murali, V. Vidhya, C. Sanjeeviraja, M. Jayachandran, Optoelectronic and electrochemical properties of nickel oxide (NiO) films deposited by DC reactive magnetron sputtering, *Phys. B Condens. Matter.* 403 (2008) 4104–4110. <https://doi.org/10.1016/j.physb.2008.08.014>.
- [15] S. Pizzini, R. Morlotti, Thermodynamic and Transport Properties of Stoichiometric and Nonstoichiometric Nickel Oxide, *J. Electrochem. Soc.* 114 (1967) 1179. <https://doi.org/10.1149/1.2426441>.
- [16] W.L. Dudley, Nickelo-nickelic hydrate, $\text{Ni}_3\text{O}_4 \cdot 2\text{H}_2\text{O}$, *J. Am. Chem. Soc.* 18 (1896) 901–903. <https://doi.org/10.1021/ja02096a003>.
- [17] T.P. Murphy, M.G. Hutchins, Oxidation states in nickel oxide electrochromism, *Sol. Energy Mater. Sol. Cells.* 39 (1995) 377–389. [https://doi.org/10.1016/0927-0248\(96\)80003-1](https://doi.org/10.1016/0927-0248(96)80003-1).
- [18] E. Zhang, Y. Tang, Y. Zhang, C. Guo, L. Yang, Hydrothermal synthesis of β -nickel hydroxide nanocrystalline thin film and growth of oriented carbon nanofibers, *Mater. Res. Bull.* 44 (2009) 1765–1770. <https://doi.org/10.1016/j.materresbull.2009.03.005>.
- [19] D.P. Dubal, V.J. Fulari, C.D. Lokhande, Effect of morphology on supercapacitive properties of chemically grown β -Ni(OH)₂ thin films, *Microporous Mesoporous Mater.* 151 (2012) 511–516. <https://doi.org/10.1016/j.micromeso.2011.08.034>.
- [20] H. Strathmann, Electromembrane Processes: Basic Aspects and Applications, in: *Compr. Membr. Sci. Eng.*, Elsevier Ltd., 2017: pp. 355–392. <https://doi.org/10.1016/b978-0-12-409547-2.12257-7>.
- [21] J. Wang, J. Wang, E.H. Han, Influence of Conductivity on Corrosion Behavior of 304 Stainless Steel in High Temperature Aqueous Environment, *J. Mater. Sci. Technol.* 32 (2016) 333–340. <https://doi.org/10.1016/j.jmst.2015.12.008>.
- [22] J.E. Saiers, G.M. Hornberger, The influence of ionic strength on the facilitated transport of cesium by kaolinite colloids, *Water Resour. Res.* 35 (1999) 1713–1727. <https://doi.org/10.1029/1999WR900055>.
- [23] J. Won, S.E. Burns, Influence of Ionic Strength on Clay Particle Deposition and Hydraulic Conductivity of a Sand Medium, *J. Geotech. Geoenvironmental Eng.* 143 (2017) 04017081.
- [24] A. J. Bard Larry R., Faulkner, *Electrochemical Methods Fundamentals and Applications*, Wiley, 2001.
- [25] Y. Liu, Z. Zhang, N. Bhandari, Z. Dai, F. Yan, G. Ruan, A.Y. Lu, G. Deng, F. Zhang, H. Al-Saiari, A.T. Kan, M.B. Tomson, New Approach to Study Iron

Sulfide Precipitation Kinetics, Solubility, and Phase Transformation, *Ind. Eng. Chem. Res.* 56 (2017) 9016–9027. <https://doi.org/10.1021/acs.iecr.7b01615>.

- [26] D.S. Chernavskii, A.A. Polezhaev, S.C. Müller, A model of pattern formation by precipitation, *Phys. D Nonlinear Phenom.* 54 (1991) 160–170. [https://doi.org/10.1016/0167-2789\(91\)90115-P](https://doi.org/10.1016/0167-2789(91)90115-P).
- [27] A.A. Polezhaev, S.C. Müller, Complexity of precipitation patterns: Comparison of simulation with experiment, *Chaos.* 4 (1994) 631–636. <https://doi.org/10.1063/1.166040>.
- [28] M. Li, Galvanic Corrosion of Carbon Steel-Stainless Steel Welds, *Electron. Thesis Diss. Repos.* 7162, University of Western Ontario (2020).
- [29] R.F. Sultan, A.F.M. Abdel-Rahman, On dynamic self-organization: Examples from magmatic and other geochemical systems, *Lat. Am. J. Solids Struct.* 10 (2013) 59–73. <https://doi.org/10.1590/S1679-78252013000100006>.
- [30] T.I. Sutherland, C.J. Sparks, J.M. Joseph, Z. Wang, G. Whitaker, T.K. Sham, J.C. Wren, Effect of ferrous ion concentration on the kinetics of radiation-induced iron-oxide nanoparticle formation and growth, *Phys. Chem. Chem. Phys.* 19 (2017) 695–708. <https://doi.org/10.1039/c6cp05456k>.
- [31] L.M. Alrehaily, J.M. Joseph, A.Y. Musa, D.A. Guzonas, J.C. Wren, Gamma-radiation induced formation of chromium oxide nanoparticles from dissolved dichromate, *Phys. Chem. Chem. Phys.* 15 (2013) 98–107. <https://doi.org/10.1039/c2cp43150e>.
- [32] K. Daub, X. Zhang, L. Wang, Z. Qin, J.J. Noël, J.C. Wren, Oxide growth and conversion on carbon steel as a function of temperature over 25 and 80 °c under ambient pressure, *Electrochim. Acta.* 56 (2011) 6661–6672. <https://doi.org/10.1016/j.electacta.2011.05.047>.
- [33] P. Taylor, Ostwald Ripening In Emulsions, *Adv. Colloid Interface Sci.* 75 (1998) 107–163.

CHAPTER 7

INVESTIGATING THE TIME-DEPENDENT EFFECT OF pH AND RADIATION ON THE CORROSION OF NICKEL IN NON-BUFFERED SOLUTION AT 150 °C

7.1. INTRODUCTION

Corrosion is a complex process involving multiple electrochemical and chemical reactions coupled with interfacial charge transfer processes and solution transport of metal cations. Different solution parameters affect the kinetics of the elementary steps differently, which leads to different metal oxidation paths and overall oxidation rates. The kinetics of the elementary reactions are not independent of each other but strongly coupled, which leads to a cyclic feedback loop (systemic feedback) between different elementary steps. Due to systemic feedback the overall metal oxidation rate does not follow linear dynamics. Because of this complexity, any change in solution conditions can have a significant impact on the corrosion behaviour of metals [1,2]. This impact is more pronounced when the solution is not buffered, and solution pH evolves with time during the progression of corrosion [3].

In chapter 5, the combined effect of pH and ionic strength (I_s) on the evolution of Ni oxidation was investigated in large volume and Ar-purged solutions at 80 °C. This study was performed at pH 6.0 or pH 10.6 using electrochemical technique which include

corrosion potential measurement as a function of time, potentiodynamic (PD) polarization measurement, multiple cycles of CV with different vertex potentials, and potentiostatic (PS) polarization measurements. The results presented in this Chapter have shown that the overall metal oxidation occurs through a series of elementary rate-determining steps (RDS) with some steps occurring in parallel. Basically metal oxidation involves interfacial transfer of metal atom and the intermediate oxidation products can undergo their own chemical processes. The rate determining step (RDS) that comprises the overall oxidation process can evolve as the intermediate products accumulate in the interfacial region. The metal oxidation dynamic system may transition from one (pseudo-) steady state to another before it reaches the final steady state. The final steady state (dynamic phase) the system reaches, and how fast the system passes through intermediate steady states (kinetic stages) to reach the final steady state, depend on solution reaction environments in the interfacial region. At pH 6.0 when the solubility of Ni^{2+} is large $(a_{\text{Ni}^{2+}})_{int}$ does not accumulate above its saturation capacity. The chemical reactions of Ni^{2+} , (hyd), (gel) and (M2), in Ar-purged environment are too slow to compete with (trans). Consequently, the metal oxidation dynamic system does not progress beyond Phase I, i.e., the RDS of the final steady state are (M1) and (trans). Ionic strength (I_s) affects ion mobility and has a significant effect on the rate of (trans). At pH 10.6, when the solubility of Ni^{2+} is significantly reduced, $(a_{\text{Ni}^{2+}})_{int}$ quickly reaches its saturation capacity. The hydrolysis equilibrium quickly shifts to $\text{Ni}(\text{OH})_2$ formation, accelerating (gel) and (M2). The metal oxidation system quickly progresses beyond Phase I and into Phases II (and perhaps Phase III at longer times). I_s does not affect the kinetics of (gel) and (M2) directly. However, the kinetics of (gel) and (M2) strongly influence the rate of

(trans). Hence, in large volume Ar-purged solutions, the effect of I_S on the overall oxidation rate is diminished at pH 10.6, compared to that at pH 6.0.

In Chapter 6, we explored the combined effect of pH and I_S in small volume and stagnant solutions under Ar saturated conditions, either in the absence or presence of a continuous flux of γ -radiation. The long-term corrosion dynamics was studied by examining the changes in oxide composition and morphology using optical microscopy, SEM and AES and the dissolved (and dispersed) Ni^{2+} concentration using ICP-OES as a function of time. In a smaller solution volume the bulk concentration of Ni^{2+} ($[\text{Ni}^{2+}]_{\text{bulk}}$) increases faster at a same metal oxidation rate. Because the rate of (trans) depends on concentration gradient, the faster increase in $[\text{Ni}^{2+}]_{\text{bulk}}$ will decelerate (trans). The overall metal oxidation progresses quickly to Phase III. At long times, the overall metal oxidation may be very slow but the chemical processes of corrosion products, (trans), (gel) and (oxide), can continue. Ionic strength affects the oxide growth by Ostwald ripening from precipitation-redissolution of dissolved species. The results obtained from this study have shown that ionic strength increases the ion transport and thus increases the rate of the nickel corrosion process. However, the predominant corrosion pathway is determined by the solution pH. The dissolution rate is initially affected by both pH and I_S . At near-neutral pH (6.0), nickel species are highly soluble and therefore the main corrosion pathway is dissolution. At higher pHs (8.4 and 10.6), the solubility of nickel species is lower, oxide formation dominates over dissolution, and a thicker oxide layer forms on the surface. Solvation of metal cation increases with pH and I_S initially increases dissolution rate. But increasing pH has a considerable effect of the maximum concentration, and diffusion rate at longer times. Hence, the overall effect of pH on

dissolution is not linear. Based on the obtained results the RDS that comprise the overall Ni corrosion process occurring in small volume Ar-purged buffer solutions in the presence of radiation was schematically illustrated in Chapter 6.

In this Chapter, the general effect of solution conditions on nickel corrosion is investigated in low ionic strength non-buffered solution where the solution pH can change during nickel corrosion and in turn affect the general corrosion behaviour of nickel over time. To achieve that the corrosion dynamics of nickel are investigated by performing coupon exposure tests in non-buffered low ionic strength solutions with different initial pHs (6.0, 8.4 and 10.6) at high temperature (150 °C), in the presence and absence of γ -radiation. The corrosion behaviour of nickel is studied by monitoring the dissolved ion concentrations and surface morphology in parallel with the solution pH over test durations of 5 to 144 h. This study will enhance our mechanistic understanding of the dynamics of nickel corrosion in low ionic strength non-buffered solution, under high-temperature conditions in the presence and absence of γ -radiation.

7.2. EXPERIMENTAL

7.2.1. Materials and Solutions

Ni coupons with a diameter of 6.20 mm and thickness of 3 mm were used for this study and both sides of the sample with a total surface area of 1.187 cm² were exposed to the test solution. Prior to each experiment, the flat coupon surfaces were mechanically polished successively with 400, 600, 800, and 1200 grit silicon carbide papers, followed by mirror-polishing on a Texmet microcloth (Buehler) with the 1 μ m MetaDi Supreme

diamond paste suspension (Buehler). Samples were rinsed in a 1:1 acetone/ethanol mixture in an ultrasonic bath for 5 min to remove surface residues, then rinsed with Type 1 water and dried with Ar.

All experiments were conducted in argon-purged buffer-free solutions with initial pHs adjusted to 6.0, 8.4 and 10.6. Solutions were prepared using water (purified using a NANO pure Diamond UV ultra-pure water system from Barnstead International) with a resistivity of 18.2 M Ω ·cm. The pH was adjusted to 8.4 or 10.6 by dropwise addition of NaOH and for pH 6.0 experiments the water was used without adjustment. The pH of the solution was measured using an Accumet[®] Basic AB15 pH meter using an Ag/AgCl electrode.

7.2.2. Coupon Exposure Tests

All corrosion tests in the presence and absence of γ -radiation were carried out for test durations of 5 to 144 h in sealed Pyrex vials which were deaerated and prepared in an Ar-purged glove box. The coupons were placed on a pedestal at the bottom of the vial and immersed in solution by adding 7 ml of the test solution to each vial. The vials were sealed using aluminum crimp caps fitted with PTFE silicone septa (Agilent Technologies). The vials were then placed in a 300 mL AISI 316 stainless steel autoclave (Parr Instrument Company) and heated to 150 °C. The temperature was maintained at 150 °C during the test duration using a thermostat. Irradiation experiments were performed using a MDS Nordion Gammacell 220 Excel Cobalt-60 irradiator. The experimental setup used was similar to that used in Chapter 6 as shown in **Figure 7.1**. The dose rate at the time of these experiments was 1.6 kGy·h⁻¹.

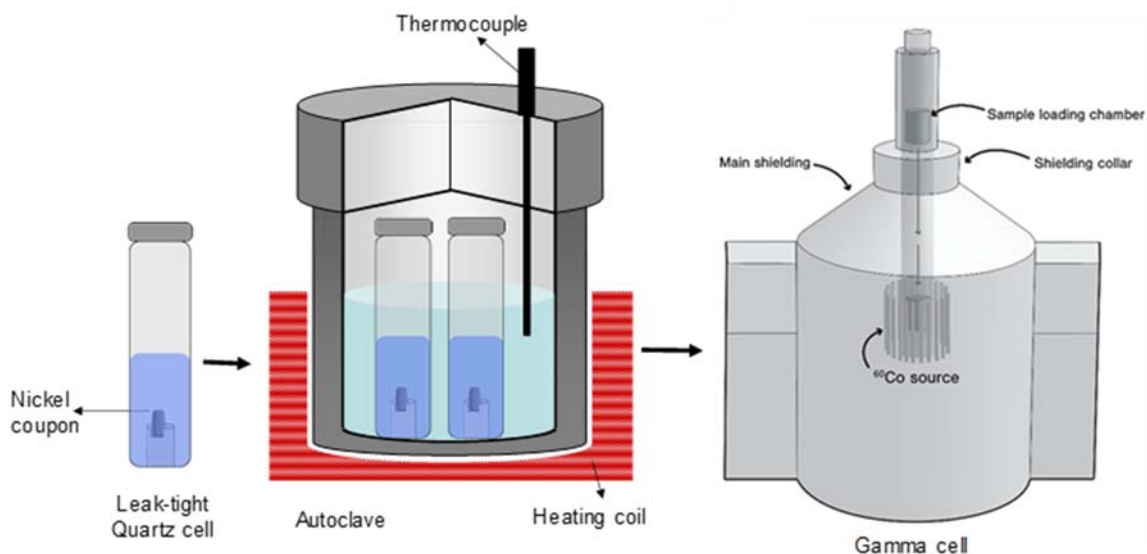


Figure 7.1 Experimental setup for coupon exposure tests in the absence and presence of gamma radiation.

7.2.3. Post-Test analysis

After the test duration the nickel coupons were removed from the vials, washed with water, and dried with flowing argon. Coupon samples were then stored in a vacuum chamber to await surface analysis. The solutions were transferred into glass vials, allowed to cool to room temperature, and the pH of the solution was measured. The test solutions were then digested using TraceMetal™ grade nitric acid (Fisher Chemical) and the concentration of dissolved nickel ions in solution was analyzed using ICP-OES. The morphology and composition of the oxide layer formed on the coupon surface was investigated using optical microscopy and scanning electron microscopy (SEM) and X-ray photoelectron spectroscopy (XPS). The optical images were taken using a Leica DVM 6A digital microscope. The same lighting settings were used to image each sample. A LEO 1540XB field emission SEM was used in the high-resolution mode for analyzing

the surface morphology. The XPS analysis was performed on a KRATOS Axis Nova spectrometer using monochromatic Al K_{α} radiation and operating at 210 W, with a base pressure of 10^{-8} Pa.

7.3. RESULTS AND DISCUSSION

The corrosion dynamics of nickel in low ionic strength non-buffered solutions with initial pHs 6.0, 8.4 and 10.6 were studied at 150 °C under de-aerated conditions in the presence (RAD) and absence (No RAD) of radiation. These pHs were chosen since the solubility of Ni ions changes by several orders of magnitude from pH 6.0 to 10.6, as shown in **Figure 7.2**.

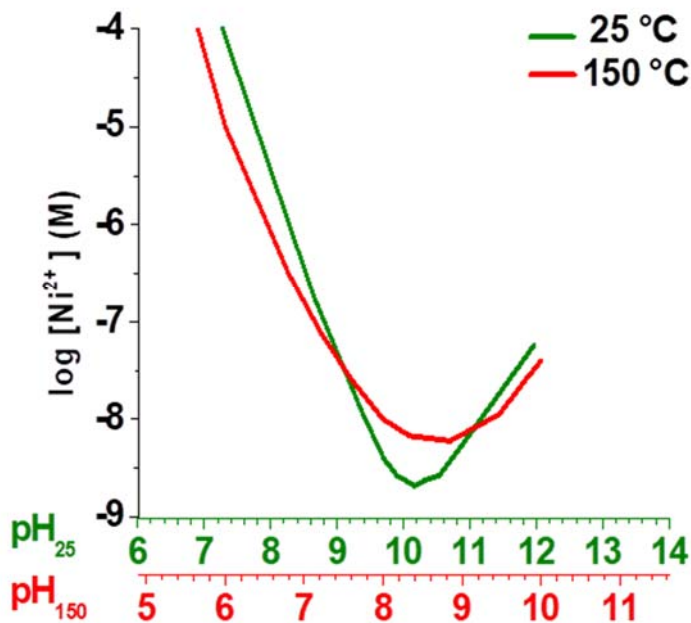


Figure 7.2: The solubility of Ni ions in water at 25 and 150 °C [4,5]

7.3.1. Corrosion Dynamics of Nickel in the absence of Radiation (No RAD)

In this section, the corrosion behaviour of nickel in low ionic strength non-buffered solutions in the absence of γ -radiation is discussed. The solution and surface analysis results for experiments performed with initial pH 6.0 are discussed first and compared with the results obtained with initial pHs 8.4 and 10.6. By comparing the results in this section with those obtained in the presence of γ -radiation (Section 7.3.2), a better understanding of the general effect of γ -radiation on nickel corrosion behaviour can be obtained.

7.3.1.1. Effect of pH 6.0 (No RAD)

Figure 7.3 shows the low and high magnification optical micrographs of the surface, the concentration of Ni^{2+} dissolved in the solution ($[\text{Ni}^{2+}]_{\text{bulk}}$) and the pH evolution during the test duration. The optical images show that the nickel surface has a uniform green colour during the initial hours of corrosion (**Figure 7.3A**). This green colour is due to the formation of a thin layer of $\text{Ni}(\text{OH})_2$ and/or NiO that uniformly covers the surface [6,7]. Over time, a darker green layer (greenish brown) partially covers the surface. This darker layer is the result of the formation of a higher oxidation state nickel compound, $\text{Ni}(\text{OH})_3$, on the surface [8]. As described in chapter 6, nickel hydroxide is green [6–8], NiO is green [9,10], $\text{Ni}(\text{OH})_3$ is expected to be brownish [8], and Ni_3O_4 and Ni_2O_3 are black in colour [11,12]. The colours of nickel oxide/hydroxide powder samples (Alfa Aesar) are presented in **Figure 7.4**. Optical images can provide

qualitative information about the types of nickel hydroxide or oxide formed on the surface based on their characteristic colours.

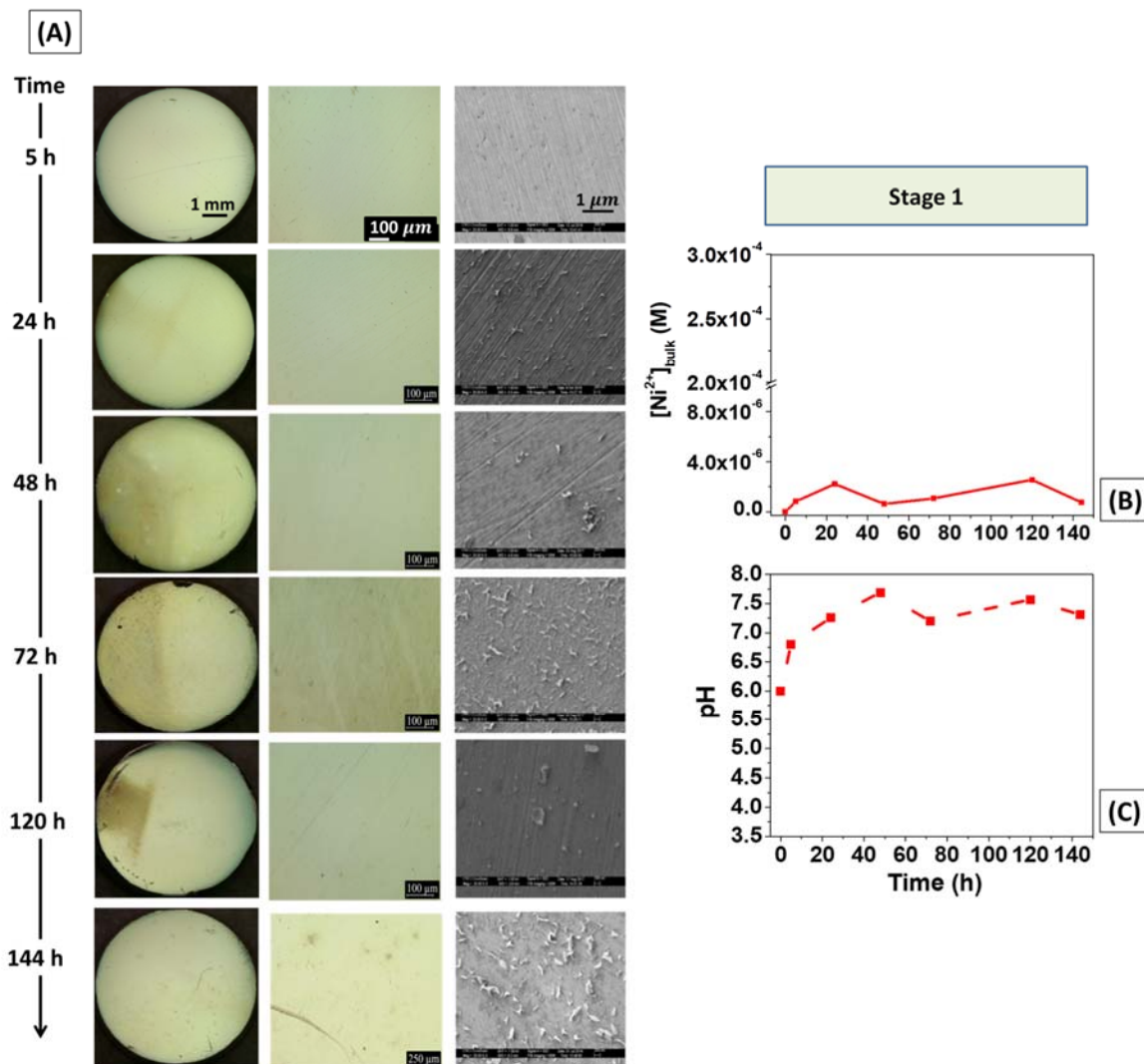


Figure 7.3: Nickel coupons corroded in de-aerated non-buffered solution at initial pH 6.0 in the absence of radiation for test duration of 5-144 h: A) Low magnification optical images of the entire surfaces, high magnification optical micrographs and SEM images, B) Concentration of dissolved nickel ions in solution, and C) pH measured after the test duration. All image sets have the same scales - low magnification optical: 1 mm scale bar, high magnification optical: 100 μm, and SEM: 1 μm.

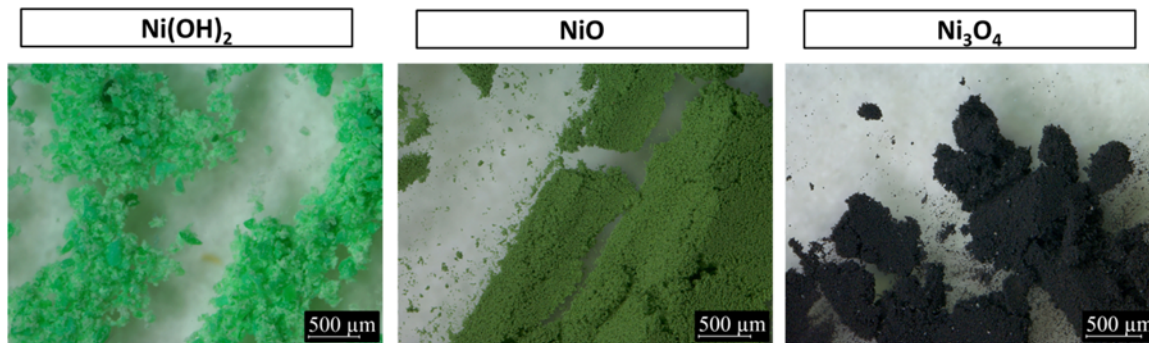


Figure 7.4: Ni hydroxide/oxide (Alfa Aesar) characteristic colours observed by optical microscopy.

In **Figure 7.3A**, the SEM images of the surface (5-48 h) show distinct polishing lines and the growth of filament-like oxide, which initiates along the polishing lines. This indicates that the oxide formed on the surface is thin and does not cover the whole surface. After 48 h, the polishing lines are less distinct, indicating that the surface has become uniformly covered by an oxide film. Further discussion of the oxide composition is found in Section 7.3.3.

These surface behaviour are complemented by the solution analysis results shown in **Figure 7.3B**. Solution analysis provides information about the concentration of nickel cations dissolved in the solution ($[\text{Ni}^{2+}]_{\text{bulk}}$) during corrosion. The concentration of dissolved nickel ions remains relatively low (compared to that in the presence of γ -radiation (Section 7.3.2.1) and fluctuates slightly (in the range 0 to 3×10^{-6} M) over the measured period of 144 h. The fluctuations observed in the dissolved nickel ion are expected when dealing with multi-phase systems and are not due to experimental error. These fluctuations indicate a cyclic feedback loop between different elementary steps.

In general, corrosion is an electrochemical process in which a metal oxidation half- reaction is coupled with a solution reduction half-reaction. During nickel corrosion,

H^+ is consumed in reduction reaction. In the absence of radiation, consuming H^+ results in an increase in solution pH as corrosion progresses, since the proton is not continuously produced, as in the presence of γ -radiation. It is important to note that H^+ consumption closely follows the rate of metal cation production. Moreover, an increase in OH^- concentration can facilitate significant precipitation of nickel hydroxide/oxide on the surface which can decrease the amount of Ni ions dissolved into the solution (**Figure 7.3B**). Hence, solution pH alteration during corrosion process can facilitate fluctuations in $[Ni^{2+}]_{bulk}$.

In order to measure H^+ consumption during the test duration of 144 h, and investigate the trend of pH change, the solution pH was measured after each test and its evolution is presented in **Figure 7.3C**. The solution pH initially increased slightly (from pH 6.0 to 7.8), and afterward remained stable between 7.5-7.8 during 144 h of nickel corrosion. This behaviour corresponds closely with the production of Ni ions. Comparison of the steady state pH with the known pKa values for nickel reactions indicates that it is close to the pKa of $Ni(OH)_2$ [13].

The surface and solution analysis results indicate that although during 144 h of corrosion the amount of dissolved nickel in the solution slightly increases over time, this amount is in quasi-equilibrium between the solid and aqueous phases. This means that nickel undergoes continuous metal dissolution, and oxide formation which causes the system to continue to evolve through different quasi-steady states over time. As a result, the overall corrosion process of nickel will not follow linear dynamics but instead involves the nonlinear combinations of different elementary processes [2,14].

Nonlinear corrosion dynamics occur in systems where strong coupling exists between elementary processes. This coupling may occur between nickel oxidation, dissolution, transport and oxide precipitation reactions. As a result of this strong coupling, concentric circular patterns (known as Liesegang rings), can form on the surface. Liesegang rings are a result of chemical waves and occur in systems undergoing precipitation reactions in stagnant solutions under certain conditions. The most important of the conditions required for ring formation is the supersaturation of ions in a gel medium, which causes a feedback loop between oxidation reactions and solution transport [15]. The observation of Liesegang features after 48 h of nickel corrosion therefore indicates that the system is under mass transport control after within this time. **Figure 7.5** illustrates some of these patterns. These features are more prominent and discussed in more detail in Section 7.3.4.

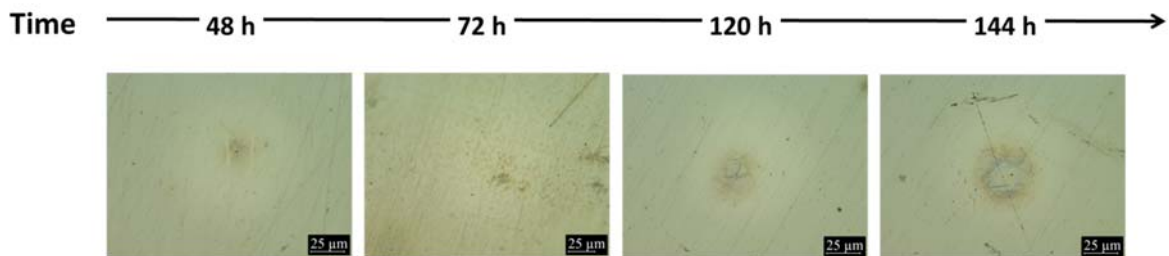


Figure 7.5: Evolution of circular surface features on nickel corroded in a solution with initial pH 6.0 in the absence of γ -radiation. All optical images have the same scales (25 μm scalebar).

7.3.1.2. Effect of pH 8.4 and 10.6 (No RAD)

Figure 7.6 shows the results obtained from nickel corrosion over 144 h in the absence of radiation for pH 8.4 and 10.6. For a better comparison of solution pHs, the

results from initial pH 6.0 are also included. For initial pH 6.0, as corrosion progresses the pH of the solution increases from 6.0 to 7.8 (over 48 h) and for higher pHs (8.4 and 10.6), the pH initially decreases and eventually stabilizes at a value between 7.3-7.8. Regardless of the initial solution pH, the solution pH becomes constant and plateaus at pH 7.5 - 8.0 after 48 h of corrosion. This pH is close to the pKa of Ni(OH)₂ which is approximately 8.5 [13]. In all three solutions, the dissolved nickel concentration fluctuates over a similar range of concentrations during the corrosion duration of 144 h. Similar fluctuations in the [Ni²⁺]_{bulk} were observed for the high ionic strength buffered solutions as described in Chapter 6. This indicates that in the absence of radiation (change in pH around the pKa of Ni(OH)₂), the effect of pH on [Ni²⁺]_{bulk} is not pronounced over the time studied. However, the effect of I_s at low pH is more significant. Therefore, in the absence of γ -radiation the concentration of dissolved nickel ions remains relatively low and fluctuates slightly over the measured period.

The nickel surface remains uniform and is covered with a green oxide during the initial hours of corrosion. The oxide thickens gradually and transforms to a darker green layer. The SEM images show the morphology of the oxides formed on the surface for different pHs, **Figure 7.7**. The results indicate that oxide forms earlier on the surface for solution with higher initial pH, for pH 10.6, oxide starts to form on the surface after 5 h. The time required to form a filament-like oxide increases with decreasing initial solution pH. Moreover, due to the trend of decreasing pH with time, for initial high solution pHs, the oxide that initially formed on the surface can re-dissolve as corrosion progresses and re-precipitate again later on. This behaviour is observed clearly for pH 10.6 case where the more compact oxide with finer oxide particles formed during 5 h of the test partially

re-dissolve (e.g. 24h) and precipitate again later. This is due to decrease in solution pH with time and increasing nickel solubility. Also, at later times the oxide particles formed are larger and less compact.

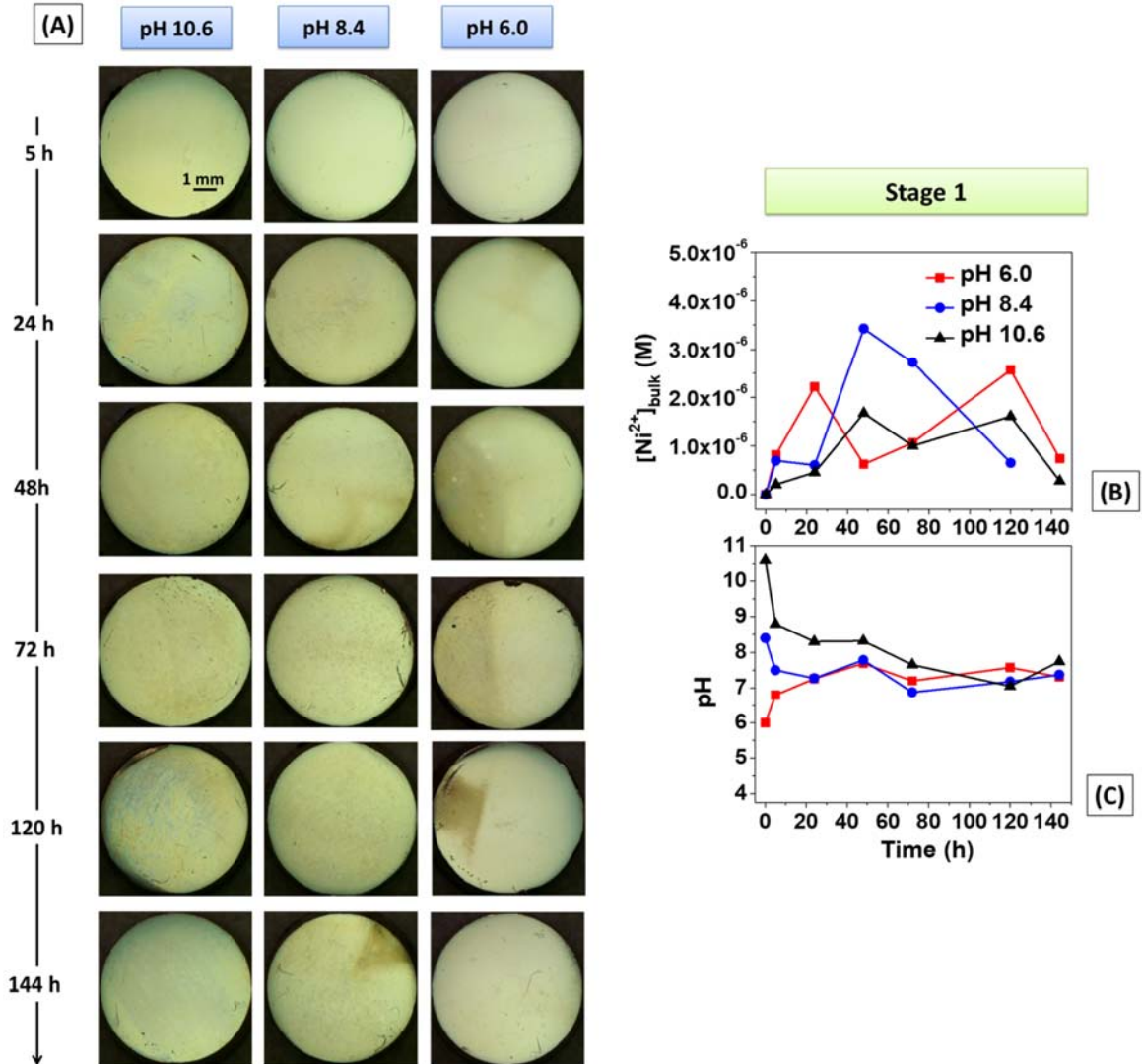


Figure 7.6: Nickel samples corroded in deaerated non-buffered solution at initial pH 6.0, 8.4 and 10.6 in the absence of γ -radiation during test durations of 5-144 h: A) Low magnification optical images of the entire surfaces B) concentration of dissolved nickel ions in solution, C) solution pH measured after the experiment. All optical images have the same scale (see 1 mm scalebar).

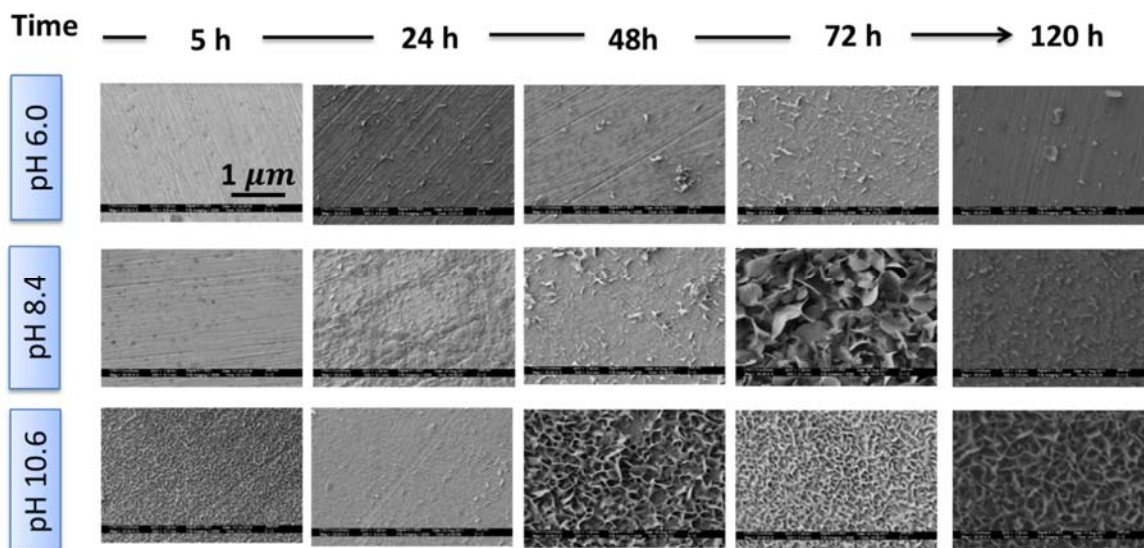


Figure 7.7: SEM images of nickel corroded at initial pHs 6.0, 8.4 and 10.6 in the absence of γ -radiation from the same experiments presented in Figure 7.6. All SEM images have the same scale (see 1 μm scalebar).

7.3.2. Dynamics of Ni Corrosion in the Presence of Gamma Radiation (RAD)

In this section, the surface and solution analysis results obtained from corrosion studies with initial pH 6.0, 8.4 and 10.6, in the presence of γ -radiation, are reviewed. Gamma radiation makes the solution more oxidizing by decomposing water and producing a number of oxidizing species. The water radiolysis products (notably H_2O_2) change the primary redox reactions which are involved in the corrosion process. The results reveal several unusual behaviours that have not been reported in previous nickel corrosion studies. The observed behaviours are particularly unexpected in view of the known high corrosion resistance of nickel. These results demonstrate that nickel

corrosion in low ionic strength non-buffered solutions and in the presence of γ -radiation progresses through different stages in which different elementary processes determine the overall corrosion rate.

7.3.2.1. Effect of pH 6.0 (RAD)

The surface and solution analysis results for nickel coupons corroded in the presence of γ -radiation at pH 6.0 for durations of 144 h is shown in **Figure 7.8**. The low and high magnification optical micrographs and the SEM images that illustrate the surface evolution and morphology are shown in **Figure 7.8A**, the total nickel concentration in solution is shown in **Figure 7.8B** and **Figure 7.8C** shows the solution pH measured after the experiments.

In general, the optical images indicate that the surface underwent a gradual change due to continuous dissolution and precipitation of a oxide layer on the surface within 144 h (**Figure 7.8A**) combined with fluctuations of nickel ions in solution (**Figure 7.8B**) and a gradual decrease in solution pH (**Figure 7.8C**). From the general trend observed in the results presented in **Figure 7.8**, it can be concluded that the non-linear nature of the evolution of the surface morphology and dissolved nickel ion concentration is amplified in the presence of γ -radiation. This is due to the high probability of the system establishing feedback loops between redox reactions and solution mass transport processes in the presence of γ -radiation [14].

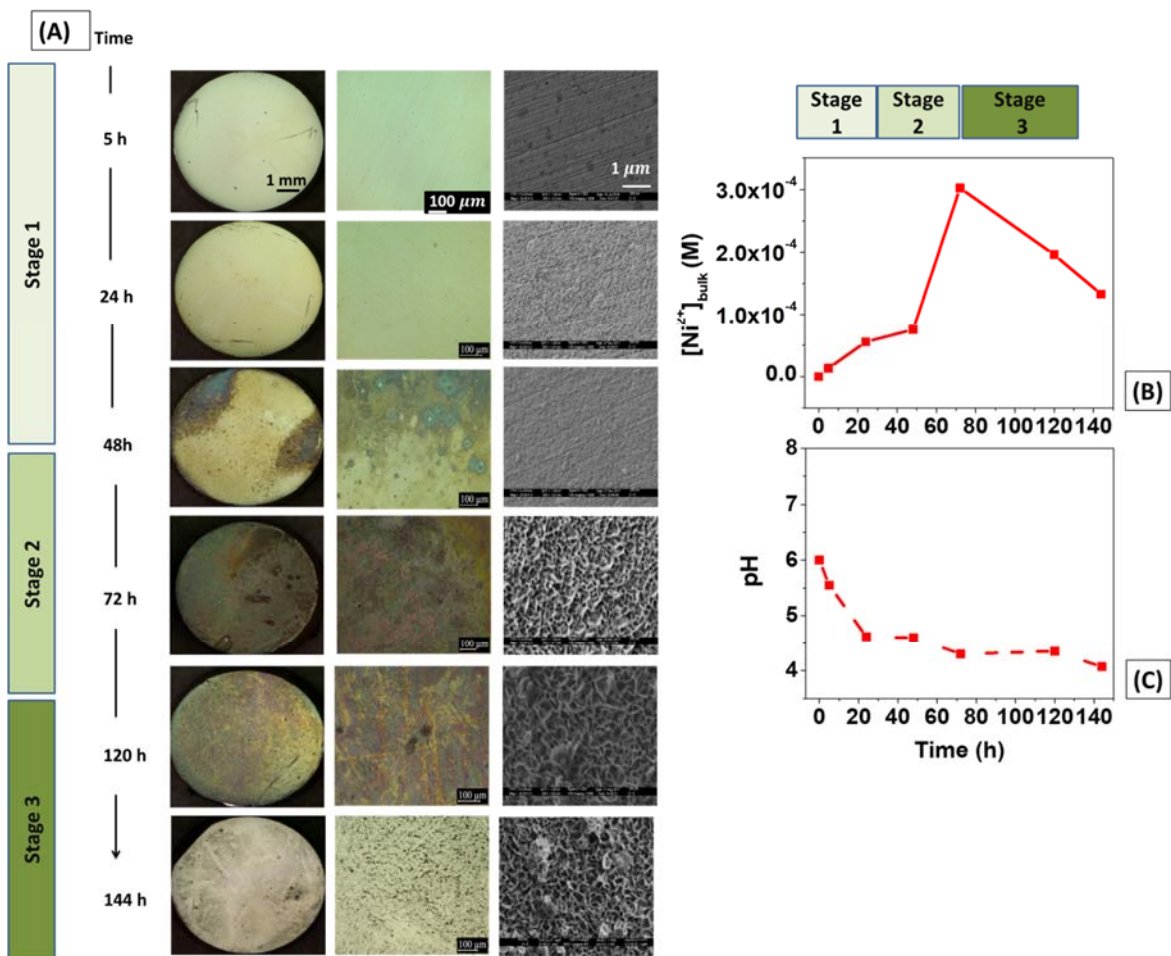


Figure 7.8: Nickel coupons corroded in de-aerated non-buffered solutions at initial pH 6.0 in the presence of γ -radiation at a dose rate of $1.8\text{kGy}\cdot\text{h}^{-1}$ over test durations of 5-144 h: A) Low and high magnification optical micrographs and SEM images, B) Concentration of dissolved nickel ions in solution as a function of time, and C) Solution pH measured after the experiment. All image sets have the same scales - low magnification optical: 1 mm scale bar; high magnification optical: 100 μm scale bar; SEM: 1 μm scale bar.

This non-linear dynamic behaviour occurs in three distinct kinetic stages. This behaviour is also observed for pHs 8.4 and 10.6 for non-buffered solution (see more detail about pH 8.4 and 10.6 in section 7.3.2.2. The kinetic stages observed were similar

to the stages observed for pH 6.0 buffered solution with low ionic strength in the presence of γ -radiation (see Chapter 6).

Stage 1 relates to the early stages (0-48 h) of the corrosion process where the total amount of nickel ions dissolved in the solution is relatively small, fluctuating slightly within a small concentration range. The surface images show that the surface remains relatively clean. This indicates that nickel corrosion in this stage mainly involves metal dissolution (mostly $t_{corr} < 24$ h) and the evolution of $[\text{Ni}^{2+}]_{\text{bulk}}$ during this time reveals that nickel dissolution occurs with a slope of $\sim 2.5 \times 10^{-6} \text{ M}\cdot\text{h}^{-1}$. During this stage, the solution pH decreases from its initial value of 6.0 to 4.5, due to production of H^+ via water radiolysis along with metal cation hydrolysis. The drop in the solution pH directly affects the solubility limit of Ni ions and hence the amount that can dissolve into the solution.

During the initial hours of nickel corrosion ($t_{corr} < 24$ h), the main corrosion pathway is the oxidation of Ni^0 to Ni^{2+} (M1) and the dissolution of Ni^{2+} ions. Generally, the effect of radiation on dissolution is very small in this stage. This is consistent with previous understanding that (M1) is mostly controlled by solvation of Ni^{2+} , not by the reduction of oxidant present in the solution, nor (trans) and (gel).

The nickel surface is uniformly green during this time. This green oxide is due to the formation of a thin layer of $\text{NiO}/\text{Ni}(\text{OH})_2$ on the surface (**Figure 7.4**). After 24 h immersion, the surface colour turns to light brown, which indicates the onset of formation of mixed $\text{Ni}^{\text{II}}/\text{Ni}^{\text{III}}$ hydroxide/oxide on the surface. This continues until 48 h, when **Stage 2** begins, and thicker oxide layer precipitates on top of the initially formed one.

Stage 2 corresponds to a rapid increase in the concentration of nickel ions close their saturation limit (**Figure 7.8B**) and the solid black mixed Ni^{II}/Ni^{III} hydroxide/oxide formation coincides with the increase in dissolved metal (see **Figure 7.8A**). At pH 6.0 this stage occurs between 48 to 72 h. The beginning of **Stage 2** at 48 h is characterized by the formation of a non-uniform layer of dark brown oxide growth on the edge of the surface that eventually spreads across the surface and covers the entire surface by 72 h. The coverage of the surface by this oxide layer is accompanied by a nearly linear increase in the concentration of dissolved Ni ions (from 48 to 72 h) at a rate of $\sim 1.97 \times 10^{-5} \text{ M}\cdot\text{h}^{-1}$. This rapid increase in nickel concentration is due to continuing production of oxidizing species H₂O₂ in the presence of γ -radiation and decrease in the solution pH (to pH = 4.5) that increases Ni²⁺ solubility. Observation of this stage at initial pH 8.4 and 10.6 indicates that pH has a significant effect on occurrence of this stage (Section 7.3.2.2).

In **Stage 2**, along with metal dissolution, hydrogel layer converts to solid products, which increases transport of Ni²⁺ (trans). Moreover, as corrosion continues production of solution oxidizing agents facilitates further oxidation of Ni^{II}/Ni^{III} (M2). Hence, as the corrosion progresses, reaction (M2) can impact surface reaction and dissolution process. After the drastic increase in nickel concentration, the bulk solution reaches close to its saturation limit and undergoes hydrolysis forming Ni(OH)₂ colloids (nucleation of colloid particles in the bulk solution is possible in irradiated solution due to •OH production **Figure 7.9**). Nickel ions in solution at this point aggregate and form nanoparticle clusters large enough to be observable by the naked eye. The TEM images in **Figure 7.9** provide evidence of the presence of nickel colloid particles in the solution at this stage.

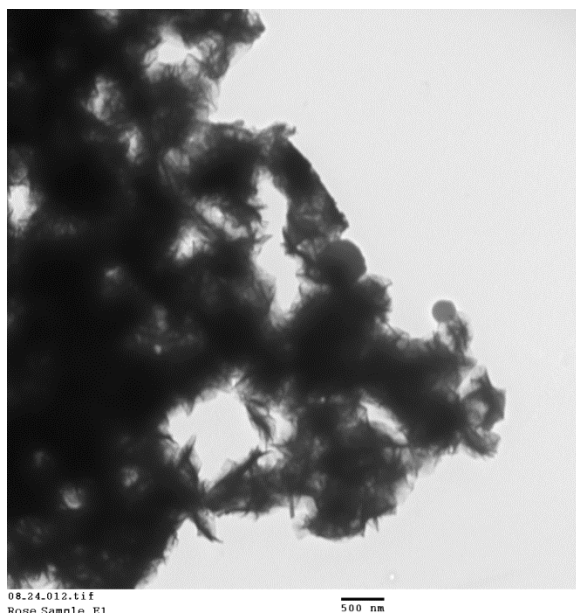


Figure 7.9 TEM image of solution in contact with nickel coupons corroded for 72 h at pH 6.0. Nanoparticle clusters have formed due to saturation of Ni ions in solution.

After the maximum dissolved nickel ion concentration is reached, there is a transition to **Stage 3** during which the total amount of nickel in solution drops. At pH 6.0, this stage corresponds to the period after 72 h. In this stage the solution pH has reached a stable value. As the optical images and SEM images in **Figure 7.8** show, the decrease in Ni concentration occurs due to the precipitation of Ni hydroxide/oxide on the surface [3]. Hence, in this stage the overall metal oxidation to produce Ni^{II} & Ni^{III} become smaller and the changes in the metal oxidation products (dissolved or precipitated) are more due to the metal atom transfer between the solution and solid-oxide phases.

7.3.2.2. Effect of pH 8.4 and 10.6 (RAD)

Figure 7.10 shows the results obtained from solutions with initial pH 8.4 and 10.6 in the presence of γ -radiation, and for better comparison the results from initial pH 6.0 are also included. **Figure 7.11** presents the SEM images that show the oxide morphologies. Similarly, to pH 6.0, at the two higher pHs (pH 8.4 and 10.6) corrosion progresses through three distinct kinetic stages. However, the amount of dissolved Ni is slightly lower for higher pH solutions. This demonstrates that the rate of nickel ion dissolution is higher at a lower solution pH.

As mentioned previously, **Stage 1** represents the early stages of the corrosion process where the total amount of nickel dissolved in the solution is relatively small and fluctuates over a small range of concentrations. At initial pH 6.0, during **Stage 1** the slope of the ion dissolution graph is $\sim 2.5 \times 10^{-6} \text{ M}\cdot\text{h}^{-1}$. Note that this value decreases to $9.88 \times 10^{-7} \text{ M}\cdot\text{h}^{-1}$ and $9.54 \times 10^{-8} \text{ M}\cdot\text{h}^{-1}$ for pH 8.4 and 10.6 respectively. In all solutions, upon placement in the gamma irradiator, the pH sharply decreases due to the production of H^+ via water radiolysis.

Stage 2 corresponds to a rapid increase in nickel ion concentration accompanied by clearly evident surface changes and a decrease in solution pH to ~ 4.5 for all solutions. The solubility of Ni ions in solution increases gradually as pH decreases, and the amount of nickel in solution increases accordingly. At pH 6.0, the concentration of dissolved nickel increases with time at a rate of $\sim 9.54 \times 10^{-6} \text{ M}\cdot\text{h}^{-1}$. These rates are $\sim 6.81 \times 10^{-6}$ and $4.94 \times 10^{-6} \text{ M}\cdot\text{h}^{-1}$ for pH 8.4 and 10.6 respectively. Observation of this stage an initial pH 8.4 and 10.6 indicates that pH has a significant effect on occurrence of this stage. In non-buffered solution pH drastically decreased in the presence of radiation which facilitates

this stage. However this stage was observed in buffered solutions at pH 8.4 and 10.6 (Chapter 5).

Stage 3 is achieved when the total amount of nickel in solution drops after the pH becomes constant and reaches stable value. This drop occurs after the solution becomes saturated with Ni cations. The precipitation of a large amount of dissolved Ni ions on the surface causes the concentration of Ni ions in the solution to decrease. This stage starts after 72 h at pH 6.0 and after 120 h at pH 8.4 and 10.6. The solution pH reaches a stable value of 4 to 4.5.

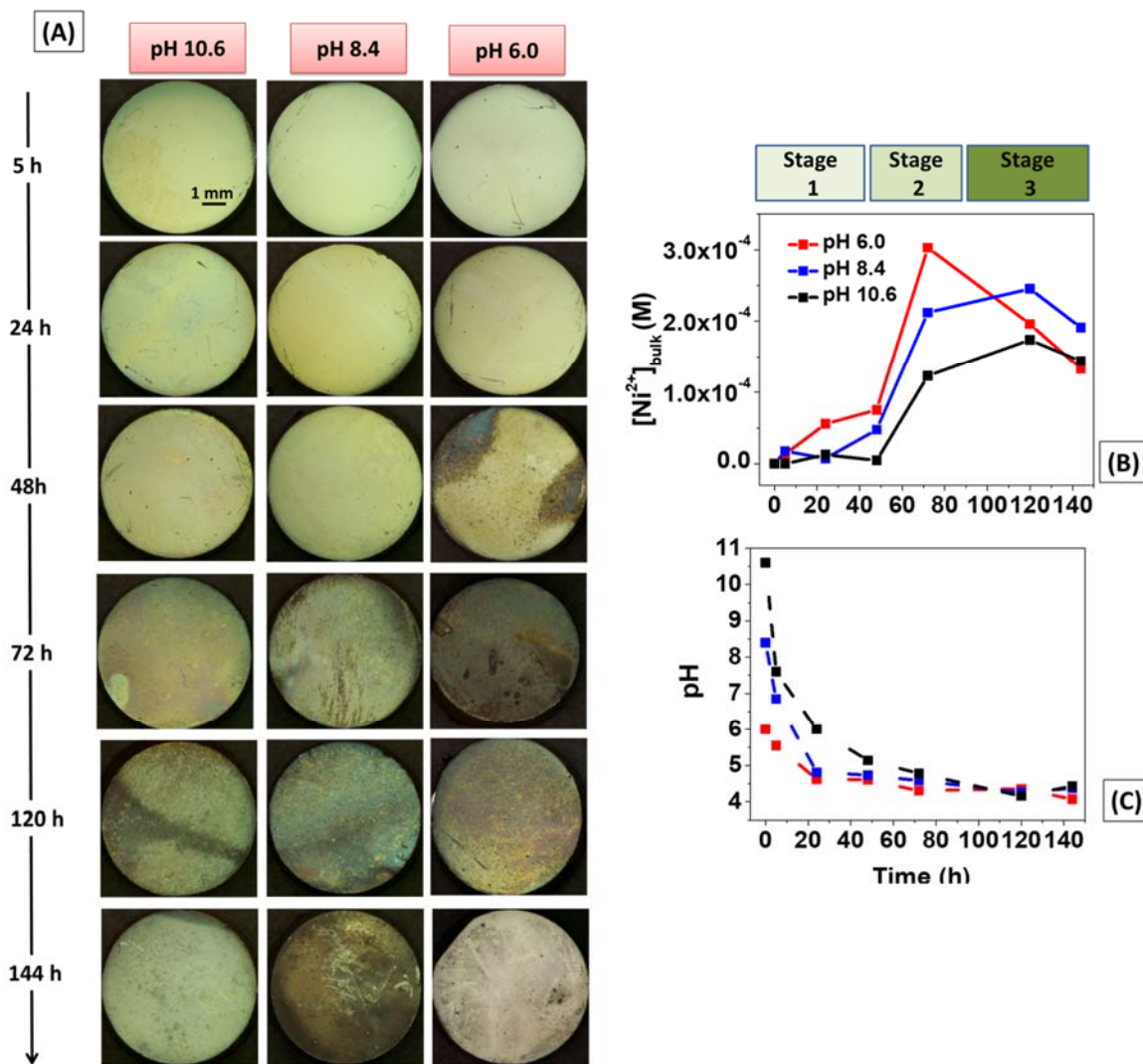


Figure 7.10: Nickel coupons corroded in deaerated non-buffered solution at initial pH 6.0, 8.4 and 10.6 in the presence of γ -radiation during test durations of 5-144 h: A) Low magnification optical images of the entire surfaces B) concentration of dissolved nickel ions in solution, C) measured solution pH after the experiment. All optical images have the same scale (see 1 mm scalebar).

Similar to the results obtained in the absence of radiation, the oxide morphologies in the presence of γ -radiation (**Figure 7.11**) show that oxide formation occurs earlier for higher pHs. For pH 10.6, a filament-like nickel hydroxide is observed on the surface of the samples corroded for 5 h. At pH 6.0 and 8.4, formation of filament-like oxide occurs

at later times – close to 72 h. Prior to this period the surface shows signs of dissolution along the polishing lines along with nucleation/growth of the oxide on some regions of the surface.

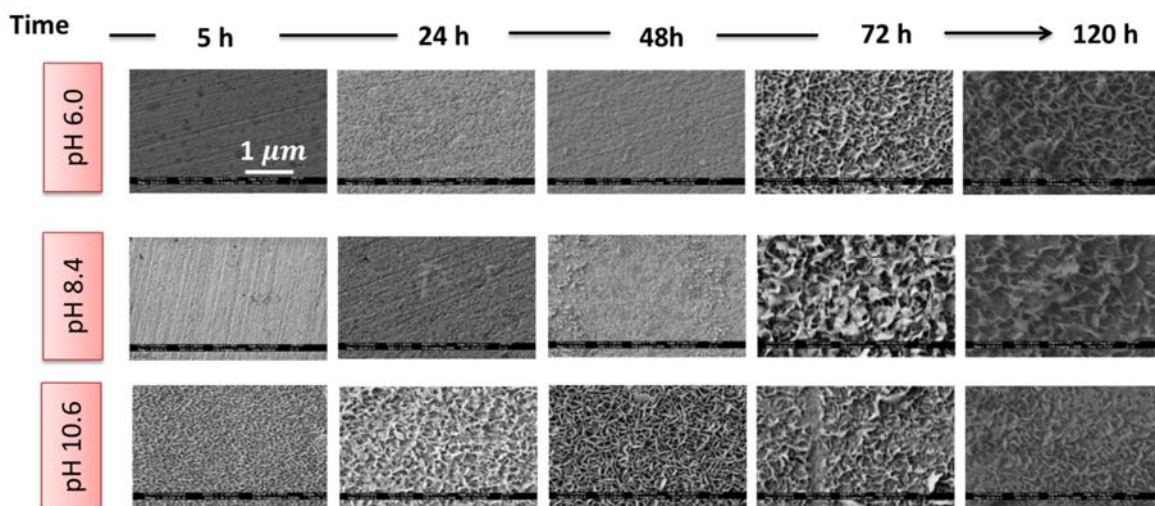


Figure 7.11: SEM images of nickel corroded at initial pHs 6.0, 8.4 and 10.6 in the presence of γ -radiation from the same experiments presented in Figure 7.10.

7.3.3. Characterization of Oxide Formed on the Surface

In this section, the composition of the oxide layers formed on corroded nickel surfaces is described. This characterization is obtained using the characteristic colours of nickel hydroxide and oxide particles using optical microscopy [6], and via XPS techniques.

The analysis of the Ni 2p bands in the high resolution XPS spectra of corroded nickel surfaces is presented in **Figure 7.12**. The results presented in this figure pertain to nickel coupons corroded at initial pH 6.0 after 120 h in the absence of radiation, 72 h in

the presence of γ -radiation and 144 h corroded at initial pH 8.4 in the presence of γ -radiation.

The results indicate that the oxide layer formed on nickel coupons corroded in the presence and absence of γ -radiation consists mostly of $\text{Ni}(\text{OH})_2$ and NiO [16]. At different initial solution pHs and/or in the presence of γ -radiation the oxide composition is different. A thin oxide layer was observed on the surface in the absence of radiation at pH 6.0, in which the fractions of NiO and $\text{Ni}(\text{OH})_2$ are almost equal. In the presence of γ -radiation, the oxide consists predominantly of $\text{Ni}(\text{OH})_2$ with greater thickness than in its absence; however at pH 8.4 it is less thick than at pH 6.0.

Despite obtaining useful characterization results from XPS, this technique could not detect the amount of Ni^{3+} present on the surface since the distribution of Ni^{3+} is not as uniform as Ni^{2+} and in most areas of the surface the amount of this oxide is small. So, in order to gain a better understanding of the oxide layer composition, optical microscopy was also used for qualitative oxide characterization, making use of the observed colours of the oxides.

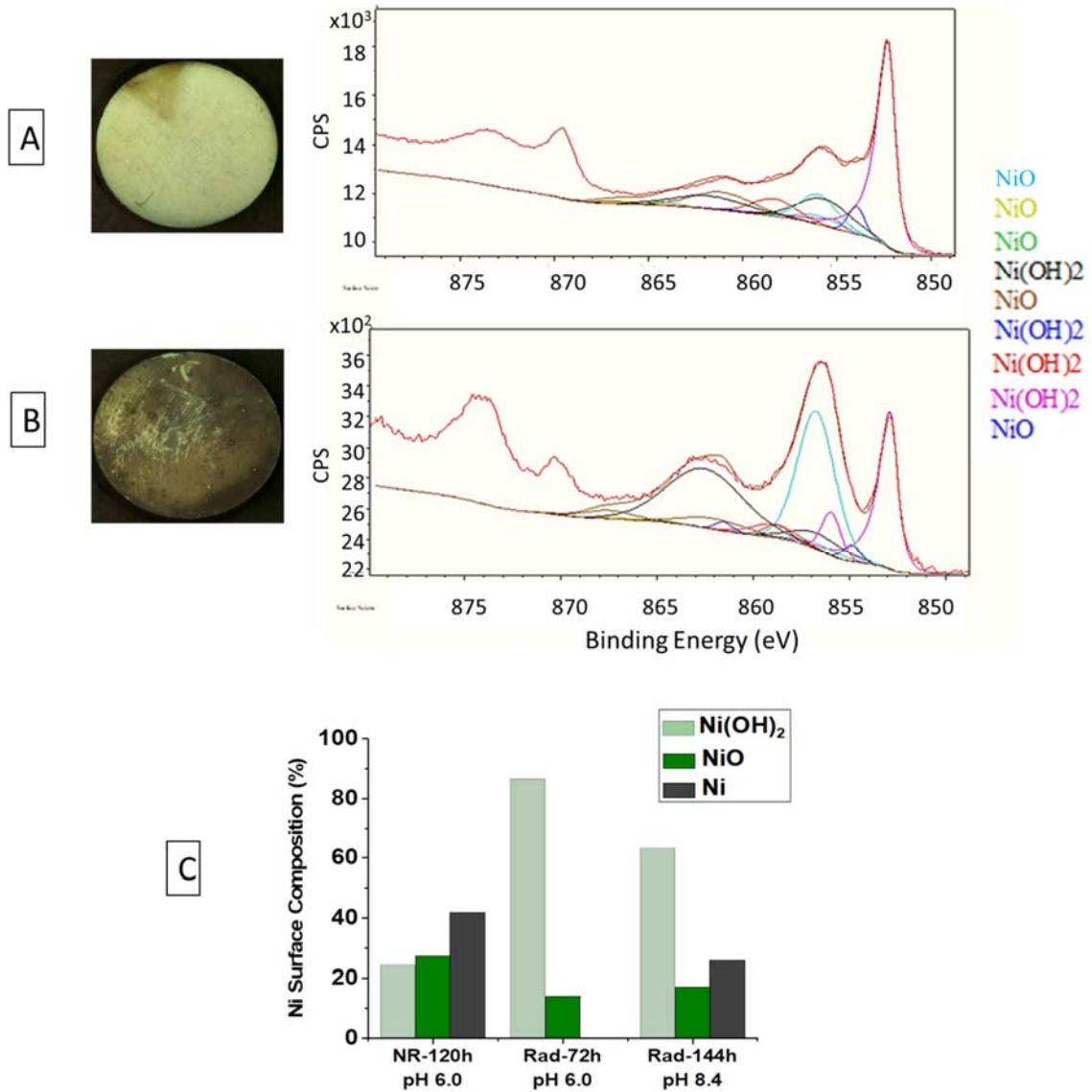


Figure 7.12: The Ni 2p bands from the high resolution XPS of a nickel surface corroded for A) 120 h without radiation (No RAD) at initial pH 6.0, and B) 144 h with γ -radiation (RAD) at pH 8.4; C) Ratio of the Ni oxide component and Ni metal.

As shown in **Figure 7.4**, the oxide colour-based characterizations using the optical microscope, the formation of NiO and Ni(OH)₂ is easily detectable during short term nickel corrosion (or **Stage 1**). At longer times (**Stage 3**), black oxide, which

corresponds to Ni_3O_4 and Ni_2O_3 , is visible, particularly near the Liesegang rings. The surface colours of nickel coupons corroded at initial pH 6.0 in the presence of γ -radiation are shown in **Figure 7.13**.

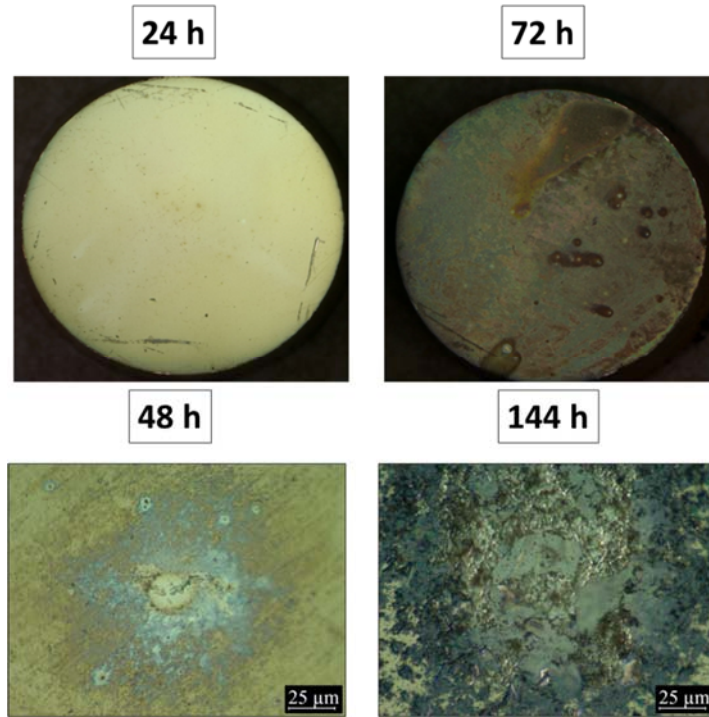


Figure 7.13: Surface colours on nickel coupons corroded at initial pH 6.0 in the presence of γ -radiation. A green colour indicates the presence of $\text{Ni}(\text{OH})_2$ and NiO while black indicates Ni_3O_4 and Ni_2O_3 . Brown indicates the presence of $\text{Ni}(\text{OH})_3$.

7.3.4. Corrosion Mechanism for Nickel Corrosion in presence of γ -radiation

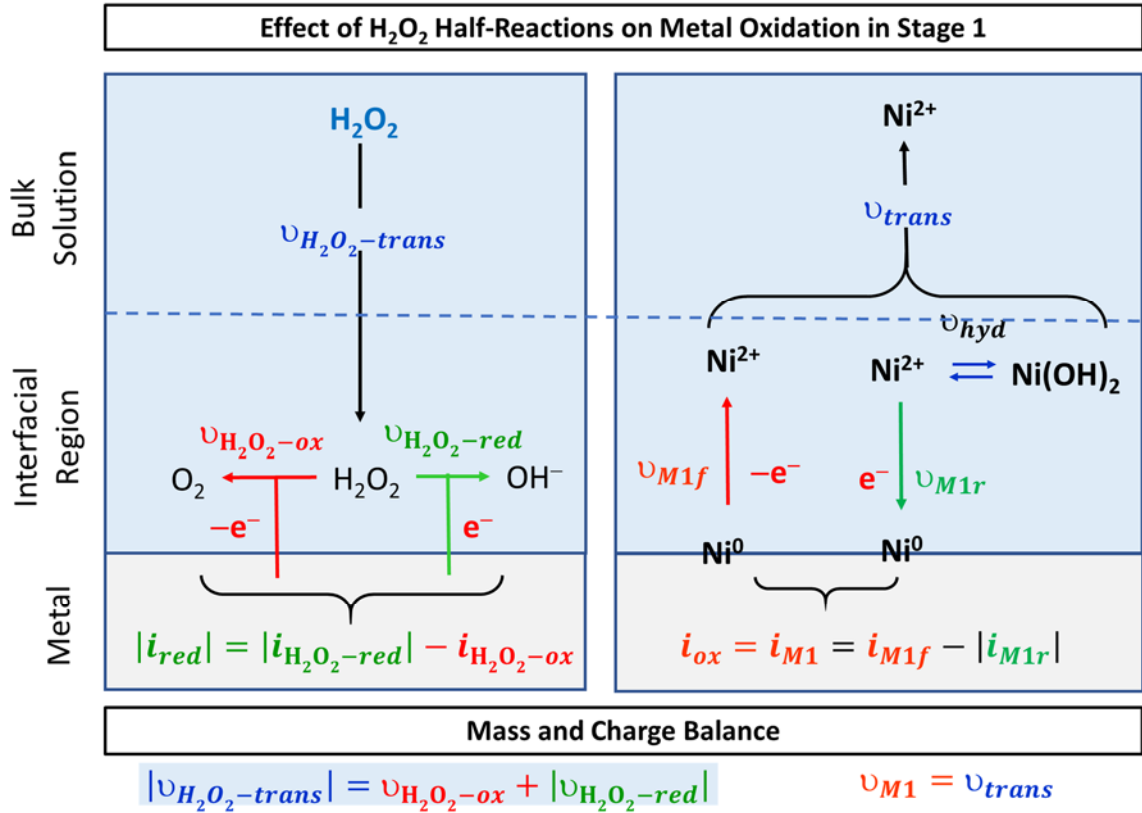
As described in Chapter 6, nickel corrosion evolves through three different kinetic stages. The predominant corrosion processes occurring in each stage is summarized below and explained in detailed in Chapter 6. The corrosion mechanism shown in Chapter 6 are also shown in this section.

Stage 1:

The predominant process occurring in this stage involves is the oxidation of $\text{Ni}^0_{(m)}$ to Ni^{2+} (M1f) at the metal surface. However, the overall nickel oxidation process consists of elementary steps such as reduction of Ni^{2+} presented at the interface (M1r) and reduction of oxidant present in the solution, hydration of nickel cations (hyd), and the transport of Ni cations from the metal surface to the bulk solution (trans). In presence of γ -radiation, the main oxidant that can affect the corrosion of metals is the H_2O_2 . H_2O_2 is a more powerful and kinetically facile oxidant than O_2 . The schematics of the H_2O_2 half reaction on metal oxidation in **Stage 1** is shown in **Figure 7.14**.

During corrosion, the nickel cations ($\text{Ni}^{2+}_{(aq)}$) produced continuously move to the interfacial region and then transport to the bulk solution (trans). The transport of nickel cations is affected by the pH and the ionic strength of the solution. During **Stage 1**, concentration of nickel cations at the interface can reach its saturation limit and remain at the level, and as a result a hydrogel layer can be formed on the surface. Due to formation of this hydrogel layer Liesegang rings can gradually be initiated on the surface.

During this stage, in the initial first few hours of nickel corrosion at pH 6.0 surfaces looked relatively clean and no oxides were observed on the surface but with increasing time green/brown layer forms on the surface. At higher solution pHs gradual formation of oxide on the surface occurs faster on the surface and is observed in early hours of nickel corrosion at pH 10.6. Albeit due to decreasing solution pH the oxide might dissolve to solution and precipitate again at longer times.



Note: $i_{rxn} = nF \cdot \nu_{rxn}$ $|i_{red}| = i_{ox}$ at E_{corr}

Figure 7.14: The schematics of the H₂O₂ half reaction on metal oxidation occurring during Stage 1 of the corrosion process. For metal oxidation, the ν_{M1f} is forward nickel oxidation rate of $\text{Ni} \rightleftharpoons \text{Ni}^{2+}$ and ν_{M1r} is the rate of reverse reaction, and ν_{trans} is the rate of nickel cation transport to bulk solution. For the solution species half-reaction $\nu_{\text{H}_2\text{O}_2\text{-red}}$ is the H₂O₂ reduction rate and $\nu_{\text{H}_2\text{O}_2\text{-trans}}$ is the rate of H₂O₂ transfer from the bulk solution to the interface.

Stage 2:

In **Stage 2**, the concentration of Ni^{2+} in the bulk solution increases at a faster rate until it reaches near saturation limit. This drastic increase can be attributed to decrease in solution pH to value ~ 4.5 at all three pHs. As a result of the presence of γ -radiation, continuous production of oxidizing agents (H_2O_2) and decreasing solution pH can facilitate this stage and more of nickel cations can dissolve and be transported to the bulk solution. This results in an increase in the concentration nickel ions in the solution phase during this stage. Presence of this stage in initial pH 8.4 and 10.6 results indicates the importance of pH drop in occurring of this stage, while this wasn't occurred in buffered solution at high pHs (see Chapter 6).

During this stage the interface is already saturated by nickel cations which can precipitate at the same time and form oxides on the surface. Hence at this stage, along with rapid metal dissolution, oxide formation is happening at the same time. Furthermore, at the interface further oxidation of Ni^{2+} to higher oxidation state within the hydrogel can be facilitated by continuously producing oxidizing species in the solution. The evidence for this assertion includes the development more of a greenish brownish colour on the coupon surface and the observation of filament-like oxide on the coupon surface. The schematics of the corrosion process occurring during **Stage 2** is shown in **Figure 7.15**. Increasing concentration of Ni^{2+} at the interface also facilitates the further oxidation of Ni^{2+} ions to Ni^{3+} (M2). After sufficient mixed $\text{Ni}^{2+}/\text{Ni}^{3+}$ hydroxide colloids are presented at the interface they can nucleate and grow as solid crystalline particles on the surface.

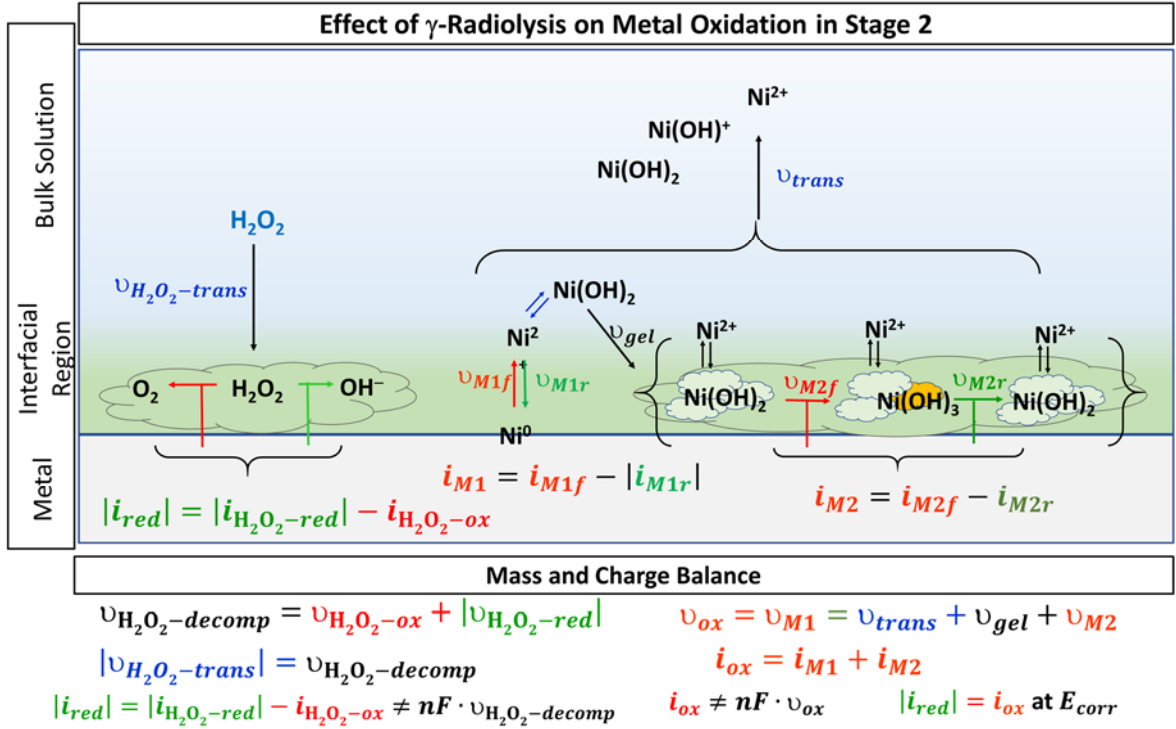


Figure 7.15: The schematics of the effect of γ -radiation on Stage 2 of the corrosion process. The Rate Determining Steps (RDS) arising during the corrosion process include metal oxidation, the ν_{M1f} is forward nickel oxidation rate of $\text{Ni} \rightleftharpoons \text{Ni}^{2+}$ and ν_{M1r} is the rate of reverse reaction, ν_{M2f} is the forward nickel oxidation rate of $\text{Ni}^{2+} \rightleftharpoons \text{Ni}^{3+}$ and ν_{M2r} is the reverse reaction. ν_{gel} , ν_{hyd} and ν_{trans} are the rates of gel, hydrolysis and nickel cation transport to bulk respectively.

Stage 3:

In Stage 3, once the bulk solution becomes supersaturated the Ni^{2+} undergoes hydrolysis resulting in the formation of $\text{Ni}(\text{OH})_2$ colloids that can precipitate on the nickel surface. As a result, the total amount of nickel in solution drops and the oxide formation predominates over ion dissolution. In this stage, in the presence of the hydrogel layer on the surface, the oxidation of Ni^{2+} ions to higher oxidation states (Ni^{3+}) increases, resulting in $\text{Ni}^{\text{II}}\text{Ni}^{\text{III}}$ hydroxide/oxides on the surface. In a slow transport medium, oxide

growth by Ostwald ripening can be coupled with the redox reactions of Ni^{2+} and Ni^{3+} species and we refer to this process as “redox-assisted Ostwald ripening”, as described in in Section 7.3.5. The schematics of the effect of γ -radiation on **Stage 3** of the corrosion process is shown in **Figure 7.16**.

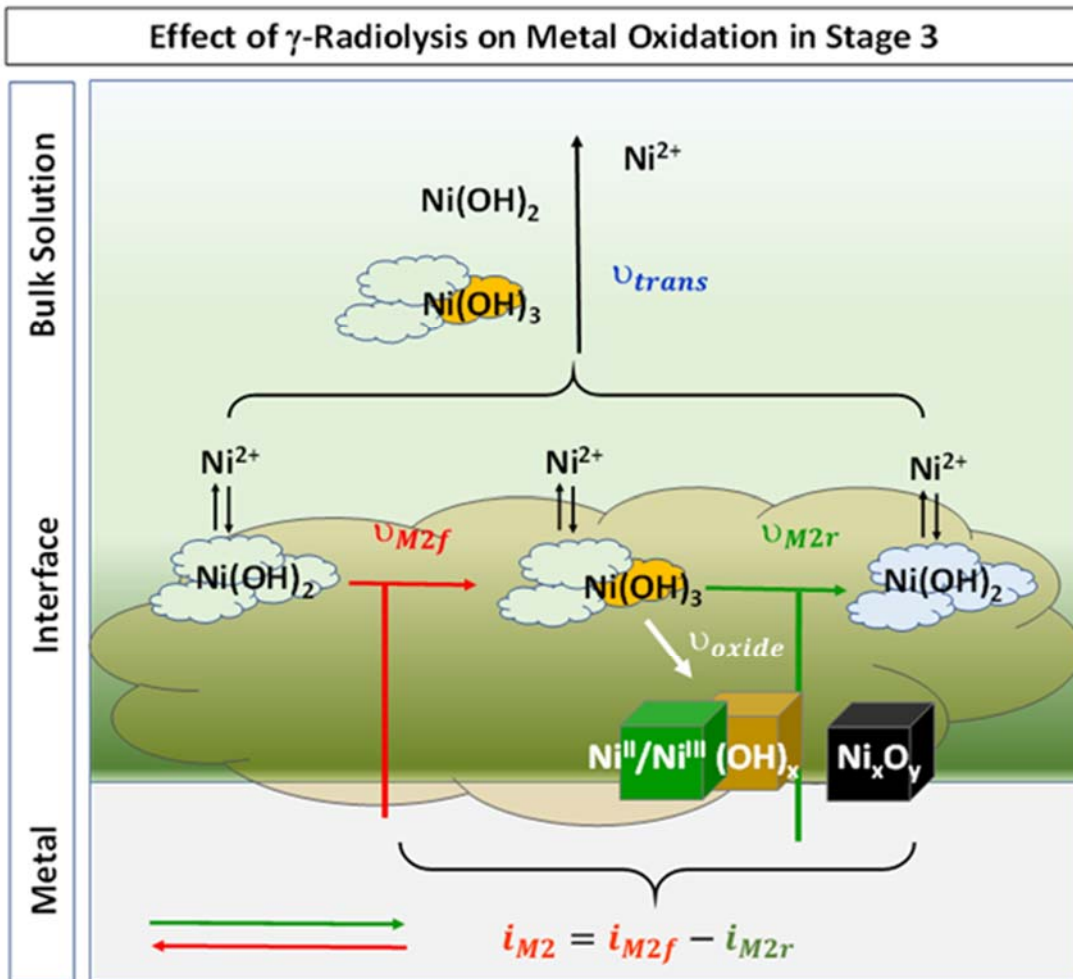


Figure 7.16: The schematics of the effect of γ -radiation on Stage 3 of the corrosion process. The Rate Determining Steps (RDS) arising during the corrosion process include for metal oxidation, the v_{M1f} is forward nickel oxidation rate of $\text{Ni} \rightleftharpoons \text{Ni}^{2+}$ and v_{M1r} is the rate of reverse reaction, v_{M2f} is the forward nickel oxidation rate of $\text{Ni}^{2+} \rightleftharpoons \text{Ni}^{3+}$ and v_{M2r} is the reverse reaction. v_{gel} , v_{trans} , v_{hyd} v_{oxide} are the rate of gel, hydrolysis, nickel cation transport to bulk and oxide formation respectively.

7.3.5. Analysis of Unusual Surface Features at pH 6.0

As mentioned in the previous section, during the first hours of nickel corrosion the total amount of nickel dissolved in solution fluctuates over a small range of concentrations, a green layer of oxide forms on the surface, and over longer time a brown oxide layer forms on the surface.

As mentioned earlier, the formation of the hydrogel layer on the surface in **Stage 1** facilitates the initiation of certain features, which can be seen in the absence (**Figure 7.3**) and presence of γ -radiation (**Figure 7.8**). In this section, these patterns are more fully explained.

Generally, as nickel ions are produced during corrosion, they continuously transfer from the metal surface to the solution phase. As corrosion progresses, the concentrations of Ni cations and OH^- increase continuously at the interface until $[\text{Ni}^{2+}]_{\text{bulk}}$ reaches its saturation limit. These accumulated Ni cations, in combination with OH^- , can readily form hydroxides which can grow in colloidal forms and/or a hydrogel network [4,17,18]. The presence of this layer can affect the mass transport process to some degree, since the diffusion of metal cations through a viscous network (like a hydrogel) to the bulk solution is significantly more difficult than the diffusion of ions through the solution. For this reason, ion transport becomes the factor that determines the rate of corrosion progression. The slow transport layer on the surface results in feedback loops between solution processes and interfacial charge transfer, and the coupling of metal ion diffusion and precipitation during metal corrosion [14]. This strong coupling can lead to oscillation of the system between different quasi-steady states and produce oxide deposition patterns during corrosion. The presence of γ -radiation produces redox-active species in the

solution, increasing the probability of creating feedback loops between solution transport and reactions [14], which can promote the formation of these types of surface features.

A) Wave Patterns

Figure 7.17 illustrates the wave patterns observed on the surface during 24 to 120 h of nickel corrosion. The FIB cut cross-section image of this region after 72 h of nickel corrosion is also shown. These features are observed after approximately 24 h of nickel corrosion in the presence of γ -radiation and persist over longer time periods, resulting in a non-uniform layer on the surface with different colours at longer times.

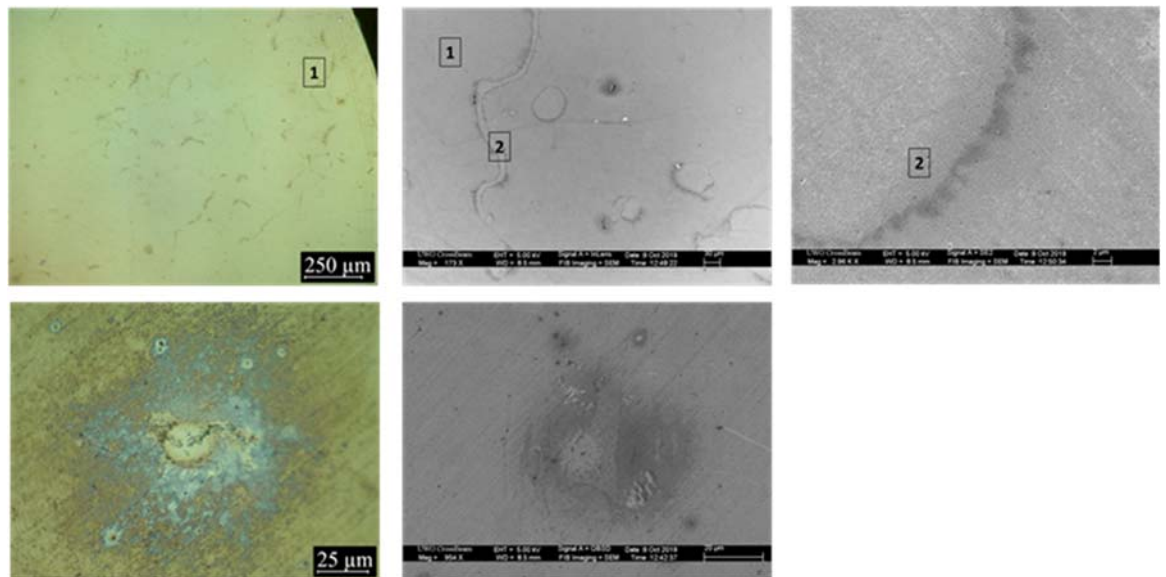


Figure 7.17: Optical images and the corresponding different magnification SEM images of particular morphological features observed after 24 h of nickel corrosion at 150 °C in de-aerated pH 6.0 solution in the presence of γ -radiation. The upper images show wave patterns and the bottom image is a Liesegang ring.

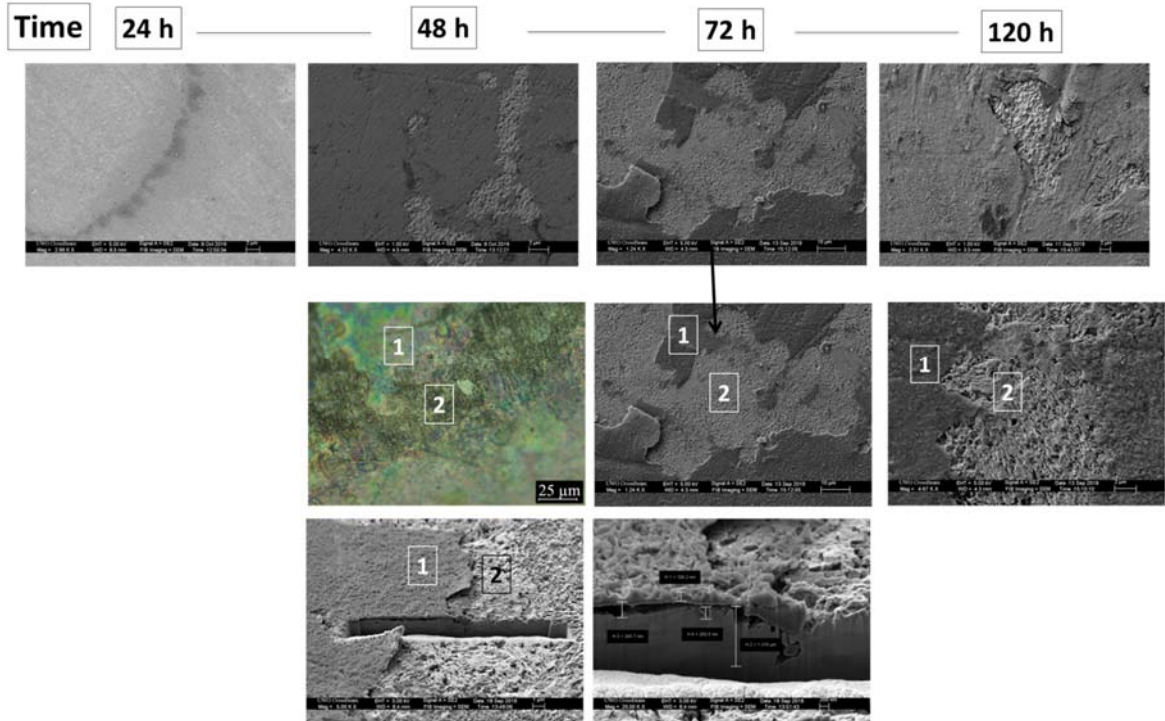


Figure 7.18: Wave patterns on the surface after 72 h of nickel corrosion at pH 6.0 due to non-uniform metal dissolution and oxide formation, and the FIB cut of the wave pattern. The numbers represent the same regions in the image taken with different magnification and FIB cut.

These patterns consist of regions of the nickel surface which are partially covered with an oxide layer. We assume that the reason for the observation of areas with no oxide is that it was removed from the surface during the removal of samples from solution and their drying under argon. The FIB cut results shown in **Figure 7.18** indicate that the surface is covered by an unattached oxide layer on the surface at regions near the wave patterns. Considering that the surface was covered with a loosely attached oxide layer (shown in the FIB cut **Figure 7.18**), it is reasonable to assume that the oxide would be removed from the surface during collection of the sample and drying with argon.

The presence of an unattached oxide layer is an indication of the formation of a type of wave-produced patterns in which the oxide layers are separated by void volumes. This formation is due to the development of oxide layer from hydrogel layer that initially spread uniformly on the surface [14]. The layers below are formed as the solution diffused in and out of the initial hydroxide/oxide layer forming Liesegang oxide bands over time which resulted in the formation of a void between the metal and the oxide layer [14]. The void forms as nickel continuously dissolves out, even after the formation of the gel layer. Although the gel layer controls the transport of nickel ions into the bulk solution, water can still diffuse in through the hydrogel, metal can still oxidize, and cations can dissolve at the interface and later on adsorb onto and merge into the gel layer. This continues until the gel layer transforms to solid, which completely stops oxidation underneath the oxide layer.

B) Liesegang Ring Growth

Liesegang rings are concentric circular patterns that form due to systemic feedback between the transport processes of metal cations in solution, and chemical reactions. In the presence of systemic feedback chemical systems exhibit periodic oscillation over time [14,19]. This phenomenon is possible when a slow transport medium is present at the interface. This slow mass transport medium is generated when high concentration Ni cations form a hydrogel layer at the interface. The observation of Liesegang features is therefore an indication that the main form of accumulated hydrated nickel ions on the surface is a hydrogel.

In the presence of a gel layer on the surface the rate of ion diffusion is limited, which can eventually lead to chemical waves involving coupling of metal ion diffusion

and precipitation. This strong coupling can lead to oscillation of the system between different quasi-steady states and produce Liesegang patterns during corrosion [15]. This oscillation causes solid products to precipitate and re-dissolve periodically during nickel corrosion [20–24].

As corrosion time increases and the system progresses to subsequent stages, the Liesegang rings grow and more distinct banding can be observed. The high magnification optical and SEM images of Liesegang rings over 24 to 144 h at pH 6.0 in the presence of γ -radiation are presented in **Figure 7.19**. The number of bands increases with time, and the colour of the bands changes, making them more visible. The different colours in each band indicate that ring formation is very strongly coupled with redox reactions [14]. Formation of greenish NiO/Ni(OH)₂, black Ni₃O₄, Ni₂O₃ and the brownish mixed Ni(OH)₂/ Ni₂O₃ are an indication of this strong coupling and they are more visible at longer times.

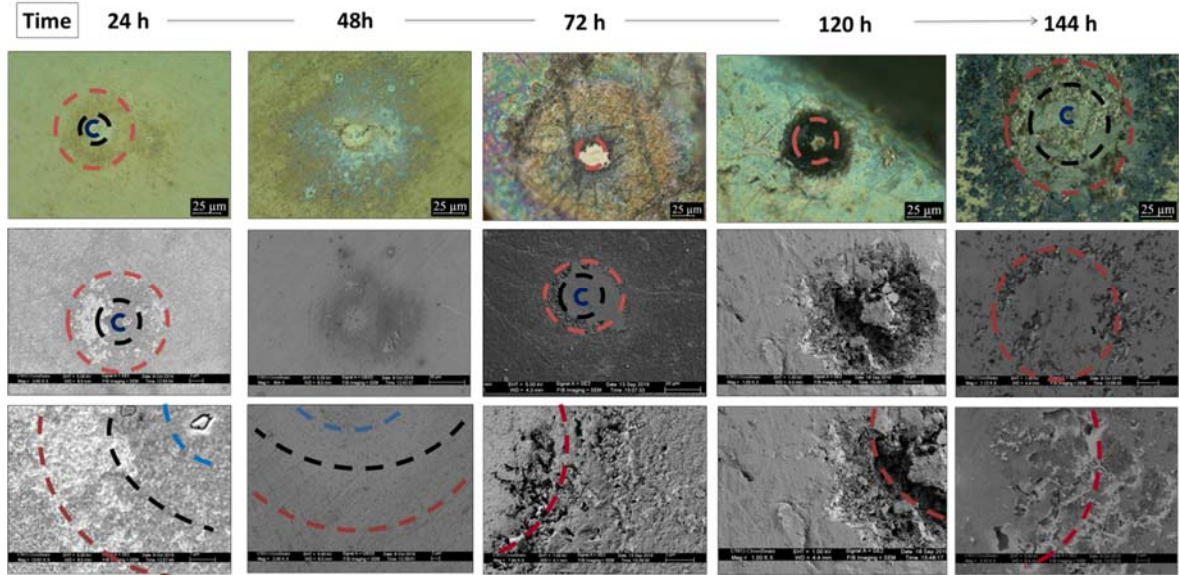


Figure 7.19: Liesegang ring growth on nickel samples corroded in de-aerated non-buffered solution at initial pH 6.0 in the presence of γ -radiation. The upper row shows high magnification optical images, the middle row SEM images, and the bottom row is the boundary of the central region and the surrounding band. The dashed lines show the different regions of the bands. The blue, black and red colours represent the central region, middle region, and outer ring, respectively.

As illustrated in **Figure 7.19**, the early stages of Liesegang ring development at 24 h show at least three different regions: the central region, (1) (indicated with blue lines), middle region (2) (black line) and surrounding region (3) (red line).

The central region (1) is mostly a localized dissolving area. Although over longer times, this area is covered with a precipitated oxide layer, the cross-sectional images after 72 h of corrosion in **Figure 7.20** show that this localized metal dissolution in the central region propagates intergranularly beneath the oxide layer on the surface. This region is in the form of a hole with maximum depth of 2.3 μm after 72 h of nickel corrosion. The

cracks observed in this region are due to the presence of a void underneath and form in the hydrogel layer during the drying process [14].

The middle region (2) is indicated with a black dashed line in **Figure 7.19**. In this region, metal dissolution is less evident than in the central region, but it is mainly covered by the nickel oxide produced in the central and surrounding regions. The FIB cut obtained from this region does not show any areas where dissolution is propagating underneath the oxide. So, the nickel ions produced during corrosion in the middle part (1) and outer ring (3) precipitate in this region.

The surrounding region (the boundary of the middle region and the outer ring (3)) is the area with more nickel dissolution. As time progresses, metal dissolution in the surrounding region continues to a depth of 1.8 μm , while precipitation occurs simultaneously. **Figure 7.21** shows a Liesegang ring after 72 h of nickel corrosion in the presence of γ -radiation. The surrounding boundary region is covered by an oxide layer. The cross-sectional images show the propagation of metal dissolution underneath the surface oxide.

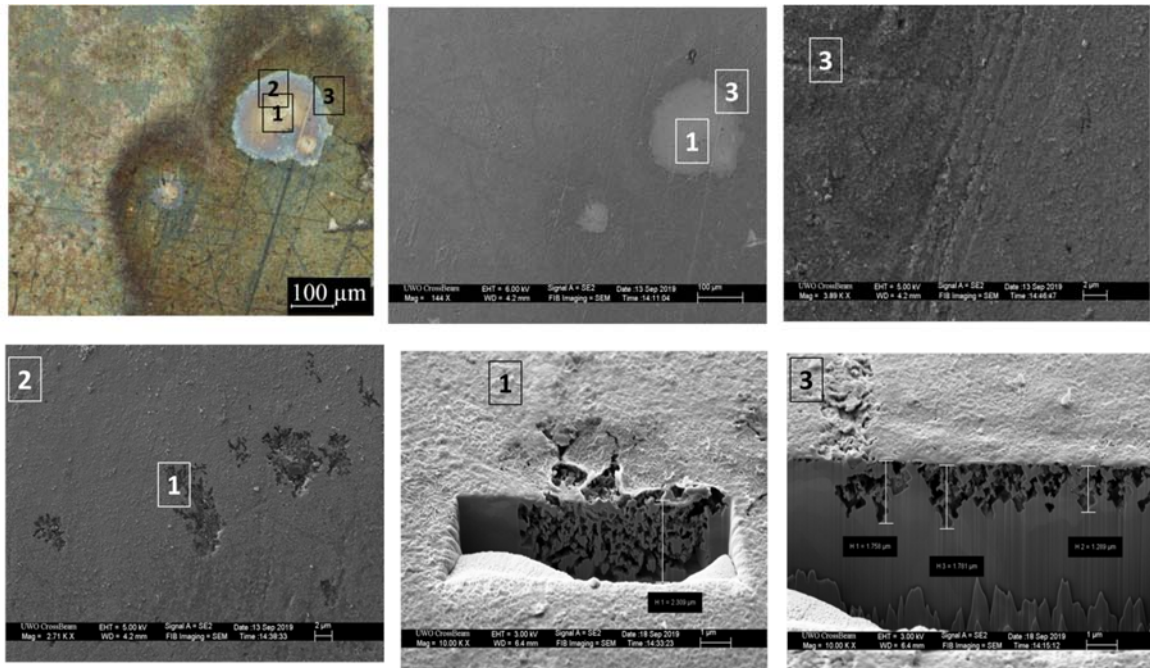


Figure 7.20: Localized metal dissolution in the centre and surrounding regions of Liesegang rings after 72 h of nickel corrosion in the presence of γ -radiation.

The cross-section of another Liesegang ring feature observed after 72 h of nickel corrosion with three banding regions is presented in **Figure 7.19**. The central region (1) and surrounding boundary (3) are regions with more nickel dissolution. Due to the presence of an oxide layer on the surface, the metal dissolution regions are not observed in the 2-dimensional SEM images. However, the cross-sectional images show the propagation of nickel dissolution in the surrounding regions to a depth of 1.3 μm over 72 h of nickel corrosion.

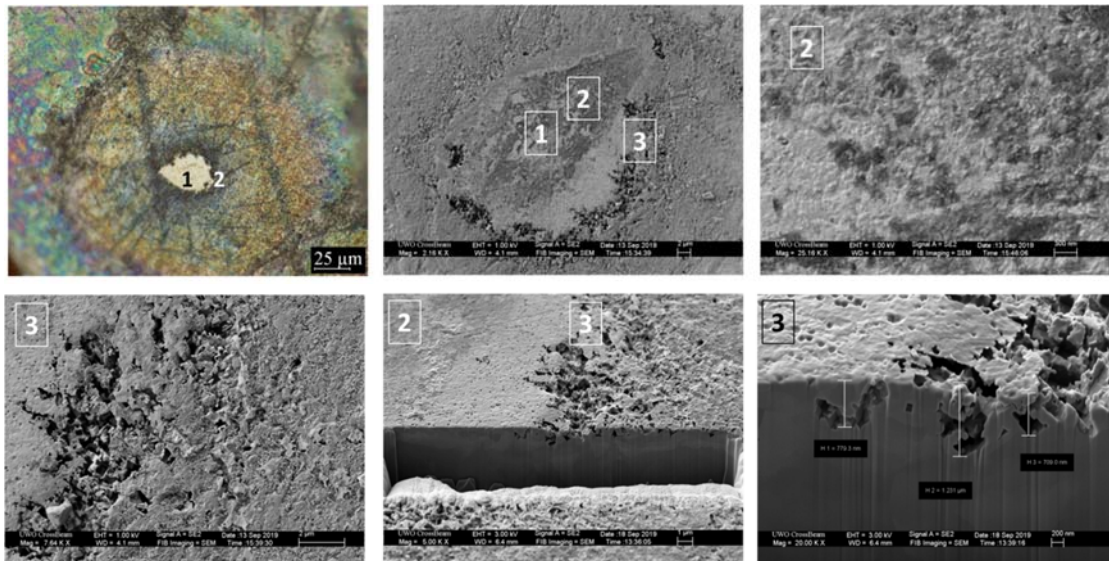


Figure 7.21: A Liesegang ring on a nickel surface after 72 h of corrosion in the presence of radiation.

Metal dissolution in the surrounding region continues to the point where after 120 h the area is completely dissolved, and a hole has formed containing the centre and outer ring regions (**Figure 7.19**). With increasing immersion time (144 h), region 3 is covered by a flaky unattached oxide layer, and severe dissolution is observed underneath the oxide layer. As time progresses, the colour of the oxide on the surface becomes more black, corresponding to the formation of a higher oxidation state nickel oxide.

Continuous oxide formation and dissolution in ring patterns is the result of a wave of supersaturation, which is based on the mechanism proposed for Ostwald ripening (a repetitive occurrence of dissolution and supersaturation in space vs time that influences the rate of nucleation of solid particles and their growth kinetics) [15,25]. The driving force for this process is the differences in the interfacial energies of the surfaces and particles [14,18,26]. The reason for the instability is that the equilibrium concentration

near the surface of a solid particle depends on the curvature of the particle surface and the system instability increases as the curvature grows [15,25]. As the system tries to lower the instability by decreasing the interfacial energy difference, it is more favorable for the ions to dissolve from metal or oxides from smaller particles and diffuse to and adsorb on the surface of the larger particles.

7.3.6. Effect of Initial Solution pH on Unusual Surface Features

In solutions with relatively high initial pHs (pH 8.4, and pH 10.6), formation of specific patterns occurs in a similar way to that observed at pH 6.0. At higher initial solution pHs, Liesegang rings are still observed on the nickel surface. These features initiate and propagate on the nickel surface in concentric circular patterns and rings. **Figure 7.22** and **Figure 7.23** show evidence of these features at pH 8.4 and pH 10.6 respectively. A detailed description of the structure, initiation and growth of these features is provided in Section 7.3.4 for pH 6.0.

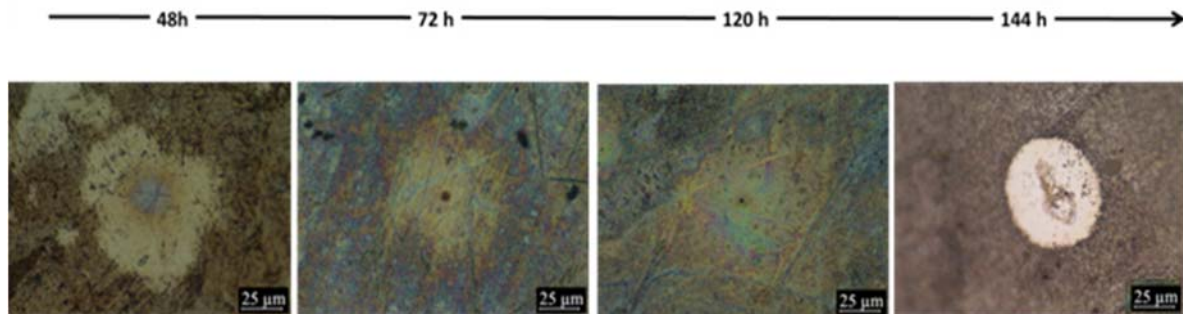


Figure 7.22: The circular surface features during the corrosion of nickel in solution with initial pH 8.4, in the presence of γ -radiation.

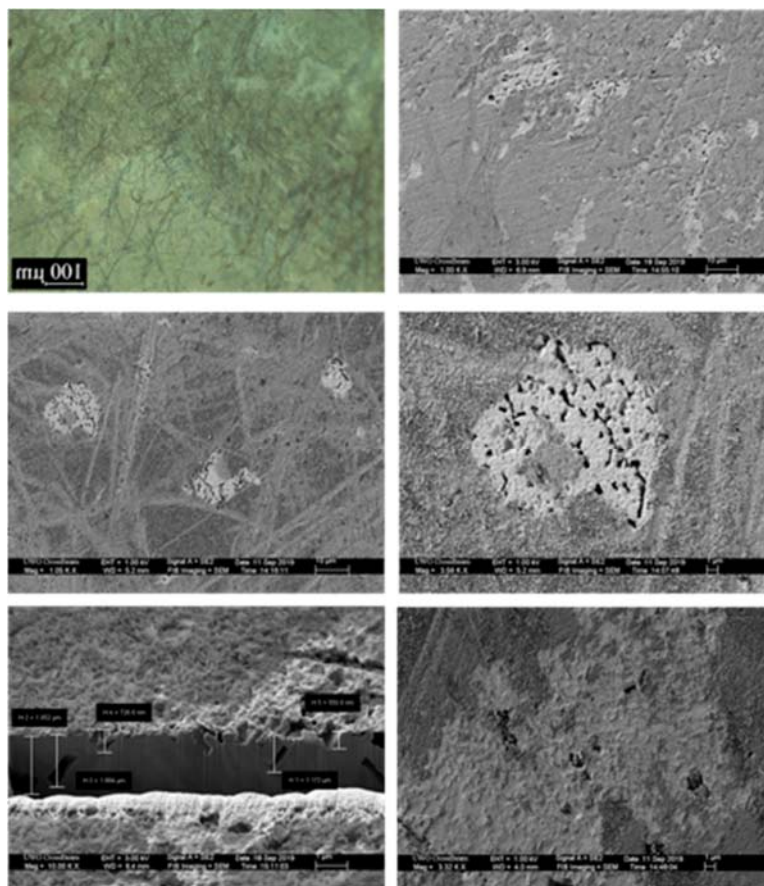


Figure 7.23: Nickel surface corroded at pH 10.6 in the presence of γ -radiation for 120 h. Particular features were observed on the sample surface in the form of wave patterns and circular concentric shapes.

Figure 7.22 shows the optical images of the surface Liesegang rings for pH 8.4. The rings start forming after 24 h of corrosion and remain on the surface over a long period (144 h of corrosion). Conversely, at pH 10.6, these morphological features on the surface (**Figure 7.23**) are mostly observed at longer corrosion times, when the solution pH has reached and remained at a low value which facilitate ion transport.

At both initial pH 8.4 and 10.6, the number density and the size of the surface features are lower than observed at pH 6.0. As mentioned earlier, one important

requirement for the formation of Liesegang rings is the presence of a gelatinous layer on the surface which can facilitate systemic feedback and coupling of solution reaction and mass transport processes. So, for both high solution pHs, due to the low nickel solubility, the gel layer transforms to a solid oxide layer earlier, and the required solution feedback processes do not occur in the solution. However, the presence of γ -radiation can facilitate systemic feedback between the chemical reactions and transport processes of nickel cations in solution. Thus, in the presence of γ -radiation some Liesegang features are observed at higher initial pHs, but with a lower number density than for pH 6.0.

The presence of Liesegang features on surfaces in non-buffered high pH solution indicates the importance of the effect of pH on formation of these features (compare with results of high pH in Chapter 6).

7.3.7. Liesegang Pattern Formation Via Ostwald Ripening

Ostwald ripening is a phenomenon in which smaller crystals dissolve, resulting in the growth of larger crystals. In other words, large crystals grow at the expense of smaller ones. The driving force is for the system to minimize the surface energy. Smaller particles have a larger surface area to volume ratio and therefore, have larger interfacial energy. Therefore, it is more favorable for the ions that constitute the crystals to desorb from the surface of the smaller particles and diffuse to and adsorb on the surface of the larger particles. A schematic representation of particle growth in the solution phase via Ostwald ripening process is presented in **Figure 7.24**.

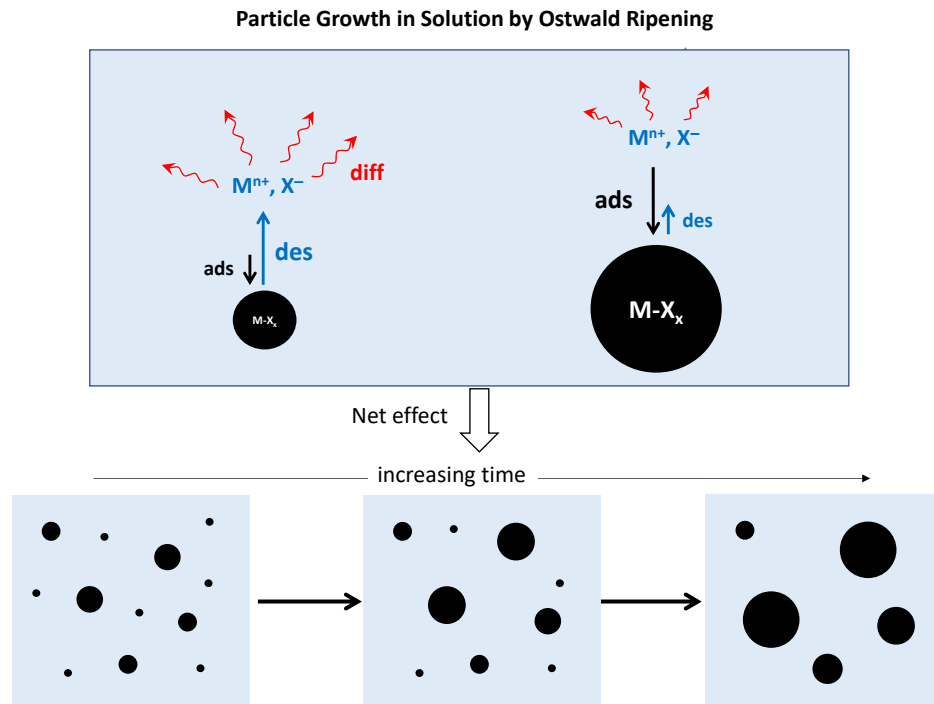
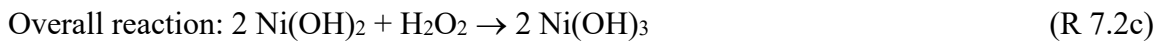
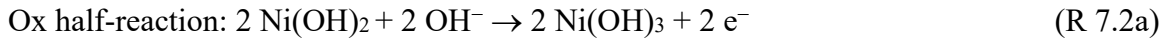


Figure 7.24: Schematic representation of particle growth in solution by Ostwald ripening [14]

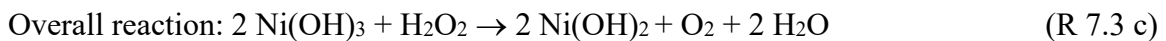
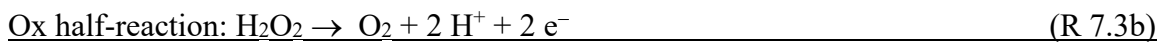
Ostwald ripening is a mechanism that can be involved in the overall nickel oxide growth mechanism. In a slow mass transport medium, oxide growth by Ostwald ripening can be coupled with the redox reactions of Ni^{2+} and Ni^{3+} species and we refer to this process as “redox-assisted Ostwald ripening” (as shown in **Figure 7.25**) [14]. This redox-assisted Ostwald ripening process can result in the formation of Liesegang bands consisting of not just one type of oxide, but bands of mixed hydroxides and oxides. Redox-assisted Ostwald ripening can occur more readily in the presence of γ -radiation. Gamma-radiation decomposes water into a range of redox-active species, of which H_2O_2 has the most significant effect on corrosion. Since H_2O_2 can be reduced ($\text{H}_2\text{O}_2 + 2 e^- \rightleftharpoons 2$

OH⁻) or oxidized ($\text{H}_2\text{O}_2 \rightleftharpoons \text{O}_2 + 2 \text{e}^- + 2 \text{H}^+$), it can effectively couple with the nickel redox half-reactions, thereby enhancing the redox-assisted Ostwald ripening process.

As described in Chapter 6, in kinetic stage 1, when the concentrations of metal oxidation products in the interfacial region are low, H₂O₂ acts primarily as an oxidant. In later stages, the oxidation and reduction of H₂O₂ can couple with the reduction of the metal oxidation product and the oxidation of a metal or metal cation with a lower oxidation state as shown below [8]:



Once enough Ni(OH)₃ has accumulated on the surface, its reduction to Ni(OH)₂ can effectively couple with the oxidation of H₂O₂ to O₂ as shown below:



In the presence of a continuous flux of γ -radiation, the concentration of H₂O₂ is maintained at a constant level and redox coupling of these reactions can occur resulting in the formation of more stable Ni oxides (Ni₃O₄ and Ni₂O₃). Because γ -radiation continuously produces H₂O₂, it can have a considerable impact on Ostwald-ripening and

Liesegang band formation (**Figure 7.26**). Because these phenomena involve metal cation diffusion, precipitation and redissolution, in the presence of radiation this process results in a prolonged period of dissolution and oxide growth [14].

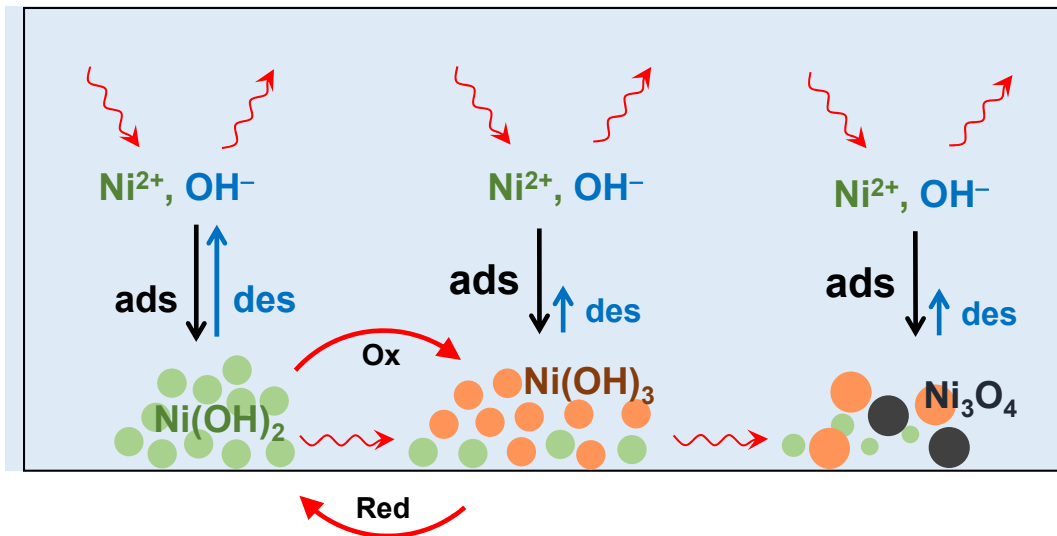


Figure 7.25: A schematic representation of redox-assisted Ostwald ripening.

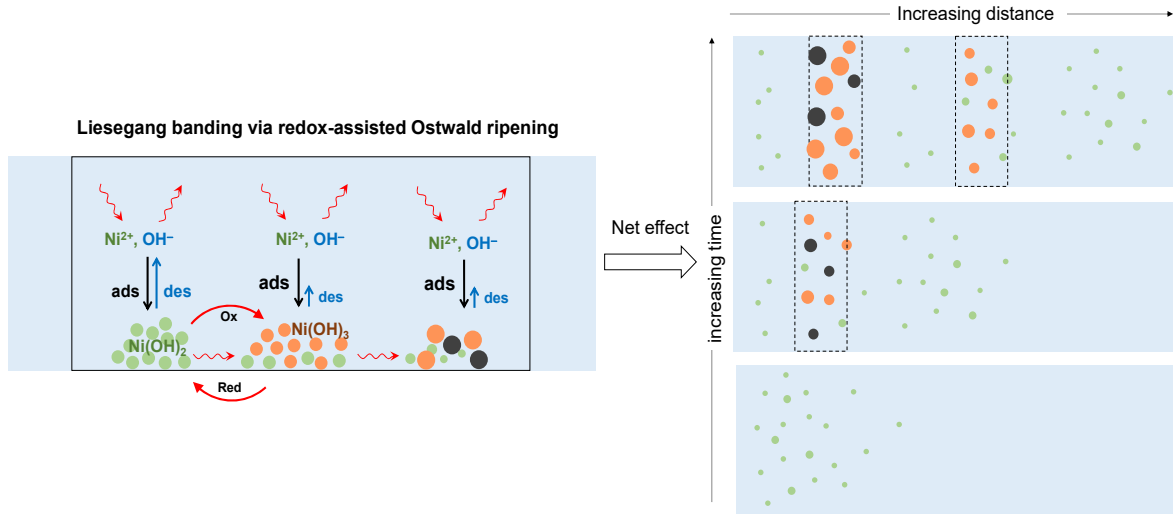


Figure 7.26: Liesegang banding via redox-assisted Ostwald ripening [14]

7.4. CONCLUSIONS

This chapter presents time-dependent nickel corrosion behaviour in non-buffered solutions in the presence and absence of γ -radiation. The results reveal several unusual observations that have not been reported in previous nickel corrosion studies. The observed behaviours are particularly unexpected in view of the known high corrosion resistance of nickel.

This non-linear dynamic behaviour in the presence and absence of radiation occurs in distinct kinetic stages. In Stage 1, the predominant corrosion process involves the oxidation of $\text{Ni}^0_{(m)}$ to $\text{Ni}^{2+}_{(aq)}$ at the metal surface (coupled with the reduction of oxidant present in the solution), and the transport of $\text{Ni}^{2+}_{(aq)}$ from the metal surface to the bulk solution. In this Stage, the nickel cations at the interface saturates and forms a hydrogel layer which facilitate initiation of surface features. In Stage 2 the concentration

of Ni^{2+} in the bulk solution increases at a faster rate until it reaches its saturation limit. At this stage the metal dissolution and oxide formation occur at the same time. In Stage 3, the Ni^{2+} undergoes hydrolysis forming nickel hydroxide ($\text{Ni}(\text{OH})_2$ and $\text{Ni}(\text{OH})_3$) in the solution phase that precipitates on the metal surface. This results in the decrease in the total amount of nickel in solution phase. In this stage oxide formation predominates over ion dissolution. Also, in the presence of gel layer, the oxidation of Ni^{2+} ions to higher oxidation states (Ni^{3+}) increases, resulting in $\text{Ni}^{\text{II}}/\text{Ni}^{\text{III}}$ hydroxide/oxides on the surface.

In the absence of radiation, the corrosion remained in Stage 1 due to the stabilization of the pH near the pKa of $\text{Ni}(\text{OH})_2$. Regardless of the initial pH, the solution pH eventually becomes constant and plateaus at pH 7.5-8.0 after 48 h of corrosion. This higher pH favours the formation of a $\text{Ni}(\text{OH})_2$ hydrogel that suppresses further dissolution. In the presence of γ -radiation, due to the decrease in the solution pH due to the production of H^+ via water radiolysis and ion hydrolysis process, nickel corrosion progresses through three different stages in which different elementary processes determine the overall corrosion rate.

The results indicate that nickel corrosion involves strong systemic feedback between nickel oxidation and ion diffusion. This systemic feedback leads to the formation of specific morphological features on the surface and non-linear nickel corrosion dynamics over long times. This behaviour is more pronounced in the presence of γ -radiation due to the decrease in pH.

7.5. REFERENCES

- [1] M. Momeni, Gamma-Radiation Induced Corrosion of Alloy 800, Electron. Thesis Diss. Repos. 5011, University West. Ontario. (2017). <https://doi.org/10.1016/j.psychres.2013.12.014>.
- [2] D. Guo, Corrosion Dynamics of Carbon Steel in Used Fuel Container Environments, Electron. Thesis Diss. Repos. 5897, University of Western Ontario. (2018).
- [3] J.C. Wren , A. Jean, M. Naghizadeh, L. Grandy, R. Morco, J.M. Joseph, M. Behazin, P.G. Keech, Radiation Induced Corrosion of Copper in Deep Geological Repositories, in: Waste Management Conference, Phoenix, Arizona, USA, 2019.
- [4] C.F. Baes, R.E. Mesmer., Hydrolysis of Cations, Wiley, 1976.
- [5] B. Beverskog, I. Puigdomenech, Revised Pourbaix diagrams for nickel at 25-300 °C, Corros. Sci. 39 (1997) 969–980. [https://doi.org/10.1016/S0010-938X\(97\)00002-4](https://doi.org/10.1016/S0010-938X(97)00002-4).
- [6] E. Cattaneo, B. Riegel, Chemistry, Electrochemistry, And Electrochemical Applications | Nickel, in: Encycl. Electrochem. Power Sources, Elsevier, 2009 https://doi.org/10.1063/9780735421578_app1.
- [7] Y. Miao, L. Ouyang, S. Zhou, L. Xu, Z. Yang, M. Xiao, R. Ouyang, Electrocatalysis and electroanalysis of nickel, its oxides, hydroxides and oxyhydroxides toward small molecules, Biosens. Bioelectron. 53 (2014) 428–439. <https://doi.org/10.1016/j.bios.2013.10.008>.
- [8] A.M. Gadalla, T.W. Livingston, Thermal behavior of oxides and hydroxides of iron and nickel, Thermochim. Acta. 145 (1989) 1–9. [https://doi.org/10.1016/0040-6031\(89\)85121-4](https://doi.org/10.1016/0040-6031(89)85121-4).
- [9] B. Subramanian, M. Mohamed Ibrahim, V. Senthilkumar, K.R. Murali, V. Vidhya, C. Sanjeeviraja, M. Jayachandran, Optoelectronic and electrochemical properties of nickel oxide (NiO) films deposited by DC reactive magnetron sputtering, Phys. B Condens. Matter. 403 (2008) 4104–4110. <https://doi.org/10.1016/j.physb.2008.08.014>.
- [10] S. Pizzini, R. Morlotti, Thermodynamic and Transport Properties of Stoichiometric and Nonstoichiometric Nickel Oxide, J. Electrochem. Soc. 114 (1967) 1179. <https://doi.org/10.1149/1.2426441>.
- [11] W.L. Dudley, Nickelo-nickelic hydrate, Ni₃O₄.2H₂O, J. Am. Chem. Soc. 18 (1896) 901–903. <https://doi.org/10.1021/ja02096a003>.
- [12] T.P. Murphy, M.G. Hutchins, Oxidation states in nickel oxide electrochromism, Sol. Energy Mater. Sol. Cells. 39 (1995) 377–389. [https://doi.org/10.1016/0927-0248\(96\)80003-1](https://doi.org/10.1016/0927-0248(96)80003-1).

- [13] J.A. Dean, *Langes Handbook of Chemistry*, 15th ed., New York, 1952.
<https://doi.org/10.1134/1.567061>.
- [14] Y.G. Shin, *Nonlinear Dynamics of Carbon Steel Corrosion under Gamma Radiation*, Electron. Thesis Diss. Repos. 7339, University of Western Ontario (2020).
- [15] D.S. Chernavskii, A.A. Polezhaev, S.C. Müller, A model of pattern formation by precipitation, *Phys. D Nonlinear Phenom.* 54 (1991) 160–170.
[https://doi.org/10.1016/0167-2789\(91\)90115-P](https://doi.org/10.1016/0167-2789(91)90115-P).
- [16] M.C. Biesinger, B.P. Payne, L.W.M. Lau, A. Gerson, R.S.C. Smart, X-ray photoelectron spectroscopic chemical state Quantification of mixed nickel metal, oxide and hydroxide systems, *Surf. Interface Anal.* 41 (2009) 324–332.
<https://doi.org/10.1002/sia.3026>.
- [17] P. Taylor, Ostwald Ripening In Emulsions, *Adv. Colloid Interface Sci.* 75 (1998) 107–163.
- [18] J.H. Yao, K.R. Elder, H. Guo, M. Grant, Theory and simulation of Ostwald ripening, *Phys. Rev.* 47 (1993) 14110–14125.
- [19] J.B. Keller, Liesegang rings and a theory of fast reaction and slow diffusion, in: *Dyn. Model. React. Syst.*, Academic Press, 1980: pp. 211–224.
- [20] K.H. Stern, The Liesegang Phenomenon, *Chem. Rev.* 54 (1954) 70–99.
- [21] H.K. Henisch, *In Vitro Veritas: Crystals in Gels and Liesegang Rings*, Cambridge University Press, 1988.
- [22] H.K. Henisch, Liesegang Ring Formation In Gels, *J. Cryst. Growth.* (1986) 279–289.
- [23] E. Nakouzi, O. Steinbock, Self-organization in precipitation reactions far from the equilibrium, *Sci. Adv.* (2016) e1601144.
- [24] S. Sadek, R. Sultan, Precipitation patterns in reaction-diffusion systems (Ed.: I. Lagzi), *Research Signpost*, 2010., Lagzi, I., Ed. Res. Signpost, Trivandrum. (2010) 1–43.
- [25] A.A. Polezhaev, S.C. Müller, Complexity of precipitation patterns: Comparison of simulation with experiment, *Chaos.* 4 (1994) 631–636.
<https://doi.org/10.1063/1.166040>.
- [26] S. Brantley, J. Kubicki, A. White, *Kinetics of Water-Rock Interaction*, Springer New York, 2007.

CHAPTER 8

THESIS SUMMARY AND FUTURE WORK

8.1. SUMMARY

The goal of this thesis was to develop a fundamental understanding of the effect of γ -radiation and solution environment on the corrosion behaviour of pure nickel. This study will provide a foundation for understanding the corrosion behaviour of nickel-based alloys and predicting their long-term corrosion behaviour and performance in the presence of a continuous flux of ionizing radiation.

Aqueous corrosion is an electrochemical process involving many elementary steps, which include interfacial transfer of electrons and metal atoms at the metal-solution boundary, solution reactions (hydrolysis), mass transport processes, and oxide particle nucleation and growth. Different solution parameters affect the kinetics of the elementary steps differently, which leads to different metal oxidation paths and overall oxidation rates. The kinetics of the elementary reactions are not independent of each other but strongly coupled, which leads to a cyclic feedback loop (systemic feedback) between different elementary steps, and therefore the overall metal oxidation rate does not follow linear dynamics. Therefore, to predict the long-term corrosion behaviour of metals and

alloys, it is important to identify the key elementary processes that control the overall corrosion rate.

In order to do this, this study examined the effect of ionic strength, temperature, pH and γ -radiation. A combination of electrochemical techniques and coupon-exposure tests combined with post-test analyses of the surface and solution phases was used in this study. The key findings from each chapter are discussed below.

In Chapter 4, the evolution of the elementary reactions and mass transfer/transport steps that control the overall metal oxidation rate was investigated using corrosion potential measurements and current vs potential relationships under potentiodynamic and potentiostatic conditions. The solution parameters investigated were pH, ionic strength, temperature, and γ -radiation. Different solution parameters affect the kinetics of the elementary steps differently, which alters metal oxidation pathways and overall oxidation rates. The pH of the solution can affect the rate and yield of electron/metal atom transfer, as well as hydrolysis and metal hydroxide precipitation. Temperature has a minor effect on interfacial charge transfer but can increase the rate of thermal processes. Ionic strength affects ion mobility through its effect on concentration gradients, and therefore an increase in ionic strength increases the rate of metal cation transport from the interface to the bulk solution.

The results shows that E_{corr} does not stay at the initial (pseudo-) steady state but evolves to (a) different steady state(s) as metal oxidation progresses and metal oxidation products accumulate and undergo reactions. The number of steady states that the metal oxidation system passes through before reaching the final steady state, the durations of the steady states, and the steady-state values depend on solution parameters. The E_{corr}

values at the steady states coincide with one of the E_{rxn}^{eq} of the half-reactions involving metal hydroxides, or the midpoint between two of the E_{rxn}^{eq} values. In a given solution redox environment, pH affects both the initial and final steady state E_{corr} , whereas temperature has a negligible effect on the initial E_{corr} but a more significant effect on the final E_{corr} . The transitions from the initial to the intermediate, and to the final steady state occurred earlier at higher pHs and at a higher temperature. In the presence of γ -radiation, the transition from one steady state to another occurs earlier and more steady states are observed.

The results show that the overall nickel oxidation dynamics evolve through different dynamic phases (or dynamic states) as corrosion progresses. Dynamic state refers to the ranges of electrochemical/chemical conditions under which the overall metal oxidation rate may change but the elementary (rate-determining) steps that comprise the overall process, and the (pseudo-) 1st-order rate coefficients of the individual steps, do not change within the state. (An analogy: a dynamic state is equivalent to an electrical circuit, consisting of a series of specific RC (or impedance) components; each elementary step is equivalent to each RC component; the chemical conditions (chemical potential or free energy of reaction) are equivalent to the external voltage applied; R to the 1st-order rate coefficient; i to the overall rate; (C is to the rate of change in the overall rate (i) when the conditions (V_{ext}) change)). In Dynamic Phase I the elementary steps that control the overall metal oxidation rate are the net electron/metal atom transfer at the metal-solution boundary ($Ni^0_{(m)} \rightleftharpoons Ni^{2+}_{(solv)} + 2 e^-$) and diffusion of Ni^{2+} from the interfacial region into the bulk solution, and hydrolysis of Ni^{2+} to produce $Ni(OH)_2$ which can condense as colloids. Dynamic Phase II represents a dynamic state of metal oxidation involving not

only the elementary steps that comprise Dynamic Phase I, but also additional elementary steps involving the Ni^{2+} hydrolysis product $\text{Ni}(\text{OH})_2$. The additional steps include interfacial electron transfer ($\text{Ni}^{2+}/\text{Ni}(\text{OH})_2 + \text{OH}^- \rightleftharpoons \text{Ni}(\text{OH})_3 + \text{e}^-$), which accelerates the precipitation of mixed $\text{Ni}^{\text{II}}/\text{Ni}^{\text{III}}$ hydroxide, growing a hydrogel network. In this phase, the kinetics of the elementary steps are strongly coupled, and it is therefore not valid to use linear dynamics to describe the overall metal oxidation dynamics as a function of the independent kinetics of individual steps. Dynamic Phase III occurs after sufficient mixed $\text{Ni}^{\text{II}}/\text{Ni}^{\text{III}}$ hydroxide colloids have precipitated to allow nucleation and growth as solid crystalline particles on the surface. In this dynamic phase, metal oxidation is generally suppressed by the growth of oxide on the metal surface. The type, morphology and size of oxide that grows depends strongly on the relative rates of Ni^{II} and Ni^{III} production in the interfacial region.

Dynamic Phase III occurs after sufficient mixed $\text{Ni}^{\text{II}}/\text{Ni}^{\text{III}}$ hydroxide colloids have precipitated to allow nucleation and growth as solid crystalline particles on the surface. In this dynamic phase, metal oxidation is generally suppressed by the growth of oxide on the metal surface. The type, morphology and size of oxide that grows depends strongly on the relative rates of Ni^{II} and Ni^{III} production in the interfacial region.

In Chapter 5, the combined effect of pH and ionic strength (I_s) on the evolution of Ni oxidation is investigated under Ar-saturated conditions at pH 6.0 or pH 10.6 at 80 °C using electrochemical techniques.

The time-dependent behaviors of E_{corr} showed that Ni^0 is oxidized to $\text{Ni}(\text{OH})_2$ and $\text{Ni}(\text{OH})_3$ in Ar-purged solutions. The E_{corr} coincided with the E_{rxn}^{eq} of metal redox

half-reactions, $E_{\text{Ni}^0 \rightleftharpoons \text{Ni}(\text{OH})_2}^{eq}$ at pH 6.0 and $E_{\text{Ni}^0 \rightleftharpoons \text{Ni}(\text{OH})_3}^{eq}$ at pH 10.6. The overall effects of pH and I_s on E_{corr} depend on their effects on the kinetics of the elementary steps and the saturation capacity for Ni^{2+} in the interfacial region. The metal cation saturation capacity depends strongly on pH. At pH 6.0 the solubility of Ni^{2+} is about four orders of magnitude higher than at pH 10.6. Hence, at pH 6.0 the Ni^{2+} concentration in the interfacial region remains below its saturation limit and overall metal oxidation does not progress beyond the oxidation of Ni^0 to $\text{Ni}^{2+}/\text{Ni}(\text{OH})_2$. The overall rate of metal oxidation consists of interfacial charge (electron/metal atom) transfer (abbreviated as “M1” and “M2”) and transport of Ni^{2+} (abbreviated as “trans”) (Dynamic Phase I). At pH 10.6, the solubility of Ni^{2+} is very low and therefore, the Ni^{2+} concentration in the interfacial region reaches its saturation limit nearly instantly. Once the interfacial region become saturated with Ni^{2+} , metal atoms cannot be transferred from the metal to the solution and the hydrolysis equilibrium (abbreviated “hyd”) leads to the formation of $\text{Ni}(\text{OH})_2$ which precipitates as hydroxide salt (abbreviated “gel”) and is oxidized to $\text{Ni}(\text{OH})_3$. The overall metal oxidation consists of not only (M1), (trans) and (hyd), but also (M2) and (gel) (in Dynamic Phase II). The effect of I_s on the overall metal oxidation rate is through its effect on the transport of Ni^{2+} (trans), which is coupled strongly with other elementary steps. Due to systemic feedback between different elementary steps the rates of individual steps change with time. At pH 10.6, (M2) becomes an important RDS even in the early stages of corrosion, and $E_{corr}(\tau_0)$ reaches a value near $E_{\text{Ni}^0 \rightleftharpoons \text{Ni}(\text{OH})_3}^{eq}$.

The observed changes in E_{corr} , $E_{i=0,PD}$ and the $\log|i_{meas-PD}|$ vs E_{elec} relationship with t_{corr} collectively indicate that the elementary reaction and transport steps that comprise the overall metal oxidation process evolve as corrosion progresses.

Because pH and I_s affect the kinetics of different steps differently, the effect of I_s on the overall metal oxidation rate is different at different pHs. The time-dependent behaviour of $|i_{meas-PS}|$ as a function of E_{elec} , and the potential-dependent behaviours of $|i_{meas-CV}|$ and $|i_{meas-PD}|$ obtained as a function of t_{corr} further support the elementary steps that have been identified as controlling the overall corrosion behaviour at pH 6.0 (Dynamic Phase I) and pH 10.6 (Dynamic Phase II).

In Chapter 6, the effect of ionic strength and pH on the long-term corrosion dynamics of nickel was studied in small stagnant solution volumes by examining the changes in oxide composition and morphology and the dissolved (and dispersed) Ni^{2+} concentration as a function of corrosion time. The results show that at pH 6.0, the main corrosion pathway is metal ion dissolution whereas at higher pH (8.4 and 10.6) oxide formation predominates. The presence of γ -radiation affects the overall metal oxidation rate primarily via production of H_2O_2 . Radiation also alters the oxide film composition, thickness, and morphology at all pHs.

This study has also revealed the non-linear nature of nickel corrosion dynamics over long time periods. These non-linear dynamics can be influenced by changing the solution ionic strength and applying γ -radiation. The non-linear behaviour occurs as a result of coupling between the redox reactions and mass transport processes. Chemical oscillation resulting in periodic ion precipitation and dissolution is one consequence of this coupling, which leads to the formation of surface features such as Liesegang rings on the nickel surface at pH 6.0, particularly at high I_s and in the presence of γ -radiation.

In Chapter 7, the long-term corrosion dynamics of nickel in low ionic strength non-buffered solution are studied in small stagnant volumes in the presence and absence of γ -radiation by examining the changes in oxide composition and morphology and the dissolved (and dispersed) Ni^{2+} concentration as a function of corrosion time.

The results show that the long-term corrosion of nickel progress through three distinct kinetic stages. In Stage 1, the predominant corrosion process involves the oxidation of $\text{Ni}^0_{(m)}$ to $\text{Ni}^{2+}_{(aq)}$ at the metal surface (coupled with the reduction of oxidant present in the solution), and the transport of $\text{Ni}^{2+}_{(aq)}$ from the metal surface to the bulk solution. In this stage, the nickel cations at the interface saturate and form a hydrogel layer which facilitates the initiation of surface features. In Stage 2, the concentration of Ni^{2+} in the bulk solution increases at a faster rate until it reaches its saturation limit. During this stage, metal dissolution and oxide formation occur simultaneously. In Stage 3, Ni^{2+} undergoes hydrolysis forming nickel hydroxide ($\text{Ni}(\text{OH})_2$ and $\text{Ni}(\text{OH})_3$) in the solution phase that then precipitates on the metal surface. This results in a decrease in the total amount of nickel in the solution phase. In this stage oxide formation predominates over ion dissolution. Also, in the presence of the gel layer, the oxidation of Ni^{2+} ions to a higher oxidation state (Ni^{3+}) increases, resulting in $\text{Ni}^{\text{II}}/\text{Ni}^{\text{III}}$ hydroxide/oxides on the surface.

8.2. OVERALL CONCLUSION

This study has demonstrated that the influence of one solution parameter (e.g., pH) on metal oxidation is dependent on other parameters (e.g., temperature and redox environment induced by radiolysis). The synergetic effect of different solution parameters on metal oxidation arises because each elementary reaction or mass transport step has its own unique kinetic behaviour and different solution parameters influence the kinetics of individual steps differently. Because the later reactions of initial and intermediate products can affect the kinetics of preceding steps, systemic feedback between different elementary steps can be established at later times leading to an acceleration or deceleration of the overall metal oxidation. Hence, it is the combination of solution parameters that dictates how fast the system can transition through different dynamic phases, and which final dynamic phase the overall metal oxidation process can reach.

The results show that the overall metal oxidation occurs through a series of elementary rate-determining steps (RDS) with some steps occurring in parallel. Because metal oxidation involves interfacial transfer of metal atoms and the intermediate oxidation products can undergo their own chemical processes, the rate determining steps (RDS) that comprise the overall oxidation process can evolve as the intermediate products accumulate in the interfacial region. That is, the set of rate determining steps that determine the steady state of the reaction system can change with corrosion time even under specific corrosion conditions. The metal oxidation dynamic system may transition from one (pseudo-) steady state to another before it reaches the final steady state. The final steady state (dynamic phase) the system reaches, and how fast the system

passes through intermediate steady states (kinetic stages) to reach the final steady state, depend on the solution reaction environments in the interfacial region.

8.3. FUTURE WORK

This work has improved the overall mechanistic understanding of nickel corrosion and how solution parameters, temperature and γ - radiation affect the elementary processes. The long-term goal of the wider project which this thesis project contributes to is to develop a high-fidelity corrosion dynamic model that can predict the long-term corrosion behaviour of nickel and nickel-based alloys. The results gathered in this thesis will be used to develop this model.

APPENDIX A: THERMODYNAMIC DATA OF NICKEL REDOX SPECIES

The connection between standard potential and Gibbs free energy are directly related in the equation Eq. A1 which ΔG^o is the change in Gibbs free energy, n is the numbers of electrons, F is Faraday constant and E^o is the standard potential. The values of ΔG_f^o (Gibbs free energy of formation) at 25 and 80 °C are listed in Table A1.

$$\Delta G^o = -nFE^o \quad (\text{Eq. A1})$$

By having the E^o of a redox reaction, equilibrium potential of the reaction can be expressed by the Nernst equations (e.g. R. A1 and Eq. A2):



$$E_{rxn}^{eq} = E^o - \frac{RT}{nF} \frac{[B]^b [H_2O]^d}{[A]^a [H^+]^m} \quad (\text{Eq. A2})$$

Which E_{rxn}^{eq} is the equilibrium potential of a redox reaction, R is the gas constant and a, b, c and d are the numbers of moles of species A, B, C and D.

Table A1: Gibbs free energy of formation for the system nickel-water at 25 °C (298.15 K) and 80 °C (353.15 K)[1–3].

T(K)	$\Delta_f G_m^0$ Ni (<i>cr</i>) $\left(\frac{kJ}{mol}\right)$	$\Delta_f G_m^0$ H₂O (<i>l</i>) $\left(\frac{kJ}{mol}\right)$	$\Delta_f G_m^0$ H⁺ (<i>l</i>) $\left(\frac{kJ}{mol}\right)$	$\Delta_f G_m^0$ Ni(OH)₂ (<i>cr</i>) $\left(\frac{kJ}{mol}\right)$	$\Delta_f G_m^0$ Ni(OH)₃ (<i>cr</i>) $\left(\frac{kJ}{mol}\right)$	$\Delta_f G_m^0$ Ni₃O₄ (<i>cr</i>) $\left(\frac{kJ}{mol}\right)$
298.15	0	-237.19	0	-458.93	-590.31	-711.91
353.15	-1.7	-241.39	0.56	-462.27	-598.10	-720.25

To determine the Gibbs free energy formation at temperature T_2 (e.g. 80 °C) the equation Eq. A3 is used:

$$\Delta G_f^0(T_2) = \Delta G_f^0(298.15K) - (T_2 - 298.15K)S^0(298.15K) - T_2 \int_{298.15}^{T_2} \frac{C_p}{T} dT + \int_{298.15}^{T_2} C_p dT \quad (\text{Eq. A3})$$

Which $\Delta G_f^0(T_2)$ and $\Delta G_f^0(298.15K)$ are the Gibbs free energy of formation at T_2 and 298.15K respectively, C_p is the heat capacity and $S^0(298.15K)$ is the Entropy of the compound at 298.15K. The value of S^0 and C_p of nickel-water system are listed in Table A2 and A3.

Table A2: Entropy of species in nickel-water system at 298.15K [1,2,4].

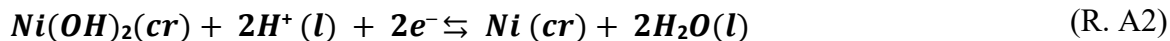
T(K)	S_m^0 <i>Ni</i> (<i>cr</i>) $\left(\frac{J}{K \cdot mol}\right)$	S_m^0 <i>H₂O</i> (<i>l</i>) $\left(\frac{J}{K \cdot mol}\right)$	S_m^0 <i>H⁺</i> (<i>l</i>) $\left(\frac{J}{K \cdot mol}\right)$	S_m^0 <i>Ni(OH)₂</i> (<i>cr</i>) $\left(\frac{J}{K \cdot mol}\right)$	S_m^0 <i>Ni(OH)₃^{-*}</i> (<i>cr</i>) $\left(\frac{J}{K \cdot mol}\right)$	S_m^0 <i>Ni₃O₄</i> (<i>cr</i>) $\left(\frac{J}{K \cdot mol}\right)$
298.15	30.12	70.08	-22.20	52.9	-133	140.0

Table A3: Heat capacity of species in nickel-water system at 298.15K [1,2].

Compound	$\Delta C_p^o(T) = a + bT + cT^{-2}$ (<i>J/mol.K</i>)		
	<i>a</i>	<i>b</i>	<i>c</i>
<i>Ni (cr)</i>	16.98	29.5×10^3	–
<i>Ni(OH)₂</i>	90	–	–
<i>Ni(OH)₃^{-*}</i>	300	–	–
<i>Ni₃O₄ (cr)</i>	28.0	–	–
<i>H₂O (l)</i>	75.44	–	–
<i>H⁺</i>	-71	–	–

*Entropy and ΔC_p used for ΔG_{T2} calculations are for ionic forms of Ni(OH)₃.

The followings are the equations and calculations for nickel redox reaction equilibrium potentials:



298.15 K:

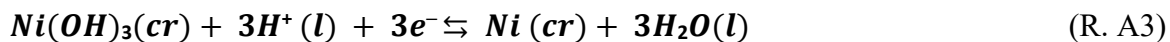
$$\Delta G_f = 2 \times -237.19 + 458.93 = -15.45 \text{ kJ/mol}$$

$$E^0 = \frac{15.27 \times 1000}{2 \times 96500} = 0.08 V_{SHE}$$

353.15 K:

$$\Delta G_f = 2 \times -241.39 - 1.7 + 462.27 - 2 \times 0.56 = -23.33 \text{ kJ/mol}$$

$$E^0 = \frac{20.33 \times 1000}{2 \times 96500} = 0.12 V_{SHE}$$



298.15 K:

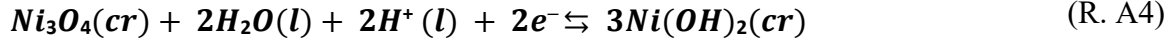
$$\Delta G_f = 3 \times -237.19 + 590.31 = -131.23 \text{ kJ/mol}$$

$$E^0 = \frac{131.23 \times 1000}{3 \times 96500} = 0.42 V_{SHE}$$

353.15 K:

$$\Delta G_f = 3 \times -241.39 - 1.7 + 598.10 - 3 \times 0.56 = -129.45 \text{ kJ/mol}$$

$$E^0 = \frac{129.45 \times 1000}{3 \times 96500} = 0.447 V_{SHE}$$



298.15 K:

$$\Delta G_f = 3 \times -458.93 + 711.91 + 2 \times 237.19 = -190.50 \text{ kJ/mol}$$

$$E^0 = \frac{190.5 \times 1000}{2 \times 96500} = 0.98 V_{SHE}$$

353.15 K:

$$\Delta G_f = 3 \times -462.27 + 720.25 + 2 \times 241.39 - 2 \times 0.56 = -184.90 \text{ kJ/mol}$$

$$E^0 = \frac{184.90 \times 1000}{2 \times 96500} = 0.96 V_{SHE}$$

A.1. Reference

- [1] H. Gamsjäger, F.J. Mompean, Issy-les-Moulineaux (France), Chemical thermodynamics of nickel, OECD Nuclear Energy Agency (2005).
- [2] B. Beverskog, I. Puigdomenech, Revised Pourbaix diagrams for nickel at 25-300°C, Corros. Sci. 39 (1997) 969–980. [https://doi.org/10.1016/S0010-938X\(97\)00002-4](https://doi.org/10.1016/S0010-938X(97)00002-4).
- [3] Noel de Nevers, Physical and Chemical Equilibrium for Chemical Engineers, Wiley, 2012.
- [4] D. Cubicciotti, Potential-pH diagrams for alloy-water systems under LWR conditions, J. Nucl. Mater. 201 (1993) 176–183. [https://doi.org/10.1016/0022-3115\(93\)90173-V](https://doi.org/10.1016/0022-3115(93)90173-V)

RAZIEH KARIMIHAGHIGHI

EDUCATION

Western University, London, Canada, Sep 2015 – April 2021

Ph.D. Candidate, Physical/Analytical Chemistry (Corrosion)

Shiraz University, Shiraz, Iran, Sep 2010 – Aug 2013

M.Sc. Materials Science and Engineering (Corrosion)

Azad University, Marvdasht, Iran, Sep 2006 – Aug 2010

B.Sc., Bachelor of Science, Chemistry

AWARDS AND SCHOLARSHIPS

Women in Nuclear Conference Award

2019-2020 University of Western Ontario

Women in Nuclear Scholarship

2018-2019 University of Western Ontario

Women in Nuclear Travel Award

2018-2019 University of Western Ontario

Queen Elizabeth II Ontario Graduate Scholarship

2018-2019 University of Western Ontario

Undergraduate Research Scholarship

2010-2011 Azad University, Fars, Iran

WORK EXPERIENCES

1. Research Assistant

University of Western Ontario

2015-present

2. Teaching Assistant

University of Western Ontario

2015-2020

Courses: • Instrumental Analytical Chemistry (Chem 3372) • Analytical Chemistry (Chem 2272) • Discovering Chemical Structure (Chem 1301) • Discovering Chemical Energetics (Chem1302).

3. Research Assistant

Shiraz University, Shiraz, Iran

2010-2013

PUBLICATIONS

1. **R.Karimihaghighi**, J.C. Wren, “The effects of Radiation, pH and Solution Ionic Strength on Corrosion and Oxide Formation on Pure Nickel at 150°C “ in preparation
 2. **R.Karimihaghighi**, J.C. Wren, “Non-Linear Effects of Solution Parameters on Nickel Oxidation “ in preparation
 3. **R.Karimihaghighi**, Brianna Rector, J.C. Wren, “Non-Linear Corrosion Dynamic Model (CDM): Beyond Interfacial Transfer of Electrons and Aqueous Transport of Metal Cations “ in preparation
 4. **R.Karimihaghighi**, J.C. Wren, “The effects of pH and Radiation on Corrosion and Oxide Formation on Pure Nickel at 80°C in buffer solutions “ in the proceedings of 41st Annual Conference of the Canadian Nuclear Society, June, 4-7, 2017, 5 pages
 5. **R.Karimihaghighi**, J.C. Wren, “The effects of Temperature and Radiation on Corrosion and Oxide Formation on Pure Nickel “ in the proceedings of 40th Annual Conference of the Canadian Nuclear Society, June 19-22, 2016, 5 pages
-

CONFERENCES

Oral presentation

- 1- **R.KarimiHaghighi** and J.C. Wren, “Effect of Radiation on Nickel Corrosion in Non-buffered Solution Near Neutral pH”. ECS Student Section 2019, London, ON, Dec 13, 2019
- 2- **R.KarimiHaghighi** and J.C. Wren, “The Time Dependence Study on The Effects of Radiation on Corrosion and Oxide Formation on Pure Nickel in Buffered and Non-buffered Solution Near Neutral pH”. ECS Student Section 2018, London, ON, Dec 13, 2018
- 3- **R.KarimiHaghighi**, T. Do and J.C. Wren, “The Time Dependence Study on The Effects of Radiation on Corrosion and Oxide Formation on Pure Nickel in Buffered and Non-buffered Solution”. Nace Southern Ontario Student Section 2018, Toronto, ON, July 26-27, 2018
- 4- **R.KarimiHaghighi** and J.C. Wren, “The Time Dependence Study on The Effects of pH, Temperature and Radiation on Corrosion and Oxide Formation on Pure Nickel”. ECS Student Section 2017, London, ON, Dec 14, 2017
- 5- **R.KarimiHaghighi** and J.C. Wren, “The Time Dependence Study on The Effects of pH, Temperature and Radiation on Corrosion and Oxide Formation on Pure Nickel”. Nace Southern Ontario Student Section 2017, Hamilton, ON, July 19-20, 2017
- 6- **R.KarimiHaghighi** and J.C. Wren, “The Effects of pH, Temperature and Radiation on Corrosion and Oxide Formation on Pure Nickel”. Nace Southern Ontario Student Section 2016, London, ON, July 28, 2016

Poster Presentation

- 1- **R.KarimiHaghighi** and J.C Wren. **Poster**, “New Approach to Study Corrosion of Steam Generator”. UNENE Conference, Toronto, December 12-13, 2019
- 2- **R.KarimiHaghighi** and J.C Wren. **Poster**, “The effects of Temperature, pH and Radiation on Corrosion and Oxide Formation on Pure Nickel”. UNENE Conference, Toronto, December 11-12, 2017
- 3- **R.KarimiHaghighi** and J.C. Wren, **Poster**, ” The Time Dependence Study on The Effects of pH, Temperature and Radiation on Corrosion and Oxide Formation on Pure Nickel”. Nace Southern Ontario Student Section 2017, Hamilton, ON, July 19-20, 2017
- 4- **R.KarimiHaghighi** and J.C Wren. **Poster**, “The effects of pH and Radiation on Corrosion and Oxide Formation on Pure Nickel at 80°C in buffer solutions”. Canadian Nuclear Society (CNS) conference 2017, Niagara Falls, ON, June, 4-7, 2017
- 5- **R.KarimiHaghighi**, M.Momeni, J.C Wren. **Poster**, “The effects of pH, Temperature and Radiation on Corrosion and Oxide Formation on Pure Nickel”. CSC Conference 2017, Toronto, ON, May 28- June 1, 2017
- 6- **R.KarimiHaghighi**, M.Momeni, J.C Wren. **Poster**, “The effects of Temperature and Radiation on Corrosion and Oxide Formation on Pure Nickel”. Canadian Nuclear Society (CNS) conference 2016, Toronto, ON, June, 19-22, 2016